

Mechanistic characterization of photoisomerization reactions in organic molecules and photoreceptors

Dissertation
zur Erlangung des Doktorgrades
der Naturwissenschaften

Vorgelegt beim Fachbereich
Biochemie, Chemie und Pharmazie
der Johann Wolfgang Goethe-Universität
in Frankfurt am Main

von

Tobias Fischer
aus Frankfurt am Main

Frankfurt am Main 2023
(D30)

Vom Fachbereich Biochemie, Chemie und Pharmazie der Johann Wolfgang Goethe-Universität als Dissertation angenommen

Dekan: Prof. Dr. Clemens Glaubitz

1. Gutachter: Prof. Dr. Josef Wachtveitl

2. Gutachter: Prof. Dr. Jens Bredenbeck

Datum der Disputation: 14.11.2023

Publications

Peer-reviewed publications as first or co-first author (indicated by *):

- [I] **The interplay between chromophore and protein determines the extended excited state dynamics in a single-domain phytochrome**
C. Slavov*, T. Fischer*, A. Barnoy*, H. Shin*, A.G. Rao, C. Wiebeler, X. Zeng, Y. Sun, Q. Xu, A. Gutt, K.-H. Zhao, W. Gärtner, X. Yang, I. Schapiro, J. Wachtveitl
Proc. Natl. Acad. Sci. USA **2020**, 117(28), 16356-16362.
DOI: 10.1073/pnas.1921706117

- [II] **Effect of the PHY Domain on the Photoisomerization Step of the Forward $P_r \rightarrow P_{fr}$ Conversion of a Knotless Phytochrome**
T. Fischer, Q. Xu, K.-H. Zhao, W. Gärtner, C. Slavov, J. Wachtveitl
Chem. Eur. J. **2020**, 26, 17261-17266.
DOI: 10.1002/chem.202003138

- [III] **Ultrafast Photoconversion Dynamics of the Knotless Phytochrome *SynCph2***
T. Fischer, L.J.G.W. van Wilderen, P. Gnau, J. Bredenbeck, L.-O. Essen, J. Wachtveitl, C. Slavov
Int. J. Mol. Sci. **2021**, 22, 10690-10704.
DOI: 10.3390/ijms221910690

- [IV] **Influence of the PHY domain on the ms-photoconversion dynamics of a knotless phytochrome**
T. Fischer, L. Köhler, T. Ott, C. Song, J. Wachtveitl, C. Slavov
Photochem. Photobiol. Sci. **2022**, 21, 1627-1636.
DOI: 10.1007/s43630-022-00245-9

- [V] **Conserved Tyrosine in Phytochromes controls the Photodynamics through Steric Demand and Hydrogen Bonding Capabilities**
T. Fischer, L. Köhler, P.D. Engel, C. Song, W. Gärtner, J. Wachtveitl, C. Slavov
Biochim. Biophys. Acta - Bioenerg. **2023**.
DOI: 10.1016/j.bbabi.2023.148996

[VI] **Mechanistic Elucidation of the Hula-Twist Photoreaction in Hemithioindigo**

T. Fischer*, J. Leitner*, A. Gerwien*, P. Mayer, A. Dreuw, H. Dube, J. Wachtveitl

J. Am. Chem. Soc. **2023**, 145, 14811-14822.

DOI: 10.1021/jacs.3c03536

Conference Contributions

- **ESP-IUPB World Congress - "Light and Life"**
Barcelona, Spain, 25.08.2019 - 30.08.2019
Poster: *Photoconversion kinetics of a phytochrome like cyanobacteriochrome GAF domain*
- **Joint Workshop on Photoreceptors**
Berlin, Germany, 09.10.2019
Presentation: *Ultrafast dynamics of the knotless phytochrome GAF domain All2699g1*
- **IPTC Annual Symposium**
Hirschegg, Austria, 20.03.2023
Presentation: *The environment matters! - A phytochrome case study*

Zusammenfassung

Licht spielt eine zentrale Rolle in der Regulation biologischer Prozesse wie dem Sehprozess in Tieren und Menschen oder der Phototaxis in Pflanzen und Cyanobakterien. Diese Prozesse werden durch lichtensitive Proteine, sogenannte Photorezeptoren, gesteuert, welche für ihre regulatorische Funktion das absorbierte Licht in ein biochemisches Signal umwandeln. Der erste Schritt dieser Umwandlung basiert auf der Absorption eines Photons durch ein lichtempfindliches organisches Molekül, dem Chromophor, das daraufhin eine photochemische Reaktion durchläuft. Durch diese Reaktion ändern sich die sterischen oder elektronischen molekularen Eigenschaften des Chromophors. Dies löst eine Signalkaskade innerhalb des Photorezeptors aus, die schlussendlich das biochemische Signal erzeugt. Einen besonders bedeutenden Reaktionsmechanismus dieser Primärreaktion stellt die Photoisomerisierung dar. Diese ist nicht nur in biologischen Systemen relevant, sondern kommt auch in einer Vielzahl von organischen Photoschaltern vor und findet beispielsweise in der Grundlagenforschung, Informationstechnik und Photopharmakologie Anwendung.

Die Effizienz und spezifische Dynamik dieser Reaktionen ist von zentraler Bedeutung für die jeweilige Anwendung, weshalb die Reaktionskontrolle und -optimierung ein Kernziel der Forschung darstellt. Um Kontrolle realisieren zu können, besteht die Notwendigkeit eines grundlegenden Verständnisses der im Femto- bis Pikosekundenbereich ablaufenden Primärreaktionen und der zentralen Einflussgrößen auf ihre Kinetik und Effizienz, welche mit heutigen hochentwickelten zeitaufgelösten Spektroskopiemethoden untersucht werden können.

Die vorliegende Arbeit befasst sich mit der Erforschung dieser grundlegenden Mechanismen und Kontrollfaktoren von Photoisomerisierungsreaktionen in Phytochromen und indigoiden Photoschaltern. Im Bereich der Phytochrome wurde die Untergruppe der knotenlosen Phytochrome anhand zweier Modellsysteme im Blick auf den Einfluss der direkten Proteinumgebung des Chromophors, besonders des konservierten Tyrosins 142, der PHY Domäne und der Heterogenität dieser Umgebung untersucht und eine erste Beschreibung der Photodynamik knotenloser Phytochrome erstellt. Das Phytochrom-Projekt wurde in Kollaboration mit den Arbeitsgruppen von Prof. Dr. Wolfgang Gärtner (Proteinpräparation All2699, Universität Leipzig), Dr. Igor Schapiro (Computergestützte Photochemie, Hebrew University of Jerusalem), Dr. Xiaojing Yang (Röntgenkristallographie, University of Illinois Chicago), Prof. Dr. Lars-Oliver Essen (Proteinpräparation *SynCph2*, Philipps-Universität Marburg) und Prof. Dr. Jens Bredenbeck (zeitaufgelöste, transiente Absorptionsspektroskopie im infraroten Spek-

tralbereich, Johann Wolfgang Goethe-Universität Frankfurt) durchgeführt.

Im Bereich der indigoiden Photoschalter wurde in einem ersten Teilprojekt der bisher wenig charakterisierte Mechanismus des Hula-Twists, eine kombinierte Bewegung aus Doppelbindungsisomerisierung und Einzelbindungsrotation anhand eines speziell modifizierten Hemithioindigo Photoschalters untersucht. Durch den Einbau sterisch anspruchsvoller Liganden wird hier die Einzelbindungsrotation gehemmt, wodurch die Produkte der Kombinationsbewegung des Hula-Twists von denen der Doppelbindungsisomerisierung unterscheidbar werden und damit gezielt untersucht werden können. Das Projekt wurde in Zusammenarbeit mit den Arbeitsgruppen von Prof. Dr. Henry Dube (Organische Synthese und Quantenausbeutenbestimmung, Friedrich-Alexander-Universität Erlangen) und Prof. Dr. Andreas Dreuw (quantenchemische Rechnungen, Universität Heidelberg) umgesetzt.

In einem zweiten Teilprojekt wurden in Zusammenarbeit mit den Arbeitsgruppen von Prof. Dr. Alexander Heckel (Synthese der Dipeptide, Bestimmung von Extinktionskoeffizienten, Johann Wolfgang Goethe-Universität Frankfurt) und Prof. Dr. Jens Bredenbeck (zeitaufgelöste, transiente Absorptionsspektroskopie im infraroten Spektralbereich, Johann Wolfgang Goethe-Universität Frankfurt) zwei molekulare Heizer für Schwingungsenergieübertragungsstudien auf Basis der neuartigen Klasse der Iminothioindoxyl (Iminothioindigo) Photoschalter konzipiert und deren Photodynamik charakterisiert.

Die Photodynamik von komplexen biologischen Systemen kann in der Regel nicht durch einzelne Exponentialfunktionen beschrieben werden. Dennoch ist auf dem Gebiet der Phytochrome diese Interpretation der kinetischen Daten besonders etabliert. Die Beobachtung verteilter (nicht-exponentieller) Kinetiken wird hier oft dem Vorliegen mehrerer leicht unterschiedlicher Grundzustandskonformationen des Chromophors und seiner direkten Proteinumgebung zugewiesen, was als Grundzustandsheterogenität bezeichnet wird. Jeder dieser Grundzustände kann durch Licht angeregt werden und entwickelt durch die entsprechend unterschiedliche Umgebung eine andere Photodynamik, was sich in der Beobachtung mehrphasiger Kinetiken äußert. In diesem etablierten Bild wird daher nahezu jede Lebenszeit im Rahmen einer globalen Lebenszeitenanalyse einem eigenen Grundzustand und dessen Evolution im angeregten Zustand zugewiesen. Dieses Bild stellt somit eine relativ statische Sicht eines hochdynamischen und komplexen Prozesses dar und wird zunehmend in Frage gestellt. In dieser Arbeit wurde dieses statische Bild am Beispiel von knotenlosen Phytochromen überprüft und durch eine dynamische Beschreibung erweitert.

Das untersuchte Modellsystem, bestehend aus der einzelnen chromophor-bindenden

GAF-Domäne All2699g1 und dem zugehörigen vollständigen knotenlosen Phytochrom All2699g1g2 aus *Nostoc* sp., bietet sich besonders für diese Art der Untersuchung an. In Festkörper-NMR Studien wurde bereits festgestellt, dass All2699g1g2 einen weitestgehend homogenen Grundzustand aufweist, während All2699g1 einen heterogenen Grundzustand zeigt. Entsprechend können gemäß dem etablierten statischen Bild signifikant unterschiedliche Kinetiken im angeregten Zustand erwartet werden, da eine separate Dynamik der einzelnen Grundzustände sichtbar sein sollte. Die Untersuchungen mittels Femtosekunden zeitaufgelöster Anrege-Abtast-Spektroskopie im Rahmen dieser Arbeit konnten zeigen, dass die Kinetik der Vorwärtsreaktion aus dem Dunkelzustand P_r der beiden Proteine mehrphasig und nahezu identisch ist, weshalb sich die Notwendigkeit mehrerer Exponentialfunktionen zur Beschreibung der Kinetik nicht auf die Anwesenheit von Grundzustandsheterogenität zurückführen lässt. Durch Lebenszeitendichteanalyse konnte die Photodynamik der untersuchten Systeme in zwei verschiedene zentrale Prozesse aufgetrennt werden. Zunächst wird eine multiexponentielle, initiale Chromophordynamik im Bereich bis 30 ps beobachtet, welche anschließend eine nicht-exponentielle Reorganisation der Proteinmatrix um den Chromophor auslöst, die schließlich zur Isomerisierung und der Bildung des Photoprodukts im Zeitbereich von hunderten Pikosekunden führt. Dies wurde nochmals durch zeitaufgelöste Anrege-Abtast-Spektroskopie im infraroten Spektralbereich am knotenlosen Phytochrom *SynCph2* bestätigt. In dieser Reorganisation nimmt das konservierte Tyrosin 142 eine zentrale Rolle ein, da es im Rahmen der Reorganisation den Weg freimachen muss, um die sterische Blockade der Photoisomerisierung des Chromophors aufzulösen und die Bildung des Photoprodukts Lumi-R zu ermöglichen. Diese Rolle wurde durch quantenchemische Berechnungen der Schapiro-Gruppe sowie Mutationsstudien im Rahmen dieser Arbeit bestätigt. Besonders die durchgeführten Mutationsstudien heben hervor, dass die initiale Chromophordynamik von der Reorganisation der Proteinmatrix und der anschließenden Isomerisierung des Chromophors getrennt werden kann, da nur die Kinetik der Proteinmatrix von Mutationen des konservierten Tyrosins betroffen ist, während die initiale Chromophordynamik unverändert bleibt. Dieser Trend konnte anhand von Untersuchungen an einer Reihe von Phytochromen, darunter auch Gruppe I und III Phytochrome, generalisiert werden. Hier unterscheidet sich ebenfalls nur die zeitliche Position der Reorganisation der Proteinmatrix und nicht die initiale Chromophordynamik, wodurch ein genereller Mechanismus für die Photodynamik des Dunkelzustands P_r in Phytochromen entwickelt werden konnte. Gemäß dem aufgestellten Modell hängt die Photodynamik des Dunkelzustands P_r stark von der exakten Umgebung des Chromophors ab, wobei besonders die Flexibi-

lität der Chromophorbindetasche, der sterische Anspruch des konservierten Tyrosins und die Wasserstoffbrückenbindungen in der direkten Umgebung eine zentrale Rolle spielen. Kurze Lebenszeiten des angeregten Zustands in anderen Phytochromen mit einer größeren Flexibilität können im Rahmen dieses Modells mit einer vereinfachten Bewegung des konservierten Tyrosins erklärt werden.

Im Gegensatz zur Vorwärtsreaktion ist die Rückreaktion des belichteten Zustands P_{fr} signifikant beschleunigt. Sowohl in All2699g1g2 als auch in *SynCph2* zerfällt der angeregte Zustand bereits im sub-ps Zeitbereich, gefolgt von der Relaxation mehrerer Grundzustandsintermediate. Bemerkenswert ist, dass die Rückkehr zum initialen Grundzustand nicht direkt aus dem angeregten Zustand stattfindet, sondern aus einem heißen Grundzustandsintermediat, was im Gegensatz zur typischerweise beobachteten Dynamik in anderen Phytochromen steht. Die Rolle von Grundzustandsheterogenität auf die Photodynamik konnte erneut durch den Vergleich mit All2699g1 untersucht werden. Während All2699g1g2 und *SynCph2* nur einen Zerfall des angeregten Zustands zeigen, weist All2699g1 drei Zerfallsprozesse des angeregten Zustands auf, welche mit drei verschiedenen Grundzustandspopulationen assoziiert werden. Die Untersuchung diverser Mutanten in *SynCph2* und All2699g1 zeigt, dass das Auftreten von Grundzustandsheterogenität sich hauptsächlich Unterschieden in den Wasserstoffbrücken des Chromophors zum konservierten Tyrosin 142 und einem konservierten Serin in der PHY-Domäne zuordnen lässt. Somit konnten erste Erklärungen für die auftretende Heterogenität und die strukturellen Unterschiede zwischen den Grundzustandspopulationen geliefert werden.

Anhand dieser Ergebnisse lassen sich unterschiedliche Rollen von Grundzustandsheterogenität für die Photodynamik von Phytochromen feststellen und erklären. Im Fall der vergleichsweise langsamen Vorwärtsdynamik des P_r Zustands besteht die Möglichkeit der Äquilibration der verschiedenen Populationen im angeregten Zustand, wodurch kein signifikanter kinetischer Unterschied mehr sichtbar bleibt. Bei der schnellen Rückreaktion dagegen besteht diese Möglichkeit aufgrund der geringen Verweildauer im angeregten Zustand nicht und jede Population weist eine eigene Kinetik im Rahmen des bereits etablierten Modells der Grundzustandsheterogenität auf. Somit konnte gezeigt werden, dass der Einfluss von Grundzustandsheterogenität keinesfalls verallgemeinert werden kann und stark von den genauen strukturellen Unterschieden und Barrieren zwischen einzelnen Populationen sowie der Verweildauer im angeregten Zustand abhängt.

Zuletzt wurde die Rolle der PHY Domäne auf die proteinbestimmte Mikro- bis Millisekundendynamik in knotenlosen Phytochromen untersucht. Es konnte gezeigt wer-

den, dass die PHY Domäne besonders die frühen Relaxationsprozesse des Chromophors auf der Mikrosekundenzeitskala signifikant verlangsamt, während die späteren, weitreichenden Proteinreorganisationsprozesse nur wenig beeinflusst werden. Dadurch wird deutlich, dass die PHY Domäne vor allem dazu beiträgt eine kompaktere Chromophorbindetasche zu gewährleisten, in der eine weitgehend homogene Protein- und Chromophorkonformation vorliegt. Diese kompaktere Umgebung verlangsamt besonders die frühen, thermischen Relaxationsprozesse des Chromophors. Zudem konnte ein komplexes Protonierungsgleichgewicht in der Vorwärtsreaktion der untersuchten Phytochrome identifiziert werden, welches sich auf Unterschiede im Protonierungszustand des Wasserstoffbrückennetzwerk des Chromophors im Meta-R_c Intermediat zurückführen lässt und eine biphasische Kinetik induziert.

Die erhaltenen Ergebnisse heben die Rolle der PHY Domäne hervor, die, besonders durch ihre direkte Interaktion mit der Chromophorbindetasche über eine zungenartige Struktur, den konformationellen Raum in der Bindetasche verringert und damit zur Reduktion von Grundzustandsheterogenität und der Erhöhung der Quantenausbeute der Photoreaktion beiträgt. Insgesamt konnte gezeigt werden, dass die Photoisomerisierung in Phytochromen von einem komplexen Zusammenspiel des Chromophors und seiner Proteinumgebung kontrolliert wird, woraus ein generelles Konzept für die Photodynamik der Vorwärtsreaktion des Dunkelzustands P_r abgeleitet werden konnte.

Eine weitere prototypische Photoisomerisierungsreaktion findet man in indigoiden Photoschaltern. Diese wird typischerweise als klassische *Z/E* Isomerisierung betrachtet, in der die Rotation um die Einzelbindungen der entsprechenden Doppelbindungssubstituenten einen alternativen Relaxationspfad darstellt. Der bisher selten beobachtete Hula-Twist Mechanismus stellt eine konzertierte Bewegung aus diesen beiden klassischen Mechanismen dar, dessen Relevanz für die Photodynamik von Photoschaltern noch wenig erforscht ist.

Um den Hula-Twist Mechanismus zum ersten Mal in Hemithioindigo Photoschaltern in einer dynamischen Studie zu untersuchen, wurde hier ein speziell modifizierter, sterisch überfrachteter Hemithioindigo Photoschalter der Dube Gruppe verwendet. Die durchgeführten Untersuchungen mittels zeitaufgelöster Anrege-Abtast-Spektroskopie im Femtosekundenbereich in verschiedenen Lösungsmitteln zeigen, dass der angeregte Zustand des gewählten Moleküls über zwei Deaktivierungspfade verfügt: einen produktiven Pfad, der nach quantenchemischen Berechnungen der Dreuw Gruppe einem Hula-Twist Mechanismus folgt und einem unproduktiven Deaktivierungspfad. Die sterische Überfrachtung sorgt hier für hohe Barrieren im angeregten Zustand, wodurch die entsprechenden Lebenszeiten im Bereich von einigen Nanosekunden liegen. Dies

ändert sich in polaren Lösungsmitteln, in denen der unproduktive Deaktivierungspfad durch die starke Stabilisierung des Charge-Transfer Charakters im angeregten Zustand bevorzugt wird, während der produktive Deaktivierungspfad durch eine steigende Barriere unerreichbar wird. Dementsprechend wird in polaren Lösungsmitteln keine produktive Photochemie mehr beobachtet. Diese Arbeit konnte somit eine erste dynamische Charakterisierung eines Hula-Twist Mechanismus in Hemithioindigo Photoschaltern liefern und verdeutlichen, dass dieser Mechanismus eine relevante Rolle in der Photochemie dieser Molekülklasse neben dem klassischen Mechanismus der Z/E Photoisomerisierung einnimmt.

Als Kontrast zu den produktiven Photoisomerisierungsreaktionen in den anderen Teilprojekten wurde im letzten Projekt die besondere Eigenschaft zweier neuartiger Iminothioindoxyl Photoschalter genutzt, die nach Anregung große Mengen an Schwingungsenergie freizusetzen. Diese Schwingungsenergie kann im Rahmen von Schwingungsenergietransferstudien gezielt in ein biologisches System, beispielsweise ein Protein, injiziert werden, um die Ausbreitung der Schwingungsenergie in diesen Systemen zu verfolgen. Es wird hierbei vermutet, dass diese Energie sich auf anisotropen, spezifischen Pfaden im System ausbreitet und an Signaltransferprozessen beteiligt ist.

Es konnte gezeigt werden, dass die dafür von der Heckel Gruppe synthetisierten Dipeptide, bestehend aus einer künstlichen Aminosäure basierend auf den Iminothioindoxyl Photoschaltern und dem Schwingungsenergiesensor Azidohomoalanin, eine für biologische Systeme vorteilhafte Absorption im grünen bis roten, sichtbaren Spektralbereich mit hohen Extinktionskoeffizienten um $20000 \text{ LMol}^{-1}\text{cm}^{-1}$ aufweisen. Dies stellt eine signifikante Verbesserung zum bis dahin etablierten Schwingungsenergie-donor Azulenylalanin dar. Mittels zeitaufgelöster Anrege-Abtast-Spektroskopie im Femtosekundenbereich an diesen Dipeptiden konnte anschließend gezeigt werden, dass der angeregte Zustand dieser Systeme innerhalb weniger hundert Femtosekunden zerfällt und anschließend ein heißer Grundzustand gebildet wird. Dieser Zustand kühlt über wenige Picosekunden unter Abgabe seiner Schwingungsenergie ab und kehrt vollständig in den Ausgangsgrundzustand zurück. Der beobachtete Mechanismus konnte als unabhängig von der Anregungswellenlänge und den untersuchten Lösungsmitteln charakterisiert werden, was zusammen mit dem Ausbleiben von bleibenden strukturellen Änderungen im Chromophor ein vielseitiges Anwendungspotenzial verspricht. Der erfolgreiche Schwingungstransfer des heißen Grundzustands des Donors auf den Schwingungsenergiesensor konnte von der Bredenbeck Gruppe anschließend erfolgreich verifiziert werden.

Insgesamt konnten in der vorliegenden Doktorarbeit die Mechanismen verschiedener

Photoisomerisierungsreaktion in fundamental unterschiedlichen Systemen charakterisiert und die zentralen Einflussgrößen auf die jeweilige Reaktionen bestimmt werden.

Table of Contents

1	Introduction	1
2	Theoretical Framework	3
2.1	Methodology	3
2.1.1	Ultraviolet/Visible Spectroscopy	3
2.1.2	Circular Dichroism Spectroscopy	7
2.1.3	Transient Absorption Spectroscopy	7
2.1.4	Data Analysis	15
2.2	Phytochromes	18
2.2.1	Classification of Phytochromes	19
2.2.2	Chromophore Variety and Color Tuning Mechanisms	21
2.2.3	Conserved Residues of the Binding Pocket	22
2.2.4	Heterogeneity in the Parental States	30
2.2.5	The Photocycle	33
2.2.6	Aim of Research	38
2.3	Indigoid Photoswitches	42
2.3.1	Hemithioindigo Photoswitches	42
2.3.2	Iminothioindoxyl Photoswitches	43
2.3.3	Aim of Research	44
3	Research Projects	47
3.1	Phytochromes	47
3.1.1	Ultrafast Forward Dynamics of Knotless Phytochromes	47
3.1.2	Ultrafast Reverse Dynamics of Knotless Phytochromes	55
3.1.3	The Role of Ground State Heterogeneity in the Ultrafast Dynamics of Knotless Phytochromes	61
3.1.4	Millisecond-Dynamics of Knotless Phytochromes	61
3.1.5	The Influence of the PHY Domain on the Photodynamics of Knotless Phytochromes	66
3.2	Indigoid Photoswitches	68
3.2.1	Hula-Twist Mechanism in a Sterically Crowded HTI	68
3.2.2	ITI Photoswitches as Vibrational Energy Donors for VET	71
4	Conclusion	79

Table of Contents

5 Publications	83
5.1 Declaration of Author Contributions	83
5.2 Reference [I] Slavov <i>et al.</i> , <i>Proc. Natl. Acad. Sci. USA</i> 2020 , 117(28), 16356-16362	86
5.3 Reference [II] Fischer <i>et al.</i> , <i>Chem. Eur. J.</i> 2020 , 26, 17261-17266	94
5.4 Reference [III] Fischer <i>et al.</i> , <i>Int. J. Mol. Sci.</i> 2021 , 22, 10690-10704	101
5.5 Reference [IV] Fischer <i>et al.</i> , <i>Photochem. Photobiol. Sci.</i> 2022 , 21, 1627-1636	117
5.6 Reference [V] Fischer <i>et al.</i> , <i>Biochim. Biophys. Acta - Bioenerg.</i> 2023	128
5.7 Reference [VI] Fischer <i>et al.</i> , <i>J. Am. Chem. Soc.</i> 2023 , 145, 14811-14822	136
List of Abbreviations	149
List of Figures	153
List of Tables	157
Bibliography	159

Chapter 1: Introduction

Life on our planet has, for billions of years, developed a fundamental dependence on the sun and its electromagnetic radiation reaching earth as light and heat in the form of infrared and microwave radiation and visible light. While the less energetic infrared and microwave radiation plays a central role in the climate and environment, visible light not only allows us to perceive our world visually, but is most importantly the main provider of energy for plants, algae and photosynthetic cyanobacteria.^[1,2] These organisms then provide the converted energy to other forms of life as a nutrient source. The sun has become an important source of renewable energy as well in the context of photovoltaics and solar cells which try to imitate the energy generation of the photosynthetic organisms.^[3] A more challenging approach aims to copy the sun's way of generating energy by nuclear fusion with first major breakthroughs in recent years to obtain a strong and more sustainable source of energy.^[4,5]

However, solar radiation should not be reduced merely to the energy it provides. Visible and ultraviolet (UV) light in particular are ubiquitously used for regulation purposes in all kinds of organisms. Whether it is vision in humans and animals,^[6,7] phototaxis and photomorphogenesis in plants,^[8] or chromatic climatic adaptation in cyanobacteria,^[9] light represents a core regulator of many processes essential for the prospering of life on earth resulting in a multitude of different mechanisms which have evolved to convert light into a biological response. The first step in this signal transmission cascade requires the initial absorption of a photon by a light-sensitive organic molecule termed chromophore. To generate a photochemical signal, these chromophores undergo an initial light-dependent reaction altering their molecular properties like photoisomerizations as observed in rhodopsins and phytochromes or a redox reaction occurring in cryptochromes and phototropins. The alteration of the chromophore's molecular properties then entails the induction of a protein response through protein reorganization or transfer of charge, electrons, energy or protons.^[8] The simple mechanism of photoisomerizations is also applied in the scientific field of molecular photoswitches which often employ such reactions in their light response.^[10,11]

The underlying principles governing this reaction have been a focal point of research within the last decades; which was only made possible by the revolutionary developments in physics and the resulting rise of advanced analytical methods like laser spectroscopy. This advancement initially enabled studying processes like isomerizations occurring on the sub-ps timescale in a time-resolved manner. Analytical techniques with structural resolution like infrared (IR), resonance raman (RR), and

1 Introduction

X-ray spectroscopy - often based on the application of laser spectroscopy - have further accelerated research in this field and are an essential basis of the scientific advancements.

The acquired conceptual understanding is utilized in tailoring the properties of photoreceptors and photoswitches to match the desired purposes. The variety of applications comprises the improvement of analytical techniques by introducing novel fluorescent probes, enacting photocontrol on biological systems like ligand-binding in proteins, folding of deoxyribonucleic acid (DNA) or ribonucleic acid (RNA), optogenetics, and even creation and optimization of molecular motors that are capable of performing specific motions upon illumination.^[10,12-16] This ubiquitous pool of methods relies on the optimization of photoreactions in general, and photoisomerizations as one of the dominant reaction mechanisms in particular. Therefore, improving the general understanding of the factors controlling the efficiency and dynamics of this type of reaction represents an important goal of scientific research to this day.

In this work, various determining factors on the progression of photoisomerizations as one of the central basic principles of light-dependent regulation have been studied by taking a closer look at the photodynamics of phytochromes and two indigoid photoswitches undergoing this type of photoreaction. For this purpose, time-resolved spectroscopy in the UV/visible (Vis) has been applied shedding light onto several factors like the ionic environment, steric restrictions imposed by the surroundings of the double bond, the polarity of the solvent and the presence of associated hydrogen bonds. In the first part of the dissertation, the theoretical framework of the applied methods and the investigated systems will be introduced. Next, the findings of the individual research projects will be presented, discussed, put into context of the respective scientific field and summarized. Lastly, the publications based on the results presented in the thesis and the respective contributions of this work presented in these publications are displayed.

Chapter 2: Theoretical Framework

2.1 Methodology

The investigation of photoisomerizations in both light-dependent proteins and organic photoswitches requires sophisticated time-resolved spectroscopic techniques on the fs-ps timescale. The subsequent reaction steps of the light-activated proteins can then be observed on the μ s-ms timescale. To achieve the appropriate time resolution, laser spectroscopic methods, especially pump-probe spectroscopy, are typically applied. These methods are complemented by stationary spectroscopic techniques to characterize the basic properties of the thermostable states and facilitate the analysis of the more complex time-resolved data.

2.1.1 Ultraviolet/Visible Spectroscopy

The basis of spectroscopy is the interaction of electromagnetic radiation with matter and the observation of the transitions between the energetic levels of molecules. Depending on the energy of the radiation, different transitions can be induced that give insight into specific molecular properties. Optical or UV/Vis spectroscopy applies visible light and UV radiation in a wavelength range between 200 to 800 nm to investigate electronic transitions in molecules. The absorption of a photon in this spectral range by a molecule induces an electronic transition from the ground state (GS) to an excited state (ES) which may be accompanied by an additional vibrational transition to an excited vibrational state within the electronic ES. A combined transition of vibrational and electronic transitions is termed vibronic transition. These transitions reveal detailed information on the energy levels and electronic structure of the respective chromophore. The occurrence of optical transitions requires matching of the energy of the interacting photon with the energy gap between two energy levels and the transition dipole moment being unequal to zero. The transition dipole moment $\mu_{gs,exc}$ predominantly depends on the wave function symmetry of the electronic and vibrational states involved in the transition and can be expressed as (equation (eq) 2.1)

$$\mu_{gs,exc} = \int \Psi_{exc}^* \hat{\mu} \Psi_{gs} d\tau, \quad (2.1)$$

where Ψ_{gs} is the wavefunction of the GS, Ψ_{exc} is the wavefunction of the ES, and $\hat{\mu}$ is the transition dipole operator.

Within this equation, the Franck-Condon^[17,18] approximation is applied which states

2 Theoretical Framework

that an electronic transition occurs initially without displacement of the nuclei as the electrons move and react much faster to the radiation due to their lower weight in accordance with the Born-Oppenheimer-approximation.^[19] Hence, the wavefunction can be separated into an electronic and a nuclear part. The molecular geometry of an excited electronic state but unchanged nuclei is referred to as the Franck-Condon region. After the electronic transition occurred, the nuclei start to adapt to the altered electronic environment on the ES surface and the wavepacket departs from the Franck-Condon region.

For a transition to be allowed the resulting integral (eq. 2.2) has to be unequal to zero

$$\mu_{gs,exc} = \int \psi_{e,exc} \Phi_{n,exc}^* \hat{\mu}_{e,n} \psi_{e,gs}^* \Phi_{n,gs} d\tau \neq 0, \quad (2.2)$$

where ψ_e represent electronic wavefunctions and Φ_n represent nuclear wavefunctions. The square of the transition dipole moment (eq. 2.3) determines the probability of the vibronic transition and is linked to the frequency dependent molecular extinction coefficient $\epsilon(\nu)$

$$|\mu_{gs,exc}|^2 = \frac{4\epsilon_0 m_e c^2 \ln(10)}{N_A e^2} \int \epsilon(\nu) d\nu \quad (2.3)$$

with ϵ_0 as the vacuum permittivity constant, m_e as the mass of an electron, c as the speed of light, N_A as the Avogadro constant, and e as the electronic charge. This coefficient can then be used to describe the absorptive properties of a molecule or protein.

According to the Lambert-Beer-Law,^[20,21] the absorbance A by a homogeneous sample under monochromatic light neglecting stray effects can be described as the product of the frequency dependent molecular extinction coefficient $\epsilon(\nu)$, the concentration of the absorbing species c and the optical pathway in the sample d (eq. 2.4).

$$A(\lambda) = \epsilon(\lambda) \cdot d \cdot c \quad (2.4)$$

$$-\log_{10} \left(\frac{I}{I_0} \right) = \epsilon(\lambda) \cdot d \cdot c \quad (2.5)$$

The absorbance A can be expressed in a logarithmic representation alternatively as the ratio of the light intensity I_0 before and I after passing the sample (eq. 2.5). This equation represents the basis of absorption spectroscopy and can be utilized to determine concentrations or extinction coefficients of photoactive molecules using absorption spectrometers.

Quantum Yield Determination

If the molecular extinction coefficient of a sample is known, the quantum yield (QY) of a photochemical reaction can be determined using absorption spectroscopy. The QY of a photochemical reaction or relaxation pathway is defined as the ratio of the number of reacting molecules N_r and the number of photons absorbed by the sample N_{abs} (eq. 2.6).

$$\Phi = \frac{N_r}{N_{abs}} \quad (2.6)$$

The number of reacting molecules can be determined by following the absorption changes at a specific wavelength upon illumination under the condition that the photoreaction yields thermally stable products. The difference in absorption then represents the difference in concentration before and after the photoreaction as the optical pathway and extinction coefficient are constant under the experimental conditions. The number of reacted molecules N_r is hence described as (eq. 2.7)

$$N_r = \frac{V \cdot N_A \cdot \Delta A}{\epsilon \cdot d}, \quad (2.7)$$

where V is the volume of the sample and ΔA the difference in absorption.

The number of absorbed photons depends on the time of irradiation t , the total number of photons and the fraction of absorbed photons. The total number of photons can be obtained by dividing the light power P by the energy of one photon at the excitation wavelength E_{hv} . The fraction of absorbed photons is taken into account by a factor based on the initial absorption at the wavelength of irradiation A_0 which yields the following expression for N_{abs} (eq. 2.8):

$$N_{abs} = \frac{P \cdot (1 - 10^{-A_0}) \cdot t}{E_{hv}} = \frac{P \cdot (1 - 10^{-A_0}) \cdot t \cdot \lambda}{h \cdot c} \quad (2.8)$$

By combining eq. 2.7 and eq. 2.8 the final expression for the QY of a photoreaction can be obtained in eq. 2.9

$$\Phi = \frac{V \cdot h \cdot c \cdot N_A \cdot \Delta A}{P \cdot (1 - 10^{-A_0}) \cdot d \cdot \epsilon(\lambda_{det}) \cdot t \cdot \lambda_{exc}}, \quad (2.9)$$

where P , V , the extinction at the detection wavelength ϵ_{det} , $\Delta A/t$ and the excitation wavelength λ_{exc} have to be determined in the experiment.^[22]

Photochemical Deactivation Processes

Following the absorption of a photon, molecules typically transition to an excited vibronic singlet state almost instantaneously on the fs timescale. This excited vibronic state then has to return to the GS leading to limited ES lifetimes. The relaxation process can proceed on several different pathways which are categorized into radiative and non-radiative pathways and are summarized in the Jablonski diagram (Fig. 2.1).

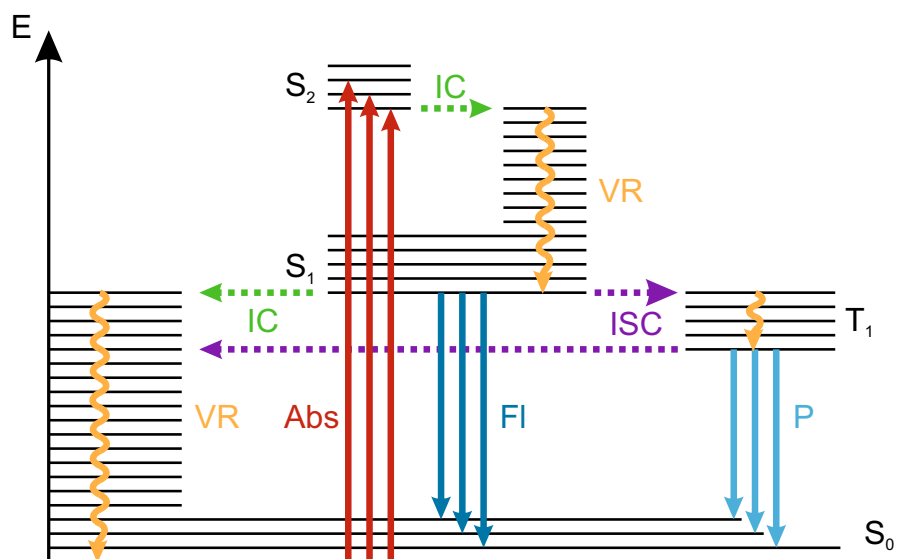


Figure 2.1 – Radiative and non-radiative relaxation pathways in excited molecules summarized in the Jablonski diagram.^[23] Transitions involving radiation are indicated by solid straight lines comprising the processes of absorption (Abs, red), fluorescence (Fl, dark blue) and phosphorescence (P, light blue). Meanwhile, non-radiative vibrational relaxation (VR) is represented by wavy solid lines (yellow), while isoenergetic transitions like internal conversion (IC, green) and intersystem crossing (ISC, purple) are displayed as dotted lines.

In terms of non-radiative pathways, the excited molecule can dissipate energy via intramolecular vibrations leading to relaxation towards lower vibrational energy levels within the same electronic ES. If the energy of a vibrational state in a higher electronic ES matches with the energy of a highly excited vibrational level of the adjacent lower electronic ES, an isoenergetic transition termed internal conversion is possible. The molecule then converts to the lower electronic ES and proceeds via vibrational relaxation in this state. These non-radiative relaxation pathways may lead back into the initial GS or form a photoproduct depending on the ES potential energy surface. Under specific circumstances, singlet-triplet transitions termed intersystem crossing (ISC) represent alternative relaxation pathways where population from an excited singlet state

is transferred to a vibrationally excited triplet state. Then, this state may undergo vibrational relaxation and cross back to the singlet GS or relax in a radiative manner via phosphorescence. Finally, radiative relaxation from the vibrational GS of the lowest excited singlet state to different vibrational energy levels of the electronic singlet GS may occur which is defined as fluorescence. This process can be stimulated by irradiation with photons of similar energy, in which case it is termed stimulated emission (SE).

2.1.2 Circular Dichroism Spectroscopy

As an electromagnetic wave, light is characterized by an electric and a perpendicularly oriented magnetic field. If the electric field vectors within a light beam align in a single direction, traveling in phase perpendicular to the propagation vector, the light is described as linear-polarized. In spectroscopy, linear-polarized light is used to investigate anisotropy and its origin in molecules and bulk media. In addition, linear-polarized light can be converted to circular-polarized light by passing it through a quarter-waveplate with its axis at a 45° angle to the polarization axis, where the electric and magnetic field vectors rotate in a concerted motion clockwise or anti-clockwise about the propagation direction. The interaction of circular-polarized light with optically active molecules differs between clockwise and anti-clockwise rotation depending on the chirality. This difference in absorption is called circular dichroism (CD) and can be utilized to investigate the conformations of proteins, DNA, RNA, and optically active chromophores in confined environments.^[24-27]

2.1.3 Transient Absorption Spectroscopy

Transient absorption spectroscopy is a powerful time-resolved technique to resolve the kinetics of light-dependent transitions and is based on the pump-probe principle.^[28-30] A spectrally narrow, tunable, and temporally short pump pulse is used as an excitation pulse to induce a desired electronic transition within a sample. The absorption of the excited sample is then probed by a spectrally broad probe pulse to measure the spectral response initiated by the excitation. Introduction of a time dependence is achieved via a variable time delay between pump and probe pulse which is implemented by either electronic or mechanic means depending on the desired time window. In fs-transient absorption experiments, the implementation of a time delay is achieved by a variable, mechanic delay stage that varies the distance the pump pulse has to travel in respect to the probe pulse in μm steps. In this way, with a 30 cm delay stage, a time span of ~ 2 ns can be investigated by passing the stage twice corresponding to an optical pathlength of

2 Theoretical Framework

60 cm. The time resolution can be adjusted in the low fs time regime by tuning the step size limited by the temporal pulse width of the pump pulse. Obviously, this method is not feasible beyond the ns timescale where the delay is introduced electronically instead.

In order to obtain a spectrally narrow, tunable, and temporally short pump pulse, fundamental pulses from a laser source with already short pulse lengths and high intensities are required. As such laser sources are typically not tunable in a wide wavelength range, non-linear optical processes have to be applied to tune the pump pulse to its desired wavelength. In a similar manner, the spectrally broad probe pulse has to be generated by converting the provided fundamental pulses using non-linear optical processes. The underlying principles and technical implementations to tailor the fundamental, high intensity laser pulses provided by a commercially available Ti³⁺ doped sapphire (Ti:Sa) laser to the desired specifications using non-linear optics are described in the following sections.

Non-linear Wavelength Conversion Processes

The electric field $\vec{E}(t)$ of electromagnetic waves is characterized by the amplitude of the respective electric field \vec{E}_0 , the direction of propagation \vec{z} , the wavevector \vec{k} , and the wave frequency ω (eq. 2.10).

$$\vec{E}(t) = \vec{E}_0 \cos(\omega t - \vec{k}\vec{z}) \quad (2.10)$$

In linear optics, the polarization of a material interacting with an electromagnetic wave can be sufficiently approximated by a first-order linear dependence on the strength of the electric field inducing a change in charge distribution within the material. However, if the light intensity of the laser pulses exceeds a specific threshold the polarization starts to respond on the strength of the electric field in a non-linear manner (eq. 2.11). The polarization $\vec{P}(t)$ at a specific time point can be expressed in a Taylor series including higher orders of the electric field $\vec{E}(t)$

$$\vec{P}(t) = \epsilon_0 \chi^{(1)} \vec{E}(t) + \epsilon_0 \chi^{(2)} \vec{E}(t)^2 + \epsilon_0 \chi^{(3)} \vec{E}(t)^3 + \dots, \quad (2.11)$$

with $\chi^{(2)}, \chi^{(3)}, \dots$ as the non-linear susceptibility tensors with their order in brackets and ϵ_0 as the vacuum permittivity constant. On this basis, the non-linear optical effects are divided according to their order of the non-linear susceptibility. For wavelength conversion, a number of $\chi^{(2)}$ effects are applied to achieve frequency mixing of multiple

electromagnetic waves. These non-linear optical phenomena can be derived from the second order of the polarization of two interacting waves according to eq. 2.10 and 2.11:

$$\vec{P}(t)^{(2)} = \epsilon_0 \chi^{(2)} \left[\vec{E}_1 \cos(\omega_1 t) + \vec{E}_2 \cos(\omega_2 t) \right]^2 \quad (2.12)$$

Eq. 2.12 contains three different types of frequency mixing processes: the doubling of the initial frequency of the incoming electromagnetic wave, also termed second harmonic generation (SHG) (2.13a), the sum of the frequencies of both waves (sum frequency generation (SFG)) (2.13b), and the difference of the frequencies (difference frequency generation (DFG)) (2.13c).

$$\vec{P}(t)^{(2)} = \frac{\epsilon_0 \chi^{(2)}}{2} \vec{E}_1^2 \cos(2\omega_1 t) + \frac{\epsilon_0 \chi^{(2)}}{2} \vec{E}_2^2 \cos(2\omega_2 t) + \quad (2.13a)$$

$$\epsilon_0 \chi^{(2)} \vec{E}_1 \vec{E}_2 \cos(\omega_1 t + \omega_2 t) + \quad (2.13b)$$

$$\epsilon_0 \chi^{(2)} \vec{E}_1 \vec{E}_2 \cos(\omega_1 t - \omega_2 t) \quad (2.13c)$$

In order to use these processes efficiently, the respective waves have to travel in phase to avoid destructive interference. The conditions for phase matching differ for the respective processes and can be derived based on energy and momentum conservation. The phase matching conditions for the processes mentioned above can be derived as

$$\Delta \vec{k} = \vec{k}_{SHG} - 2\vec{k}_1 = 0, \quad (2.14a)$$

$$\Delta \vec{k}(t) = \vec{k}_{SFG} - \vec{k}_1 - \vec{k}_2 = 0, \quad (2.14b)$$

$$\Delta \vec{k}(t) = \vec{k}_{DFG} - \vec{k}_2 + \vec{k}_1 = 0, \quad (2.14c)$$

with $\vec{k} = \frac{2\pi}{\lambda} n(\lambda) \vec{e}$. To fulfill this condition, birefringent crystals like β -barium borate (BBO) or lithium triborate (LBO) are utilized which exhibit different refractive indices depending on the polarization and direction of the incoming light. Phase matching is then achieved by adjusting the polarization or direction of the incoming light and the orientation of the crystal and consequentially its optical axes. In the case of second order processes, the material must not contain an inversion center which would lead to destructive interference.

Supercontinuum Generation

A combination of non-linear optical processes of third or higher order is applied to generate a spectrally broad supercontinuum (white light) pulse from a spectrally narrow

2 Theoretical Framework

fundamental pulse. For third order non-linear optical processes, the refractive index of a material depends on the intensity of the incident light which is termed Kerr-Effect; leading to effects like self-focussing and self phase modulation. The latter causes a phase shift within the pulse resulting in the broadening of its frequency spectrum. These two effects are suggested as main contributors to the generation of supercontinua within non-linear media.^[31] To avoid coinciding second order processes, media with an inversion symmetry like sapphire, CaF_2 , or MgF_2 are commonly used for supercontinuum generation.^[28]

Optical Parametric Amplifiers

In analogy to frequency mixing, where a higher energy photon is generated from two lower energy photons, a higher energy photon can be split into two lower energy photons in a non-linear optical medium. The input photon is termed pump, while the output photons are termed signal and idler, following energy conservation with $\omega_{\text{pump}} = \omega_{\text{signal}} + \omega_{\text{idler}}$. This process is called optical parametric generation and is applied in optical parametric amplifiers (OPAs) one of the most commonly used tools for non-linear wavelength conversion (Fig. 2.2).

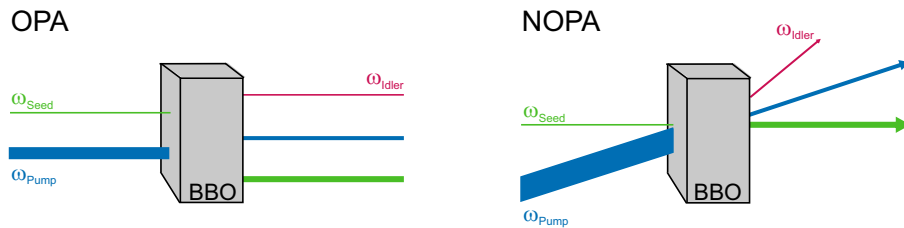


Figure 2.2 – Amplification of a seed pulse with a pump pulse in an OPA and a non-collinear optical parametric amplifier (NOPA). In the OPA all beams travel in a collinear way for the amplification making them hard to separate afterwards. In the non-collinear geometry the beams can be easily separated at the expense of reduced amplification efficiency but improved temporal resolution.

The output of optical parametric generation is typically weak as the energy splitting is rather broad and photons are emitted in a divergent manner resulting in a superfluorescence ring containing a wide range of colors within the visible spectral range. To solve this problem, a supercontinuum seed pulse is added and temporally and spatially overlapped with the pump pulse, resulting in the amplification of a defined wavelength range within the seed pulse and a weakening of the pump pulse. The amplified wavelength range depends on the phase matching conditions and can be adjusted accordingly. The overlap of pump and seed pulse in the non-linear optical medium can

be realized in collinear and non-collinear manner (NOPA) where the former is more efficient resulting in higher signal intensities due to increased spatial overlap within the crystal (Fig. 2.2).^[32,33] The advantages of the non-collinear geometry are an improved time resolution and the facilitated separation of the idler and remaining pump pulse at the cost of reduced amplification efficiency. Hence, collinear OPAs are used when higher intensities are required and temporal broadening of the pulse is not critical, like in flash photolysis, while NOPAs are used when a short pulse duration is desired like in fs-transient absorption spectroscopy.

For the technical implementation of a NOPA in the transient absorption setups used here, the fundamental laser pulse is split into two unequal parts; where the major part is frequency doubled by SHG in a BBO crystal, while the minor part is focused into a sapphire crystal to generate the supercontinuum seed pulse. Both beams are then focused and spatially overlapped into a BBO crystal with a variable vertical distance between the seed and pump beam to attain a non-collinear geometry. A variable delay stage is incorporated into the seed pathway to precisely tune the temporal overlap of the two pulses. With this setup a wavelength range of 450 nm to 950 nm can be achieved. For further amplification, the resulting pulse can be subjected to a second NOPA as a seed pulse.

Experimental Procedure of a fs-Transient Absorption Experiment

In order to resolve the ES dynamics of molecules, the difference in absorption between their GS and ES has to be recorded based on the pump-probe principle. Hence, the setup for performing such experiments consists mainly of three parts: the probe pulse generation, the pump pulse generation, and the signal detection and its corresponding electronics (Fig. 2.3).

The fundamental laser pulses driving the pump and probe pulse generation are provided by a Ti:Sa laser using CPA^[34] to generate pulses centered at 775 nm (Clark, MXR-CPA-iSeries) or 800 nm (Spitfire Ace-100F-1K, Spectra-Physics) with a 1 kHz repetition rate and 120 fs pulse width. The pump pulses are generated using a home-built two stage NOPA with a prism compressor located between the NOPAs. When passing through media, *i.e.*, air, crystals, lenses etc., the refractive index and accordingly the group velocity differs depending on the wavelength. This leads to a temporal broadening of the pulse termed positive chirp where the longer wavelengths precede the shorter ones. To compensate this broadening, the pulses are guided through a prism compressor, where the shorter wavelengths travel shorter distances compared to the

2 Theoretical Framework

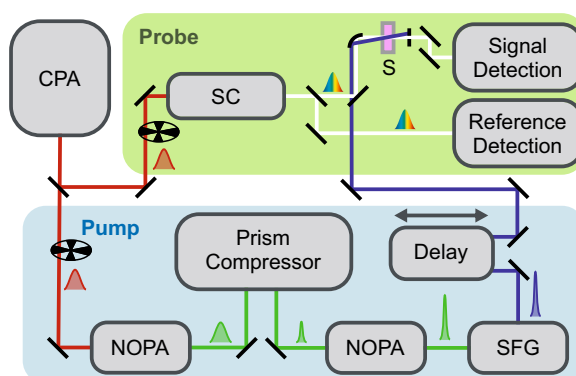


Figure 2.3 – Schematic depiction of the fs-transient absorption setup. The fundamental ultrashort laser pulses provided by a Ti:Sa laser using chirped pulse amplification (CPA) are split into a pump and a probe pathway. The pump pulse can be tuned in energy using non-linear optical effects (NOPA, SFG) and is compressed in a prism compressor to ensure ultrashort pulses. The supercontinuum probe pulses are generated by focusing the fundamental into a CaF₂ crystal. Both pulses are overlapped in the sample (S) and the desired time delay is generated using an electronic delay stage. The signals are detected in a referenced manner where one spectrometer detects the signal of the supercontinuum without passing the sample, while the pump-probe signal induced in the sample is detected in a separate spectrometer.

longer wavelengths, resulting in a temporally compressed pulse. In case a pump pulse wavelength outside the NOPA wavelength range is required, a SFG offers further wavelength tuning possibilities into the UV range. The pump pulse is then guided across an electronic delay stage and focused into the sample. To suppress anisotropic contributions, the relative polarization between the pump and probe pulse is set to the magic angle (54.7°) by a half-wave plate in the pump pathway. The intensity of the pump pulse is adjusted to excite between ~5 to ~10% of the molecules within the focal volume.

The supercontinuum probe pulses are generated by focusing the fundamental into a CaF₂ window which is constantly moved in a plane perpendicular to the direction of pulse propagation to avoid crystal damage. Then, the probe pulses are split into a reference and sample pathway; the reference pulses are guided directly to a detector, whereas in the sample pathway they are focused into the sample and spatially overlapped with the pump pulses before being detected as well. The advantage of recording a reference is that fluctuations of the probe light can be taken into account improving the signal-to-noise ratio using statistic filtering methods. The pulse detection in each pathway consists of a monochromator splitting the two probe pulses into their wavelength components and a photodiode array. The specifications of the used setup and the detection systems are displayed in more detail in the supporting information of the

respective publications. In order to measure the absorption of both the ES and GS of the sample, chopper wheels operated at 333 Hz are used to block every third of the pump and probe pulses. The blocking is phase shifted between pump and probe to achieve a chopping scheme where the signals of three different pulse combinations are recorded: Pump and probe pulse (I_{PP}), only the probe pulse (I_{GS}) and only the pump pulse (I_{Sca}) (Fig. 2.4). The difference between the first two translates into the transient absorption signal of the ES, while the latter is used to correct noise due to pump scattering.

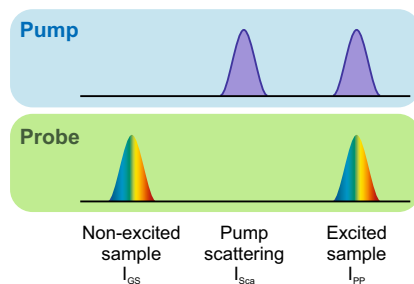


Figure 2.4 – Chopping scheme applied in the transient absorption experiments. Three different signals are created by shifting the phase of the chopping wheels with respect to each other while operating at a frequency of 333 Hz: I_{GS} , the signal of the non-excited sample in the GS; I_{Sca} , the signal of the pump scattering induced by the cuvette and sample; I_{PP} , the signal of the sample in its ES.

Based on this chopping scheme, the transient absorption difference signal $\Delta A(t)$ is calculated according to eq. 2.15

$$\Delta A(t) = -\log \left(\frac{I_{sample,PP} - I_{sample,Sca}}{I_{ref,PP} - I_{ref,Sca}} \cdot \frac{I_{ref,GS} - I_{ref,dark}}{I_{sample,GS} - I_{sample,dark}} \right), \quad (2.15)$$

where the indices indicate the sample (I_{sample}) or reference (I_{ref}) pathway and the chopping state. I_{dark} represents a background spectrum without light recorded before the experiment.

The obtained time-resolved difference spectrum contains positive and negative contributions that can be attributed to specific processes on the potential energy surface of the excited molecules. Positive signals correspond to an increased absorption of the excited molecule compared to the GS at the specified wavelength. Such additional absorption can be assigned either to absorption of the ES (ESA), representing a transition to a higher ES, or absorption of a GS photoproduct formed after the decay of the ES. These positive signals overlap with the negative signals which result from a reduced GS absorption or the SE of photons (Fig. 2.5).

The former can be rationalized by the transition of a portion of the GS population to

2 Theoretical Framework

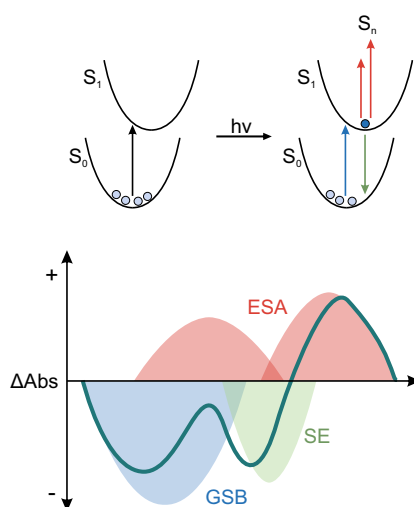


Figure 2.5 – Origin of the absorption difference signals observed in transient absorption experiments. Positive signals originate from excited state absorption (ESA) or photoproduct absorption, whereas negative signals stem from ground state bleach (GSB) and SE contributions.

the ES upon photoexcitation resulting in an amplitude reduction of the GS absorption band called ground state bleach (GSB).

Monochromatic Transient Flash Photolysis

Transient flash photolysis^[35] represents a spectroscopic technique based on the pump-probe principle that is used to investigate slower photodynamics on the μs -s timescale which are particularly relevant in proteins. In contrast to fs-transient absorption, the delay between pump and probe is generated electronically as delay stages with pathways over 100 m would be required otherwise. This also requires a different laser source where higher pulse intensities are favored over time resolution and a high repetition rate. The setup used here (Fig. 2.6), uses a Nd:YAG laser (SpitLight 600, Innolas Laser) with a repetition rate of 10 Hz at a central wavelength of 1064 nm.

These fundamental pulses are then doubled in frequency to 532 nm in a LBO medium and further converted to 355 nm in a second LBO medium by SFG with the fundamental. An optical parametric oscillator (OPO) (preciScan, GWU-Lasertechnik) is pumped by this third harmonic, yielding pump pulses in a wavelength range between 412 nm and 702 nm. The wavelength conversion is operated by motor-controlled adjustment of the inclination angle of the BBO medium used in the OPO. After exiting the OPO via a periscope, the size of the pump beam is adjusted with a telescope before being guided

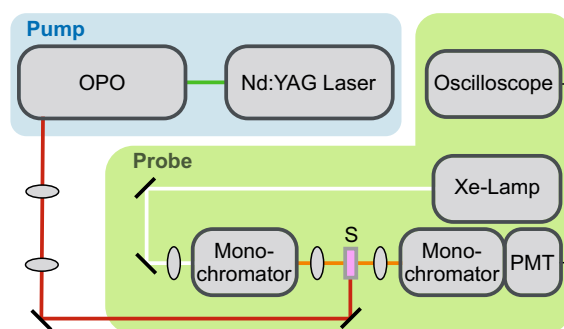


Figure 2.6 – Schematic representation of the monochromatic flash photolysis setup. The tunable pump pulses provided by the OPO are adjusted in size by a telescope and guided to the sample (S) afterwards. The spectrally broad continuous wave (cw) probe light provided by a Xe-lamp is guided into a monochromator to select the desired probe wavelength, led through the sample and collected into a second monochromator to reduce stray light. The signal is then detected by a photomultiplier tube and recorded by an oscilloscope.

onto the sample.

The probe light is provided as a continuous wave by a spectrally broad xenon lamp (Hamamatsu LC-8). To obtain the monochromatic light used for recording the transients, the desired wavelength is selected by two matched monochromators before and after the sample to avoid stray light. A photomultiplier tube ultimately detects the signal and the data are recorded on an oscilloscope (DPO5204B-10RL, Tektronix). Data acquisition is initiated by a trigger signal of the pump pulse on a photodiode with a time resolution down to tens of ps. However, due to limitations in data size, the time resolution has to be adjusted with the oscilloscope to the investigated timescale.

2.1.4 Data Analysis

The transient absorption data have to be processed, corrected, and kinetically analyzed to reveal the contained kinetic information. In this work, the data analysis was performed using OPTIMUS,^[36] a MATLAB based program for kinetic analysis of time-resolved data. Due to the ultrafast timescale of fs-transient absorption experiments, dispersion and chirp of the spectrally broad supercontinuum probe pulse cannot be neglected and have to be accounted for. The dispersion of the probe pulse is analyzed and fitted based on a measurement of the coherent artifact of the pure solvent. Coherent artifacts are commonly observed in ultrafast spectroscopy and originate from the alteration of the refractive index induced by the high intensity of the pump pulse when pump and probe pulse temporally overlap. This manipulation of the phase of one pulse by refractive index changes induced by another pulse is termed cross phase

2 Theoretical Framework

modulation and ultimately gives rise to the coherent artifact.^[37-39] As the coherent artifact is also present in the sample measurement, the fitting parameters obtained from the measurement of the pure coherent artifact in a solvent can be applied to account for the coherent artifact in the sample measurement. One of the fitting parameters, the instrument response function (IRF), specifies the temporal width of the coherent artifact and is associated directly with the time resolution of the experiment.

For kinetic analysis, different analytical techniques can be applied depending on the type of kinetics and the expected underlying kinetic model. The analytical techniques are generally divided into model independent and model dependent methods, where the result of the fitting is influenced by the assumed kinetic model. A kinetic model is defined by the number, connectivity, and population of the individual components which have to be constrained based on reasonable assumptions and knowledge derived from other techniques. Often different kinetic models approximate a given dataset sufficiently and the choice of the 'correct' model is quite complex.

The most basic model dependent technique for global analysis of transient absorption data is global lifetime analysis (GLA). Here, the signal $S(t)$ at a defined excitation wavelength λ_{exc} is approximated by the convolution of the IRF and the discrete sum of independent exponential functions for each detection wavelength λ_i with lifetimes τ_j and pre-exponential factors A_j (eq. 2.16).

$$S(t, \lambda_{exc}, \lambda_i) = \sum_{j=1}^n A_j(\tau_j, \lambda_{exc}, \lambda_i) \cdot \exp(-t/\tau_j) \otimes IRF(t) \quad (2.16)$$

Plotting the pre-exponential amplitudes of each lifetime component against the wavelength yields the decay-associated spectra (DAS) that contain the kinetic information on spectral changes of each lifetime component. Even though the assumption of independent lifetime components represents a model with no connections between the individual components, it is still considered to be a kinetic model. More complex kinetic models with connections between the components are collected under the term global target analysis (GTA) where an approach similar to GLA is used to apply a kinetic target model to the transient data.^[36,40] A sequential model represents the simplest target model, in which all states are connected in a sequential way ($A \rightarrow B \rightarrow C \dots$). From such target models, the difference spectra corresponding to the individual components, the evolution-associated difference spectra (EADS), can be extracted which are termed species-associated difference spectra (SADS), if the 'correct' kinetic model is assumed. These SADS represent an important evaluation criterion to validate the applied kinetic

model and provide important spectral information on the identified components.

The disadvantage of model dependent analysis techniques obviously stems from the necessity to pick the 'correct' kinetic model from the multitude of possibilities. Here, model independent techniques complement GTA in order to determine the number of components and other parameters. However, model independent methods like lifetime distribution analysis (LDA) offer more than just additional information for GTA.^[36] LDA in particular, is a powerful tool that can be used to identify and approximate non-exponential dynamics like protein-controlled dynamics, solvation, and cooling processes, where classical GTA struggles without specific adjustments. In LDA, the transient data are approximated by a quasi-continuous ($n > 50$) distribution of exponential functions with fixed lifetimes according to eq. 2.16.^[36,41] The kinetic information are then presented in the form of lifetime density maps (LDMs), displaying the pre-exponential amplitude of a lifetime component as a function of the wavelength.

While these techniques can also be applied to flash photolysis data, their large data size with data points every 100 ns on a timescale of up to several seconds prevents reasonable analysis. Therefore, the data size needs to be reduced prior to analysis without loss of information. For this purpose, data points are averaged on a combined linear and logarithmic timescale which is adapted to the investigated dynamics. The obtained transients are then combined into one dataset and can be analyzed globally with either GLA, GTA, or LDA.

2.2 Phytochromes

Phytochromes form a superfamily of photoreceptors. They were first discovered as one of the three main regulators of plant photomorphogenesis along cryptochromes and phototropins.^[8,42–44] With time, they were also found in a variety of other photosynthetic organisms, *e.g.*, algae,^[24,45] cyanobacteria,^[46–48] and photosynthetic bacteria^[49] and even in non-photosynthetic bacteria^[50] and fungi.^[51,52] In these organisms, phytochromes are involved in the regulation of photomorphogenesis, phototaxis, photosynthesis, and chromatic adaptation among other biologically relevant processes.^[53–58] Their regulatory function is based on the reversible *Z/E* isomerization of the C15=C16 double bond in a bilin chromophore embedded within the protein scaffold switching between a thermostable dark state and a metastable light-adapted state.^[59,60] These states are termed according to the color absorbed by the respective state, *e.g.*, a state absorbing red light is termed P_r state. Most phytochromes in fungi, plants, and bacteria contain a P_r state as the dark state, and a P_{fr} state absorbing far-red light (680–800 nm) as the light-adapted state.^[54,55,61,62] However, some cyanobacterial and algal phytochromes break this red/far-red pattern and exhibit a large spectral diversity covering the whole UV/Vis spectral region.^[24,56,57,62–70] Independent of the spectral position, the light-adapted state is often able to thermally revert to the dark state; however, the thermal rates vary significantly between phytochromes.^[54,55,61]

The precise mechanism of the signaling process of phytochromes induced by the chromophore isomerization is still under investigation. It is established that the photocycle of phytochromes proceeds via several intermediate steps after initial chromophore isomerization involving large scale protein rearrangements during the later steps.^[55] These rearrangements transmit the light-induced signal from the chromophore and its surrounding domains into the cell via a variety of different output modules (OPMs) including histidine kinases (HKs), diguanylyl cyclases (GGDEFs), phosphodiesterases (EALs), metal-dependent Ser/Thr protein phosphatases (PPMs), and even domains with no enzymatic activity (*e.g.*, Per-Arnt-Sim (PAS) and 2-helix output sensors (HOS)).^[53,55] The variety of output domains combined with the conserved architecture of phytochromes suggests a common signal input for controlling the different OPMs.^[55] Currently, three models have been proposed for the light-dependent activation of the output modules in phytochromes. An overview can be found in a review by Takala *et al.*^[55] The models suggest different motions of the photosensory core relative to the OPM to regulate the activity of the signal output and do not necessarily exclude each other. Hence, the structural activation of phytochromes may include a combination of these models.

Phytochromes have recently gathered attention due to their potential applications in optogenetics and fluorescent probes for biomedical imaging.^[13,71–74] They exhibit favorable properties for these applications such as simple modular architecture, absorption and fluorescence in the red to far-red spectral range with the possibility to span the entire UV/Vis spectral range, if cyanobacteriochromes (CBCRs) are included.^[71] Bacteriophytochromes in particular, are favorable for application in mammalian tissue, where the required biliverdin chromophore is found ubiquitously and the near infrared (NIR) fluorescence can penetrate deep into the tissue as it is spectrally located within the tissues transparency window.^[71] The red/far-red absorption also allows application in optogenetics orthogonal to the already established blue light sensing optogenetic systems.^[13]

As this dissertation focuses on the investigation of determining factors of photoisomerizations, the complex interplay of steric, ionic and hydrogen bonding interactions of the protein environment with the embedded bilin chromophore in phytochromes represents an interesting target. In this context, it is important to understand the structural nuances separating phytochromes into several subgroups, the chromophore diversity and structure as well as the arrangement and interactions of the highly conserved residues constituting the immediate chromophore environment. These aspects are highlighted in the following sections complemented by an overview of the general photodynamics of phytochromes and the relevance and presence of different chromophore environments within a protein ensemble in the context of structural heterogeneity. The presented state of the art provides the basis for the investigations conducted in this thesis.

2.2.1 Classification of Phytochromes

Phytochromes are classified into three different subgroups based on the domain architecture of their photosensory core module (PCM) (Fig. 2.7).^[61,62] The PCM comprises the domains necessary for sensing and converting the molecular changes induced by the light-dependent chromophore isomerization into a trigger for the OPM, which then translates the light-induced signal into a biochemical response within the cell.^[54,55,61,62]

In group I phytochromes including canonical plant, (*e.g.*, *OatPhyA*,^[75] *AtPhyA*,^[76] *AtPhyB*^[76]) and cyanobacterial phytochromes (*SynCph1*,^[47,77] *CphA*,^[78] *CphB*^[78]) as well as bacterial (*Agp1*,^[79] *Agp2*,^[79,80] *DrBphP1*,^[50] *PaBphP*^[50]), algal (*MpPhy*, *DtPhy*)^[45] and fungal (*NcFph1*,^[81] *AnFphA*^[51]) phytochromes, the PCM consists of an array containing a PAS domain, a cGMP-specific phosphodiesterases, adenylyl

2 Theoretical Framework

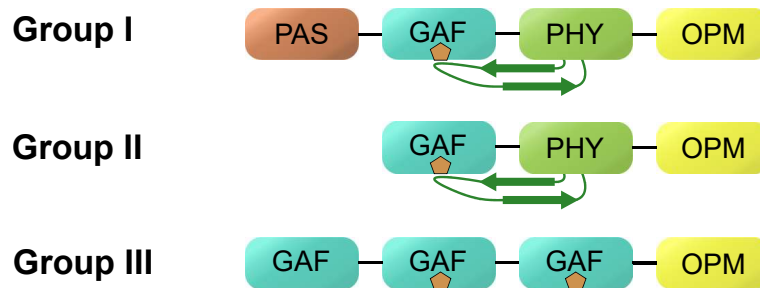


Figure 2.7 – Schematic illustration of the typical domain architectures of the characteristic PCMs for different groups of phytochromes. The chromophore (brown pentagon) is bound in the GAF domain.

cyclases, and FhlA domain, and a phytochrome specific (PHY) domain.^[54,61,62] The cGMP-specific phosphodiesterases, adenylyl cyclases, and FhlA (GAF) domain contains the embedded bilin chromophore, while the PAS domain forms a figure-of-eight-knot with the GAF domain.^[82–84] The chromophore is covalently linked to the protein via a thioether linkage with a conserved cysteine residue located either in the GAF domain in plants and cyanobacteria^[53,55,83,85] or in the N-terminal extension adjacent to the PAS domain in bacteria and fungi.^[53,55,82,86,87] The PHY domain interacts with the chromophore directly through a tongue-like extension stabilizing the chromophore and shielding it from the solvent.^[83,84,88] Via this so-called tongue, the PHY domain is also crucially involved in transferring the light-induced signal to the OPM as the tongue changes its secondary structure during the photocycle to transmit the molecular changes from the chromophore further into the protein scaffold.^[89–92] In contrast, group II and group III phytochromes lack the PAS domain or only contain an array of single GAF domains, respectively, and have so far only been reported in cyanobacteria.^[55,61,62] Due to the lack of the PAS domain and its figure-of-eight-knot, group II phytochromes are also known as knotless phytochromes^[61] (e.g., *SynCph2*,^[93,94] *Nostoc* sp. All2699g1g2^[88,95]) accordingly. While group I and group II phytochromes typically switch between a red-absorbing P_r and a far-red-absorbing P_{fr} state,^[54,55,61,62,96] group III phytochromes also known as cyanobacteriochromes (CBCRs) (e.g., *Anabaena* sp. AnPixJg2,^[64] *Synechocystis* sp. Slr1393g3,^[95,97] *Nostoc punctiforme* NpR6012g4,^[98] *Thermosynechococcus elongatus* TePixJ^[65,99]) exhibit a large spectral diversity covering the whole UV/Vis spectral range, even reaching into the NIR.^[57,63–70] Interestingly, algal group I phytochromes show a similar spectral diversity.^[24,45]

Among knotless phytochromes it has been shown that some retain their photoconver-

sion ability even with just the GAF domain,^[95,100] making them a link between group II and III phytochromes and an interesting model system for studying the influence of the PHY domain on the photodynamics of phytochromes. Therefore, this work aims to study the influence of the immediate chromophore environment on the photoisomerization and the following GS dynamics in knotless phytochromes, modulated by the presence or absence of the PHY domain.

2.2.2 Chromophore Variety and Color Tuning Mechanisms

Depending on the organism of origin, phytochromes bind different bilin chromophores as the phytochromes in plants, bacteria, and cyanobacteria contain phytochromobilin (PΦB), biliverdin IX α (BV), and phycocyanobilin (PCB) or phycoviolobilin (PVB), respectively (Fig. 2.8).^[53,55]

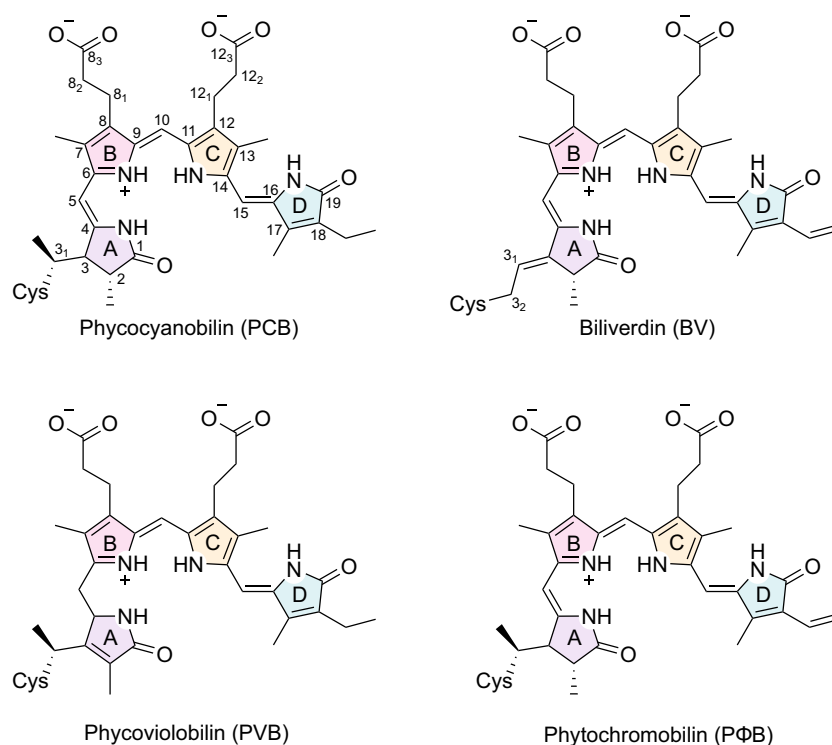


Figure 2.8 – Covalent adducts of bilin chromophores in phytochromes. Phytochromes incorporate linear tetrapyrrole precursors and form covalent adducts using a thioether linkage attached at the C3¹ atom for PCB, PVB, PΦB and the C3² atom for BV. In group I and II phytochromes, the bilin adducts commonly adopt a (5Z)-*syn*, (10Z)-*syn*, (15Z)-*anti* configuration (ZZZ ssa) in the P_r state and a (5Z)-*syn*, (10Z)-*syn*, (15E)-*anti* configuration (ZZE ssa) configuration in the P_{fr} state.^[61]

2 Theoretical Framework

All bilin chromophores incorporated in phytochromes share a common, open tetrapyrrole structure with slight variations in the substitution pattern of the outer rings, and therefore, the conjugation length (Fig. 2.8).^[54,55,61,62] With few exceptions,^[101] all pyrrole nitrogens are protonated in both the dark and light-adapted state^[100,102–105] and the chromophore carries a net positive charge which is proposed to be mainly localized at ring B in the P_r state but may be delocalized to ring C as well.^[106] In all phytochromes, light absorption results in the *Z/E* isomerization of the C15=C16 double bond which, in turn, rotates ring D.^[55,59,60,107] Note that the bilin chromophore is not planar and that the dihedral angle between the individual rings may vary significantly between different phytochromes.^[90,108–111]

In phytochromes switching between a P_r and a P_{fr} state, the difference in conjugation length between the individual bilins results in typical absorption maxima of the respective states at ~640–660 nm and ~690–710 nm for PCB,^[77,78,94,95] ~660 nm and ~730 nm for PΦB,^[42,75] and ~700 nm and ~750 nm for BV,^[51,55,79,81] however, deviations from these values are observed.^[53] PVB is not directly incorporated into phytochromes but instead formed after incorporation of PCB in some CBCRs exhibiting significantly blue-shifted absorption.^[112] Apart from the different types of bilin chromophore species, the effective conjugation length of the chromophore as the main aspect of color tuning is determined by the chromophore binding geometry, *e.g.*, the dihedral angles between the individual pyrrole rings and the electrostatics of its environment, which results in a large variety of colors available from rather similar chromophore structures.^[108,110,111] These factors are regulated by the surrounding amino acids in the chromophore binding pocket via steric and electronic interactions. Those can manipulate the tilt in the geometry and the protonation state of the chromophore.^[108,113–116] An additional mechanism exists in CBCRs, where a second thioether linkage of the C10 atom to another cysteine residue is observed to break the conjugation, reduce the effective conjugation length and shift the spectrum into the blue to UV region.^[67,68,112]

2.2.3 Conserved Residues of the Binding Pocket

The amino acid residues in the immediate vicinity of the bilin chromophore have a significant impact on the photochemical properties, the dynamics and the efficiency of the phytochrome photoreaction. Several of these amino acids form structural motifs that are highly conserved among most phytochromes. Their crucial role in maintaining efficient photochemistry has been verified in various mutational studies, however, photoswitching is rarely completely abolished upon single mutations.^[53,90,113,114,117] The

conserved motifs located in the GAF domain are the DIP motif, the aliphatic pocket surrounding ring D and two conserved histidine residues (H260 and H290 in *SynCph1*) interacting with ring D and the pyrrole nitrogens.^[55,82–84,89,90,113] Other motifs can be found in the PHY tongue where the PRXSF, the WGG and the WXE motifs are responsible for the interaction with the chromophore and its binding pocket and keep the tongue in a proper secondary structure, which was proven to be important for proper signal transmission to the output domain.^[62,83,84,89–91,118]

The specific role and importance of these residues during the photocycle will be elaborated below. An overview of the binding pocket and its most relevant conserved amino acid residues is displayed in Fig. 2.9.

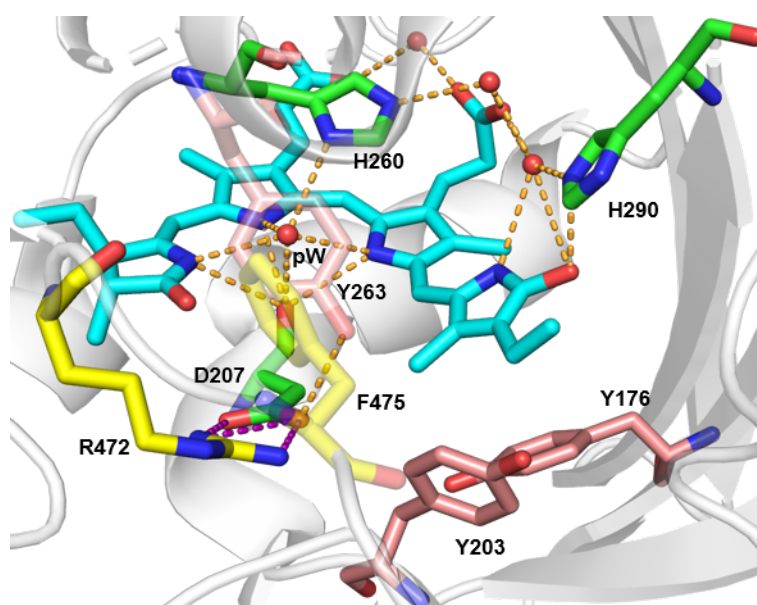


Figure 2.9 – Structural snapshot of a selection of highly conserved amino acid residues in the chromophore binding pocket of *SynCph1* in the P_r state (protein database identifier (PDB ID): 2VEA).^[83] The chromophore (cyan), D207, H260, H290 (green), and several water molecules (red spheres) form an extended hydrogen bonding network (dashed, orange). In this network, the pyrrole water (pW), a highly conserved water molecule, mediates the hydrogen bonds between the pyrrole nitrogens of the chromophore with D207 and H260, while H290 is hydrogen bonded to the ring D carbonyl. H290 is connected to H260 and the central hydrogen bonding network via multiple water molecules and the propionic side-chain of ring C. D207 forms an additional hydrogen bond to Y263 (transparent, pink) and constitutes the conserved salt bridge (dashed, purple) with R472 of the PHY tongue (yellow). Apart from hydrogen bonding, the aliphatic pocket (pink) illustrated here by Y176, Y203, and Y263 keeps the chromophore ring D in place, while F475 of the PRXSF motif (transparent, yellow) shields it from the solvent.

To avoid confusion arising due to the different numbering of amino acids in different

2 Theoretical Framework

phytochromes, the numbering of *SynCph1*, one of the best researched phytochromes, will be used consistently in the following sections. The respective numbering in other phytochromes discussed later on in this thesis is given in Tab. 2.1.

Table 2.1 – Numbering of conserved amino acids in different phytochromes.

Phytochrome	PDB ID								
<i>SynCph1</i>	2VEA ^[83]	Y176	D207	H260	Y263	H290	R472	S474	
<i>SynCph2</i>	4BW1 ^[90]	Y47	D79	H130	Y133	H160	R383	S385	
All2699g1	6OZA ^[119]	Y55	D87	H139	Y142	H169	-	-	
Agp1	5I5L ^[120]	Y166	D197	H250	Y253	H280	R462	S464	
<i>DrBphP</i>	4Q0J ^[104]	Y176	D207	H260	Y263	H290	R466	S468	
<i>OatPhyA3</i> ^[121]	-	Y241	D272	H323	Y326	H372	R552	S554	

Chromophore Arrangement in the Binding Pocket

To ensure proper chromophore positioning while still allowing enough movement for the photoinduced rotation of ring D, a very specific pocket geometry is required and conserved in phytochromes. From the multitude of residues responsible for packing of the chromophore, only the highly conserved ones and those surrounding the photoactive ring D will be described here in more detail. Of the highly conserved residues mentioned above, D207, I208, and P209 of the DIP motif together with H260 tightly pack the rings B and C to prevent isomerization of the respective C10=C11 bond.^[82,113,122] In particular, D207 is crucial for proper chromophore positioning through its hydrogen bonding interactions to the pyrrole nitrogens via the conserved pyrrole water (Fig. 2.9).^[55,122] While this water molecule is highly conserved in group I and II phytochromes, it is missing in CBCRs.^[55,63,122] Mutants of D207 often become highly fluorescent with only minimal photoswitching efficiency, showing the importance of the chromophore positioning for the photochemistry.^[103,113,117,118] P209 (DIP) and P471 (PRXSF) clamp ring A to shield it from the solvent and prevent rotation upon photoexcitation.^[83,90]

Being held in an aliphatic pocket including Y176, V186, Y/F198, Y/F203, P204, and Y263 (Fig. 2.10),^[53,82,83,113,121] ring D has substantially more space than the other rings^[55,82,122] to accommodate its rotation during photoconversion. F475 (PRXSF) in the tongue closes this pocket to shield ring D from the solvent.^[83,90] Out of these residues, Y176 and Y263 are assigned a significant role in controlling the chromophore tilt angle, acting as a steric gate for the isomerization.^[82,83,113,114,123–125]

Mutational studies of Y176 have shown that its hydroxyl group is important for the

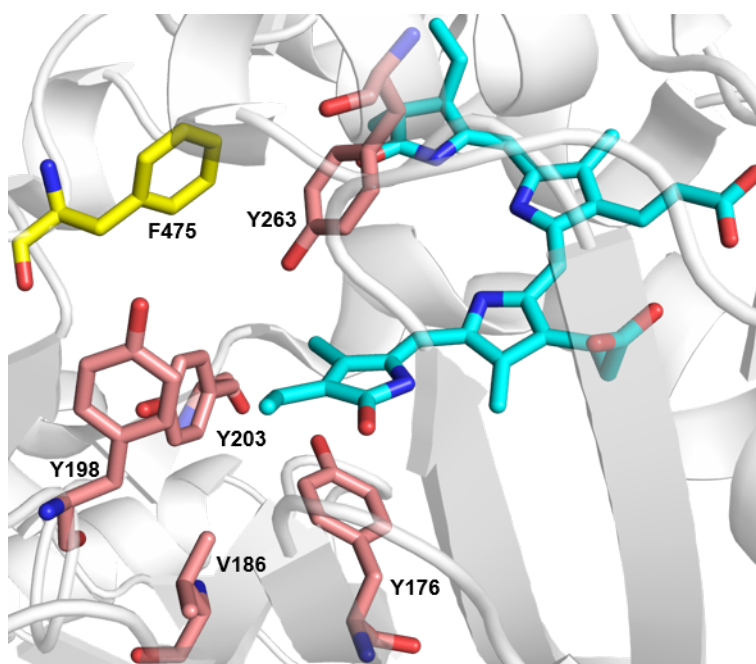


Figure 2.10 – Structural snapshot of the chromophore (cyan) in its binding pocket displaying Y176, V186, Y198, Y203, and Y263 (pink) to illustrate the hydrophobic pocket around ring D in the P_r state of *SynCph1* (PDB ID: 2VEA).^[83] This pocket is closed by F475 (yellow) to shield the chromophore from the solvent.

photochemistry as Y176H fails to photoconvert efficiently to the P_{fr} state.^[113,124,125] Interestingly, in canonical plant and cyanobacterial phytochromes these mutants become highly fluorescent,^[124,125] while in bacteriophytochromes and the knotless phytochrome *SynCph2* this effect is not observed.^[94,113] The reduction in P_{fr} formation was rationalized by the loss of a stabilizing hydrogen bond between Y176 and the hydrogen bonding network contacting the ring D carbonyl in the P_{fr} state.^[123,126,127] Another suggestion is a change in the protonation state of the central hydrogen bonding network in the binding pocket, induced by the altered or lost hydrogen bonding capability of Y176H and Y176F.^[124] Recently, it has also become evident that Y176 and F/Y203 undergo significant side-chain rearrangements following the photoisomerization to accommodate the changes in the electrostatic properties of ring D upon rotation. During the isomerization, the previously hydrophobic side of the chromophore with methyl and vinyl substituents is replaced by the hydrophilic side of ring D where the pyrrole nitrogen and the carbonyl group previously held by H290 (Fig. 2.9) are now facing the hydrophobic pocket.^[53,121,126,127] In *DrBphP*, this reorganization opens a gate for H201 to rotate towards the chromophore and stabilize the ring D carbonyl after isomerization.^[123,126,127]

2 Theoretical Framework

In case of Y263, multiple roles have been identified including optimization of photoconversion efficiency, support of the tongue interaction in the P_r state, stabilization of the P_{fr} state, and controlling the ring D tilt angle.^[60,83,113,114,128,129] The steady state P_r absorption spectra of Y263 mutants show only small spectral changes and depending on the mutation maintain similar extinction coefficients^[114] which indicates a minor change in the ring D tilt angle in the parental P_r state.^[114] In contrast, the photoconversion efficiency to the P_{fr} state is significantly reduced in Y263 mutants in favor of an amplified fluorescence efficiency and a longer ES lifetime.^[114,117,128–131] Thus, Y263 is important for tuning the ES dynamics and the efficiency of the formation of the primary photointermediate Lumi-R, potentially by acting as a steric block or gate due to its proximity to ring D.^[128–130] The role of both Y263 and Y176 as a steric gate in the isomerization is further supported by time-resolved X-ray crystallography, which shows that both residues are already moving away from the chromophore 10 ps after excitation to accommodate the isomerization.^[132]

Apart from steric interactions, the hydrogen bonding capability of Y263 is critical to stabilize the chromophore in the P_{fr} state and the interaction with the PHY tongue in the P_r state.^[60,121,128] In the P_{fr} state, Y263 forms hydrogen bonds either to the pyrrole nitrogen or the ring D carbonyl to stabilize its twisted conformation.^[60,83,121] Recent studies also suggest the possibility of an OH- π interaction stabilizing the chromophore.^[133,134]

In the P_r state, Y263 forms a hydrogen bond to D207, which keeps D207 in the proper position to interact with R472 (PRXSf) in the tongue.^[60,83,113,128] The lack of this hydrogen bond in the Y263F mutant of *DrBphP* leads to a change in tongue fold in the P_r state. Instead of the expected β -sheet fold of the tongue, an α -helix fold characteristic for the P_{fr} state is observed.^[128] Whether this is the case in other phytochromes is unclear as *e.g.*, no such effect was observed in the crystal structure of the Y263F mutant of *SynCph1*.^[114] Other studies, where a hyperactive signaling was observed in Y263F mutants of *AtPhyB* but not in *OatPhyA*, further add to this discrepancy, as a permanent P_{fr} fold of the tongue could indeed activate signaling without proper photoconversion.^[118]

As evident by the involvement of Y176 and Y263 in both hydrogen bonding and steric interactions, a classification of the conserved residues in the binding pocket into specific roles is challenging, as almost all highly conserved residues fulfill multiple roles. However, to generate a reasonable overview of the binding pocket, the classification is based on the main interactions of the respective residue. Nonetheless, all functions of the individual amino acids contribute to efficient photoconversion of phytochromes.

Protonation State and Hydrogen Bonding Interactions

Apart from the hydrophobic and steric interactions, extensive hydrogen bonding networks are necessary to stabilize the chromophore and maintain the protonation state of the bilin to preserve its photoactivity. The protonation state of the bilin is of critical importance, since neutral or deprotonated bilin species have been reported to show inhibited isomerization capabilities^[135] and reduced extinction coefficients compared to the protonated species observed typically.^[115,135,136] However, a study on *in vitro* assembled AnPixJg2 from *Anabaena* sp. showed that in this case the protonation state does not alter the absorption properties of the bilin, representing a remarkable exception.^[137] The most significant and conserved amino acid residues in the context of hydrogen bonding and controlling the protonation state of the chromophore are D207 (DIP) and the two histidine residues H260 and H290 (Fig. 2.11).^[53,82,83,113] As these amino acids are central components of the extended hydrogen bonding network surrounding the chromophore, their mutations will always alter the pKa value of the chromophore or its network; however, the magnitude of pKa change differs greatly depending on the residue.

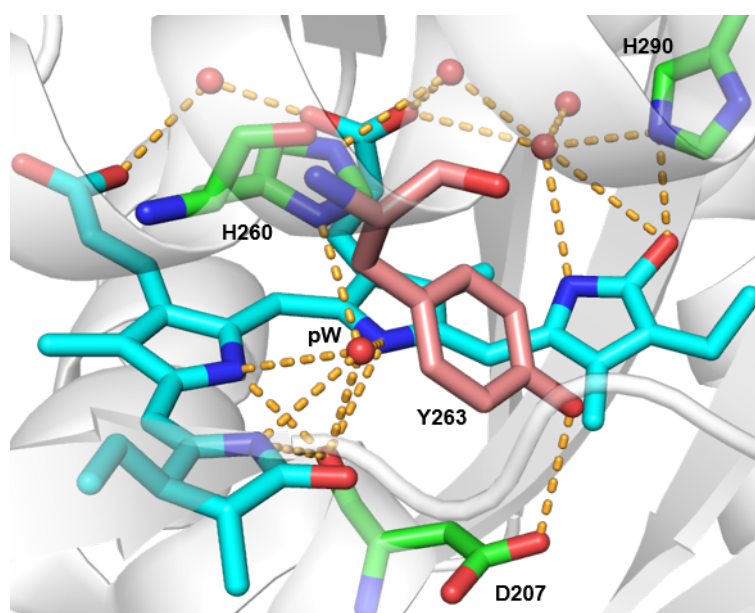


Figure 2.11 – Structural snapshot of the extended hydrogen bonding network of the chromophore (cyan), the conserved amino acid residues (green) D207, H260, H290, several water molecules (red spheres), and the highly conserved pyrrole water (pW) in the P_r state of *SynCph1* (PDB ID: 2VEA).^[83] D207 forms an additional hydrogen bond to Y263 with its carboxyl function, which is important for proper positioning of D207.

2 Theoretical Framework

H290, similar to Y263, exhibits only a minor impact on the pKa value of the chromophore and hence its protonation state.^[115] With the proximity to ring D and direct hydrogen bonding contact to its carbonyl function, H290 maintains the tilted conformation of ring D and thus stabilizes the P_r state.^[82,83,113,138] Studies also found that the amount and strength of hydrogen bonding to ring D affects the ES dynamics and photoconversion efficiency of the P_r state.^[138-142] In the P_{fr} state, this residue contacts the ring C propionate group, which illustrates the reorganization within the chromophore binding pocket and hence the hydrogen bonding network to adapt to the chromophore isomerization.^[85,121,123,138,143] The protonation state of H290 might also influence the thermal reversion kinetics by favoring an enol conformation of the chromophore ring D carbonyl and the C15=C16 double bond.^[144]

In contrast, H260 and D207 have significant impact on the chromophore pKa and the protonation state.^[103,115] Together with the pyrrole water, these residues are part of the hydrogen bonding network interacting with the pyrrole nitrogens of the chromophore and play a crucial role in stabilizing its positive charge.^[54,82,83,103] Mutations of H260 decrease the amount of protonated bilin at a fixed pH by shifting the chromophore's pKa value.^[103,113,115,145] Upon introduction of residues with long cationic side-chains at this position, chromophore binding is prevented entirely due to electrostatic repulsion.^[113] H260 also forms hydrogen contacts to the ring C propionate in the P_r state and is connected to H290 via the ring C propionate and conserved water molecules, with the amount of water molecules differing between phytochromes.^[82,83,121] In *SynCph2*, an additional serine residue is involved here as a bridge in the hydrogen bonding network instead of a water molecule due to differences in the remaining interactions of the ring C propionate.^[90] Apart from determining the chromophore pKa, the two conserved histidine residues exist in a neutral and protonated state in *SynCph1*.^[60] This introduces structural heterogeneity into the binding pocket, as the hydrogen bonding network differs depending on the respective protonation states of these histidine residues. Of the two observed species, only one is suggested to be able to photoconvert, which results in a pH dependent tuning of the photoefficiency of phytochromes.^[60,116,146]

In case of D207, most mutants still properly bind the bilin chromophore, however, the pKa value is shifted in favor of a deprotonated chromophore species.^[103,113,115] Besides the chromophore and pyrrole water, D207 additionally hydrogen bonds to Y263 and forms a salt bridge with R472 (PRXSF) in the tongue connecting the tongue to the chromophore binding pocket (Fig. 2.11).^[53,83,89,90,121] In the P_{fr} state, D207 stabilizes the chromophore conformation as part of a hydrogen bonding network involving S474, Y263, the carbonyl group, and the pyrrole nitrogen of ring D.^[85,89,121,123,147] Consider-

ing photoconversion, modifications of H260 and D207 severely disturb the photocycle when converting from P_r to P_{fr} as most of such mutants do not properly form P_{fr} upon illumination.^[103,113,145,146] Hence, it was suggested that both residues are crucial for the deprotonation and/or reprotonation of the chromophore that occur in the final steps of the photocycle making them an essential part of phytochrome photochemistry.^[103,113,145,146]

These findings highlight the importance of fine tuning the pKa of the chromophore and the protonation state of both the hydrogen bonding network and the chromophore for the photochemistry of phytochromes representing an additional level of regulation.

Tongue Interaction

The third group of highly conserved residues can be found in the tongue region of the PHY domain (Fig. 2.12).

The PRXSF, WGG, and WXE (sometimes termed HbXE where Hb represents a hydrophobic residue)^[53] motifs are essential for maintaining contact to the chromophore binding pocket, stabilizing the P_{fr} state and the correct tongue fold and hence allowing the transmission of the light-induced signal from the chromophore through the tongue into the PHY domain causing the required displacement to activate the OPM.^[53,83,85,89,90]

The PRXSF motif is highly conserved in group I and II phytochromes.^[55,83,90] As mentioned above, P471 (PRXSF) clamps ring A with P209 (DIP) to stabilize the P_r conformation.^[83,90,120] The adjacent R472 (PRXSF) interacts with D207 to form the salt bridge stabilizing the tongue conformation in the P_r state,^[53,55,83,89,90,121] while S474 (PRXSF) is initially pointing away from the chromophore in the P_r state.^[90,121] In the P_{fr} state, S474 rotates to form hydrogen bonds to D207, the pyrrole nitrogen and carbonyl of ring D and Y263 stabilizing the strained isomerized chromophore conformation.^[84,89,121,123,127] F475 (PRXSF) shields the chromophore binding pocket from the solvent and forms a strong contact to the interface of the GAF domain, securing the tongue to the GAF domain.^[83,85,90] The central role of these residues in stabilizing the P_{fr} state and the overall photoconversion is revealed by mutational studies. Mutants of the PRXSF motif significantly influence the dark reversion by either destabilizing the P_{fr} state or introducing barriers to regain the P_r tongue conformation and may affect the photoconversion abilities overall.^[85,90,120]

The WGG motif and the WXE motif anchor the PHY tongue to the GAF domain.^[53,85,90] The former interacts with a hydrophobic pocket on the surface of the GAF domain in the P_r state and, according to the proposed tryptophan switch/toggle model,

2 Theoretical Framework

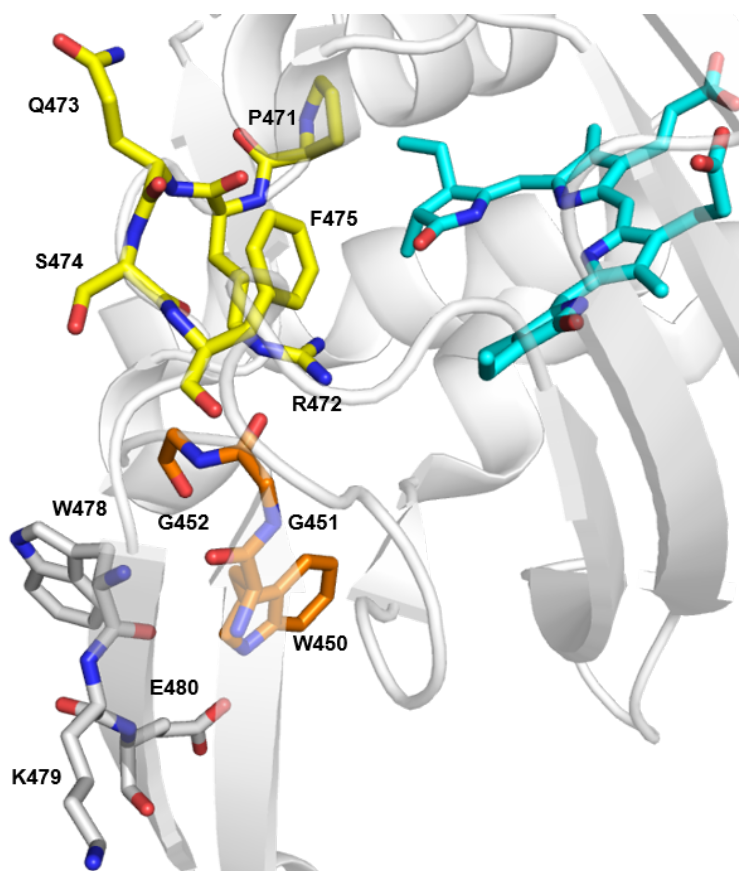


Figure 2.12 – Illustration of the conserved PRXSF (yellow), WGG (orange), and WXE (white) motifs in the PHY tongue in the P_r state of *SynCph1* (PDB ID: 2VEA).^[83] Here, the WGG motif is oriented towards the binding pocket, whereas the WXE motif is facing away. This orientation is reversed in the P_{fr} state.^[53,90]

is replaced by the WXE motif which fulfills a similar role in the P_{fr} state.^[53,85,90,96] Mutations of these residues, even though they are more distant to the chromophore binding pocket, influence the photochemistry and dark reversion via a link to the chromophore through a conserved hydrogen bonding network.^[53,85,90,96,104] The proposed switching of these two motifs is considered an essential part of light-induced signaling in phytochromes.^[53,85,90]

2.2.4 Heterogeneity in the Parental States

The structural arrangement of the described motifs is essential for the photochemistry of phytochromes. While X-ray crystallography represents a major tool for obtaining information on these structural relations in phytochromes, its drawback is that it may

only capture one specific set of conformations that crystallizes well. However, this subset may not represent the relevant protein conformations in solution to a sufficient extent. Indeed, using more dynamic methods like nuclear magnetic resonance (NMR), RR, and ultrafast IR or UV/Vis spectroscopy, phytochromes were found to be both structurally^[60,88,121,148–150] and spectrally heterogeneous adding another layer of complexity to the photochemistry of phytochromes.^[97,109,116,151–155] Structural heterogeneity can be straightforwardly understood as the existence of distinct substates that differ in conformation, orientation, or protonation state of one or multiple residues. Depending on the magnitude of the conformational differences, they may result in different spectral and/or photochemical properties of the individual substates. The ratio of such substates may depend on pH, temperature, or other external conditions making structural heterogeneity another tuning mechanism of phytochrome photochemistry.^[116,150,153,156]

It is important to distinguish between structural and spectral heterogeneity since different GS structures do not necessarily have to yield different photochemical properties as barriers present in the GS may not necessarily exist or could be overcome easily after the high energy excitation with visible light. An example for this can be found in the study of two bacteriophytochromes, where the ES dynamics proceeds homogeneously despite ground state heterogeneity (GSH).^[157] Additionally, it needs to be considered that some structural techniques are carried out at low temperatures where conformations interchangeable at room temperature might be frozen out. At room temperature a set of distinct substates could instead appear as a continuous distribution of conformations which would behave differently in dynamic studies than distinct substates. However, spectral heterogeneity can often be linked to structural heterogeneity and distinct GS substates with different conformations. This frequently leads to a wavelength dependence of photoefficiency and photodynamics.^[97,150–152] Due to the complicated relation between structural and spectral heterogeneity, it still remains a subject of investigation and debate in the field of phytochromes.

Heterogeneity has been found to be particularly widespread among CBCRs, where it is commonly observed in both dynamics and structure.^[97,98,109,153,158–162] In group I and II phytochromes, such strong heterogeneity is less common, which has been attributed to the presence of the PHY domain tongue.^[88,163] The interactions between the tongue and the chromophore binding pocket limit the conformational space in the binding pocket and hence reduce the amount of available distinct conformations.^[88]

The occurrence of heterogeneity in group I and II phytochromes also differs between the P_r and the P_{fr} state. In the P_r state, the chromophore is considered to be loosely embedded in a soft pocket, which is more flexible and capable of accommodating multiple

2 Theoretical Framework

distinct conformations.^[121] In contrast, in the P_{fr} state, the chromophore is rigidly fixed by extensive and strong hydrogen bonds to maintain its twisted conformation allowing typically less heterogeneity or heterogeneity based on substates with smaller barriers, and therefore, faster interconversion.^[121,149,164,165] This concept has been described as a soft-to-hard transition of the binding pocket upon photoswitching from the P_r state to the P_{fr} state.^[105,121]

The origin of heterogeneity in the different states of phytochromes has not been investigated in all phytochromes. However, the major forms of known structural heterogeneity are differences in side-chain rotamers,^[109,160] chromophore conformation, and the protonation state of either the two conserved histidines or the chromophore.^[60,116,144,146,159,166]

Heterogeneity of the P_r State

In the P_r states of *SynCph1* and several bacteriophytochromes, evidence has been presented for the existence of multiple protonation states of the two conserved histidines H260^[60,116,146,159,166] and H290.^[144,167] Especially, the protonation state of H260 has been identified as the main cause of heterogeneity in *SynCph1*^[60,116,146,159] and AnPixJg2^[159] from *Anabaena* sp. With a pKa at ~7.5 in *SynCph1*, H260 is in a protonation equilibrium between its protonated and neutral form when working at physiological conditions.^[116,146] The presence of the positive charge alters the rest of the hydrogen bonding network and the interaction to the equally positively charged pyrrole nitrogens of the chromophore.^[60,146] In turn, the conformation of the chromophore and its spectral properties are slightly altered allowing spectral separation of the two isoforms P_r -I and P_r -II.^[60,116,152] In the protonated state P_r -I, the hydrogen bonding network is disrupted and the stabilizing interaction of H290 to ring D is lost, potentially facilitating the isomerization.^[60,116,150] This effect of hydrogen bonding strength of H290 to the chromophore was demonstrated in bacteriophytochromes in more detail.^[138–141] The two observed substates together with a substate containing a deprotonated chromophore are assigned as the basis of the multiphasic ES dynamics observed in *SynCph1*.^[116]

In many cases, structural heterogeneity of both the P_r and the P_{fr} state is suggested on the basis of multiphasic ultrafast ES dynamics.^[98,150–152,155] In *SynCph1*^[60,116,146] and several CBCRs,^[97,98,109,153,159,159,160,168] this concept has been supported by structural investigations and theory. However, not all multiphasic ES dynamics are related to structural heterogeneity in the sense of distinct substates. Recently, especially in phytochromes with long ES lifetimes, alternative explanations have been proposed such as

ES branching^[169] and solvation- or protein-controlled dynamics.^[130,170] The latter are non-exponential, and thus, mathematically require multiple exponential functions to be fitted correctly rendering them hard to distinguish from dynamics of distinct substates. Hence, these processes can instead be described as the decay of one distributed population whose dynamics are controlled by solvent or protein reorganization.^[130,170,171]

Heterogeneity of the P_{fr} State

The occurrence and structural basis of heterogeneity in the P_{fr} state of phytochromes have been investigated in much less detail. Here, no protonation heterogeneity of H260 is observed,^[60,146] however, two P_{fr} isoforms have been suggested in a knotless and in multiple canonical phytochromes.^[149,151,154,156] In contrast to the P_r state, the differences between these isoforms are much more subtle and differ only in small structural details, which were identified as the C-D methine bridge torsional angle and minor modifications to the A-B methine bridge geometry.^[121,149,156] The most plausible origin of these differences was proposed to be a difference in the amount of hydrogen bonds holding ring D in its E configuration, changing the tilt angle of the C-D methine bridge which modulates the photodynamics and photoefficiency of the respective isoforms.^[149,154] The relative ratio of these isoforms is often more sensitive to temperature than in the P_r state indicating a facilitated and fast interconversion between the forms on a ns timescale due to a smaller thermal barrier.^[121,149,156]

2.2.5 The Photocycle

The photodynamics of phytochromes consist of an intricate interplay between chromophore and protein dynamics to relay the light-induced signal to the OPM as evidenced by the influence of structural heterogeneity (see 2.2.4) and the presence of a highly conserved chromophore environment (see 2.2.3). These dynamics can be summarized in a photocycle comprising the forward ($P_r \rightarrow P_{fr}$) and reverse reaction ($P_{fr} \rightarrow P_r$) which are divided into several intermediate steps with different extents of structural reorganization. The photocycle introduced here (Fig. 2.13) displays the intermediates for phytochromes of group I and II forming a P_r dark state and a P_{fr} light-adapted state.

Parts of this photocycle may also apply to CBCRs and respective information will be discussed when appropriate. However, due to the spectral and structural differences the observed dynamics might be substantially different in CBCRs. Especially the μ s- to ms-dynamics is still under investigation, and is much less understood than the respective dynamics in group I and II phytochromes. The general photocycle of phy-

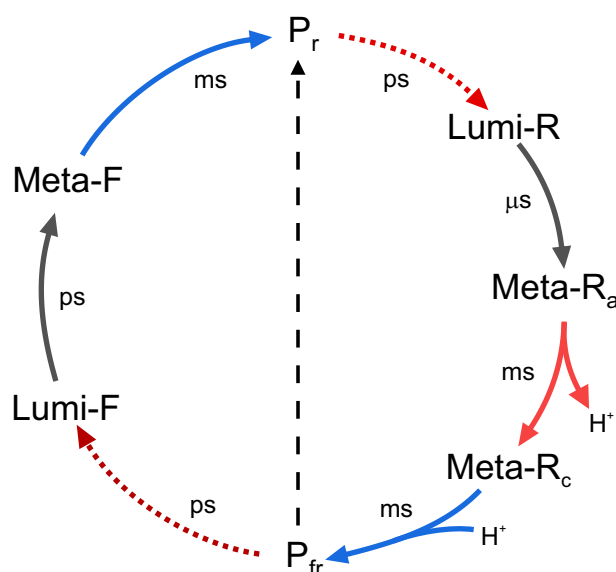


Figure 2.13 – Schematic photocycle of group I and II phytochromes. The dotted arrows in the cycle represent the light-dependent isomerization of the bilin chromophore, while the following processes (solid arrows) are light-independent. The approximate timescale of the individual steps is given next to the arrows of the respective transition. The dashed line marks the dark reversion of the P_{fr} state to the P_r state which is reversed in bathyphytochromes.^[55]

tochromes consists of the dark and light-adapted state and the intermediates termed Lumi-R and Meta-R or Lumi-F and Meta-F for the forward and reverse photoreaction, respectively.^[55] Note that the nomenclature is based on the color of the excited parent state (*e.g.*, $P_r \rightarrow \text{Lumi-R} \rightarrow \text{Meta-R}$). The Lumi intermediates are formed after the photoisomerization on the ps timescale and represent the primary GS intermediates, whereas the Meta intermediates are formed afterwards often on the μs to ms timescale.^[55] In the following, the underlying structural changes will be discussed separately for the individual intermediates in the forward and reverse direction of the photocycle.

Forward Dynamics $P_r \rightarrow P_{fr}$

The first step in the forward reaction of phytochromes is the light-dependent transition from the parent dark state P_r to the primary photointermediate Lumi-R.^[55] This step is induced by excitation with visible light and involves dynamics in the electronic ES, while the following processes proceed light-independently in the GS.

In canonical phytochromes, upon photoexcitation, the excited bilin chromophore exhibits an ultrafast departure from the Franck-Condon region on the sub-ps timescale.

The succeeding ~2-5 ps lifetime has been interpreted either as a distinct population in the context of GSH or conformational dynamics of the chromophore on the ES initiating ring D rotation.^[107,150,152,172–176] In *SynCph1*, the evolution of this population is described as non-reactive due to a differently twisted ring D geometry (see 2.2.4).^[60,150,152,176] Similar observations were made in red/green CBCRs where multiphasic ES dynamics were commonly observed and assigned to static GSH.^[98,161,177,178] Finally, the primary photoproduct Lumi-R is formed on the ~30-50 ps timescale after overcoming a barrier on the ES surface.^[107,150,172–175] The formed Lumi-R intermediate exhibits red-shifted absorption due to its isomerized chromophore and persists into the μ s timescale.^[55]

Interestingly, CBCRs generally exhibit longer ES lifetimes on the hundreds of ps timescale.^[97,98,161,177,178] Some bacteriophytochromes exhibit such longer ES lifetimes as well, which were attributed to ES proton transfer and reorganization of the hydrogen bonding network prior to the isomerization.^[139–141,157,167,179] In other long-lived phytochromes, non-exponential dynamics were observed and linked to active-site solvation and protein reorganization dynamics limiting the speed of the isomerization.^[130,170,171]

On these ultrafast timescales, structural changes are expected mostly in the direct vicinity of the chromophore, in particular around the rotating ring D.^[123,163,180] Indeed, studies have shown the occurrence of several important events for the signaling process already during this early stage of the photocycle. The *Z/E* isomerization of the C15=C16 methine bridge causes a displacement of Y263 and D207 and breaks the hydrogen bond of the ring D carbonyl to H290.^[123,132,181] The movement of Y263 and Y176 prior to the isomerization was confirmed by time-resolved X-ray crystallography supporting their role as a steric gate which has to be displaced to allow a ring D rotation by 180°.^[132] These rearrangements are likely to trigger the observed disruption of the salt bridge between D207 and R472, consequently weakening the connection of the tongue to the chromophore binding pocket and marking the onset of tongue refolding.^[123,132,181] As a consequence, the hydrogen bonding network starts to rearrange forming a new but still disordered network consisting of R472, D207, Y263, a water molecule, and the carbonyl and pyrrole group of ring D.^[123] This stabilizes the strained geometry of ring D in its isomerized state.^[163] Recent studies suggest that these processes can be split in two Lumi-R states.^[134,163] In Lumi-R_I, the structural changes are restricted to the isomerization site at ring D and its vicinity, whereas in Lumi-R_{II}, changes can be observed in the whole chromophore and its immediate environment.^[134,163]

On the μ s timescale, the Lumi-R intermediate evolves to the Meta-R intermediate.^[96,103,136,182,183] In many group I and II phytochromes, the Meta-R intermediate

2 Theoretical Framework

is split into two consecutive states termed Meta-R_a and Meta-R_c.^[96,103,136,182–184] In the transition from Lumi-R to Meta-R_a, the strained chromophore undergoes thermal relaxation,^[134,163,185,186] which can be associated with the observed red-shifted absorption of Meta-R_a. Otherwise, no significant structural changes in the protein backbone or hydrogen bonding network are observed in Meta-R_a.^[123,163]

In a next step, the bilin chromophore or its hydrogen bonding network is suggested to undergo deprotonation on the early ms timescale^[96,103,136,182] forming the blue-shifted Meta-R_c intermediate.^[55,103,136,182] The respective proton is released to the external medium.^[103,136,182,187] This deprotonation is suggested as a key step to allow the following transition to the P_{fr} state as the overall mobility of the protein is increased upon chromophore deprotonation.^[165] Mutational studies suggest that D207 is of significant importance for the proton-release as the alanine mutant in Agp1 does not show any proton-release despite reaching the Meta-R_c intermediate spectrally.^[103] However, the general applicability of this mechanism is still under debate as deprotonation and the consecutive reprotonation have not been observed in all phytochromes and may depend on the specific protein environment as well as the chromophore's pK_a in the Meta-R_c step.^[123,185]

Finally, the photoproduct P_{fr} is formed by reprotonation of the chromophore or its hydrogen bonding network on the tens to hundreds of ms timescale.^[90,91,103,136,182,183,188] This transition has been reported as biphasic in some phytochromes with yet unknown origin.^[136,188] The proton-reuptake seems to be coupled to H260, which is underlined by studies on H260A mutants, which are stuck in Meta-R_c and show no or inhibited progression to the P_{fr} state and no measurable proton-reuptake despite earlier proton release.^[103,113] Until this point, the structural changes in the photocycle are mostly limited to the local environment of the chromophore and the binding pocket. In contrast, large scale structural changes throughout the whole protein are observed during the conversion to P_{fr} including refolding of the PHY tongue from a β -sheet to an α -helix conformation,^[89–91,123] establishment of the final hydrogen bonding network^[123] and final rearrangement of the chromophore binding pocket to accommodate the isomerized bilin chromophore.^[123] The removal of the PHY domain does not change the overall timescale of the Meta-R_c to P_{fr} transition indicating that the chromophore transition during this final step is not kinetically controlled by the PHY domain or its tongue which could be expected based on the large structural changes associated with this step.^[91] Instead, the tongue is suggested to have greater influence on the early relaxation of Lumi-R to Meta-R_a, accelerating the respective dynamics.^[91,163] Therefore, the rate-limiting step for P_{fr} formation was suggested to be internal to the PAS-GAF domains.^[91,123,163]

Reverse Dynamics $P_{fr} \rightarrow P_r$

The reverse dynamics of phytochromes were investigated in much less detail compared to the forward dynamics and are, in general, less understood in both the fs-ps and the μ s-ms time regimes. It is important to note that most of the structural information on the reverse dynamics stems from investigations on bathyphytochromes,^[59,143,189] and the general applicability to other phytochromes is strongly suggested but still needs further verification.

The primary photointermediate Lumi-F contains an isomerized chromophore and is formed by the ultrafast photoreaction of the P_{fr} state.^[55,59,190] In comparison to the forward reaction, the formation of Lumi-F proceeds often on the sub-ps timescale and is, therefore, much faster.^[151,154,155,172,173,175,191–193] The generated Lumi-F intermediate then undergoes several GS relaxation steps to form the Meta-F intermediate on the ps timescale, which already exhibits a P_r -like absorption.^[151,154,172]

The nomenclature of these states is under debate as cryotrapping studies, preceding the availability of ultrafast transient absorption studies on the P_{fr} state, assigned the Lumi-F intermediate to a blue-shifted species.^[184,194,195] However, time-resolved studies found that the primary photointermediate is red-shifted compared to P_{fr} and is only blue-shifted on the later ps timescale.^[151,154,172,173,192] This led to the inconsistency that the red-shifted primary intermediate was not termed Lumi-F in earlier works.^[173] Due to its short lifetime and consequently small thermal barrier to the next blue-shifted state, the red-shifted primary intermediate most likely cannot be observed in the cryotrapping studies. To stay consistent with the established nomenclature that the first photointermediate is termed Lumi, the red-shifted state is termed Lumi-F in more recent time-resolved studies, whereas the blue-shifted species is termed Meta-F.^[151,154,192]

Similar to the forward dynamics, the role of GSH in the ultrafast ES dynamics is actively discussed for the reverse dynamics. In *SynCph1*, multiphasic ES dynamics were attributed to separate evolution of a productive and a non-productive GS subpopulation distinguished by either different chromophore conformations or hydrogen bonding patterns.^[151,154,155] In contrast, in *Agp1* and *PaBPhP*, multiphasic ES dynamics were assigned instead to branching on the ES surface.^[169,191]

On a structural level, only minor side-chain adjustments occur in the chromophore binding pocket during Lumi-F to accommodate the isomerized chromophore.^[59,143] Interestingly, the partner swap of the propionic side-chain of ring C already occurs on this early timescale.^[190,193] The chromophore then relaxes from its distorted conformation in Lumi-F to form Meta-F.^[59,143,190] These events trigger the reorganization of several

2 Theoretical Framework

amino acid residues in the binding pocket leading to a destabilization of the tongue fold, initiating the refolding of the tongue.^[143,189,190]

The final transition from Meta-F to P_r then proceeds on the μ s-ms timescale, and involves rearrangement of the hydrogen bonding network, tongue refolding and the deprotonation of the propionic side-chain of ring C, which is suggested as a key event for tongue refolding.^[96,143,183,189,190,196,197] Simultaneously, a hydrophobic pocket around ring D is formed similar to the one observed in the P_r state.^[189] In contrast to the forward dynamics, these changes do not result in major spectral changes in the visible spectral range.^[96,183,196,197]

2.2.6 Aim of Research

The central role of the immediate chromophore environment for the dynamics and efficiency of photoisomerization reactions in phytochromes is strongly suggested by its high level of conservation and the impact GSH is suggested to enact on the photodynamics. In the phytochrome community, several key elements are highly debated in this context. As the immediate protein environment greatly influences the dynamics of the photoisomerization, the question arises which amino acids are critical for the kinetics and efficiency of the photoproduct formation and how they specifically alter the respective dynamics. Hence, this thesis aims to identify and investigate the specific influence of the chromophore's protein environment on the photodynamics. In particular, the role of a conserved tyrosine in proximity to the chromophore as part of the steric gate and the relevance of dynamic protein reorganization were studied, as well as the impact of the PHY domain on the overall photocycle. Another point of discussion is the significance of GSH as a general approach to describe the multiphasic ES photodynamics of phytochromes. Here, the separate evolution of the different chromophore conformations due to slightly different immediate surroundings is suggested as the basis of most to all kinetics associated with the ES of phytochromes. However, this represents a rather static approach without considering dynamic movements of the protein environment or solvation effects that may contribute to the multiphasic nature of phytochrome photodynamics. This work aims to answer if GSH impacts the photodynamics, using a model system where GSH can be abolished without significantly altering the stationary spectroscopic properties. From the results, an alternative dynamic description of the multiphasic ES kinetics on the basis of dynamic protein reorganization was developed. The thesis also clarifies the role of GSH in the forward and reverse dynamics of phytochromes. Lastly, this thesis aims to bring the first insights into the yet unexplored

photodynamics of knotless or group II phytochromes to highlight their unique aspects as a link between canonical phytochromes and CBCRs.

To address these questions, two key proteins, the knotless phytochromes All2699g1g2 and *SynCph2* were studied, using predominantly fs time-resolved transient absorption and flash photolysis.

All2699

The central system of interest in this work is the phytochrome All2699 from *Nostoc* sp. All2699 consists of three GAF domains followed by a HK as the OPM.^[95] The first and third GAF domains bind a PCB chromophore, while the second GAF domain interacts with the GAF1 domain via a PHY-like tongue, similar to the structurally related *SynCph2*.^[88] The first and second GAF domains are, therefore, categorized as a knotless phytochrome (All2699g1g2), while the third GAF (All2699g3) domain represents a CBCR with red/orange photochemistry and remarkably fast thermal reversion.^[88,95] The All2699g1 and All2699g1g2 samples investigated here were provided by Qianzhao Xu and Lisa Köhler from the group of Wolfgang Gärtner and Jörg Matysik (University Leipzig).

Remarkably, the single GAF1 domain (All2699g1) is able to photoconvert reversibly between a P_r dark state ($\lambda_{\max} = 637$ nm) and a P_{fr} light-adapted state ($\lambda_{\max} = 689$ nm),^[95] even in the absence of the GAF2/PHY domain.^[95] The presence of the GAF2/PHY domain in the complete knotless phytochrome All2699g1g2 shifts the absorption of the P_{fr} state ($\lambda_{\max} = 705$ nm), but does not spectrally influence the P_r state.^[88] Structurally, magic angle spinning nuclear magnetic resonance (MAS-NMR) experiments carried out on the P_r state of both constructs showed that the addition of the PHY domain reduces the available space within the binding pocket and, in turn, abolishes the heterogeneity of the chromophore, otherwise observed in All2699g1.^[88] However, despite the reduced available space, the amino acid Y142 (Y263 in *SynCph1*), which acts as a steric gate for ring D rotation, is located further away from the chromophore which may influence the ultrafast photodynamics.^[88] These findings make All2699g1 and All2699g1g2 an important model system to study not only the influence of structural heterogeneity and the positioning of the conserved Y142 on the photochemistry of phytochromes, but also the role of the PHY domain in the overall photodynamics. Comparison to group II and III phytochromes gives a perspective on the evolutionary role of the PHY domain, since group III phytochromes lack this domain. Additionally, as the ultrafast dynamics of knotless phytochromes have remained unexplored until now, the investigation of

2 Theoretical Framework

All2699g1g2 provides first insights into these dynamics and allows a comparison to the dynamics of group I and III phytochromes.

SynCph2

The second system of interest in this work is the knotless phytochrome Cph2(1-2) from *Synechocystis* sp., the most prominent member of group II phytochromes.^[61,62,93] The samples were provided by Petra Gnau from the group of Lars-Oliver Essen (Philipps-University Marburg). The full-length phytochrome of *SynCph2* consists of an array of two GAF domains, a GGDEF, an EAL, a third GAF, and a second GGDEF domain.^[90,93] It functions as a light-dependent regulator of cyanobacterial motility and phototaxis by controlling cytosolic c-di-GMP levels.^[90,198] Out of the three GAF domains only the first and third carry a PCB chromophore, while the second GAF domain interacts with the first via a PHY-like tongue.^[90,94] Due to this interaction, the GAF2 domain is considered a PHY domain. The fold of PHY domains is in general related to a GAF fold with a central five-stranded β -sheet core with the fold of the PHY/GAF2 domain in *SynCph2* being especially similar to GAF domains.^[53,90,96] In comparison to other PHY folds, the fold and core of *SynCph2* GAF2 differ from typical PHY domains of canonical PCB binding phytochromes like *SynCph1* and remain closer to BV-binding bathyphytochromes.^[90] Therefore, both terms, GAF2 and PHY, have been used to describe this domain. Consequently, the first two GAF domains can be classified as a knotless phytochrome, whereas the third single GAF domain is considered a CBCR with blue/green photochemistry.^[90,93] In this dissertation, the PCM of *SynCph2*(1-2), the knotless phytochrome consisting of GAF1 and GAF2, was selected as a representative for investigation of group II phytochromes and is in the following referred to as just *SynCph2*.

SynCph2 photoconverts between a P_r dark state ($\lambda_{\max} = 643$ nm) and a P_{fr} light-adapted state ($\lambda_{\max} = 690$ nm)(Fig. 2.14).^[94,199] The photoconversion efficiency of the $P_r \rightarrow P_{fr}$ reaction is 12%, while the reverse reaction $P_{fr} \rightarrow P_r$ shows a larger QY of 19%.^[94] On the ms timescale, the photodynamics of *SynCph2* adopt the typical photocycle described above for other phytochromes. However, the ultrafast forward and reverse dynamics have not been studied prior to this work.^[96]

A major advantage of *SynCph2* as a model system is the availability of a crystal structure and a basic photochemical characterization of mutants of key amino acids, facilitating comparison to canonical and bacterial phytochromes and their binding pocket structure in terms of available space and positioning of amino acids.^[90,94] Hence,

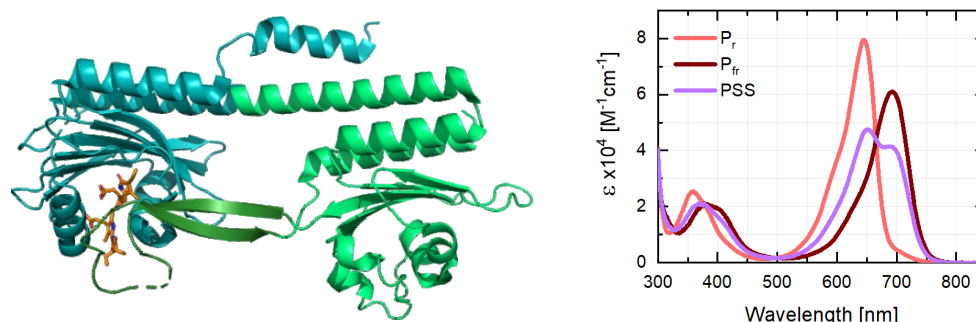


Figure 2.14 – Left: Crystal structure of the P_r state of *SynCph2* module (PDB ID: 4BWI).^[90] The PCB chromophore (orange) is embedded into the GAF domain. The PHY domain (light green) contacts the chromophore binding pocket via a tongue-like protrusion (dark green). Right: Absorption spectra of *SynCph2* in the P_r (light red) state, the photostationary state (PSS) (purple), and the P_{fr} (dark red) state. The pure P_{fr} spectrum was obtained by subtracting 36% of the pure P_r spectrum (factor determined by visual inspection of the resulting spectrum) from the PSS spectrum and multiplying the resulting spectrum with a factor of 1.56 to simulate complete conversion to the P_{fr} state. Figure taken from Ref. [III].

SynCph2 is a complementary model system to All2699g1 and All2699g1g2 to study the relationship between the structure and photodynamics of knotless phytochromes on the basis of the available crystal structure.^[90] As *SynCph2* is the most well known knotless phytochrome, studying and comparing its ultrafast photodynamics to All2699g1g2 and the extensively studied photodynamics of group I and III phytochromes also represents a central target of this work.

2.3 Indigoid Photoswitches

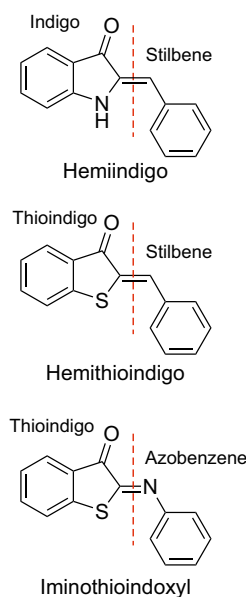


Figure 2.15 – Basic structure of Hemiindigo, Hemithioindigo, and Iminothioindoxyl photoswitches.

Indigoid photoswitches comprise a class of organic chromophores derived from the indigo dye exhibiting absorption in the visible spectral region in both isomeric states even without complex substitution patterns at the indigo core.^[11,200–203] The photoactivation using visible light promises great potential for applications in biological systems intolerant to the often damaging high energy UV light due to its cell toxicity.^[11,203,204] This property combined with fast and efficient photoconversion, pronounced photochromism, typically high thermal bistability, robust photostability, and simple synthetic functionalization and access lead to the extensive characterization and application of indigoid photoswitches.^[11,201,203] In order to diversify their potential, several subtypes of indigoid photoswitches have been developed including Hemiindigo (HI), Hemithioindigo (HTI), and more recently Iminothioindoxyl (ITI) photoswitches. Each of these classes shows unique properties while employ-

ing a rather similar hybrid chromophore structure, combining an indigo or thioindigo fragment with a hemistilbene or hemiazobenzene (Fig. 2.15).^[11] HTI derivatives, in particular, have been exploited for researching the driving forces of distinct photochemical pathways of C=C double bonds in indigoid photoswitches with the perspective of tailoring the photodynamics to desired applications.^[201,202,205–210]

2.3.1 Hemithioindigo Photoswitches

HTIs consist of a thioindigo and a stilbene fragment connected by a C=C double bond (Fig. 2.15) that undergoes *Z/E* isomerization upon photoexcitation. They have found numerous applications in biological chemistry,^[211–213] supramolecular chemistry^[214–218] and as molecular machines^[219–222] based on their favorable photochemical properties such as spectral tunability in the visible range, high thermal bistability, and photofatigue-resistance.^[11,201,202,206,223–228]

HTIs have also been employed as model systems to study light-induced reaction mechanisms of substituted C=C double bonds.^[205,206,208–210] Their photoreaction typi-

cally involves *Z/E* isomerization of the central C=C double bond (double bond isomerization (DBI)) between a few fs up to hundreds of ps.^[202,206,209,227–229] Additionally, the formation of twisted intermediate charge transfer (TICT) states associated with single bond twisting (SBT) has been proposed as an alternative deactivation pathway.^[209,210] The occurrence and efficiency of the TICT pathway is determined by the substitution pattern and the solvent polarity.^[209,210] In general, inducing a pre-twist in the single bond adjacent to the central double bond with sterically demanding substituents, adding electron donating groups to the stilbene moiety and using solvents with high polarity favor the TICT pathway and diminish DBI yield.^[209,210]

However, since the photoproduct of a SBT/TICT reaction is not distinguishable from the educt of the photoreaction, direct proof of such mechanisms remained rather elusive. To provide solid evidence, double bond substituted HTIs with an oxidized sulfur were developed.^[230,231] These compounds contain a significantly pre-twisted single bond ideal for TICT formation, which cannot rotate freely due to strong steric constraints induced by the steric clash between the oxidized sulfur and the double bond substituents. The introduction of *ortho*-substituents on the stilbene moiety then renders these compounds non-symmetric turning the two rotamers of the same double bond configuration into two atropisomers yielding four geometrically distinct diastereomeric states.^[205] Photoexcitation of such HTIs shows three distinct possible photoreaction pathways with diastereomers as photoproducts distinguishable by NMR spectroscopy:^[205] DBI, a full rotation of the single bond termed single bond rotation (SBR) potentially accessible via SBT/TICT, and a third mechanism representing a combined process of DBI and SBR called Hula-Twist (HT).^[232–234] The ratio between these processes can be controlled by solvent polarity, viscosity, and temperature. Consequently, this study provided the first experimental evidence for the previously proposed HT mechanism.^[205] These findings render HTIs an interesting target system to study the photochemistry and photodynamics of constrained C=C double bonds and the differences and similarities of the respective photochemical pathways.

2.3.2 Iminothioindoxyl Photoswitches

Recently, the newly developed class of ITI photoswitches has raised interest based on their favorable photochemistry showing a predominantly solvent independent band separation of over 100 nm in the visible spectral range between the isomers.^[235,236] Structurally, ITIs employ a thioindigo scaffold similar to HTIs with the second half of the photoswitch being a hemiazobenzene instead of a hemistilbene.^[235] The introduction

2 Theoretical Framework

of the C=N double bond leaves the absorption spectrum mostly unaffected compared to HTIs, but changes the photochemical properties tremendously. The thermostable Z-isomer undergoes photoisomerization on the fs timescale, forming the metastable E-isomer and the hot GS of the Z-isomer that cools within ~10 ps.^[235] Thermal relaxation of the E-isomer to the Z-isomer then proceeds on the ms timescale.^[235] Hence, compared to HTIs, the photodynamics in ITIs proceed much faster and only metastable photoproducts are formed with reduced QY.^[235] The addition of strong protonating agents like trifluoroacetic acid improves the thermal stability of the E-isomer by protonating the nitrogen of the C=N double bond, which, in turn, hinders the nitrogen inversion.^[236] However, a thermal bistability of the photoswitch has not been achieved for the ITI system. Interestingly, the photochromism is reversed by substituting the sulfur in the thioindigo scaffold with an N-acetyl or N-methyl moiety rendering the E-isomer the thermostable form due to increased steric repulsion of the azobenzene and the N-acetyl moiety in the Z-form.^[237]

The fast thermal recovery rate is a promising feature for application in photocontrol of fast biological processes like signal transduction and neuronal activity where photoswitches with quick reversion have been employed previously.^[235,238,239] To broaden the field of application, development of ITIs exhibiting thermal bistability by exploring the multitude of potential substitution patterns represents a long term goal for this newly developed class of photoswitches.

2.3.3 Aim of Research

Hemithioindigo

The primary goal of the HTI project was the photochemical investigation of a sterically crowded HTI compound to provide direct dynamic evidence of the Hula-Twist (HT) photoisomerization mechanism. The investigated HTI was synthesized by Aaron Gerwien from the group of Henry Dube (Friedrich-Alexander-University Erlangen). It employs an electron donating dimethylamino (DMA) group in the *para* position at the hemistilbene scaffold, an oxidized sulfur and a *tert*-butyl group attached at the C=C double bond next to the hemistilbene. These substitutions increase thermal bistability, introduce pre-twist into the double bond to favor TICT and abolish thermally driven SBR.^[230,231] A non-symmetric methyl substitution in the *ortho*-position of the hemistilbene yields four diastereomers (Fig. 2.16), which can be interconverted by light via DBI, HT and SBR.

Applying transient absorption spectroscopy, the individual photochemical pathways

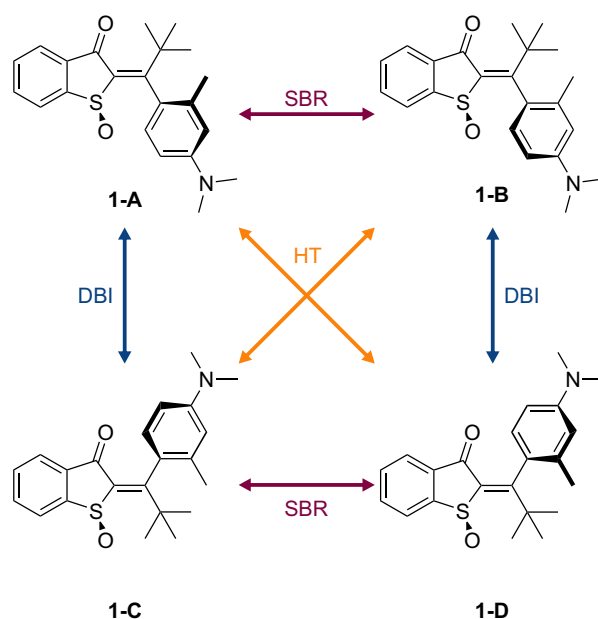


Figure 2.16 – Diastereomers 1-A to 1-D of the investigated HTI compound with indicated reaction mechanisms for photoconversion between the diastereomers. Of the eight total diastereomers only the ones with the sulfinyl oxygen placed above the paper plane are displayed to indicate the non-planarity of the sulfinyl group. However, all isomers are racemic mixtures containing both conformations.

should be identified and investigated in terms of their solvent dependence to provide evidence for the HT photomechanism. To support the mechanistic interpretation, quantum mechanical calculations were conducted by Jonas Leitner from the group of Andreas Dreuw (University Heidelberg) identifying the minimum energy pathway and the related conical intersections between ES and GS.

Iminothioindoxyl

In the ITI project, predominant relaxation of ITIs via a hot GS and the consequential release of substantial amounts of vibrational energy was applied to develop a vibrational energy donor for biological systems. Such probes can be utilized for the identification of anisotropic vibrational energy transfer (VET) pathways - specific pathways that distribute vibrational energy in complex systems like proteins - which were suggested to be involved in long distance signaling within proteins by theory.^[240-246] Studies of VET require a pair of donor and sensor depositing and detecting vibrational energy at specific positions in the protein. The challenge lies in finding probes that show favorable photochemical properties like strong absorption in the visible spectral region, ultrafast

2 Theoretical Framework

relaxation, little to no product formation, and a small size providing more precise spatial information and preventing major structural changes upon incorporation into proteins.^[247] The ultrafast relaxation is required to avoid temporal overlap of the energy transfer between donor and acceptor and the vibrational relaxation of the acceptor itself. ITIs possess most of these properties^[235] and represent a promising alternative to the available vibrational energy injectors.^[248,249]

To further enhance their potential in biological applications, Larita Luma from the group of Alexander Heckel (Johann Wolfgang Goethe-University Frankfurt) synthesized two ITI compounds, the DMA-ITI and the Julolidin (J)-ITI, with further red-shifted absorption than previously known (Fig. 2.17).^[235,236]

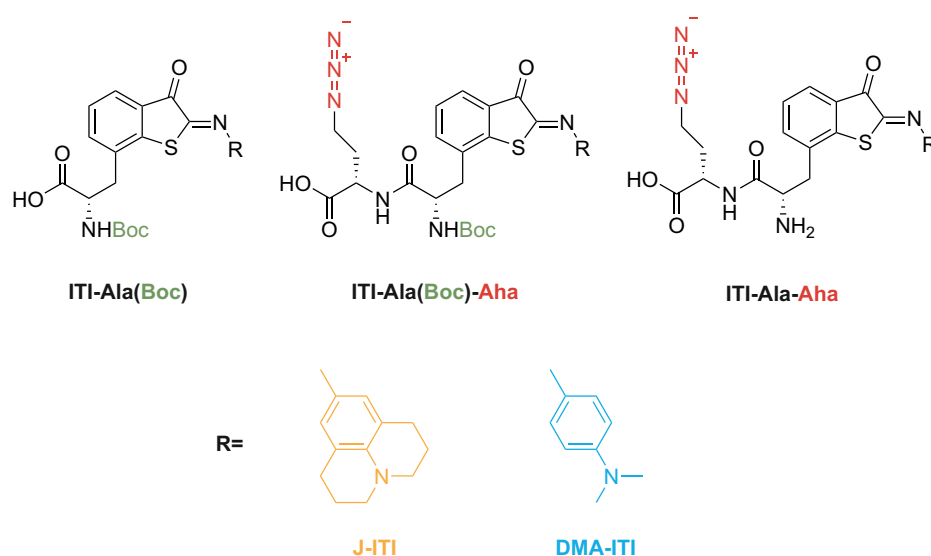


Figure 2.17 – ITI compounds investigated in this thesis. The J and DMA-ITI were converted to L-alanine (Ala) analogues still carrying a *tert*-Butyloxycarbonyl (Boc) protecting group (ITI-Ala(Boc)). These amino acids were coupled to L-azidohomoalanine (Aha), a vibrational energy sensor (ITI-Ala(Boc)-Aha) to create a minimal model system. In a last step, the protecting group was removed (ITI-Ala-Aha).

In this thesis, the photochemical properties and ES dynamics of a minimal VET dipeptide model system were investigated in dependence on the solvent and the excitation wavelength. The model dipeptide consists of an ITI photoswitch converted to a non-canonical Ala amino acid and the established vibrational energy sensor Aha.^[247,248] The results represent the basis for the proof of principle VET studies of the same minimal model system in the IR spectral region by Carolin Feid from the group of Jens Bredenbeck (Johann Wolfgang Goethe-University Frankfurt).

Chapter 3: Research Projects

This chapter presents the accumulated results and central conclusions of the research projects conducted in this dissertation. Results that have been published and the respective papers are indicated at the appropriate place. The results are split into projects related to phytochromes and indigoid photoswitches. The two main topics are divided into appropriate subtopics where several publications and aspects can be attributed to the same subtopic.

3.1 Phytochromes

The phytochrome related results are split into five sections. In section 3.1.1, the results on the ultrafast forward dynamics of all investigated phytochromes are discussed in different contexts comprising the publications [I]-[III] and [V]. Next, the unpublished ultrafast reverse dynamics of All2699g1 and All2699g1g2 as well as the results on *SynCph2* published in reference [III] will be elaborated in section 3.1.2. Based on the results presented in these two sections the role of GSH in the ultrafast dynamics of knotless phytochromes is summarized in section 3.1.3. In the following section 3.1.4, the obtained results on the ms-dynamics of knotless phytochromes will be presented in section which are published in reference [IV]. Finally, the effect of the PHY domain on the general photodynamics of knotless phytochromes is discussed in section 3.1.5 as a summary of the results of this dissertation in this regard.

3.1.1 Ultrafast Forward Dynamics of Knotless Phytochromes

The main contents of this section and its subsections have been published in references [I]-[III] and [V]. The ultrafast forward dynamics of knotless phytochromes have remained unexplored prior to this work despite their interesting evolutionary position located between group I phytochromes and CBCRs in terms of domain architecture. In contrast, extensive research has been conducted on these dynamics in groups I and III producing a variety of mechanisms to describe the complex ES dynamics including models based on static GSH^[98,150,152,161,176-178] and ES proton transfer.^[139,140,157,167,179] The variability in the ES lifetime, ranging from ~30 ps in some canonical phytochromes^[107,150,172-175,250,251] to up to ~1 ns in CBCRs,^[97,98,161,177,178] in spectrally and structurally similar P_r states employing similar chromophores is remarkable. Based on these observations, a strong influence of the protein environment is

3 Research Projects

expected predominantly determining the ES dynamics of phytochromes. Studying this influence requires a model system where the protein environment can be modified without disturbing efficient photochromism. One major factor determining the protein environment of the chromophore is the PHY domain, specifically the interaction of the tongue with the chromophore binding pocket, which compacts and shields the chromophore from the solvent.^[83,84,88] Considering these two aspects, the single GAF domain All2699g1 and its corresponding knotless phytochrome All2699g1g2 represent a unique model system to not only study the effect of the PHY domain and its modulation of the pocket environment, but also the photodynamics of knotless phytochromes in general. The finding that the addition of the PHY domain to All2699g1 abolishes its previously pronounced GSH in the P_r state according to MAS-NMR^[88] stresses the potential of this model system. By comparing the photodynamics in presence and absence of the PHY domain, this system offers the unique possibility to study the effect of GSH on the photodynamics of phytochromes directly in one model system.

All2699g1 represents a minimal photoswitchable model of knotless phytochromes that can be readily compared to CBCRs in terms of the occurrence of structural heterogeneity based on MAS-NMR^[88] with a P_r and P_{fr} state spectrally similar to canonical cyanobacterial phytochromes like *SynCph1*.^[77,95] As such, the mechanistic study [I] on All2699g1 provides the first insight into the photodynamics of knotless phytochromes and their relation to CBCRs and group I phytochromes.

Apart from the similar absorption spectra of All2699g1 compared to canonical group I phytochromes, its CD spectra are also quite similar and retain the pattern and pattern shift upon photoconversion, indicative of comparable conformations of the bilin rings A and D in respect to the B-C plane. In contrast, the QY of both the forward and reverse reaction are lower than typically observed in both group I and III phytochromes. The lack of the PHY domain could cause this reduced efficiency as *SynCph2* shows QYs similar to group I phytochromes.^[96]

The ultrafast photodynamics of All2699g1 proceeds in two major steps: First, chromophore-related spectral shift dynamics occur without loss of ES population on the sub 30 ps timescale, then the ES decays on the timescale of hundreds of ps in one step with a temporally broad lifetime distribution. The temporally broad distribution was assigned to non-exponential dynamics, which result from the isomerization being controlled by the protein environment or solvation processes (Fig. 3.1). An evolution of distinct GS substates in context of GSH was excluded based on the lifetime distribution pattern, the excitation wavelength independence, the lack of ES decay in the early lifetimes and an equally good fit by using a stretched exponential instead of two expo-

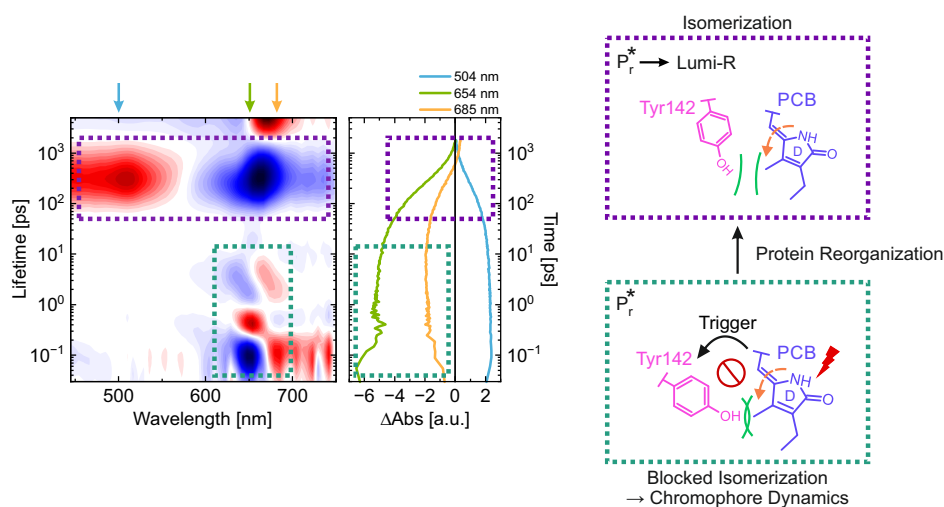


Figure 3.1 – Illustration of the conserved kinetic pattern and its associated processes in the LDM and single transients of the ultrafast forward dynamics of the P_r state of All2699g1. (Left) LDM corresponding to the ultrafast forward dynamics of All2699g1 after excitation at 635 nm. [I] Arrows indicate the location of the respective transients shown in the center of the figure. The dotted boxes highlight the two separate processes of chromophore dynamics (teal) and protein controlled ES decay (purple) and the associated pattern in the LDM. (Center) Selected transients in the ESA (cyan) and the GSB/SE overlap region (blue side (green), red side (orange)). The dotted boxes highlight the chromophore dynamics and protein controlled ES decay. Note that the ESA is not affected by the chromophore dynamics as indicated by the lack of amplitude changes in the respective transient (cyan) on the tens of ps timescale. (Right) Schematic representation of the envisioned model for the chromophore isomerization. While the isomerization is blocked initially by Y142, the chromophore dynamics trigger a reorganization of the protein matrix withdrawing the tyrosine and enabling the completion of the chromophore isomerization. Adapted from [I],[II].

nentials in GTA despite the presence of GSH. The involvement of ES proton transfer reactions previously observed in other phytochromes was excluded due to a lack of kinetic isotope effect in D_2O .^[139,140,157,167,179] Based on this, a model was constructed where the chromophore dynamics trigger the non-exponential reorganization of the protein matrix which are required for the isomerization to proceed. With support of hybrid quantum mechanics/molecular mechanics calculations from the Schapiro group (Hebrew University of Jerusalem), Y142 was identified as a steric gate preventing the ring D from rotating and completing the isomerization prior to protein reorganization. During this reorganization, Y142 is pulled away from the chromophore far enough for the isomerization to proceed. However, immediately after isomerization its steric demand is required to stabilize the Lumi-R intermediate. A movement of Y142 on the ps

3 Research Projects

timescale was later on verified by time-resolved X-ray crystallography in *DrBphP*.^[132] The high barrier imposed by Y142 matches well with the observed extended ES lifetime of ~270 ps. Furthermore, its predicted movement away from the chromophore to allow isomerization and formation of the primary photoproduct can be reasonably associated with the distributed non-exponential kinetics. The widespread use of GTA for analyzing similar phytochrome time-resolved data does not easily allow the description of these non-exponential kinetics without explicit consideration within the expected model. In contrast, the applied LDA is able to describe such dynamics without previous knowledge which represents a valuable advantage in identifying this type of kinetics. Establishment of this technique within the field of ultrafast phytochrome dynamics will aid in the future assignment of this type of kinetics to prevent confusion of non-exponential dynamics and multiphasic evolution of distinct GS substates.

The constructed model is further supported by follow-up studies on the complete knotless phytochromes *All2699g1g2* [II] and *SynCph2* [III] observing a similar two step mechanism. Strikingly, neither the dynamics assigned to the chromophore, nor the distributed nature of the ES decay changes and are, therefore, present in both constructs. This supports the assignment towards non-exponential dynamics instead of multiphasic ES kinetics based on GSH. If the distributed decay were to originate from GSH, the homogeneous GS of *All2699g1g2* should exhibit monoexponential kinetics instead of the observed distributed decay. Hence, the distributed nature can be clearly associated with non-exponential dynamics, most likely protein reorganization dynamics as suggested by the model derived in reference [I]. Note that this entails that static GSH does not necessitate multiphasic ES kinetics with a separate evolution of each excited GS substate. However, GSH may contribute slightly to the width of the distribution describing the ES decay in *All2699g1* instead of being its underlying origin.

Fs-transient Vis-pump IR-probe data of *SynCph2* presented in reference [III] further solidified the nature of the two observed steps. In the sub-50 ps time regime, changes occur only in chromophore related vibrations like the $C_{19}=O$ and the $C_9=C_{10}$ vibrations confirming that the first step is, indeed, predominantly limited to chromophore dynamics that is conserved in the investigated knotless phytochromes. The lack of simultaneous decay of all ESA features, again, rules out the assignment of the early dynamics to ES decay in the context of co-evolution of distinct subpopulations typically suggested in other phytochromes. Only at later delay times the repopulation of the GS becomes apparent, matching the distributed excited state decay in the Vis-pump Vis-probe measurements.

These results are in contrast with studies on other phytochromes exhibiting GSH

where the distinct evolution of separate GS substates was suggested as the origin of both the early dynamics and the distributed decay instead of early chromophore dynamics and a distributed evolution dependent on protein reorganization.^[150,152,176] The concept of protein reorganization controlling the isomerization kinetics and the application of non-exponential functions to describe this process represent a breakthrough in understanding the dynamics of photoreceptors in general and phytochromes in particular. This extends to the assignment of the early dynamics being related to chromophore dynamics acting as a trigger for the following protein reorganization, which may extrapolate to other photoreceptors as well. Later studies on other phytochromes supported this concept, where multiple exponential decays were described in terms of one non-exponential process related to active-site solvation or protein reorganization instead of the distinct evolution of GS substates as a result of GSH.^[130,170,171] Hence, the approach presented in this dissertation adds to the already ongoing discussion on the influence of GSH on the photodynamics in phytochromes, highlighting that not all GSH observed by solid state nuclear magnetic resonance (ssNMR) or other low temperature techniques necessarily yields a separate evolution of the distinct GS substates. It also showcases the power of LDA as a model independent analysis method to unveil non-exponential dynamics. The observed influence of Y142 and the significance of the protein environment, furthermore, are the starting points for the following studies within the dissertation.

The Role of Y142 in the Ultrafast Forward Dynamics of Knotless Phytochromes

The conserved tyrosine Y142 and its equivalents in other phytochromes have been considered to play a significant role in tuning the photophysical properties and photodynamics of phytochromes through steric interactions^[128-130] and hydrogen bonding capabilities.^[60,83,113,121,128,130] Replacement of the tyrosine by phenylalanine increases the ES lifetime and hence boosts the fluorescence efficiency in a variety of phytochromes,^[114,117,128,130] however, the exact mechanism behind this behavior has yet to be understood. Following up on our findings on the role of Y142, which sterically gates the isomerization until it is withdrawn from the chromophore via protein reorganization, a study of the photochemistry and the ultrafast photodynamics of Y142 mutants was conducted in this work and published in reference [V].

Without relying on mutants, some conclusions may already be drawn from the investigations on All2699g1 and All2699g1g2. A MAS-NMR study suggests that the steric clash of Y142 with the chromophore is reduced in All2699g1g2 by a positional shift of this residue despite an overall reduction of space in the chromophore binding pocket.^[88]

3 Research Projects

The observed decrease of the ES lifetime of All2699g1g2 confirms that the positioning and steric demand of Y142 indeed affects the distributed protein controlled kinetics as suggested by the calculations on All2699g1 [I]. Furthermore, time-resolved X-ray crystallography on *DrBphP* reveals a movement of Y263 away from the chromophore as early as 10 ps after excitation.^[132]

In this work, the effect of the Y142F and Y142W mutations on the ultrafast forward dynamics of All2699g1 was studied. The tryptophan in this position was selected in reference to red/green CBCRs like Slr1393g3, where a position similar to Y142 is adopted by a tryptophan.^[252] The Y142F mutant shows the expected reduction in product formation QY and increase of fluorescence QY, whereas Y142W shows an almost complete loss of productive photochemistry and a fluorescence QY similar to the wildtype (WT). The LDA of the ultrafast dynamics reveals that the kinetic pattern in the LDMs remains conserved in the mutants until ~30 ps, while the distributed ES decay shows significant variations in lifetime and temporal broadness. The similarities until 30 ps suggest that the initiation dynamics of the chromophore is not affected by the mutation. This correlates well with the lack of striking spectral changes in P_r absorption and emission. Only the distributed kinetics related to the reorganization of the protein environment and more specifically Y142 are strongly affected confirming our initial model that this distributed decay is related to the properties of Y142 and consequentially changes when this residue is mutated. Here, the decay of Y142F, which interacts more closely with ring D of the chromophore, is extended into the ns timescale, while Y142W decays even faster than the WT.

Interestingly, there is no general trend that a shorter or longer ES lifetime is more productive. From studies on All2699g1g2, it would have been expected that a shorter lifetime yields more photoproduct, however, the situation appears to be more complex. The reduction in photoproduct formation of the Y142W mutant can be explained by a lack of stabilization of the primary photoproduct after the isomerization, which is most likely connected to suboptimal positioning of the tryptophan moiety as the pocket of All2699g1 is not designed to accommodate this bulky residue. The increased steric demand of the tryptophan likely requires it to be positioned further away from the chromophore rationalizing the shorter lifetime. In contrast, the smaller phenylalanine residue adopts a similar but slightly closer position compared to the native tyrosine^[114,128] yielding a longer ES lifetime in return. In this case, the similar position of the phenylalanine still allows photoproduct formation and stabilization of Lumi-R to some extent, even though the increase of the competing fluorescence and the lack of the hydrogen bonding capabilities reduce the Lumi-R QY. Hence, it is important to

note that the observed modulation of the photodynamics cannot be solely explained by steric demand and positioning. It has been shown that the hydrogen bonding capability of the tyrosine plays an important role in the stabilization of the primary intermediate^[123,128,134,142] and the P_{fr} state,^[60,83,84,113] and is potentially also involved in determining the ES kinetics.^[131] Overall, the complex interplay of the available space in and flexibility of the binding pocket and the positioning, steric demand and hydrogen bonding capabilities of this residue determines the ES dynamics in knotless phytochromes. The observation that this kinetic pattern in the LDMs is conserved despite the introduction of various mutations is quite remarkable and suggests that this mechanism may apply more generally. The extent of the extrapolation to other groups of phytochromes will be discussed in the following section.

Conserved Mechanism of the Ultrafast Forward Dynamics

At this point, this work established that a kinetic pattern consisting of specific lifetime distribution amplitudes is conserved among the knotless phytochromes All2699g1g2, *SynCph2*, the single GAF domain All2699g1, and various mutants of these phytochromes. As the application of LDA is still quite rare in studies on phytochrome dynamics, a broad comparison to multiple members of other groups is impossible at the moment, however, data on Slr1393g3, a red/green CBCR (adapted from reference^[97]) and *SynCph1*, a prominent canonical phytochrome assigned to group I have been recorded for comparison. An overview of the LDMs of the ultrafast forward dynamics of these PCB binding phytochromes employing a P_r dark state reveals that even among other phytochrome groups the same pattern is observed (Fig. 3.2).

This discovery indicates that the mechanism proposed in this work may indeed be conserved beyond group II phytochromes. Unfortunately, the lack of comparable data on plant or bacterial phytochromes containing different chromophores limits the extension and general applicability of this model, however, even among PCB binding phytochromes the degree of conservation is quite remarkable.

In summary, the studies conducted on the ultrafast forward dynamics revealed a conserved photomechanism consisting of chromophore initiation dynamics associated with slight spectral shifts of the SE and a distributed non-exponential decay of the ES related to the dynamics being controlled by the reorganization of the protein environment. While Y142 plays a central role during this reorganization, as evident by the results on All2699g1 mutants [V], other factors have to be considered. It is proposed that the available space and the flexibility of the chromophore binding pocket,

3 Research Projects

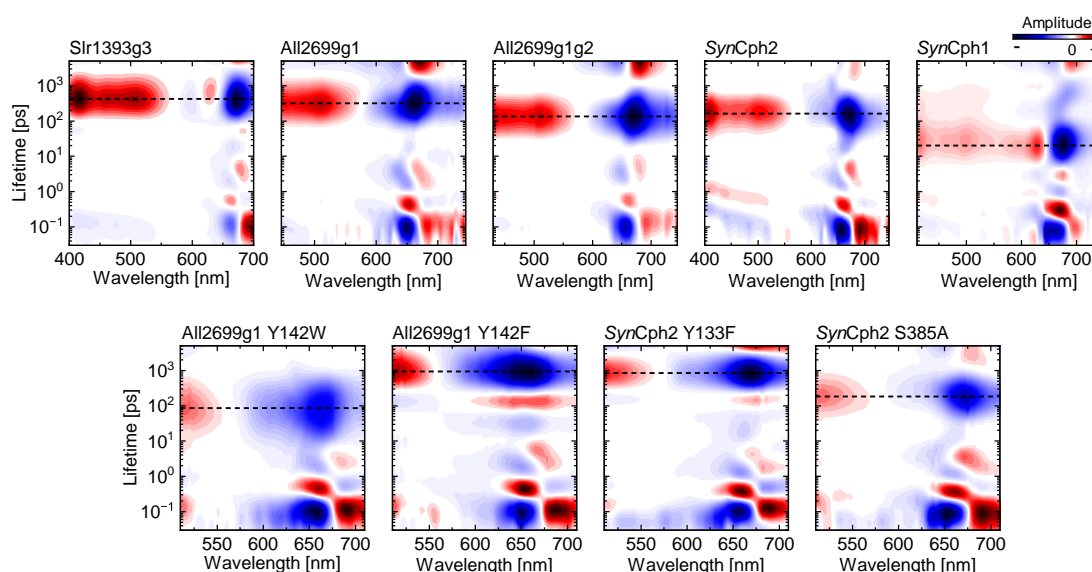


Figure 3.2 – LDMs corresponding to the P_r dynamics from all groups of phytochromes displaying the conserved kinetic footprint identified in this work. While the lifetime distribution pattern remains conserved until ~ 30 ps, the center of the distributed ES decay (black dashed line) shifts in lifetime in different phytochromes. (Top) LDMs corresponding to the P_r dynamics of WT phytochromes: Slr1393g3^[97] and All2699g1 [I] (single GAF domain phytochromes), All2699g1g2 [II] and SynCph2 [III] (knotless phytochromes) and SynCph1 (canonical phytochrome). (Bottom) LDMs corresponding to the P_r dynamics of mutant phytochromes: All2699g1 Y142W [V], All2699g1 Y142F [V], SynCph2 Y133F, and SynCph2 S385A.

the hydrogen bonding network and its protonation state as well as the hydration of the chromophore determine the extended ES dynamics of the P_r state. Whereas this work mainly focuses on the first two points, complementary studies showed that the latter two also have significant impact on the dynamics.^[130,131,167,170] This model is also capable of describing and rationalizing the dynamics of phytochromes exhibiting faster decays as the increased flexibility would facilitate the isomerization and rationalize the faster ES dynamics.^[130] In terms of GSH, a larger flexibility of the pocket would allow multiple conformations to coexist leading to GSH and potentially multiphasic ES kinetics which, however, is not imperative as shown by the results on All2699g1 [I]. Overall, the concise model envisioned in this work provides a reasonable description of the ultrafast forward dynamics of multiple phytochromes employing a P_r dark state and may be extrapolated to the general ultrafast forward photochemistry of phytochromes.

3.1.2 Ultrafast Reverse Dynamics of Knotless Phytochromes

The research on the ultrafast reverse dynamics of *SynCph2* discussed here has been published in reference [III], while the manuscript on the ultrafast reverse dynamics in All2699g1, All2699g1g2 and the *SynCph2* mutants is still in preparation.

The ultrafast reverse photodynamics of knotless phytochromes, similar to the forward dynamics, has remained unexplored prior to this dissertation. In group I phytochromes, the reverse dynamics is typically much faster than the forward dynamics with the ES decaying within a few ps.^[151,154,155,172,173,175,191,192] This is likely due to the reduced steric hindrance for reversion and the already tense conformation of the chromophore in the P_{fr} state.^[121,149,164,165] In contrast, in group III phytochromes, a larger diversity of lifetimes is observed spanning all the way into the hundreds of ps timescale.^[97,158,162,178,253] This discrepancy can be rationalized by structural differences in the photoproduct state apparent by the spectral variety of photoproduct absorption. As the discovered knotless phytochromes show spectral and structural characteristics like the tongue interaction similar to group I phytochromes, it is expected that their kinetics are more comparable to group I than group III phytochromes as well. Here, the model system of All2699g1 and All2699g1g2 offers the unique possibility to study a single GAF domain similar to CBCRs in terms of heterogeneity and the lack of the PHY domain and the complete knotless phytochrome, which is more closely related to group I phytochromes. GSH in particular represents an interesting aspect of the ultrafast dynamics as the impact of GSH on these dynamics might be different if the ES is short lived and not equilibrated for extended times on the ES surface. It can be hypothesized that the difference between the individual GS subpopulations may have a more significant effect without equilibration leading to distinct kinetics for each subpopulation and consequentially multiphasic ES kinetics as observed in *SynCph1*.^[151,154,155] Since the heterogeneity of the P_{fr} state in our model system is abolished by the PHY domain, in analogy to the P_r state, it enables a direct evaluation of the influence of heterogeneity on the ES dynamics of the reverse reaction.

On this basis, it would be expected that All2699g1g2 and *SynCph2* exhibit homogeneous ES dynamics, while All2699g1 may exhibit multiphasic ES kinetics based on GSH. The ultrafast transient absorption data of All2699g1g2 and *SynCph2* (Fig. 3.3) are indeed homogeneous and exhibit three positive signals at 450-675 nm, >730 nm, and 575-600 nm. These signals are straightforwardly assigned to ESA, the primary photointermediate Lumi-F and the Meta-F intermediate in reference to the published assignment for *SynCph2* [III]. Accordingly, the negative signal (700-740 nm) is assigned

3 Research Projects

to GSB/SE (Fig. 3.3). The ESA and GSB/SE decay on the sub-ps timescale give rise to the Lumi-F intermediate, which converts to the Meta-F intermediate within tens of ps. This intermediate then persists beyond the timescale of the transient absorption measurements.

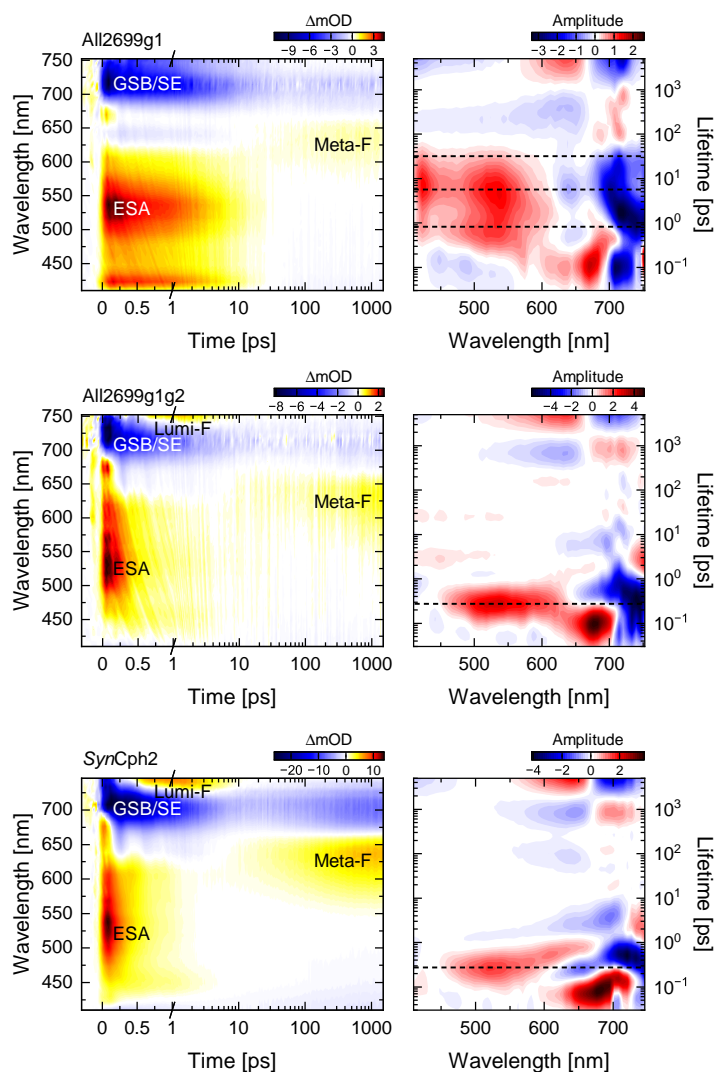


Figure 3.3 – Transient absorption data and corresponding LDMs of the ultrafast P_{fr} dynamics of All2699g1 (top), All2699g1g2 (center), and SynCph2 (bottom). The decay of the ES is indicated in the LDMs by black dashed lines with one component in All2699g1g2 and SynCph2 and three components in All2699g1, identified by kinetic modeling (unpublished results).

LDA reveals the underlying kinetic features and allows a more precise assignment of the kinetics. After departure from the Franck-Condon region described by the positive

(650-700 nm) and negative (700-750 nm) amplitude distributions at ~100 fs, the ES decays with lifetimes of ~340 fs in both proteins, forming the red-shifted Lumi-F intermediate as indicated by the pair of positive (450-650 nm) and negative amplitude (720-750 nm) distributions. Here, the spectral position of the negative amplitude does not match the GS absorption initially and is red-shifted instead, probably due to the decay of the SE and the rise of the Lumi-F intermediate that match this spectral position. At slightly later lifetimes, the negative amplitude distribution is then shifted towards the spectral range of the GS absorption matching its maximum at ~710 nm and ~690 nm in All2699g1g2 and *SynCph2* respectively. This illustrates that the GS is recovered from a vibrationally hot GS intermediate Lumi-F_{hot}, which can either relax into Lumi-F representing the pathway of productive photochemistry or restore the GS. The described branching was validated in *SynCph2* using a kinetic target model (Fig. 3.4) and supported by complementary IR-data [III]. From the relaxed Lumi-F intermediate, the reaction then proceeds via several GS intermediates to the Meta-F intermediate indicated by the pairs of positive (>725 nm, 675-750 nm) and negative (650-725 nm, 525-650 nm) amplitude distributions at ~2-4 ps and ~1 ns respectively. The final pair of positive (550-660 nm) and negative amplitude (660-750 nm) distributions describes the Meta-F intermediate that persists up to the μ s timescale and the remaining GSB.

The transient absorption data of All2699g1 exhibit similar features, although two main differences are observed: the ESA and GSB/SE signals show extended lifetimes into the tens of ps timescale and the positive feature corresponding to the Lumi-F intermediate above ~730 nm is absent. LDA reveals that the features from the complete knotless phytochromes are retained; however, they overlap significantly with two additional ES decays and their consecutive evolution either back to the P_{fr} state or to the Lumi-F intermediate (Fig. 3.4), as derived from the elongated positive and negative amplitude distributions corresponding to ESA and GSB. These decays are assigned to two additional GS populations arising from GSH and their evolution in the ES.

The lack of Lumi-F absorption can be rationalized by the spectral overlap of the GSB corresponding to these two slower ES populations with the Lumi-F absorption. Additionally, the blue-shift of the negative amplitude distribution from ~720 nm to ~700 nm between 700 fs and 30 ps confirms that the Lumi-F intermediate is still formed in analogy to the complete knotless phytochromes, and further suggests that the amount of Lumi-F formed by the individual ES populations might differ, as GS recovery is observed predominantly at longer lifetimes.

From these data, three main conclusions can be drawn. Firstly, the ultrafast dynamics of knotless phytochromes proceed similar to group I phytochromes, however, no distinct

3 Research Projects

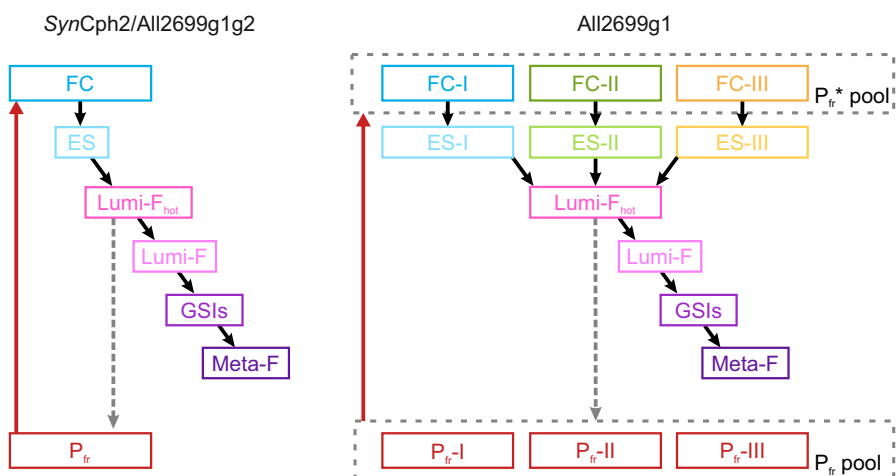


Figure 3.4 – Schematic illustration of the kinetic model derived from the transient absorption data of All2699g1g2/*SynCph2* (left) and All2699g1 (right). The left model is based on the published calculated model for *SynCph2* [III]. The model for All2699g1 was derived from the *SynCph2* model and the differences between the LDMs of *SynCph2* and All2699g1.

GSH is observed. Secondly, the addition of the PHY domain abolishes GSH in the P_{fr} state of All2699g1 similar to the P_r state. The PHY domain is, therefore, one of the main contributors to the presence of GSH in the presented model systems. Thirdly, while heterogeneity is present in both the P_r and the P_{fr} state, the evolution of separate subpopulations was only observed in the ultrafast dynamics of the P_{fr} state.

In order to identify the structural factors influencing GSH in the P_{fr} state and potentially pinpoint what slows down the dynamics of the slower subpopulations in All2699g1, site specific mutagenesis was applied in both *SynCph2* and All2699g1. The Y142F mutant in All2699g1 and the corresponding Y133F mutant in *SynCph2* (Fig. 3.5) exhibit extended ES decays and reduced quantum efficiencies when compared to their respective WT. Judging from the positive amplitude distribution (420-600 nm) assigned to the ESA of the excited P_{fr} state in the LDM of the Y142F mutant, it seems that either the relative occupancy of the population decaying with a lifetime of ~550 fs is significantly reduced in favor of the slower two (~3.5 ps and ~16.4 ps derived from a preliminary kinetic target model) or that the dynamics of all populations have gotten slower. Furthermore, the negative amplitude distribution (650-720 nm) corresponding to GS recovery is now much more pronounced, while the negative amplitude distribution (720-750 nm) assigned to Lumi-F formation in All2699g1 WT seems to have significantly decreased in the mutant. This matches the reduction in QY of the reverse reaction from ~11% to

3.1 Phytochromes

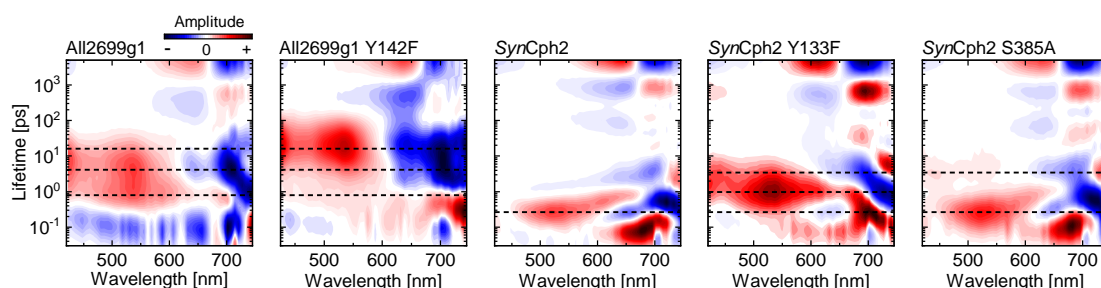


Figure 3.5 – LDMs corresponding to the P_{fr} dynamics of All2699g1 WT, All2699g1 Y142F, SynCph2 WT, SynCph2 Y133F, and SynCph2 S385A displaying the effects of the respective mutation on the lifetime and distribution of populations based on GSH. The different components of ES decay are indicated by black dashed lines in the LDMs. In All2699g1 and SynCph2 WTs, these lines were verified by kinetic modeling, while in the mutants the lines were either drawn at identical lifetimes to represent the shift in population between the components or at newly emerging distributions.

~7%. It also strongly suggests, that all populations in All2699g1 are productive, as the strong reduction of the fast population does not abolish productive photoconversion to the P_r state.

In the homogeneous SynCph2, introduction of the equivalent Y133F mutant has a smaller effect, however, it seems that a second, slower population with an approximate lifetime of a few ps emerges, causing the positive amplitude distribution (430-650 nm) corresponding to ESA decay to broaden temporally and shift towards later lifetimes. This slower population now dominates the decay of the ES and the overall lifetime distribution of the ES decay appears similar to All2699g1, suggesting the introduction of GSH into SynCph2 through the Y133F mutation. Based on the simultaneous increase in the negative amplitude distribution (650-710 nm) corresponding to GS recovery at similar lifetimes, it is likely that, indeed, a second population emerges. However, to obtain valid proof, NMR or RR studies would be required to verify heterogeneity of the Y133F mutant of SynCph2. Another interesting mutant is S385A in SynCph2 as it simulates the detachment of the tongue from the chromophore's hydrogen bonding network allowing a closer comparison to All2699g1 where these interactions are also missing due to the lack of the PHY domain. However, the tongue itself is involved in more interactions than just the hydrogen bonding of the chromophore with its PRXSF motif (see section 2.2.3), and a true removal of the tongue would probably result in more severe effects. Despite the fact that the dynamics of S385A are much less affected than in the Y133F mutant, the decay of a second population can be identified with a lifetime of a few ps by the positive amplitude distribution at 430-550 nm in analogy to Y133F.

3 Research Projects

The disturbance of the immediate chromophore environment in the P_{fr} state by mutants removing some tongue interactions or altering the conserved tyrosine Y133/Y142 in terms of size and most likely hydrogen bonding capabilities induces slower populations in *SynCph2* similar to All2699g1 and enhances the proportion of the slower populations in All2699g1 itself. From these results, the conclusion may be drawn that the slower populations in All2699g1 might be related to missing hydrogen bonds from Y142 or a mispositioning of this residue. In *SynCph2*, the presence of the tongue and the compacting of the pocket may prevent the rise of such subpopulations as indicated by the rise of multiphasic ES dynamics when starting to remove these tongue interactions, *i.e.*, in the mutant S385A.

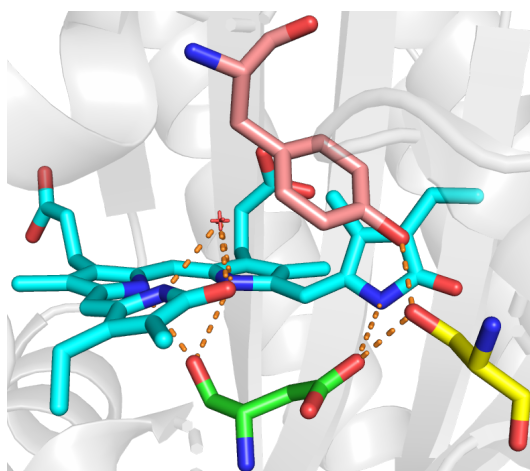


Figure 3.6 – Structural representation of the hydrogen bonding interactions of the chromophore ring D in the P_{fr} state of *DrBphP* F469W (PDB ID:5C5K).^[127] The chromophore (cyan) and ring D in particular is stabilized in its isomerized form in the P_{fr} state by hydrogen bonding interactions (orange dashes) of its pyrrole nitrogen with D207 (green), which is part of a hydrogen bonding network with Y263 (pink) and S468 (yellow).

The absence of the PHY domain in All2699g1 probably allows multiple conformations of Y142, otherwise restricted by its involvement in a hydrogen bonding network with the ring D pyrrole nitrogen, D87 (D207 in *DrBphP*), and the conserved serine (S468 in *DrBphP*) in the PRXSF motif (exemplarily shown in the crystal structure of *DrBphP* in its P_{fr} state in Fig. 3.6), which may be the underlying origin of the observed heterogeneity. Recent studies support the importance of this hydrogen bonding network^[154] and the overall water network surrounding the chromophore in the ultrafast reverse dynamics.^[193] Therefore, the results accumulated here provide first insights into the ultrafast reverse dynamics of knotless phytochromes. Additionally, suggestions for the structural factors inducing GSH which influence the respective reverse dynamics are

derived from site specific mutagenesis studies.

3.1.3 The Role of Ground State Heterogeneity in the Ultrafast Dynamics of Knotless Phytochromes

The investigation of the ultrafast forward and reverse dynamics of knotless phytochromes presented here and in the references [I-III] and [V] illustrates the different role of GSH in the ultrafast forward and reverse dynamics. While heterogeneity in All2699g1 does not lead to multiexponential kinetics in the forward dynamics (see section 3.1.1), its effect is striking in the reverse dynamics inducing separate ES decays for three subpopulations which disappear upon removal of GSH by addition of the PHY domain in All2699g1g2. On the basis of these results, one can hypothesize that the lifetime of the ES and more specifically the time the different populations have to equilibrate on the ES surface after excitation significantly impacts the effect of GSH. In the forward dynamics, the different populations equilibrate on the ES surface without being able to progress because of the high energy barrier imposed by the steric gate Y142. Due to the high energy injected into the system upon excitation, it is likely that potentially small barriers between the populations may be overcome and rendered irrelevant in light of the much higher barrier to proceed with the photoreaction given enough equilibration time. In contrast, the reverse dynamics progresses in the sub 500 fs time regime indicating a pathway without major barriers to the conical intersection with the GS. Based on the lack of time for equilibration, the evolution of the subpopulations may be significantly affected by small structural differences resulting in different lifetimes for the specific conformations of each subpopulation. Hence, heterogeneity has a more striking impact on the ultrafast reverse dynamics. To further solidify this hypothesis, more studies on model systems with similar potential need to be performed to confirm whether the observed trend is generally applicable or exclusive to All2699g1 and All2699g1g2; such systems would be the CBD and CDB-PHY constructs of *DrBphP*^[128] which have yet to be studied regarding their ultrafast reverse dynamics, especially suited due to the availability of crystal structures of CBD, CDB-PHY, and even of mutants like Y263F both in presence and absence of the PHY domain.^[128,131]

3.1.4 Millisecond-Dynamics of Knotless Phytochromes

The results presented in this section have been published in reference [IV]. In order to complete the investigations on the photocycle of knotless phytochromes and the influence of the PHY domain on these dynamics, the ms-dynamics of All2699g1 and

3 Research Projects

All2699g1g2 were studied. Unlike the ultrafast dynamics, the ms-dynamics of knotless phytochromes have been initially characterized for *SynCph2*.^[196] Its forward dynamics closely resembles those of *SynCph1* and *Agp1* showing the transition from Lumi-R to Meta-R_a on the early μ s timescale, followed by a suggested deprotonation to form the blue-shifted Meta-R_c intermediate within a few ms.^[103,136,182] Finally, the photoproduct P_{fr} is formed within tens of ms. For the reverse dynamics of *SynCph2* and *PhyA65*^[196] overall similar lifetimes have been reported, however, the lack of strong spectral changes as compared to the forward dynamics renders a comparison of the individual processes much more challenging. On these slower timescales, the role of heterogeneity is very minor and has not been considered in detail. Only protonation equilibria seem to play a role in the dynamics and were suggested as one possible origin for biphasic product formation observed in *SynCph1*.^[136] In contrast, the presence of the PHY domain is expected to significantly impact and control the dynamics as large scale rearrangements within the PHY domain are observed during the final transition to the photoproducts.

In general, the forward dynamics of All2699g1g2 resembles those of *SynCph2* with almost identical lifetimes for the transitions from Lumi-R to Meta-R_a and Meta-R_a to Meta-R_c. The only major differences are observed in the final transition from Meta-R_c to P_{fr} where All2699g1g2 shows a biphasic formation of P_{fr} with an additional second component exhibiting longer lifetimes in the range of hundreds of ms. While this differs from *SynCph2*, it resembles the kinetics observed in *SynCph1* where a similar biphasic transition was observed and connected to a difference in proton release and uptake.^[136] On this basis, pH dependent measurements are required to confirm that the two kinetic phases originate from different pH dependent species. However, a pH dependence of All2699g1g2 was not feasible due to its precipitation at most pH values far away from pH 8.

In All2699g1, the Meta-R_a intermediate represents the first observable μ s-intermediate (Fig. 3.7). Therefore, the reaction progresses faster than in All2699g1g2 where the first observable intermediate is still the Lumi-R intermediate and the transition to Meta-R_a can be observed within hundreds of μ s. The acceleration of the photodynamics becomes even more evident in the following Meta-R_a to Meta-R_c transition, where the reaction proceeds tenfold faster in All2699g1 than in All2699g1g2 indicating higher thermal barriers for the relaxation of the chromophore binding pocket in All2699g1g2 (Fig. 3.7). This is in line with previous studies suggesting that the chromophore binding pocket becomes more rigid through the interaction with the PHY domain slowing down the relaxation of the strained chromophore and the starting protein reorganization.^[88,163,254] Interestingly, the timescale of the P_{fr} formation is not strongly affected by the presence

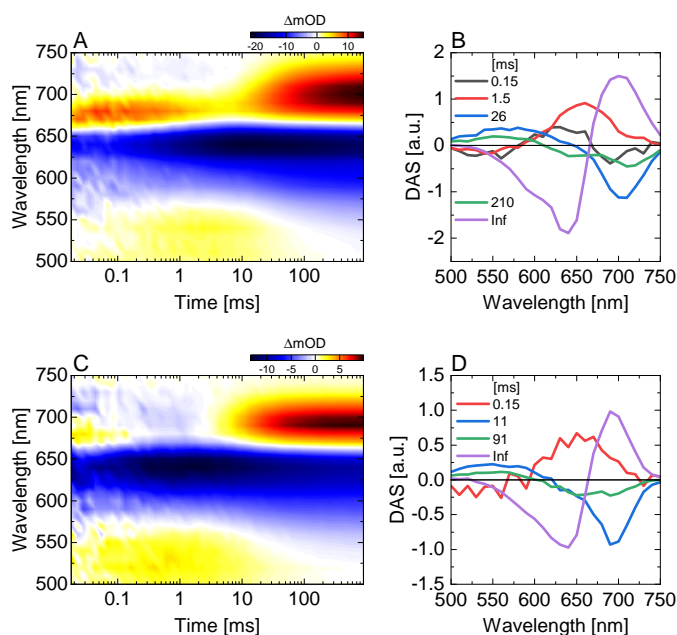


Figure 3.7 – Flash photolysis data and GLA of the P_r state in All2699g1g2 (A,B) and All2699g1 (C,D) at pH 8 after excitation at 640 nm. In All2699g1g2, the first observable intermediate is the Lumi-R intermediate (A) which evolves to Meta- R_a with a lifetime of 0.15 ms (red, B). In All2699g1, this transition cannot be observed as Meta- R_a is already present at the beginning of the measurement time frame (C). Taken from [IV].

of the PHY domain even though this final step is associated with the refolding of the PHY tongue and other large scale protein reorganization.^[89,91,96,123] As a result, the rate-limiting step of P_{fr} formation appears to be determined by the GAF domain, which was previously suggested for *DrBphP*^[91] and is now confirmed by the direct comparison provided in this dissertation.

Most importantly, the biphasic formation of P_{fr} is still observed in All2699g1 allowing a pH dependent investigation of this process as All2699g1 is much more robust to changes in the buffer conditions. By comparing the amplitudes and lifetimes of the DAS obtained for the biphasic transition in GLA, a clear trend can be isolated.

The process with the shorter lifetime is accelerated and increases in amplitude with rising pH, while the slower process dominates at low pH and almost vanishes at pH 8.4 (Fig. 3.8) providing strong evidence towards a pH dependent equilibrium of the chromophore or most likely its surrounding hydrogen bonding network, resulting in two protonation states with different kinetics. Based on the determined pKa of ~7.2, H139 and H169 represent the most likely candidates for deprotonation/protonation in this equilibrium. In particular, H139 mutants have been reported as dysfunctional be-

3 Research Projects

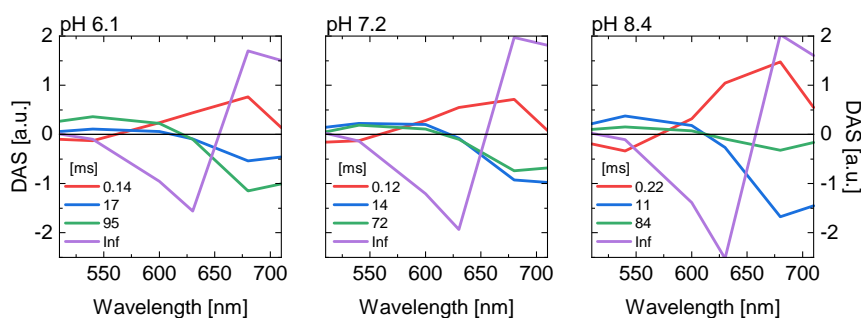


Figure 3.8 – DAS obtained from GLA of the pH dependent flash photolysis data of the P_r state in All2699g1 at pH 6.1, 7.2 and 8.4. The DAS show similar lifetimes and spectral features at all pH values. However, the amplitudes of the last two lifetimes (blue, green) describing the biphasic transition to the P_{fr} change significantly with depending on the pH. The fast lifetime (blue) increases in amplitude with rising pH, while the slower process dominates at low pH and almost vanishes at pH 8.4. Taken from [IV].

yond the Meta- R_c intermediate hinting towards a crucial role of this residue in the final transition to the photoproduct state.^[103,113,145,146] However, as no significant spectral differences between the two processes were observed, the deprotonation cannot affect the spectral properties of the chromophore, which, given the proximity of H139 to the chromophore B-C plane and the pyrrole water, seems unlikely. Therefore, the deprotonation of another residue in the hydrogen bonding network is more likely but the protonation state of this residue still has to play a role in the kinetics of the transition to the P_{fr} state. The overall acceleration of the P_{fr} formation at high pH may also be attributed to a suggested increased protein mobility as observed in *SynCph1* under these conditions.^[165] In summary, the studies on the forward ms-dynamics presented here, offer insight into the role of the PHY domain and the complex pH dependence during the later steps of the photocycle (Fig. 3.9). While a potential mechanism can be suggested based on the data, further studies using mutants and techniques with structural resolution like RR, IR, or NMR spectroscopy with freeze trapped intermediates are a target for future studies to fully decipher the processes and protonation steps occurring during the forward ms-dynamics of phytochromes.

Concerning the reverse dynamics, much smaller spectral changes can be observed in both All2699g1 and All2699g1g2. Based on the more pronounced blue shift of the major absorption band between 530-650 nm on the ms timescale, it can be concluded that a similarly blue shifted and most likely deprotonated species as Meta- R_c is formed in the reverse dynamics. This Meta- F_c intermediate was previously observed in *SynCph2* but not associated with a process similar to the forward dynamics.^[96] The population

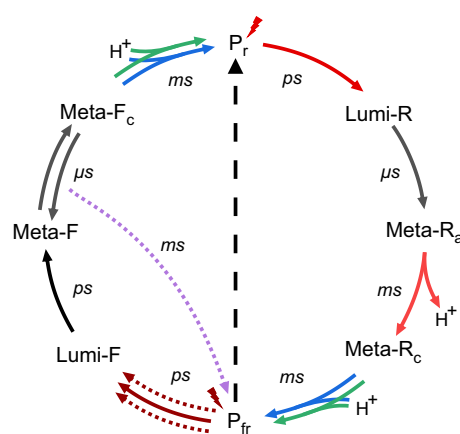


Figure 3.9 – Complete photocycle of All2699g1 and All2699g1g2. [I]-[V] Processes exclusive to All2699g1 like the multiphasic formation of Lumi-F and the shunt from Meta-F to the P_{fr} state are displayed as dotted arrows. The dashed arrow represents the thermal recovery from the P_{fr} to the P_r state. Multiple arrows pointing in the same direction for one transition indicate multiple lifetimes for this process while the arrows between Meta-F and Meta-F_c indicate an equilibrium. From this equilibrium the P_{fr} state is recovered via the shunt pathway (purple, dotted). Colors are matched to [IV]. Adapted from [IV].

of this intermediate strongly differs between the knotless phytochromes investigated here, rising from All2699g1 to All2699g1g2 to *SynCph2*. In analogy to the forward dynamics, its formation cannot be observed in All2699g1, while it can be clearly assigned to a 500 μs lifetime in All2699g1g2 related to the increased flexibility of the pocket in absence of the PHY domain. The variations in amplitude and the presence of the spectral features of both intermediates simultaneously may indicate an equilibrium between Meta-F and Meta-F_c, probably dependent on the exact protein environment and its pKa value in particular, as the process is most likely associated with the deprotonation of an amino acid residue in proximity of the chromophore. D207 (D87 in All2699g1) may play a crucial role during this deprotonation according to studies on other phytochromes;^[103,113,145] however, pinpointing an amino acid residue without time-resolved data providing structural information is rather speculative.

In contrast to the forward dynamics, All2699g1 exhibits an additional lifetime of a few ms in the reverse dynamics not observed in All2699g1g2 associated with a shunt pathway leading back to the P_{fr} GS from the Meta-F and Meta-F_c equilibrium. This shunt pathway was not observed in the same measurement at pH 7.2 leading to the conclusion that this process is also most likely pH dependent. Therefore, pH dependent measurements of the reverse reaction of All2699g1 may provide promising opportuni-

3 Research Projects

ties for further mechanistic studies on this fairly rare process otherwise only observed in the forward reaction of Agp1 and the reverse reaction of Agp2.^[255] The final transition to the P_r state is again biphasic and slower in All2699g1g2 in analogy to the forward dynamics representing a target for future pH dependent studies as well. Based on these results, a complete photocycle can be constructed for the ms-dynamics of All2699g1 and All2699g1g2, summarizing the respective findings of this work (Fig. 3.9).

3.1.5 The Influence of the PHY Domain on the Photodynamics of Knotless Phytochromes

Finally, the influence of the PHY domain on the UV/Vis photodynamics of knotless phytochromes can be evaluated from the results accumulated in the references [I]-[IV] and the additional results presented in sections 3.1.1-3.1.4. The importance of the PHY domain for phytochrome photochemistry is quite apparent based on the close interaction with the chromophore and its binding pocket in the GAF domain and the role of tongue refolding in the signal transduction of phytochromes. In contrast, the ability of single GAF or PAS-GAF constructs like All2699g1 [I] or the PAS-GAF module of *DrBphP*^[128,131] and the entire group of CBCRs to photoconvert despite lacking the PHY domain shows that it is not required for the photodynamics of phytochromes and in case of CBCRs not even for signal transduction to the OPMs. While it is most likely necessary for signaling in group I and group II phytochromes, alternative signaling pathways have to be present in group III and may be present rudimentarily in the former groups as well.^[53] This raises the question of the role of the PHY domain for the photodynamics and photophysical properties in group I and II phytochromes, and, in turn, which aspects of CBCRs photochemistry may be attributed to the lack of the PHY domain.

Based on the model systems All2699g1 and All2699g1g2, the central effects of the PHY domain were identified as the reduction or removal of GSH^[88] and the compacting of the chromophore binding pocket through the tongue interactions.^[88] The reduction of GSH represents the most apparent property lacking in CBCRs, where pronounced GSH is commonly observed most likely due to the lack of the PHY domain. Both the reduction of GSH and the compacting of the binding pocket result in the observed increase in photoconversion efficiency changing from ~10% in both directions in All2699g1 to 13% and 16% in All2699g1g2 for the forward and reverse dynamics respectively. Considering the spectral changes of the stationary absorption, the quantum efficiency and the ultrafast dynamics, the PHY domain seems to have a greater impact on the reverse

3.1 Phytochromes

dynamics and the properties of the P_{fr} state in general. While the P_r states of All2699g1 and All2699g1g2 show similar absorption maxima and only small changes of the ES lifetime, a spectral shift of more than ~15 nm, a drastic reduction of ES lifetime, and the complete removal of two ES decay components is observed in the P_{fr} state. This can be rationalized by the different effect of GSH in the forward and reverse dynamics and the much more direct interactions of the PHY tongue with the chromophore in the P_{fr} state. Here, the salt bridge between D87 and R387 in the P_r state does not have a direct impact on the ring D of the chromophore, while S389 is part of the hydrogen bonding network interacting with the ring D pyrrole nitrogen in the P_{fr} state.

In contrast to the ultrafast dynamics, where the more compact binding pocket and the optimized position of key residues and an entailing increase of directionality result in faster and more efficient photodynamics, the PHY domain decelerates the dynamics on the ms timescale. The reduction of the available space prolongs the thermal relaxation of the chromophore and the large scale protein reorganization processes defining the ms-dynamics of phytochromes. In summary, the PHY domain fulfills a complex role in the photodynamics of phytochromes that goes beyond transmitting a signal to an OPM. Through its interactions with the chromophore binding pocket, it optimizes the photoconversion by removing GSH and increases the directionality of the reaction at the cost of conversion speed on the ms timescale.

3.2 Indigoid Photoswitches

The research related to indigoid photoswitches comprises the HTI Hula-Twist project and the ITI VET project.

3.2.1 Hula-Twist Mechanism in a Sterically Crowded HTI

The results presented here have been published entirely in reference [VI]. The application of HTIs in molecular motors represents one of the main motivations to understand, control and selectively access the photochemical pathways leading to specific motions like SBR and DBI. A multitude of studies on the factors favoring SBR associated with a TICT state formation and DBI have been performed.^[205,206,208–210] However, recent efforts have been made to tailor HTI systems towards undergoing an HT pathway, a concerted motion of SBR and DBI in order to broaden the possible motions induced by photoactivation. Here, the main challenge lies in the design of molecules, where the HT photoproduct has to be spectrally distinguishable from the products of DBI or SBR, and where thermal isomerization has to be prevented.^[205] The latter is required since an HT photoproduct could also arise from light-driven DBI followed by thermal SBR otherwise, which would disqualify HT as a concerted light-driven photoreaction. Alternatively, a potential HT product could just undergo SBR to form the DBI product and would not be identified as originating from HT. These requirements hindered the direct observation of the HT mechanism and a detailed mechanistic understanding of this process, and the factors controlling it are still missing.

The conducted studies on an HTI tailored to undergo an HT upon illumination aim towards providing first direct dynamic evidence of the HT mechanism. The molecular design was based on previous findings by the Dube group, who verified the occurrence of HT in steady state illuminations using a specific molecular setup which consists of an electron donating group in the *para*- and a non-symmetric substitution in the *ortho*-position of the hemistilbene, an oxidized sulfur in the thioindigo fragment, and a second, bulky substituent at the C=C double bond.^[205,230,231] This molecular design fulfills the aforementioned conditions of preventing thermally driven isomerization, and therefore, turns two diastereomers with different double bond configuration into four geometrically distinguishable diastereomers. However, the atropisomers with similar double bond configuration can only be clearly distinguished by NMR, but not by UV/Vis spectroscopy. The diastereomer **1-A** (Fig. 3.10) was chosen for further investigation out of the four diastereomers as NMR studies by the Dube group showed that it exhibits the largest overall QYs and the highest HT QY in particular. All QYs were found to be

3.2 Indigoid Photoswitches

strongly solvent dependent with a total photoconversion QY above 50% in the apolar solvent cyclohexane whereas photoconversion was completely abolished in the polar solvent acetonitrile (MeCN).

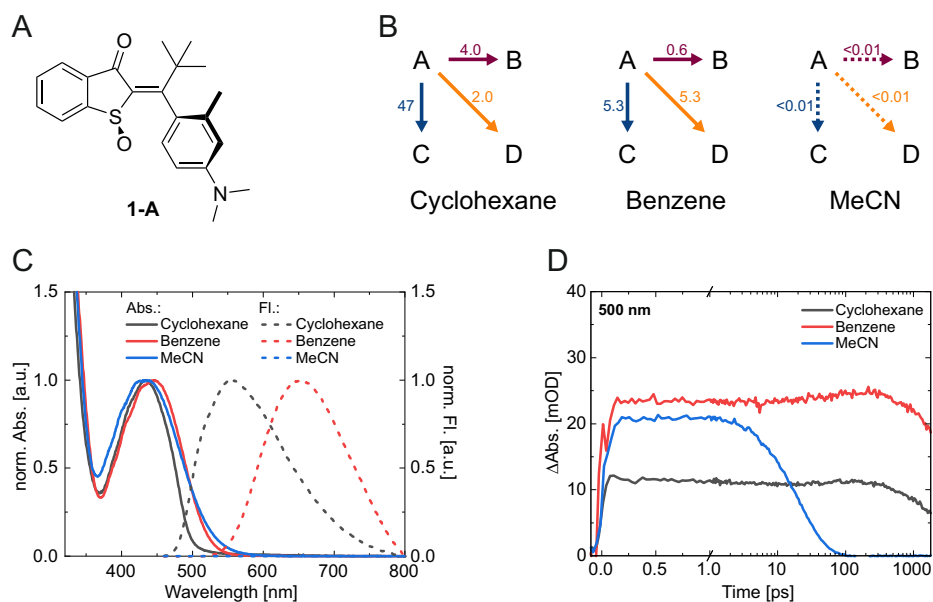


Figure 3.10 – Overview of the spectroscopic data on diastereomer **1-A**. (A) Molecular structure of the investigated HTI **1-A**. (B) Photoconversion QYs of **1-A** determined by Aaron Gerwien with NMR spectroscopy. (C) Normalized absorption (solid line) and fluorescence spectra (dashed line) of **1-A** in cyclohexane (grey), benzene (red) and MeCN (blue). (D) Selected transients at 500 nm (ESA) extracted from the transient absorption data of **1-A** in cyclohexane (grey), benzene (red) and MeCN (blue). The transients illustrate the significantly different ES lifetimes of **1-A** depending on the solvent polarity. Adapted from [VI].

Stationary UV/Vis spectroscopic studies supported this observation as illumination of **1-A** did not result in spectral changes in MeCN, whereas a significant conversion to the *E*-isomers could be observed in cyclohexane (Fig. 3.10). While the absorption spectrum of **1-A** is predominantly independent of the solvent polarity, the fluorescence shows a large Stokes shift of >100 nm in cyclohexane and an even stronger additional red shift of ~150 nm upon switching to the slightly more polar benzene, hinting towards a pronounced solvent dependent stabilization of the S_1 ES (Fig. 3.10). The fluorescence QY decreases with increasing solvent polarity and in MeCN no fluorescence can be observed predicting a significant change in ES lifetime.

To investigate the dynamics of **1-A**, UV/Vis transient absorption measurements were performed, which are dominated by strong ESA signals overcompensating the GSB

3 Research Projects

signal. In accordance to the fluorescence measurements, the ES lifetime varies strongly depending on the solvent polarity (Fig. 3.10). It increases at first from cyclohexane (~3 ns) to benzene (~4.6 ns), but decreases significantly in MeCN (~20 ps) with only one major ES decay. Based on these observations, a mechanistic model was constructed (Fig. 3.11).

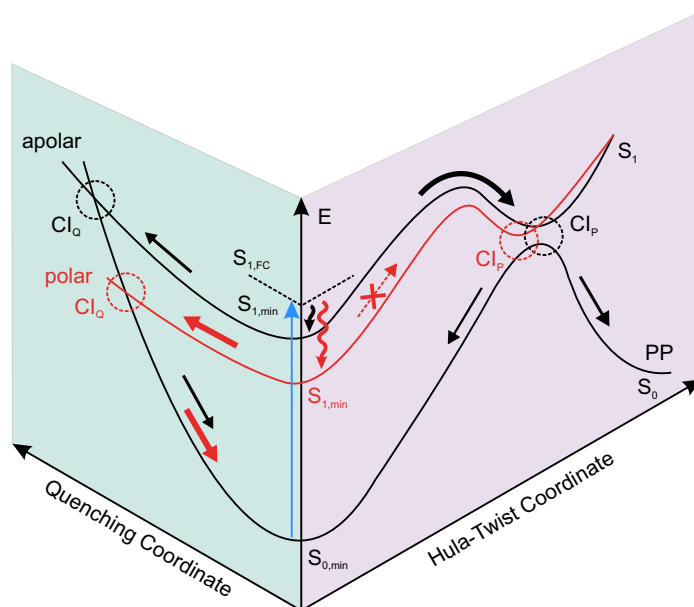


Figure 3.11 – Schematic representation of the developed mechanistic model of the kinetics of the investigated sterically crowded HTI. The $S_{1,min}$ is strongly stabilized in polar solvents (red) due to its strong charge transfer character. In contrast, the Franck-Condon region is mostly solvent independent resulting in an increased excess energy in polar solvents. Due to the stabilization, the solvent independent barrier to the productive conical intersection CI_P increases in polar solvents preventing photoproduct formation. Instead, a quenching conical intersection CI_Q becomes accessible due to the available excess energy in polar solvents and quenches the ES rapidly. Therefore, product formation is only observed in apolar solvents where both conical intersections are presumably equally accessible. Adapted from [VI].

After excitation to the solvent independent Franck-Condon region, the molecule relaxes on the ES surface into the $S_{1,min}$, which is strongly stabilized with increasing solvent polarity. The solvent reorganization stabilizing the $S_{1,min}$ geometry is reflected in a <5 ps lifetime in the transient absorption data. In benzene and cyclohexane, a high barrier then has to be overcome to access a conical intersection leading to GS recovery and photoproduct formation as evident by the long ES lifetimes. In comparison to the $S_{1,min}$ this barrier is hardly stabilized with increasing solvent polarity and therefore, rises with respect to the $S_{1,min}$ in more polar solvents. This is evident by the increase

in ES lifetime from cyclohexane to benzene. As the $S_{1,\min}$ is stabilized even further in MeCN, this productive conical intersection is inaccessible in MeCN resulting in the loss of productive photochemistry. Consequently, the short lifetime of MeCN can only be explained by the stabilization of a second conical intersection in polar solvents leading back to the initial GS of **1-A** without forming any photoproducts.

This model (Fig. 3.11) was verified by quantum mechanical calculations by Jonas Leitner from the group of Andreas Dreuw. The calculations show that the S_1 state possesses strong charge transfer character reproducing the strong stabilization of the $S_{1,\min}$ and the associated red shift of the fluorescence. The two conical intersections proposed to describe the experimental data could be distinguished as a productive conical intersection being located along an HT coordinate, suggesting the HT as the dominant reaction pathway. Conversely, the quenching conical intersection is located close to the $S_{1,\min}$ and is hardly accessible in apolar solvents. Since the HT product is not the sole product of the photoreaction, the twisted geometry of the conical intersection most likely allows SBR and DBI pathways as well. The ratios between these pathways then depend on the conical intersection's exact geometry, which was shown to be modulated by the solvent polarity.

The results provide first insight into the solvent dependence of the photochemistry in a sterically crowded and pre-twisted HTI taking the first step to understand the HT mechanism in HTIs and suggesting its existence as a relevant concerted photoreaction pathway based on the time-resolved transient absorption data. Therefore, this work extends the mechanistic understanding of HTI photochemistry by introducing a dynamic perspective on the HT mechanism.

3.2.2 ITI Photoswitches as Vibrational Energy Donors for VET

The rather new class of ITI photoswitches shows promising spectral properties with reasonably high extinction coefficients, absorption in the Vis spectral range, and a large band separation between isomers.^[235] However, their lack of thermal bistability renders them unsuitable for most biological applications, which require a photoswitch in a classical sense and major advances towards stabilizing the photoproduct state have yet to be presented. Exploring other applications, this work aims towards harnessing their promising properties and ultrafast photochemistry with predominant relaxation via a hot GS^[235] for the design of a vibrational energy donor in VET systems. Here, the predominantly unproductive photochemistry of ITIs represents a desired property for optimal release of vibrational energy without lasting photoproducts. Their potential in

3 Research Projects

biological applications of VET is further elevated by the synthesis of ITIs exhibiting a strongly red-shifted absorption beyond 500 nm.

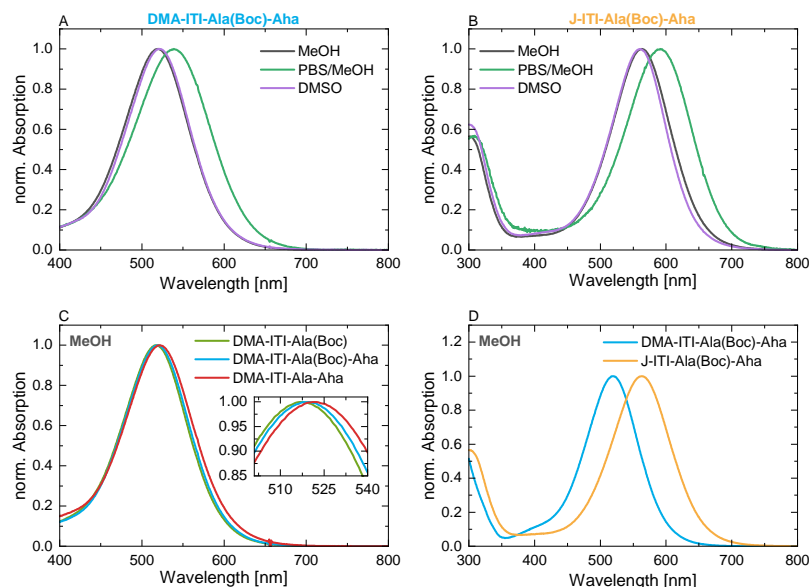


Figure 3.12 – (A) UV/Vis absorption spectra of the DMA-ITI-Ala(Boc)-Aha dipeptide in methanol (MeOH), phosphate-buffered saline (PBS)/MeOH (1:1 mixture) and dimethylsulfoxid (DMSO). (B) UV/Vis absorption spectra of the J-ITI-Ala(Boc)-Aha dipeptide in MeOH, PBS/MeOH (1:1 mixture) and DMSO. (C) Comparison of the protected Ala analog (DMA-ITI-Ala(Boc)), the protected dipeptide (DMA-ITI-Ala(Boc)-Aha) and the unprotected dipeptide (DMA-ITI-Ala-Aha) based on the DMA-ITI in MeOH. (D) Comparison of the absorption spectra of the two protected ITI dipeptides in MeOH.

The two ITI compounds synthesized by Larita Luma, the DMA- and the J-ITI, were converted into Ala analogues with a Boc protected amino group. The obtained amino acid analogues were attached to a vibrational energy acceptor, Aha, creating dipeptide model systems to explore the potential of ITIs as vibrational energy injectors for VET. The spectra of the dipeptides DMA-ITI-Ala(Boc)-Aha and J-ITI-Ala(Boc)-Aha exhibit absorption maxima at ~517 nm and 562 nm respectively (Fig. 3.12) with extinction coefficients of ~20000 M⁻¹ cm⁻¹ (determined by Larita Luma).

These maxima are red-shifted in a PBS/MeOH 1:1 mixture to 539 nm and 591 nm respectively, but remain mostly unchanged when switching to DMSO as the solvent. The addition of the Aha acceptor and the removal of the Boc protecting group result in only minor changes in the absorption spectrum inducing a bathochromic shift of ~4 nm. In summary, the absorption spectra of the investigated compounds are mostly unaffected by the performed modifications and attachment of the acceptor, while a

noticeable red shift of the absorption is observed in the presence of an aqueous buffer.

UV/Vis transient absorption experiments were performed (Fig. 3.13) to verify that the dipeptides derived from the DMA- and J-ITI still exhibit the typical photochemistry of ITIs with an ultrafast ES decay on the sub-ps timescale and consecutive cooling of a hot GS, required for VET.

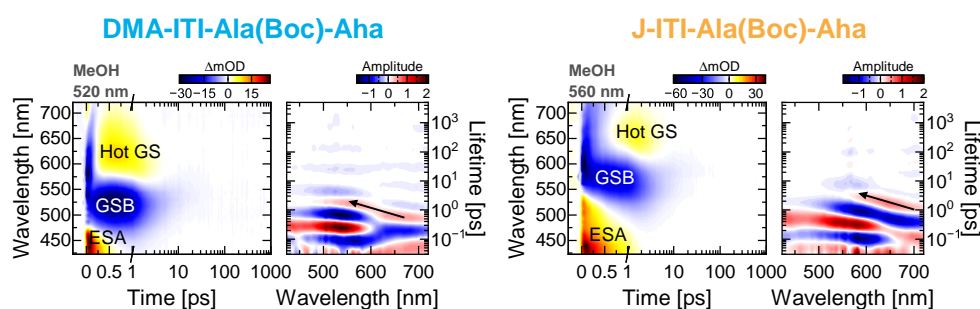


Figure 3.13 – Transient absorption data and the corresponding LDMs of the DMA-ITI-Ala(Boc)-Aha and J-ITI-Ala(Boc)-Aha dipeptides in MeOH after excitation at 520 nm and 560 nm respectively. The black arrow highlights the tilted positive lifetime distribution amplitude representing the cooling of the hot GS.

Due to a lack of unprotected sample, experiments were conducted predominantly on the protected dipeptides, and later on compared to the unprotected dipeptide for the DMA-ITI to verify that the protecting group does not affect the dynamics. Both, the DMA- and the J-ITI dipeptide, show ESA (DMA: 425-475 nm, J: 425-530 nm) and GSB/SE (DMA: 475-700 nm, J: 550-710 nm) signatures in MeOH, where only the ESA decays with sub-ps lifetimes, while the bleach remains at first. With the decay of the ES, a positive signal (DMA: 575-700 nm, J: 625-700 nm) emerges that can be associated with a GS intermediate. This intermediate undergoes a blue shift starting at ~0.5 ps and ~1 ps respectively and completely recovers the GS after ~6 ps without forming any other positive signatures. Application of LDA reveals the underlying kinetic features and allows an assignment of the respective processes. First, the departure from the Franck-Condon region with a lifetime of <100 fs is represented by the pair of negative (440-625 nm) and positive amplitude (625-710 nm) distributions indicating a red shift of the stimulated emission. Next, the positive amplitude distribution at 440-600 nm can be assigned to a decay of the ES and its associated ESA with a lifetime of 250 fs in the DMA and 360 fs in the J-ITI dipeptide, while the simultaneous rise of the GS intermediate is indicated by the negative amplitude distribution between 600 nm and 710 nm. Finally, the blue shifting behavior is represented by a tilted positive amplitude distribution (~500-710 nm, black arrow in Fig. 3.13) spanning from 400 fs to 3 ps in the DMA- and

3 Research Projects

1 ps to 4 ps in the J-ITI dipeptide. The tilt of the distribution translates to non-exponential shifting kinetics associated with cooling dynamics, which cannot be fitted adequately by monoexponential functions like in GLA. Therefore, the GS intermediate is assigned as a hot GS that cools on the ps timescale to recover the initial GS. The absence of residual signal after the cooling dynamics indicates no to very low isomerization QY ideal for VET applications. Comparing the two compounds, the DMA-ITI exhibits faster kinetics in both, ES decay and cooling of the hot GS. Additionally, more hot GS seems to be formed in the DMA-ITI judging from its higher amplitude, however, this can only be determined accurately in the IR spectral region, where overlap with the GSB can be avoided. Similarly, it can be expected that the hot GS in the DMA-ITI carries more vibrational energy due to its spectral position at shorter wavelengths, while retaining the same difference of ~100 nm to the GSB.

In order to identify tools to boost the amount of vibrational energy released and to explore the photodynamics of the investigated ITI compounds further, a solvent (Fig. 3.14) and wavelength dependence (Fig. 3.15) of the ultrafast dynamics was measured. The mechanism of the photodynamics remains unchanged in DMSO and in PBS/MeOH mixture (Fig. 3.14); however, the dynamics are accelerated in the presence of aqueous buffer and decelerated in DMSO (compare position of the white dashed line in the LDMs of Fig. 3.14), most likely due to the increased viscosity of the latter solvent. The amplitude of the hot GS (highlighted by the black circle in Fig. 3.14) is increased in DMSO, while the presence of water does not significantly alter the amplitude of the hot GS, making DMSO a promising solvent for VET studies.

The excitation wavelength dependence (Fig. 3.15) of both compounds, again, shows no major change of the mechanism itself, but the ES decay is accelerated at longer excitation wavelengths (compare position of the white dashed line in the LDMs of Fig. 3.15), while the cooling of the hot GS remains mostly unaffected by the excitation wavelength. Additionally, the spectral position of the GSB is shifted to longer wavelengths with increasing excitation wavelength revealing a second maximum within the ESA. Whether the ESA or the GSB undergo the spectral shift remains unclear. A shift of the GSB would be rather peculiar hinting towards ground state heterogeneity or different ESs that can be addressed in the main absorption band which does not alter the photodynamics. Therefore, it is more likely that the ESA undergoes an excitation wavelength dependent red shift. Furthermore, the relative amplitude of the hot GS is increased at shorter excitation wavelengths, which can be rationalized by the larger amounts of energy injected into the system depositing more energy in vibrational modes. Therefore, high energy excitation may provide a tool to generate more vibrational energy for VET elevating the

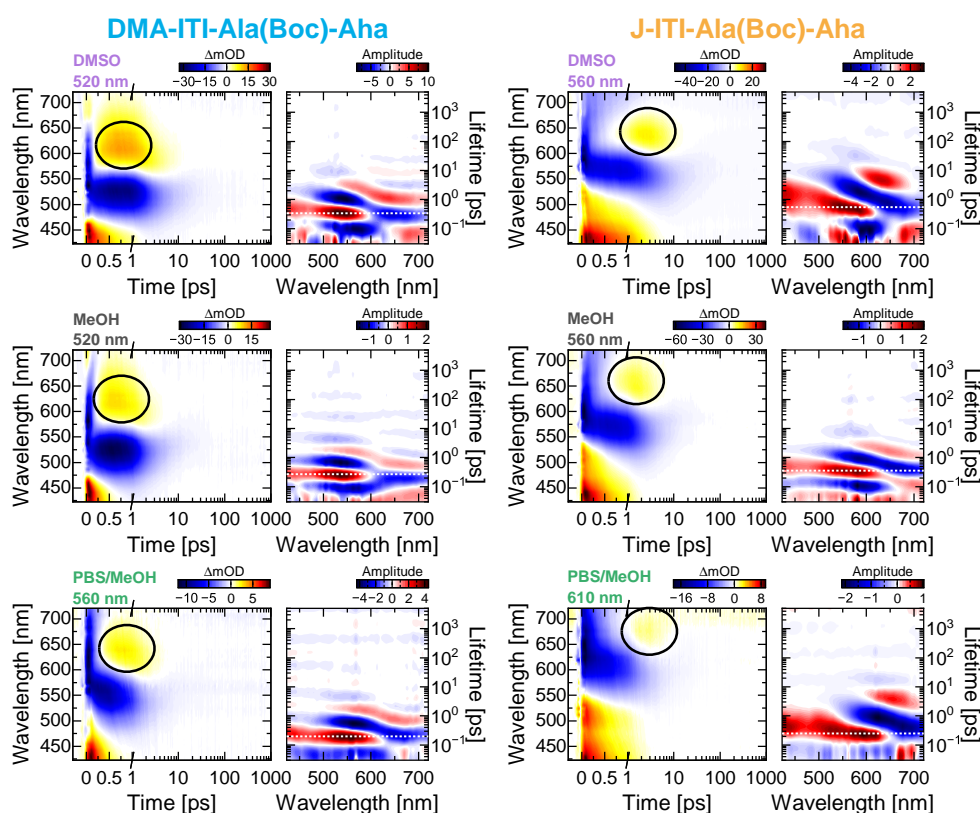


Figure 3.14 – Solvent dependence of the transient absorption data and the corresponding LDM of the DMA-ITI-Ala(Boc)-Aha and J-ITI-Ala(Boc)-Aha dipeptides in DMSO (top), MeOH (center), and PBS/MeOH (1:1 mixture) (bottom). The DMA-ITI dipeptide was excited at 520 nm, 520 nm and 560 nm and the J-ITI dipeptide at 560 nm, 560 nm and 610 nm in DMSO, MeOH, and PBS/MeOH (1:1 mixture), respectively. The white dashed line in the LDMs indicates the decay of the ES, while the black circle highlights the hot GS and its variations in amplitude.

application potential of ITIs for VET studies.

Finally, the applicability of the presented results for the unprotected dipeptides was verified by UV/Vis transient absorption measurements of DMA-ITI-Ala(Boc), DMA-ITI-Ala(Boc)-Aha and DMA-ITI-Ala-Aha under identical conditions. As the resulting transients perfectly match (Fig. 3.16), it can be reasonably assumed that the addition of Aha and the removal of the Boc protecting group do not affect the photodynamics in the dipeptides.

In summary, the UV/Vis characterization of the ITI compounds confirms their excellent photophysical properties for VET applications. This includes a broad excitation range in the Vis spectral region, high extinction coefficients, and little to no photoisomer-

3 Research Projects

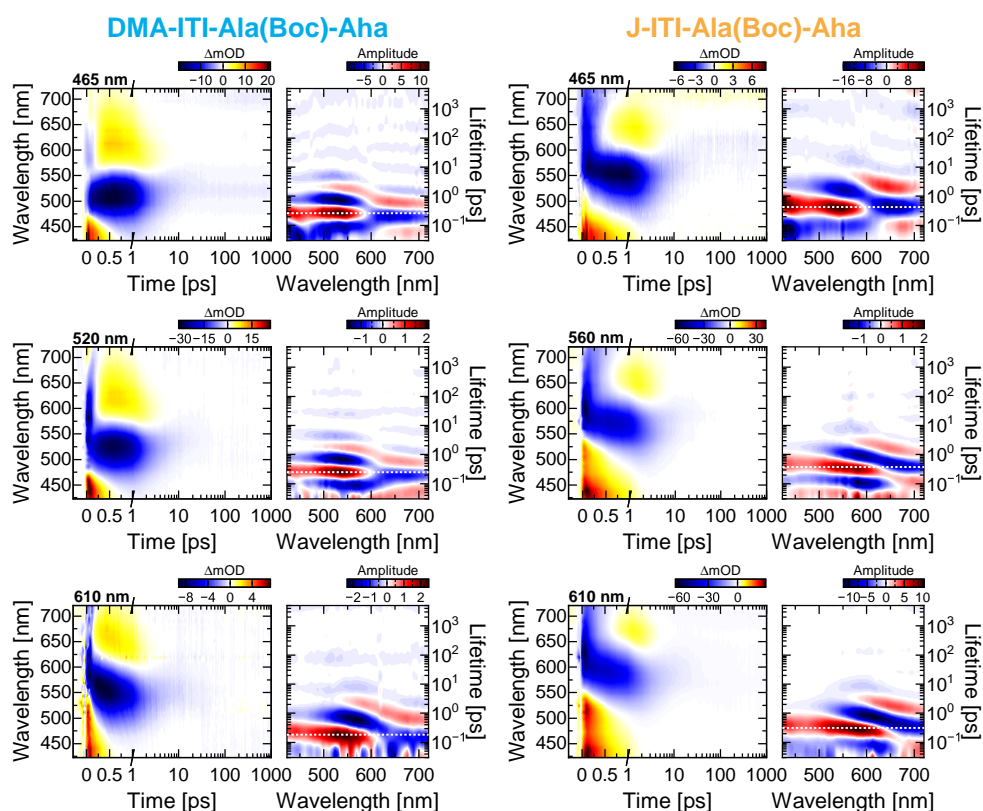


Figure 3.15 – Excitation wavelength dependence of the transient absorption data and the corresponding LDM obtained by LDA of the DMA-ITI-Ala(Boc)-Aha and J-ITI-Ala(Boc)-Aha dipeptides in MeOH. Both dipeptides were excited at 465 nm (top), their respective absorption maximum of 520 nm in the DMA-ITI-dipeptide, and 560 nm in the J-ITI-dipeptide (center), and 610 nm (bottom). The white dashed line in the LDMs indicates the decay of the ES.

ization with a high efficiency for hot GS formation instead, which is independent of the solvent. The extinction coefficients of the ITIs are especially remarkable compared to the standard VET donor azuleny alanine exhibiting an extinction coefficient of $\sim 600 \text{ M}^{-1} \text{ cm}^{-1}$ at the Vis maximum of 600 nm^[256] compared to coefficients $\sim 20000 \text{ M}^{-1} \text{ cm}^{-1}$ in the respective maxima of the investigated ITIs. These properties make them excellent donors for VET studies, especially in biological systems sensitive to UV light. IR studies by Carolin Feid have verified that VET from the ITI donors to the Aha acceptor is possible and yields higher signal amplitudes than the established azuleny alanine due to the higher extinction coefficients of the ITI compounds. The results presented in this work highlight the promising application potential of ITIs in the field of VET research and shed light onto the photodynamics of two novel ITI compounds and their related amino

3.2 Indigoid Photoswitches

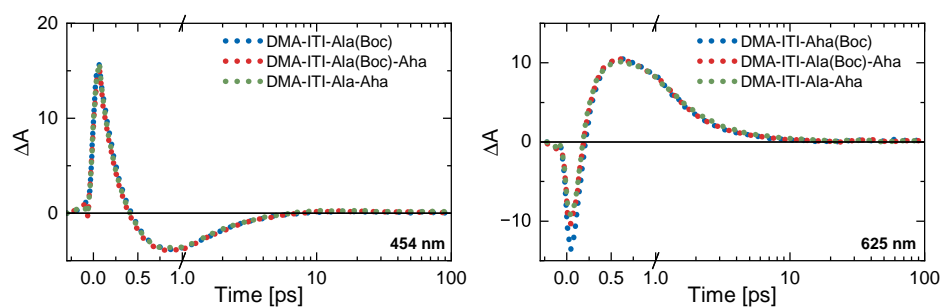


Figure 3.16 – Selected transients at 454 nm (left) and 625 nm (right) extracted from the transient absorption data of DMA-ITI-Ala(Boc) (blue), DMA-ITI-Ala(Boc)-Aha (red), and DMA-ITI-Ala-Aha (green) after excitation at 520 nm in MeOH scaled to similar intensities. The transients correspond to ESA and the hot GS respectively.

acid analogues.

3 Research Projects

Chapter 4: Conclusion

In this work, several aspects of photoisomerizations in phytochromes and indigoid photoswitches have been explored. Both fields of research share essential similarities like the guidance by steric interactions and the strong influence of polarity or ionic environment. However, there are factors that cannot be universally applied as the elaborate chromophore binding pocket with a complex hydrogen bonding network cannot be replicated for a single organic photoswitch in solution.

In the field of phytochromes, the relative positioning of knotless phytochromes within the super family of phytochromes among canonical group I phytochromes and CBCRs in terms of their photodynamics has been elaborated. It was shown that knotless phytochromes exhibit long-lived ES in their forward dynamics, which share a common kinetic pattern with both a group I and a group III phytochrome employing a similar P_r dark state. The kinetics corresponding to this pattern were unveiled based on ultrafast time-resolved investigations of the single GAF domain All2699g1 in comparison to the complete knotless phytochrome All2699g1g2 and the structurally similar knotless phytochrome *SynCph2* showing complex multiphasic ES kinetics in all cases. It was ruled out that GSH represents the origin of the multiphasic nature of the ES kinetics and the temporally distributed ES decay by performing time-resolved IR studies on *SynCph2* and kinetic modeling of All2699g1g2 containing a homogeneous P_r GS and All2699g1 exhibiting GSH. Instead, chromophore-driven initiation dynamics associated with spectral shifts at the edge between ESA and GSB/SE were described as the first part of the kinetic pattern, describing the kinetics in multiple phytochromes until ~30 ps. These dynamics trigger a reorganization of the protein matrix in vicinity of the chromophore, crucially involving the withdrawal of the conserved tyrosine 142 from the chromophore to allow the isomerization to proceed. The opening of this steric gate and the involvement of this residue was highlighted on the basis of single-point mutagenesis studies which also revealed that both the hydrogen bonding capability and the steric demand of this residue are critical for proper photochemistry in knotless phytochromes, in analogy to similar studies in other phytochromes. The derived mechanism represents a striking similarity between multiple PCB binding phytochromes that may be even further conserved among phytochromes in general, paving the way for future studies on this potentially conserved mechanism.

Concerning the light-driven back isomerization from the photoproduct state P_{fr} , a significant similarity between the kinetics in group I phytochromes and knotless phytochromes was revealed in this work. In both *SynCph2* and All2699g1g2, these dynamics

4 Conclusion

proceed ultrafast with ES lifetimes below 500 fs, followed by the evolution of multiple intermediates in the GS. A unique feature discovered here is the branching of the photoreaction towards GS recovery and productive photochemistry to the P_r state from a hot Lumi-F intermediate, assigned to the evolution of a single homogeneous population. In contrast, All2699g1 exhibits distinctive multiphasic kinetics with three overlapping ES decays most likely originating from a heterogeneous GS of All2699g1 in its P_{fr} state. These findings highlight the different role of GSH on the ultrafast dynamics depending on the equilibration time and thermal barriers between the different subpopulations.

In order to complete the description of the photodynamics of knotless phytochromes, the evolution of the primary photointermediate on the ms timescale was investigated for both the forward and reverse dynamics. The forward dynamics in particular exhibits a strong pH dependence, where the dynamics forming the photoproduct P_{fr} is accelerated at high pH, as a faster population dominates in this condition, while a slower one prevails at low pH. This complex equilibrium in the Meta- R_c intermediate was assigned to differently protonated hydrogen bonding networks and the two conserved histidines in the network in particular based on their matching pKa value.

Finally, the overall effect of the PHY domain on the photodynamics was identified in the All2699g1 and All2699g1g2 model systems. Through its tongue interaction in particular, the PHY domain controls the properties of the chromophore binding pocket, and hence, the immediate environment of the chromophore restricting the conformational space and reduces GSH in knotless phytochromes. These effects increase the efficiency of the photoreaction despite reduction of the available space and even accelerate both the ultrafast forward and reverse dynamics. In contrast, the ms-dynamics are decelerated in presence of the increased steric restrictions imposed by the PHY domain indicated by slower thermally driven progression of the photocycle on this timescale.

Overall, the findings presented here highlight the importance of the complex interplay between the chromophore and its protein environment. On top of that, a conserved kinetic footprint was identified in the forward dynamics of several PCB binding phytochromes, and first insight into the photodynamics of group II phytochromes was provided. Finally, the role of both GSH and the PHY domain on the ultrafast photoisomerizations of the bilin chromophore was elaborated.

In the field of indigoid photoswitches, the presence and relevance of the HT mechanism in a sterically crowded HTI and the influence of the solvent polarity on its photodynamics and efficiency was explored. The ES of the investigated HTI exhibits strong charge transfer character, and its minimum geometry in particular is strongly stabilized in polar solvents reflected in a large Stokes shift and an additional red-shift

upon increasing the solvent polarity. From this stabilized minimum, two conical intersections are accessible, one following an HT coordinate and the other one representing a quenching pathway for GS recovery. The height of the barriers towards these intersections strongly depends on solvent polarity, with the productive conical intersection being inaccessible in polar solvents. In contrast, the quenching conical intersection is stabilized in polar solvents and drains the ES within tens of ps rationalizing the unproductive photochemistry in polar environments. These findings highlight the relevance of steric restrictions and electronic setups to guide a photoreaction along specific pathways and provide further evidence for the existence and influence factors of the HT photoisomerization mechanism.

Finally, the results of the ITI project show that the photochemistry of photoactive double bonds can be harvested for promising applications, even when there is only one thermally stable isomerization state. As the *Z/E* isomerization of the C=N double bond forms a significantly less stable *E* intermediate due to facilitated inversion at the nitrogen atom, ITIs show fundamentally different photochemistry than the related HTIs, recovering the GS predominantly by dissipating vibrational energy. This energy release was shown to be independent of the modification of the photoswitch to an amino acid or dipeptide, the solvent polarity, and the excitation wavelength making ITIs auspicious candidates for applications as vibrational energy injectors for VET studies. While the amount of released energy may differ slightly depending on the conditions, the overall mechanism and dynamics are maintained, which stands in stark contrast to the observations in the HTI project. Overall, the promising potential of ITIs as vibrational energy donors for VET studies based on their photophysical properties was highlighted in this work. The results showcase the versatility of the photochemistry based on photoisomerizations and the importance of considering a multitude of influences when aiming towards controlling the photochemistry of respective photoswitchable compounds. It also illustrates the importance of further research on the guiding principles of photoisomerizations.

In conclusion, the control of photoisomerizations as the primary photoreaction by the properties and interactions of the immediate chromophore environment *e.g.*, the flexibility of the surrounding pocket, the electrostatic and hydrogen bonding interactions and GSH is elaborated in this dissertation on the example of phytochrome photoreceptors. Furthermore, the critical relevance of steric restrictions by substituents and the influence of solvent polarity as well as the chemical nature of the atoms participating in the double bond was demonstrated based on the investigations on indigoid photoswitches.

4 Conclusion

Chapter 5: Publications

The supporting information files of the respective publications are available online on the corresponding journal website under the DOI numbers.

(* - these authors contributed equally)

5.1 Declaration of Author Contributions

Reference [I]

The interplay between chromophore and protein determines the extended excited state dynamics in a single-domain phytochrome

C. Slavov*, T. Fischer*, A. Barnoy*, H. Shin*, A.G. Rao, C. Wiebeler, X. Zeng, Y. Sun, Q. Xu, A. Gutt, K.-H. Zhao, W. Gärtner, X. Yang, I. Schapiro, J. Wachtveitl

Proc. Natl. Acad. Sci. USA **2020**, 117(28), 16356-16362.

DOI: 10.1073/pnas.1921706117

- Execution and analysis of steady-state absorption, fluorescence and CD spectroscopic experiments, QY determination, femtosecond transient absorption experiments.
- Interpretation of the acquired data in collaboration with C. Slavov.
- Writing of the manuscript together with C. Slavov, W. Gärtner, X. Yang, I. Schapiro and J. Wachtveitl.

Reference [II]

Effect of the PHY Domain on the Photoisomerization Step of the Forward $P_r \rightarrow P_{fr}$ Conversion of a Knotless Phytochrome

T. Fischer, Q. Xu, K.-H. Zhao, W. Gärtner, C. Slavov, J. Wachtveitl

Chem. Eur. J. **2020**, 26, 17261-17266.

DOI: 10.1002/chem.202003138

- Execution and analysis of steady-state absorption, fluorescence and CD spectroscopic experiments, QY determination and femtosecond transient absorption experiments.

5 Publications

- Interpretation of the acquired data and creation of a mechanistic model in collaboration with C. Slavov.
- Preparation of the original draft with C. Slavov and refinement of the manuscript in coordination with all co-authors.
- Preparation of the table of contents figure.

Reference [III]

Ultrafast Photoconversion Dynamics of the Knotless Phytochrome *SynCph2*

T. Fischer, L.J.G.W. van Wilderen, P. Gnau, J. Bredenbeck, L.-O. Essen, J. Wachtveitl, C. Slavov

Int. J. Mol. Sci. **2021**, 22, 10690-10704.

DOI: 10.3390/ijms221910690

- Execution and analysis of Vis pump-probe femtosecond transient absorption experiments.
- Interpretation of the acquired data in collaboration with C. Slavov.
- Analysis and interpretation of Vis pump-IR probe femtosecond transient absorption experiments in collaboration with L.J.G.W. van Wilderen and C. Slavov.
- Preparation of the original draft with C. Slavov and refinement of the manuscript in coordination with all co-authors.

Reference [IV]

Influence of the PHY domain on the ms-photoconversion dynamics of a knotless phytochrome

T. Fischer, L. Köhler, T. Ott, C. Song, J. Wachtveitl, C. Slavov

Photochem. Photobiol. Sci. **2022**, 21, 1627-1636.

DOI: 10.1007/s43630-022-00245-9

- Execution and analysis of flash photolysis experiments of All2699g1 and All2699g1g2 at pH 8 and supervision of the performance of pH dependent flash photolysis experiments by T. Ott.
- Interpretation of the acquired data in collaboration with C. Slavov.

5.1 Declaration of Author Contributions

- Preparation of the original draft with C. Slavov and refinement of the manuscript in coordination with all co-authors.
- Preparation of the table of contents figure.

Reference [V]

Conserved Tyrosine in Phytochromes controls the Photodynamics through Steric Demand and Hydrogen Bonding Capabilities

T. Fischer, L. Köhler, P.D. Engel, C. Song, W. Gärtner, J. Wachtveitl, C. Slavov

Biochim. Biophys. Acta Bioenerg. **2023**.

DOI: 10.1016/j.bbabi.2023.148996

- Conceptualization of the project with C. Slavov and J. Wachtveitl.
- Execution of the transient absorption experiments of All2699g1 WT and mutants.
- Supervision of the absorption, fluorescence and CD measurements and the QY determination by P. D. Engel
- Analysis and interpretation of all data.
- Preparation of the original draft with C. Slavov and refinement of the manuscript in coordination with all co-authors.
- Preparation of the table of contents figure.

Reference [VI]

Mechanistic Elucidation of the Hula-Twist Photoreaction in Hemithioindigo

T. Fischer^{*}, J. Leitner^{*}, A. Gerwien^{*}, P. Mayer, H. Dube, A. Dreuw, J. Wachtveitl

J. Am. Chem. Soc. **2023**, 145, 14811-14822.

DOI: 10.1021/jacs.3c03536

- Execution, analysis and interpretation of all transient absorption experiments of HTI **1-A** and steady state absorption and fluorescence measurements of **1-A** in cyclohexane, benzene and MeCN.
- Preparation of the original draft together with J. Leitner and H. Dube and refinement of the manuscript in coordination with all co-authors.
- Preparation of the table of contents figure.

5.2 Reference [1]

Slavov et al., *Proc. Natl. Acad. Sci. USA* 2020, 117(28), 16356-16362

The interplay between chromophore and protein determines the extended excited state dynamics in a single-domain phytochrome

C. Slavov*, T. Fischer*, A. Barnoy*, H. Shin*, A.G. Rao, C. Wiebeler, X. Zeng, Y. Sun, Q. Xu, A. Gutt, K.-H. Zhao, W. Gärtner, X. Yang, I. Schapiro, J. Wachtveitl
Proc. Natl. Acad. Sci. USA 2020, 117(28), 16356-16362.

DOI: 10.1073/pnas.1921706117



The interplay between chromophore and protein determines the extended excited state dynamics in a single-domain phytochrome

Chavdar Slavov^{a,1,2}, Tobias Fischer^{a,1}, Avishai Barnoy^{b,1}, Heewhan Shin^{c,1}, Aditya G. Rao^b, Christian Wiebeler^{b,3}, Xiaoli Zeng^{c,4}, Yafang Sun^d, Qianzhao Xu^e, Alexander Gutt^f, Kai-Hong Zhao^d, Wolfgang Gärtner^{e,f}, Xiaojing Yang^{c,2}, Igor Schapiro^{b,2}, and Josef Wachtveitl^{a,2}

^aInstitute of Physical and Theoretical Chemistry, Goethe University, D-60438 Frankfurt, Germany; ^bFritz Haber Center for Molecular Dynamics Research at the Institute of Chemistry, The Hebrew University of Jerusalem, 9190401 Jerusalem, Israel; ^cDepartment of Chemistry, University of Illinois at Chicago, Chicago, IL 60607; ^dKey State Laboratory of Agriculture Microbiology, Huazhong Agriculture University, 430070 Wuhan, China; ^eInstitute of Analytical Chemistry, University of Leipzig, D-04103 Leipzig, Germany; and ^fMax Planck Institute for Chemical Energy Conversion, D-45470 Mülheim an der Ruhr, Germany

Edited by Arieh Warshel, University of Southern California, Los Angeles, CA, and approved May 7, 2020 (received for review December 10, 2019)

Phytochromes are a diverse family of bilin-binding photoreceptors that regulate a wide range of physiological processes. Their photochemical properties make them attractive for applications in optogenetics and superresolution microscopy. Phytochromes undergo reversible photoconversion triggered by the $Z \rightleftharpoons E$ photoisomerization about the double bond in the bilin chromophore. However, it is not fully understood at the molecular level how the protein framework facilitates the complex photoisomerization dynamics. We have studied a single-domain bilin-binding photoreceptor All2699g1 (*Nostoc* sp. PCC 7120) that exhibits photoconversion between the red light-absorbing (P_r) and far red-absorbing (P_{fr}) states just like canonical phytochromes. We present the crystal structure and examine the photoisomerization mechanism of the P_r form as well as the formation of the primary photoproduct Lumi-R using time-resolved spectroscopy and hybrid quantum mechanics/molecular mechanics simulations. We show that the unusually long excited state lifetime (broad lifetime distribution centered at ~ 300 picoseconds) is due to the interactions between the isomerizing pyrrole ring D and an adjacent conserved Tyr142. The decay kinetics shows a strongly distributed character which is imposed by the nonexponential protein dynamics. Our findings offer a mechanistic insight into how the quantum efficiency of the bilin photoisomerization is tuned by the protein environment, thereby providing a structural framework for engineering bilin-based optical agents for imaging and optogenetics applications.

knotless phytochrome | photoisomerization | ultrafast spectroscopy | X-ray structure | QM/MM

Phytochromes represent a large and versatile superfamily of photoreceptors identified in plants, fungi, and a wide range of bacteria (1, 2). These photoreceptors are involved in regulation of morphogenesis, photosynthesis, phototaxis, and physiological response to harmful radiation (1, 2). They have also been exploited as synthetic biology tools for optogenetics applications (3) and as fluorescence probes in biomedical imaging (4). Photoreceptors in the phytochrome superfamily bind tetrapyrrole chromophores (bilin) via a thioether linkage to a conserved cysteine residue and undergo reversible photoconversion with strong absorption shifts between a thermostable parental state and a photoproduct state. This photochromism arises from the $Z \rightleftharpoons E$ isomerization of the $C_{15} = C_{16}$ bond in the methine bridge connecting the pyrrole rings C and D of the bilin (*SI Appendix, Scheme S1*).

In canonical phytochromes (group I), the photosensory core module consists of the PAS-GAF-PHY array (1, 2). The PAS and GAF domains form a figure-of-eight knot, while a long extension (“tongue”) from the PHY domain interacts with the GAF domain-embedded chromophore (1, 2). In these

phytochromes all three N-terminal domains (PAS-GAF-PHY) are essential for the photoconversion (5–7). Some phytochromes, such as Cph2 from *Synechocystis* PCC6803 (8, 9), lack the PAS domain, and therefore they are classified as knotless phytochromes (group II) (1, 2). Phytochromes in those two groups photoconvert reversibly between the red light-absorbing (P_r) state and the far red-absorbing (P_{fr}) state (5). Most of them adopt P_r as the dark-adapted state and P_{fr} as the photoproduct state. In contrast, many cyanobacteriochromes (CBCRs) are modular components of larger signaling proteins that exhibit a tandem GAF domain structure, in which one or more GAF domains covalently incorporate bilin chromophores (10). CBCRs

Significance

Bilin-binding photoreceptors are light-signaling proteins that mediate various processes from photomorphogenesis, phototaxis, chromatic acclimation, to photosynthesis. They are also promising tunable optical agents for use in optogenetics and superresolution microscopy. Using an integrated approach of crystallography, spectroscopy, and QM/MM calculations, this work examines the ultrafast dynamics of a photoactive single-domain phytochrome. Our work reveals in detail the critical role of the protein environment in defining the excited state lifetime and thereby the quantum efficiency of the bilin photoisomerization. This insight provides design principles for engineering of bilin-based photoreceptors for biotechnological and medical applications.

Author contributions: C.S., W.G., I.S., and J.W. designed research; C.S., T.F., A.B., H.S., A.G.R., C.W., X.Z., Y.S., Q.X., A.G., and K.-H.Z. performed research; C.S., T.F., A.B., H.S., A.G.R., C.W., A.G., X.Y., and I.S. analyzed data; and C.S., T.F., W.G., X.Y., I.S., and J.W. wrote the paper.

The authors declare no competing interest.

This article is a PNAS Direct Submission.

Published under the PNAS license.

Data deposition: The coordinates and structure factor amplitudes of the All2699g1-PEB and All2699g1-PCB structures have been deposited to the Protein Data Bank (<https://www.rcsb.org>) under accession numbers 6OZA and 6OZB, respectively.

¹C.S., T.F., A.B., and H.S. contributed equally to this work.

²To whom correspondence may be addressed. Email: chslavov@theochem.uni-frankfurt.de, xiaojing@uic.edu, igor.schapiro@mail.huji.ac.il, or wweitl@theochem.uni-frankfurt.de.

³Present addresses: Leibniz Institute of Surface Engineering, D-04318 Leipzig, Germany and Institute for Analytical Chemistry, University of Leipzig, D-04103 Leipzig, Germany.

⁴Present address: Institute of Hydrobiology, Chinese Academy of Sciences, 430072 Wuhan, China.

This article contains supporting information online at <https://www.pnas.org/lookup/suppl/doi:10.1073/pnas.1921706117/-DCSupplemental>.

First published June 26, 2020.

are characterized by wide spectral diversity with absorption maxima spreading over the near-ultraviolet, visible, and near-infrared (near-IR) spectral regions (11–15). Moreover, single GAF domains from CBCRs preserve their photoconversion capability. The compact size and diverse photochemistry make photoactive GAF domains attractive as optical probes in optogenetics applications and superresolution microscopy (4). However, to tailor such modular photoreceptors for specific applications, a better understanding of their photochemistry at the molecular level is needed.

The primary photoconversion kinetics varies significantly among phytochromes and CBCRs. In canonical phytochromes (e.g., PhyA, Cph1, Agp1), the forward ($P_r \rightarrow P_r^*$) photoisomerization commences with an ultrafast (subpicosecond [sub-ps]) departure of the excited bilin from the Franck-Condon (FC) region. This is followed by conformational dynamics (~ 2 - to 5-ps lifetimes) of the chromophore on the excited state (ES), involving the onset of ring D rotation. The process is completed (~ 30 - to 50-ps lifetimes) with the formation of the primary, redshifted intermediate (Lumi-R) after overcoming a barrier on the S_1 ES surface (16–22). Recent studies on photoisomerization in the P_r state of Cph1 suggested ground state (GS) heterogeneity with two different GS populations of the bilin (23): 1) a faster (~ 5 -ps lifetime) nonreactive population and 2) a slower (~ 30 - to 50-ps lifetime), reactive population with a pretwisted ring D geometry (22, 24). In contrast, results from two-dimensional spectroscopy support a homogeneous model (25). In some bacteriophytochromes (e.g., RpBphP3,

DrBph) including bathy phytochromes (Agp2, PaBphP), longer ES lifetimes (100–300 ps) were attributed to ES proton transfer (ESPT) and reorganization of the hydrogen-bonding network of the chromophore (26–30). Compared to canonical phytochromes, the early ES dynamics of the P_r state in CBCRs is generally slowed down, extending to hundreds of picoseconds (31–34). It was proposed that a GS heterogeneity is responsible for different P_r^* reactive and nonreactive populations (31–33). Alternatively, the P_r^* decay was described by a single very broad lifetime distribution at ~ 400 ps (34).

In this work, we present the crystal structure of a photoactive single GAF domain obtained from a knotless phytochrome in the P_r state and investigate the primary forward photoconversion ($P_r \rightarrow \text{Lumi-R}$) dynamics using ultrafast spectroscopy and hybrid QM/MM simulations. This single-domain phytochrome system offers a unique link between the CBCR and phytochrome subfamilies, allowing us to study how the photoisomerization dynamics is modulated by the protein environment. Our results provide a mechanistic framework for engineering phytochrome photoreceptors for biotechnological applications.

Results and Discussion

Crystal Structure of All2699g1 Reveals a Single-Domain Phytochrome Photoreceptor. All2699 from *Nostoc* sp. PCC7120 consists of three tandem GAF domains at the N terminus followed by a histidine kinase (*SI Appendix, Fig. S1A*). The first bilin-binding

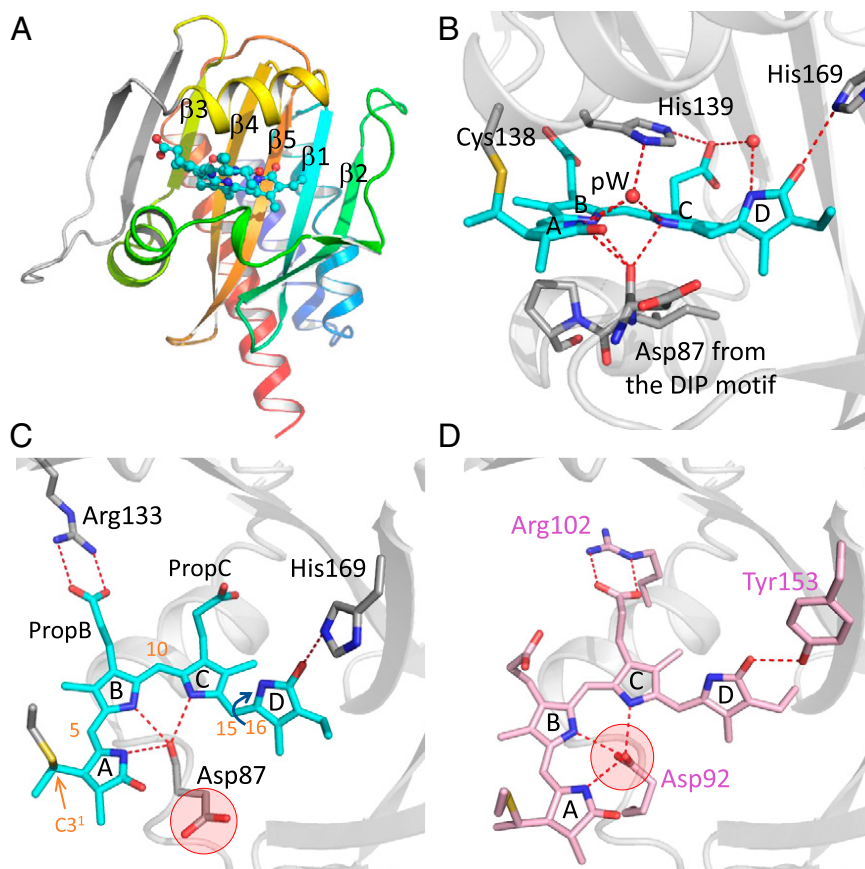


Fig. 1. Crystal structure of All2699g1. (A) Ribbon representation of the structure highlights the conserved GAF core domain shown in rainbow colors from the N (blue) to C terminus (red) except for the two extra β -strands (gray). (B) All2699g1 shows the transfacial Asp87O-pW-His139N ϵ coordination highly conserved among phytochromes. Red dashed lines mark the hydrogen bonds and ionic interactions between the bilin chromophore and the protein moiety. (C and D) Side-by-side comparison between All2699g1 (in gray and cyan) (C) and a representative CBCR AnPixJ (PDB ID/3WZ2) (in gray and pink) (D). Red shaded circles mark the acidic side chain of the highly conserved Asp, which points away from the chromophore in All2699g1 while forming hydrogen bonds with the pyrrole nitrogen atoms in AnPixJ.

GAF domain of All2699, denoted All2699g1, binds phycocyanobilin (PCB) and photoconverts reversibly between the P_r (λ_{max} : 637 nm) and P_{fr} (λ_{max} : 689 nm) states (35). We have determined the crystal structure of All2699g1 (PDB ID 6OZA) using the molecular replacement method (SI Appendix, Methods and Table S1). Although All2699g1 was first categorized as a CBCR due to its ability to undergo full $P_r \rightleftharpoons P_{fr}$ photoconversion in a single bilin-binding GAF domain (35, 36), All2699g1 exhibits all of the structural elements characteristic of a phytochrome, specifically the presence of a pyrrole water and hydrogen bonding of the pyrrole nitrogen atoms to the backbone carbonyl of the conserved Asp counterion (Fig. 1). In addition, All2699g1 features two extra β -strands to the central 2–1–5–4–3 β -sheet in the GAF core, while a much shorter linker is found in CBCRs (Fig. 1A and SI Appendix, Fig. S2B). This region topologically corresponds to a large loop insertion found in canonical phytochromes where the figure-of-eight knot structure between the PAS and GAF domains is formed (SI Appendix, Fig. S2). Further evidence is provided by sequence alignment (SI Appendix, Fig. S5) and a homology model (36) that features a tongue-like extension from the second GAF domain of All2699, similar to the PHY domain in phytochromes.

The P_r state of the All2699g1-PCB crystal was confirmed by the crystal color and single-crystal absorption spectrum (for comparison, see Fig. 2B and SI Appendix, Fig. S1D). The simulated annealing omit map shows a ZZZssa chromophore covalently attached to Cys138 via a thioether linkage at the C_3^1 position (Fig. 1 and SI Appendix, Scheme S1) in an R configuration (SI Appendix, Fig. S3). At the β -face (i.e., below the rings B–C coplane) of the bilin, All2699g1 features the DIP motif (residues 87–89, SI Appendix, Fig. S5) which is highly conserved among phytochromes (Fig. 1B and C and SI Appendix, Fig. S6A). Specifically, the main chain carbonyl of Asp87 forms hydrogen bonds with the pyrrole nitrogen atoms of rings A/B/C. This disposition contrasts with those found in CBCRs where the acidic side chain of Asp mediates hydrogen bonds with the pyrrole nitrogens (SI Appendix, Fig. S6B). Furthermore, All2699g1 features a highly conserved His139 at the α -face (i.e., above the rings B–C coplane), which interacts with the pyrrole rings via a pyrrole water molecule, denoted pW. Such *trans*-facial coordination, i.e., Asp87O–pW–His139N ϵ , is characteristic for all phytochromes from plant, cyanobacteria, and nonphotosynthetic bacteria (Fig. 1B). Additional similarities are found near the propionate groups, where the ring B propionate forms salt bridges with Arg133, while the ring C propionate adopts a recoiled conformation forming hydrogen bonds with His139 and a water molecule that bridges to ring D (Fig. 1B and C and SI Appendix, Fig. S6A). In contrast, the ring B propionate recoils in CBCRs while an extended ring C propionate interacts with a conserved Arg residue (corresponding to Arg102 in AnPixJ) from the GAF- β 3 strand (Fig. 1D and SI Appendix, Fig. S6B). Based on these crystallography data and structural comparisons, we categorize All2699 as a knotless phytochrome. Therefore, All2699g1 represents a phytochrome-like single-domain photoreceptor that is distinct from CBCRs.

Photochromism of the Red-/Far Red-Absorbing All2699g1. In both solution and crystals, the dark-adapted P_r state of All2699g1 has an absorption maximum at 637 nm (Q band) and a fluorescence maximum at 666 nm independent of the excitation wavelength (Fig. 2B and SI Appendix, Fig. S1C and D) (35). The photo-product P_{fr} state shows an absorption maximum at 689 nm, and its fluorescence is not detectable in steady state experiments, possibly due to a very short lifetime of the P_{fr}^* state. Under steady state irradiation (590 nm), the extent of $P_r \rightarrow P_{fr}$ conversion is $\sim 65\%$, limited by a significant spectral overlap between the two forms. The photoisomerization efficiencies of both

the forward ($P_r \rightarrow P_{fr}$) and the reverse ($P_{fr} \rightarrow P_r$) reactions were determined to be $\sim 8\%$ (SI Appendix, Methods).

We computed the absorption spectrum of the P_r state of All2699g1 (Fig. 2B) by performing QM/MM calculations with a molecular dynamics (MD) sampling protocol (SI Appendix, Methods) based on the crystal structure (Fig. 1). The lowest energy maxima at 654 nm (1.89 eV) and 367 nm (3.38 eV), corresponding to the Q and Soret bands, respectively, show a slight redshift (0.05 eV and 0.13 eV) compared to the experimental counterparts. The same simulation protocol also yielded good agreement between the calculated and observed absorption spectra for the P_r state of the CBCR Slr1393g3 (37).

Circular dichroism (CD) spectroscopy shows that the P_r and P_{fr} states of All2699g1 switch their sign of the CD signal corresponding to the Q band (35). The P_r state shows a negative, while the P_{fr} state shows a positive CD signal above 500 nm (Fig. 2C). For bilin-binding proteins, the signs of the Soret and Q bands in the CD spectrum are indicative of the orientation of the peripheral rings A and D with respect to the coplane of rings B and C (38). The calculated CD spectrum in the P_r state (Fig. 2C) shows a negative sign of the Q band and a positive sign of the

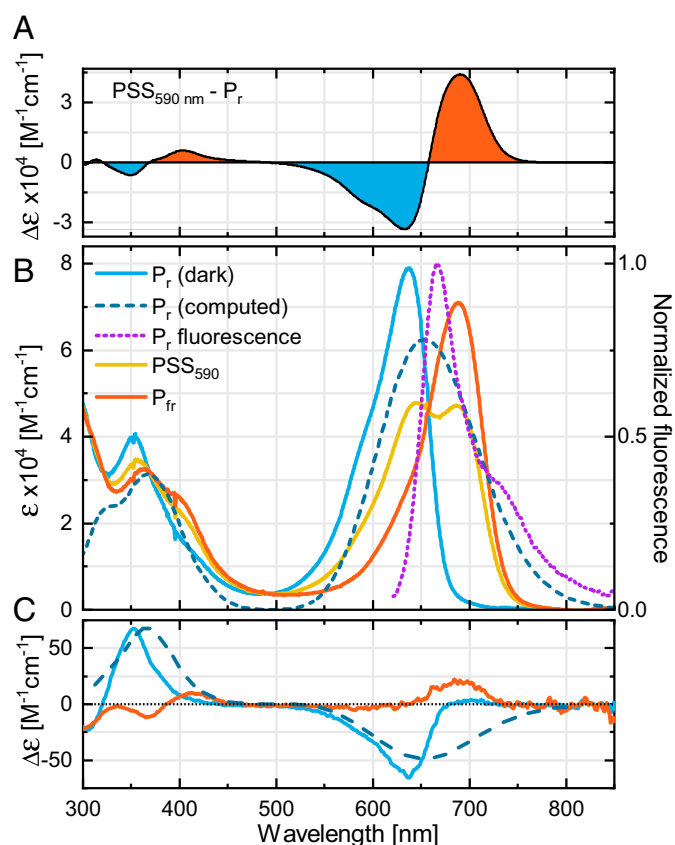


Fig. 2. Photoconversion of All2699g1 in solution. (A) Absorption difference spectrum for the $P_r \rightarrow P_{fr}$ photoconversion. (B) Steady state absorption and fluorescence spectra of the P_r and P_{fr} forms and computed P_r spectrum. The P_r spectrum was computed using the resolution-of-identity algebraic-diagrammatic construction through second order [(RI-ADC(2))]. The pure P_{fr} spectrum was obtained by subtraction of the pure P_r spectrum (35%, upper limit contribution) from the spectrum of the photostationary state at 590 nm irradiation (PSS₅₉₀) and then multiplying by a factor of 1.5 to yield the spectrum for a fully converted system. The extinction coefficient of P_r is $\sim 79,000 \text{ M}^{-1} \text{ cm}^{-1}$, as determined previously (35). The extinction coefficient of P_{fr} was determined to be $\sim 70,000 \text{ M}^{-1} \text{ cm}^{-1}$ from that of $^{152}\text{P}_r$, and using the isosbestic point at 660 nm. (C) CD spectra of the P_r and P_{fr} , and computed P_r CD spectrum [(RI-ADC(2))]. The CD spectrum of pure P_{fr} was obtained from the PSS₅₉₀ CD as described in B.

Soret band (intensity ratio of 4:3), which is in good agreement with the experimental CD data (intensity ratio 1:1). This result is consistent with the facial disposition of rings A and D in the All2699g1 structure (Fig. 1B). This behavior is analogous to what is observed for plant and cyanobacterial phytochromes, but differs from bacteriophytochromes and many CBCRs where the Q band in the CD spectrum does not switch its sign upon conversion into the photoproduct state and remains negative (31, 38–40).

Ultrafast Dynamics of P_r^* and the Formation of Lumi-R. To examine the early dynamics in the $P_r \rightarrow P_{fr}$ transformation, we conducted femtosecond (fs) transient absorption (TA) experiments (Fig. 3 and *SI Appendix*, Fig. S12; see *SI Appendix* for details on the setup). The results did not show any significant kinetic isotope effect (*SI Appendix*, Fig. S15) suggesting that ESPT, such as the one found in some bacteriophytochromes (26), is not involved in the P_r^* kinetics of All2699g1. Further, no major excitation wavelength dependence was detected which indicates homogeneity of the absorption band (*SI Appendix*, Figs. S12 and S13). Therefore, we focus on the 635-nm excitation dataset (Fig. 3). The TA data show a broad positive signal in the spectral range below ~ 575 nm due to ES absorption (ESA). Above 575 nm, the TA data are dominated by the negative signals of the GS bleach (GSB) and the stimulated emission (SE). These spectral features are very similar to those found in the forward dynamics of red/green CBCRs (31, 34). The ESA, GSB, and SE signals appear to decay simultaneously on the 0.1- to 1-ns timescale forming a very clear isosbestic point signature at ~ 575 nm (Fig. 3A and *SI Appendix*, Fig. S12). Their decay uncovers a new product absorption signal in the 650- to 700-nm range (Fig. 3A) that can be straightforwardly assigned to the primary photoproduct Lumi-R.

The lifetime-distribution analysis (see *SI Appendix* and ref. 41 for explanation of the methodology) reveals further details of the early ES dynamics of P_r (Fig. 3B and *SI Appendix*, Fig. S13). The pair of negative- and positive-amplitude lifetime distributions at ~ 100 fs in the 600- to 750-nm range account for the redshift of the SE signal, and thus we assign them to the departure of the ES wavepacket from the FC region. The next lifetime distributions (~ 500 fs and 2- to 8-ps ranges) are located in the overlap region between the steep edges of the GSB and the SE signals (600–700 nm), which makes them very sensitive to any spectral shift dynamics (Fig. 3B). In addition, on this scale we do not observe any substantial P_r^* decay (no lifetime distribution with positive amplitude in the ESA spectral range below 600 nm). Therefore, we attribute these features to dynamics on the ES potential energy surface (PES) possibly correlated with conformational changes in the chromophore.

The LDM is dominated by the lifetime distributions above 100 ps. The spectrally broad (< 600 nm) lifetime distribution with positive amplitude that stretches from ~ 50 ps to ~ 1.1 ns describes the P_r^* decay. Above 600 nm, a very pronounced, oblong, lifetime distribution with negative amplitude is present in the 650- to 700-nm region, which is overlaid onto a weaker but spectrally much broader distribution (600–750 nm). The two negative-amplitude lifetime distributions match the combined spectral shape of the GSB and the SE. Therefore, they can be assigned to the P_r^* decay and the associated recovery of the GSB. The more pronounced, negative-amplitude lifetime distribution (650–750 nm) also describes the rise of the primary photoproduct Lumi-R, which gives this component its stretched shape (in lifetime). The negative and the positive distributions > 1 ns represent the nondecaying (on this timescale) GSB and Lumi-R signals.

The near-IR TA data show a broad positive absorption difference signal that is not contaminated by GSB or SE (*SI Appendix*, Fig. S14A). The dynamics of this signal is described by three lifetime components (*SI Appendix*, Fig. S14B). The two short lifetimes

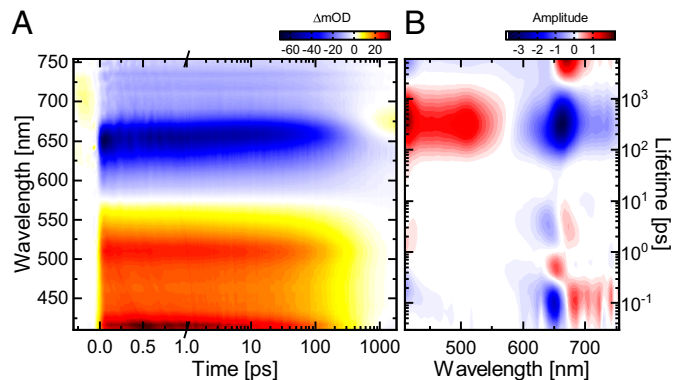


Fig. 3. Ultrafast ES dynamics of the P_r state. (A) TA data from the forward, $^{152}P_r \rightarrow ^{156}P_{fr}$, dynamics of All2699g1 after 635 nm excitation. (B) Corresponding lifetime density map (LDM) obtained from the lifetime-distribution analysis of the TA data.

(100 fs and 2.2 ps) have derivative-like decay-associated spectra (DAS) and thus, similarly to the shorter lifetime distributions from the data in the visible range (Fig. 3A and *SI Appendix*, Fig. S13), represent spectral shift dynamics. On the other hand, the long lifetime component (270 ps) has an all-positive DAS that matches very well the center of the visible ESA decay lifetime distribution (Fig. 3B) and can thus also be assigned to the P_r^* decay. Consequently, the near-IR data reaffirm that no significant P_r^* decay occurs on the sub-50-ps timescale.

Distributed Character of the P_r^* Photoisomerization Kinetics. We performed combined data analysis of the experimental datasets using a sequential model (Global Target Analysis) (41, 42). This analysis yields the so-called evolution-associated difference spectra (EADS). Five states were necessary to obtain a satisfactory fit quality (Fig. 4A). The first three EADS show identical amplitudes in the ESA spectral range, thereby confirming that no major ES decay occurs with lifetimes shorter than 50 ps (Fig. 4A). This result contrasts with studies on some canonical phytochromes (Cph1, PhyA, Agp1) and some CBCRs where shorter decay components have been associated with P_r^* relaxation (16–22, 31). However, in All2699g1 and in Slr1393g3 (34), the ~ 3 -ps component is due to a shift dynamics as evidenced by the EADS of S2 and S3 showing identical amplitude with shifted spectral position (Fig. 4A and *SI Appendix*, Fig. S16 B, D, and F). Similar picosecond components were also observed in some bacteriophytochromes (e.g., RpBphP3 and Agp2) (26, 29).

The first detectable decay of the EADS is associated with the 50-ps lifetime component, while the major decay occurs with the ~ 300 -ps component (*SI Appendix*, Fig. S16). The EADS of these two components are spectrally identical. Similar lifetime components have been observed in some CBCRs and assigned to reactive P_r^* populations in the frame of a heterogeneous kinetic model. However, the lifetime-distribution analysis (Fig. 3 and *SI Appendix*, Fig. S13), the identical EADS (*SI Appendix*, Fig. S16 B, D, and F), and the relatively small contribution of the 50-ps component (*SI Appendix*, Fig. S16 A, C, and E) raise the question whether the observed ES decay in All2699g1 has a distributed rather than distinctly heterogeneous kinetics. Therefore, we performed combined analysis with a four-state sequential model, where the third state was modeled with a stretched exponential decay (43, 44). This analysis yielded equally good results (Fig. 4B and *SI Appendix*, Figs. S17 and S18). Moreover, the use of a stretched exponential is in line with the remarkably broad lifetime distribution characterizing the P_r^* decay (Fig. 3B). Most importantly, the description of the extended ES kinetics by a broad lifetime distribution and a stretched exponential bring the

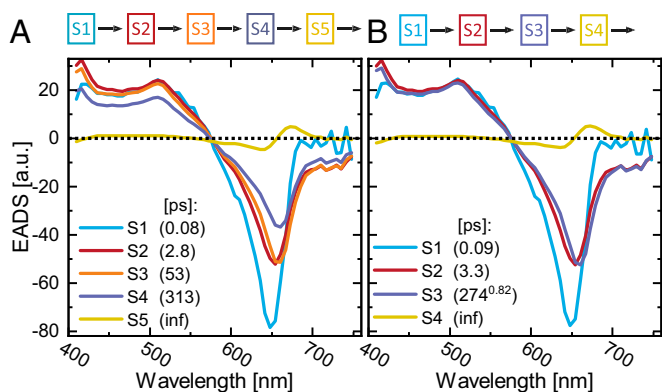


Fig. 4. Modeling of the ultrafast P_r kinetics. Analysis of the experimental data from the $P_r \rightarrow P_{fr}$ dynamics of All2699g1 after 635 nm excitation using a sequential kinetic scheme. The kinetic model fitting results in the so-called EADS. (A) EADS from fitting a sequential scheme with five states. (B) EADS from fitting a sequential scheme with four states, with the third state (S3) being modeled with a stretched exponent with $\beta = 0.82$.

question about the role of the dynamics of the protein environment in the observed kinetics.

The use of stretched exponentials as a phenomenological description of distributed kinetics occurring in constrained environments and during protein dynamics is well documented (45–47). The distributed kinetics can arise from static heterogeneity or from dynamic changes in the environment. However, the long ES lifetime of P_r , which indicates the presence of a significant energetic barrier on the ES PES, rather suggests that the observed distributed relaxation kinetics is associated with dynamic reorganization of the protein. Therefore, based on this association, we propose a mechanistic picture for the steps involved in the P_r^* photoisomerization. In essence, after the initial FC relaxation (~ 100 fs), the excited bilin undergoes conformational changes, which are reflected in the 2- to 5-ps minor spectral shift dynamics. These conformational changes of the chromophore trigger larger-scale protein motions, involving the nearby amino acid residues. We suggest that these changes are necessary to accommodate the rotation of ring D. In effect, the excited chromophore can proceed along the isomerization reaction coordinate and reach a conical intersection with the GS. Under such conditions, the photoisomerization dynamics of the bilin is modulated by the protein dynamics, thereby exhibiting the observed distributed kinetics. This proposed mechanism not only explains the observed distributed kinetics in All2699g1 and in the CBCR Slr1393g3 (34), but also accounts for the relatively slow relaxation kinetics of the embedded chromophore as compared to isolated bilins (48–51) or bilins embedded in other phytochromes (e.g., PhyA, Cph1, Agp1) (16–20, 22). We note here that while GS heterogeneity possibly plays a role in the dynamics of CBCRs and phytochromes with sub-50-ps lifetime components [e.g., in some CBCRs (31) or Cph1 (22, 24)], this effect is diminished for systems with longer lifetime components, for which the protein dynamics takes a leading role in controlling the relaxation kinetics.

Mechanism of the Photoisomerization in P_r^* . To investigate the molecular mechanism of photoisomerization and the origin of the extended ES lifetime of the P_r state of All2699g1, we calculated a relaxed scan along the torsion of the $C_{15} = C_{16}$ bond of the PCB chromophore (Fig. 5A). The relaxed scan was started from the FC point in S_1 . The corresponding GS geometry is pretwisted around the $C_{15} = C_{16}$ double bond ($C_{14}-C_{15} =$

$C_{16}-C_{17}$ dihedral angle of -166°), in line with the crystal structure (Fig. 1B) and the CD spectrum (Fig. 2C) of the P_r state. There are two possible directions of rotation for ring D, clockwise and counterclockwise. During the rotation in both senses the $C_{14}-C_{15}$ bond is shortened and the $C_{15} = C_{16}$ bond is elongated (Fig. 5B). Such changes in the bond lengths, which are well known from retinal proteins (52), are due to a change of the electronic structure in the ES. However, in contrast to the inversion of single and double bond lengths observed in protonated retinal Schiff base, we find that the $C_{15} = C_{16}$ double bond of the PCB chromophore is shorter than the $C_{14}-C_{15}$ single bond during the rotation in both the clockwise and the counterclockwise direction. Inversion of the bond length alternation was achieved after $\sim 30^\circ$ of counterclockwise rotation (Fig. 5B). The clockwise rotation requires high distortion ($\sim 70^\circ$ from the FC point or $\sim 55^\circ$ from planarity) to reach bond lengths nearly equal to those in the case of the counterclockwise rotation. The counterclockwise rotation appears to be energetically more favorable with the ES energy exceeding that of the FC starting only at -135° of the torsion angle. In comparison, the clockwise rotation reaches this point already at 155° , which is much closer to a planar structure. However, in both directions of rotation there is an ES energy barrier that prevents the completion of the isomerization. To pass the barrier, a large rearrangement of the protein is required, which cannot be addressed by a relaxed scan. Nevertheless, we deduce that the counterclockwise rotation is favored due to the pretwist of ring D in the GS and a smaller barrier on the ES. The progress in rotation is associated with a decrease in the S_0-S_1 energy gap, but a crossing between the GS

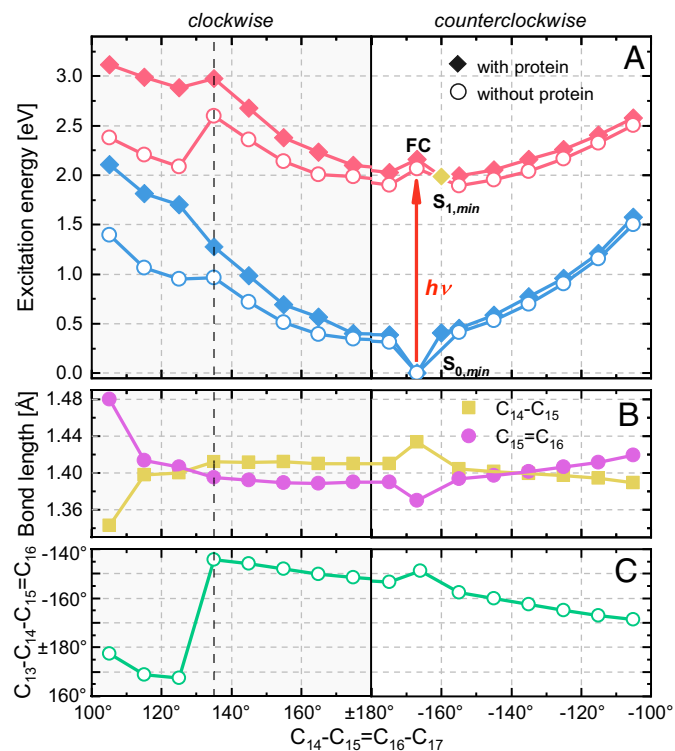


Fig. 5. ES relaxed scan. (A) Relaxed scan along the torsion angle $C_{14}-C_{15} = C_{16}-C_{17}$ of the PCB chromophore in the P_r form with and without the protein environment. (B) Change in the bond lengths of the methine bridge between rings C and D of the bilin. (C) Change in the dihedral angle of $C_{13}-C_{14}-C_{15} = C_{16}$ as a function of the change in the dihedral angle $C_{14}-C_{15} = C_{16}-C_{17}$. The red arrow indicates the $S_0 \rightarrow S_1$ excitation. The vertical dashed gray line indicates the last point before the hydrogen-bonding network with ring D disrupts.

and the ES was not encountered. This finding is in line with the 2- to 8-ps lifetime-distribution component found in our ultrafast data and assigned to conformational changes of the bilin (see above).

To estimate the role of the protein environment in the isomerization process we recalculated the optimized points of the scan without the protein (empty circles in Fig. 5A). These are single point calculations where the protein is removed but the chromophore remains in the conformation induced by the protein. The resulting energy profiles show that the ES barrier does not disappear after removal of the protein environment, which is in agreement with previous computational studies in the gas phase (51, 53). In the absence of the protein the isomerization path shows a slightly lower barrier in the counterclockwise sense with a nearly constant offset. In the clockwise direction, the barrier decreases with the progress in rotation. Overall, a larger lowering in the S_1 energy is observed for the clockwise rotation compared to the counterclockwise. Hence, there is a difference in the interaction of ring D with the protein for the two senses of rotation.

At the FC point, the $C_{15} = C_{16}$ double bond has a dihedral angle of -166° . This deviation from planarity is due to the involvement of ring D in a hydrogen-bonding network with surrounding amino acid residues and water molecules. The pyrrole nitrogen hydrogen-bonds to a water molecule (1.80 Å) forming a bridge to the Tyr142 side chain and the propionate at ring C, and the pyrrole carbonyl group hydrogen-bonds with the ϵ -NH group of His169 (2.01 Å) (Fig. 6). Clockwise rotation of ring D would disrupt this hydrogen-bonding network. To prevent rupture of this network, the methine single bond $C_{14}-C_{15}$ compensates the motion by rotating counterclockwise out of plane with respect to the B-C coplane (Fig. 5C and Movie S1). In addition, Tyr142, His169, and the bridging water molecule follow the displacement of ring D to maintain the hydrogen bonding. Nevertheless, further clockwise rotation of the double bond beyond 135° results in the breaking of the hydrogen-bonding network. As a consequence, the single bond planarizes (Fig. 6A and Movie S1) and changes by $\sim 50^\circ$ in the course of the relaxation.

In contrast, rotation in the counterclockwise direction retains the hydrogen-bonding network until the last obtained point of the relaxed scan (-105°). The rotation of ring D is accommodated by a minor displacement of the Tyr142 residue (the distance between the pyrrole moiety of ring D and ϵ -CH1 of Tyr142 decreases from 2.66 Å at the FC point to 2.21 Å at a torsion angle of -105°), while the His169 remains in its position (Movie S2). The torsion of the double bond occurs along with an out-of-plane movement of the methine bridge, where the bridge moves up relative to the B-C coplane. Further rotation beyond -105° is hindered by Tyr142 which would have to move away from the binding pocket (Fig. 6B and Movie S2). However, convergence of the relaxed scan beyond -105° was not obtained, suggesting that large motions of Tyr142 and other surrounding residues are required. This necessity of larger changes in the protein supports the model derived on the basis of the analysis of the time-resolved data and explains the long ES lifetime (~ 300 ps, broad lifetime distribution).

Conclusion

By combining X-ray crystallography, ultrafast spectroscopy, and QM/MM calculations, this work provides a mechanistic insight into the photoisomerization of the bilin chromophore in the single-domain phytochrome All2699g1. A coherent picture emerges, revealing that the early picosecond dynamics of P_r^* is associated with conformational changes in the chromophore, while the long ES lifetime is attributed to a large barrier for the ring D rotation in a confined environment. Relaxed scans along the rotational trajectory about the $C_{15} = C_{16}$ bond further show asymmetric barriers for the clockwise and counterclockwise

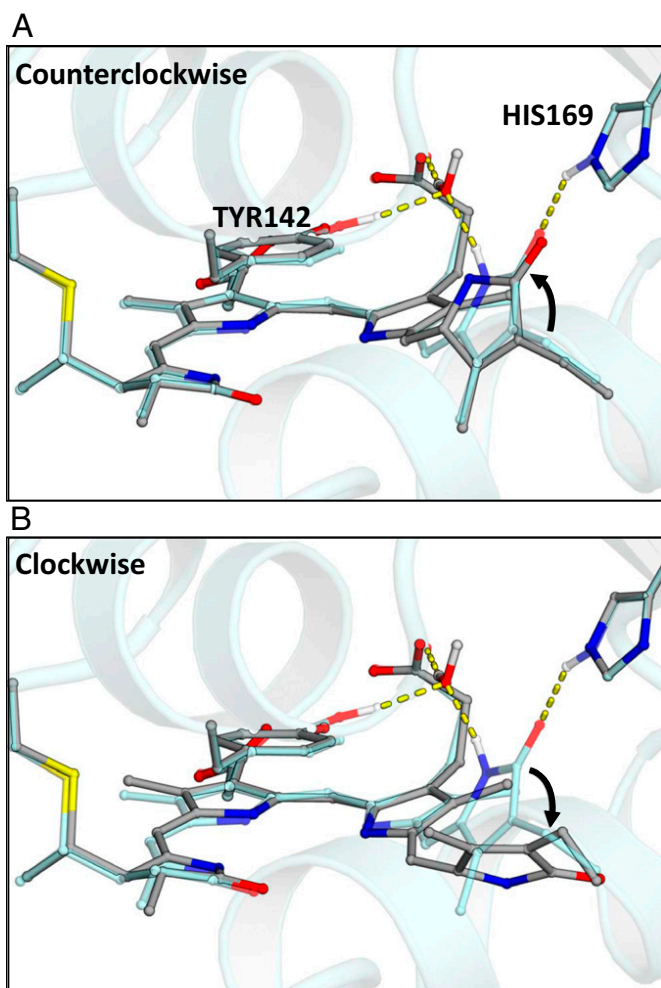


Fig. 6. Molecular rearrangements along the relaxed scan. Counterclockwise (A) and clockwise (B) rotation of ring D with the amino acid residues in the vicinity. The initial structure is shown in light blue, while the final point in each sense of direction is shown in gray (solid).

directions of rotation arising from specific protein–chromophore interactions. The heights of these energetic barriers imply that a significant reorganization of the chromophore environment is required for the isomerization to proceed. This protein reorganization and the associated reduction in the energetic barrier cannot occur spontaneously but are rather initiated by the early conformational changes in the excited chromophore as indicated by the 2- to 8-ps lifetime. Once activated, the protein moiety reorganizes to accommodate the rotation of ring D on the longer timescale as evidenced by the extended P_r^* lifetime (broad distribution around 300 ps). In other words, the photoisomerization dynamics is governed by an intricate interplay between the excited chromophore and the protein, in which the chromophore acts as a trigger, while the protein moiety controls the reaction dynamics. In effect, the protein dictates the lifetime and the ensuing quantum yield of photoisomerization. This mechanistic insight provides a framework for design and engineering of novel photoreceptors for optogenetics and fluorescence probes for superresolution microscopy.

Materials and Methods

Detailed description of the materials and methods is provided in the *SI Appendix*. This includes information on the sample preparation, crystallization, and structure determination; the spectroscopic and data analysis methods; as well as details on the QM/MM computations.

Data Availability. The coordinates and structure factor amplitudes of the All2699g1-PEB and All2699g1-PCB structures have been deposited to the Protein Data Bank (<https://www.rcsb.org>) under the accession numbers 6OZA and 6OZB, respectively.

Note Added in Proof.

After the acceptance of this work, a manuscript on the same protein was published (54).

ACKNOWLEDGMENTS. C.S. and J.W. acknowledge the Deutsche Forschungsgemeinschaft (WA 1850/4-2). A.G. and W.G. are grateful to the Max Planck

Society. K.-H.Z. acknowledges the National Natural Science Foundation of China (NSFC: 31861143029; 44131770822). A.B. is thankful to the Moscona Foundation and the Center for Nanoscience and Nanotechnology at the Hebrew University. I.S. acknowledges the European Research Council (Horizon 2020, Grant 678169 "PhotoMutant") and the SFB 1078 "Protonation Dynamics in Protein Function" (Mercator fellowship). C.W. is thankful for funding by the Deutsche Forschungsgemeinschaft (WI 4853/1-1 and WI 4853/2-1). We thank the Life Science Consortium Access Team staff at the advanced Photon Source for support in X-ray diffraction data collection. X.Y. acknowledges the NIH (NIH R01EY024363), Chicago Biomedical Consortium (CBC C-086), and the University of Illinois at Chicago. We thank J. Clark Lagarias for insightful discussions.

1. K. Anders, L.-O. Essen, The family of phytochrome-like photoreceptors: Diverse, complex and multi-colored, but very useful. *Curr. Opin. Struct. Biol.* **35**, 7–16 (2015).
2. N. C. Rockwell, J. C. Lagarias, Phytochrome diversification in cyanobacteria and eukaryotic algae. *Curr. Opin. Plant Biol.* **37**, 87–93 (2017).
3. C. Gasser *et al.*, Engineering of a red-light-activated human cAMP/cGMP-specific phosphodiesterase. *Proc. Natl. Acad. Sci. U.S.A.* **111**, 8803–8808 (2014).
4. O. S. Oliinyk, A. A. Shemetov, S. Pletnev, D. M. Shcherbakova, V. V. Verkhusha, Smallest near-infrared fluorescent protein evolved from cyanobacteriochrome as versatile tag for spectral multiplexing. *Nat. Commun.* **10**, 279 (2019).
5. N. C. Rockwell, Y.-S. Su, J. C. Lagarias, Phytochrome structure and signaling mechanisms. *Annu. Rev. Plant Biol.* **57**, 837–858 (2006).
6. N. C. Rockwell, J. C. Lagarias, The structure of phytochrome: A picture is worth a thousand spectra. *Plant Cell* **18**, 4–14 (2006).
7. A. Möglich, X. Yang, R. A. Ayers, K. Moffat, Structure and function of plant photoreceptors. *Annu. Rev. Plant Biol.* **61**, 21–47 (2010).
8. C.-M. Park *et al.*, A second photochromic bacteriophytochrome from *Synechocystis* sp. PCC 6803: Spectral analysis and down-regulation by light. *Biochemistry* **39**, 10840–10847 (2000).
9. B. L. Montgomery, J. C. Lagarias, Phytochrome ancestry: Sensors of bilins and light. *Trends Plant Sci.* **7**, 357–366 (2002).
10. M. Ikeuchi, T. Ishizuka, Cyanobacteriochromes: A new superfamily of tetrapyrrole-binding photoreceptors in cyanobacteria. *Photochem. Photobiol. Sci.* **7**, 1159–1167 (2008).
11. R. Narikawa, Y. Fukushima, T. Ishizuka, S. Itoh, M. Ikeuchi, A novel photoactive GAF domain of cyanobacteriochrome AnPixJ that shows reversible green/red photoconversion. *J. Mol. Biol.* **380**, 844–855 (2008).
12. N. C. Rockwell, S. S. Martin, A. G. Gulevich, J. C. Lagarias, Phycoviolobin formation and spectral tuning in the DXCF cyanobacteriochrome subfamily. *Biochemistry* **51**, 1449–1463 (2012).
13. N. C. Rockwell, S. S. Martin, K. Feoktistova, J. C. Lagarias, Diverse two-cysteine photocycles in phytochromes and cyanobacteriochromes. *Proc. Natl. Acad. Sci. U.S.A.* **108**, 11854–11859 (2011).
14. N. C. Rockwell, S. S. Martin, J. C. Lagarias, Identification of cyanobacteriochromes detecting far-red light. *Biochemistry* **55**, 3907–3919 (2016).
15. K. Fushimi, M. Ikeuchi, R. Narikawa, The expanded red/green cyanobacteriochrome lineage: An evolutionary hot spot. *Photochem. Photobiol.* **93**, 903–906 (2017).
16. M. Bischoff, G. Hermann, S. Rentsch, D. Strehlow, First steps in the phytochrome phototransformation: A comparative femtosecond study on the forward (Pr → Pfr) and back reaction (Pfr → Pr). *Biochemistry* **40**, 181–186 (2001).
17. C. Schumann, R. Gross, N. Michael, T. Lamparter, R. Diller, Sub-picosecond mid-infrared spectroscopy of phytochrome Agp1 from *Agrobacterium tumefaciens*. *ChemPhysChem* **8**, 1657–1663 (2007).
18. M. G. Müller, I. Lindner, I. Martin, W. Gärtner, A. R. Holzwarth, Femtosecond kinetics of photoconversion of the higher plant photoreceptor phytochrome carrying native and modified chromophores. *Biophys. J.* **94**, 4370–4382 (2008).
19. J. Dasgupta, R. R. Frontiera, K. C. Taylor, J. C. Lagarias, R. A. Mathies, Ultrafast excited-state isomerization in phytochrome revealed by femtosecond stimulated Raman spectroscopy. *Proc. Natl. Acad. Sci. U.S.A.* **106**, 1784–1789 (2009).
20. Y. Yang *et al.*, Real-time tracking of phytochrome's orientational changes during Pr photoisomerization. *J. Am. Chem. Soc.* **134**, 1408–1411 (2012).
21. M. Linke *et al.*, Electronic transitions and heterogeneity of the bacteriophytochrome Pr absorption band: An angle balanced polarization resolved femtosecond VIS pump-IR probe study. *Biophys. J.* **105**, 1756–1766 (2013).
22. Y. Yang *et al.*, Active and silent chromophore isoforms for phytochrome Pr photoisomerization: An alternative evolutionary strategy to optimize photoreaction quantum yields. *Struct. Dyn.* **1**, 14701 (2014).
23. C. Song *et al.*, Two ground state isoforms and a chromophore D-ring photoflip triggering extensive intramolecular changes in a canonical phytochrome. *Proc. Natl. Acad. Sci. U.S.A.* **108**, 3842–3847 (2011).
24. P. W. Kim, N. C. Rockwell, S. S. Martin, J. C. Lagarias, D. S. Larsen, Dynamic inhomogeneity in the photodynamics of cyanobacterial phytochrome Cph1. *Biochemistry* **53**, 2818–2826 (2014).
25. L. A. Bizimana, J. Epstein, J. Brazdar, D. B. Turner, Conformational homogeneity in the P_r isomer of phytochrome Cph1. *J. Phys. Chem. B* **121**, 2622–2630 (2017).
26. K. C. Toh, E. A. Stojković, I. H. M. van Stokkum, K. Moffat, J. T. M. Kennis, Proton-transfer and hydrogen-bond interactions determine fluorescence quantum yield and photochemical efficiency of bacteriophytochrome. *Proc. Natl. Acad. Sci. U.S.A.* **107**, 9170–9175 (2010).
27. H. Lehtivuori *et al.*, Fluorescence properties of the chromophore-binding domain of bacteriophytochrome from *Deinococcus radiodurans*. *J. Phys. Chem. B* **117**, 11049–11057 (2013).
28. T. Mathes *et al.*, Femto- to microsecond photodynamics of an unusual bacteriophytochrome. *J. Phys. Chem. Lett.* **6**, 239–243 (2015).
29. P. Singer, S. Wörner, T. Lamparter, R. Diller, Spectroscopic investigation on the primary photoreaction of bathy phytochrome Agp2-Pr of *Agrobacterium fabrum*: Isomerization in a pH-dependent H-bond network. *ChemPhysChem* **17**, 1288–1297 (2016).
30. C. Wang *et al.*, Bacteriophytochrome photoisomerization proceeds homogeneously despite heterogeneity in ground state. *Biophys. J.* **111**, 2125–2134 (2016).
31. P. W. Kim *et al.*, Femtosecond photodynamics of the red/green cyanobacteriochrome NpR6012g4 from *Nostoc punctiforme*. 1. Forward dynamics. *Biochemistry* **51**, 608–618 (2012).
32. S. M. Gottlieb *et al.*, Primary photodynamics of the green/red-absorbing photoswitching regulator of the chromatic adaptation E domain from *Fremyella diplosiphon*. *Biochemistry* **52**, 8198–8208 (2013).
33. C.-W. Chang *et al.*, Reactive ground-state pathways are not ubiquitous in red/green cyanobacteriochromes. *J. Phys. Chem. B* **117**, 11229–11238 (2013).
34. C. Slavov, X. Xu, K. H. Zhao, W. Gärtner, J. Wachtveitl, Detailed insight into the ultrafast photoconversion of the cyanobacteriochrome Slr1393 from *Synechocystis* sp. *Biochim. Biophys. Acta* **1847**, 1335–1344 (2015).
35. Y. Chen *et al.*, Photophysical diversity of two novel cyanobacteriochromes with phycocyanobilin chromophores: Photochemistry and dark reversion kinetics. *FEBS J.* **279**, 40–54 (2012).
36. Q.-Z. Xu *et al.*, MAS NMR on a red/far-red photochromic cyanobacteriochrome All2699 from *Nostoc*. *Int. J. Mol. Sci.* **20**, 3656 (2019).
37. C. Wiebeler, A. G. Rao, W. Gärtner, I. Schapiro, The effective conjugation length is responsible for the red/green spectral tuning in the cyanobacteriochrome Slr1393g3. *Angew. Chem. Int. Ed. Engl.* **58**, 1934–1938 (2019).
38. N. C. Rockwell, L. Shang, S. S. Martin, J. C. Lagarias, Distinct classes of red/far-red photochemistry within the phytochrome superfamily. *Proc. Natl. Acad. Sci. U.S.A.* **106**, 6123–6127 (2009).
39. N. C. Rockwell *et al.*, A second conserved GAF domain cysteine is required for the blue/green photoreversibility of cyanobacteriochrome Tlr0924 from *Thermosynechococcus elongatus*. *Biochemistry* **47**, 7304–7316 (2008).
40. Y. Hirose *et al.*, Green/red cyanobacteriochromes regulate complementary chromatic acclimation via a photochromic photocycle. *Proc. Natl. Acad. Sci. U.S.A.* **110**, 4974–4979 (2013).
41. C. Slavov, H. Hartmann, J. Wachtveitl, Implementation and evaluation of data analysis strategies for time-resolved optical spectroscopy. *Anal. Chem.* **87**, 2328–2336 (2015).
42. I. H. M. van Stokkum, D. S. Larsen, R. van Grondelle, Global and target analysis of time-resolved spectra. *Biochim. Biophys. Acta* **1657**, 82–104 (2004).
43. R. Kohlrausch, Theorie des elektrischen Rückstandes in der Leidener Flasche. *Ann. Phys.* **167**, 179–214 (1854).
44. G. Williams, D. C. Watts, Non-symmetrical dielectric relaxation behaviour arising from a simple empirical decay function. *Trans. Faraday Soc.* **66**, 80–85 (1970).
45. H. Frauenfelder, S. G. Sligar, P. G. Wolynes, The energy landscapes and motions of proteins. *Science* **254**, 1598–1603 (1991).
46. H. Yang *et al.*, Protein conformational dynamics probed by single-molecule electron transfer. *Science* **302**, 262–266 (2003).
47. O. Flomenbom *et al.*, Stretched exponential decay and correlations in the catalytic activity of fluctuating single lipase molecules. *Proc. Natl. Acad. Sci. U.S.A.* **102**, 2368–2372 (2005).
48. M. Bischoff *et al.*, Excited-state processes in phycocyanobilin studied by femtosecond spectroscopy. *J. Phys. Chem. B* **104**, 1810–1816 (2000).
49. B. Dietzek *et al.*, The excited-state dynamics of phycocyanobilin in dependence on the excitation wavelength. *ChemPhysChem* **5**, 1171–1177 (2004).
50. P. Altoè *et al.*, Deciphering intrinsic deactivation/isomerization routes in a phytochrome chromophore model. *J. Phys. Chem. B* **113**, 15067–15073 (2009).
51. A. Strambi, B. Durbeej, Initial excited-state relaxation of the bilin chromophores of phytochromes: A computational study. *Photochem. Photobiol. Sci.* **10**, 569–579 (2011).
52. S. Gozem, H. L. Luk, I. Schapiro, M. Olivucci, Theory and simulation of the ultrafast double-bond isomerization of biological chromophores. *Chem. Rev.* **117**, 13502–13565 (2017).
53. B. Durbeej, On the primary event of phytochrome: Quantum chemical comparison of photoreactions at C4, C10 and C15. *Phys. Chem. Chem. Phys.* **11**, 1354–1361 (2009).
54. Q.-Z. Xu, L. Goett-Zink, W. Gärtner, K.-H. Zhao, T. Kottke, Tongue refolding in the knotless cyanobacterial phytochrome All2699. *Biochemistry* **59**, 2047–2054 (2020).

5.3 Reference [II]

Fischer et al., *Chem. Eur. J.* 2020, 26, 17261-17266

Effect of the PHY Domain on the Photoisomerization Step of the Forward $P_r \rightarrow P_{fr}$ Conversion of a Knotless Phytochrome

T. Fischer, Q. Xu, K.-H. Zhao, W. Gärtner, C. Slavov, J. Wachtveitl

Chem. Eur. J. 2020, 26, 17261-17266.

DOI: 10.1002/chem.202003138

Photochemistry

Special
CollectionEffect of the PHY Domain on the Photoisomerization Step of the Forward $P_r \rightarrow P_{fr}$ Conversion of a Knotless PhytochromeTobias Fischer,^[a] Qianzhao Xu,^[b] Kai-Hong Zhao,^[c] Wolfgang Gärtner,^[b] Chavdar Slavov,^{*,[a]} and Josef Wachtveitl^{*,[a]}

Abstract: Phytochrome photoreceptors operate via photoisomerization of a bound bilin chromophore. Their typical architecture consists of GAF, PAS and PHY domains. Knotless phytochromes lack the PAS domain, while retaining photoconversion abilities, with some being able to photoconvert with just the GAF domain. Therefore, we investigated the ultrafast photoisomerization of the P_r state of a knotless phytochrome to reveal the effect of the PHY domain and its “tongue” region on the transduction of the light signal. We show that the PHY domain does not affect the initial confor-

mational dynamics of the chromophore. However, it significantly accelerates the consecutively induced reorganizational dynamics of the protein, necessary for the progression of the photoisomerization. Consequently, the PHY domain keeps the bilin and its binding pocket in a more reactive conformation, which decreases the extent of protein reorganization required for the chromophore isomerization. Thereby, less energy is lost along nonproductive reaction pathways, resulting in increased efficiency.

Introduction

Phytochromes are bilin-binding photoreceptors that regulate various biologically relevant processes (e.g., photosynthesis, morphogenesis, phototaxis, and photoprotection).^[1,2] They function via a light-induced transformation between a thermostable parental state and a photoproduct state. The transformation is triggered by a $Z \rightleftharpoons E$ photoisomerization of the $C_{15}=C_{16}$ double bond and a subsequent rotation of the D-ring of the embedded bilin chromophore (Scheme 1).

Phytochromes consist of chromophore-binding GAF domains, PAS and PHY domains (Figure 1).^[1,2] The PHY domain

forms an antiparallel β -sheet (“tongue”) which interacts with the chromophore embedded in the GAF domain, and the PAS and the GAF domains form a figure-eight knot.^[1,2] A complete PAS-GAF-PHY array is required for photoconversion in canonical phytochromes (e.g., PhyA, Cph1, Agp1),^[3–5] while knotless phytochromes (e.g., Cph2)^[6,7] lack the PAS domain.^[1,2]

Interestingly, single GAF domains of cyanobacteriochromes (CBCRs)^[9] and some knotless phytochromes^[8,10] preserve their photoconversion capability, which makes them attractive for biotechnological applications.^[11,12] The parental and the photoproduct states of canonical and knotless phytochromes are red-light (P_r) and far-red-light (P_{fr}) absorbing, respectively.^[5] The photoisomerization reaction and the primary photoproduct (Lumi-R) formation in the forward ($P_r \rightarrow P_{fr}$) photoconversion of these phytochromes proceeds with a lifetime of tens^[13–20] to hundreds^[21–25] of picoseconds. Photoisomerization in other mo-

[a] T. Fischer, Dr. C. Slavov, Prof. J. Wachtveitl
Institute of Physical and Theoretical Chemistry
Goethe University Frankfurt am Main
Max-von-Laue Straße 7, 60438 Frankfurt (Germany)
E-mail: chslavov@theochem.uni-frankfurt.de
wweitl@theochem.uni-frankfurt.de

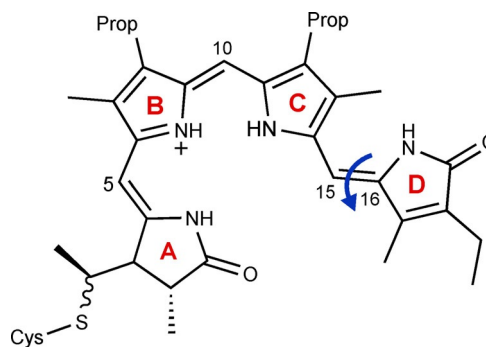
[b] Q. Xu, Prof. W. Gärtner
Institute of Analytical Chemistry
University of Leipzig
Linnéstr. 3, 04103 Leipzig (Germany)

[c] Prof. K.-H. Zhao
Key State Laboratory of Agriculture Microbiology
Huazhong Agriculture University Wuhan
Shizishan Street, Hongshan District, Wuhan 430070 (P. R. China)

Supporting information and the ORCID identification number(s) for the author(s) of this article can be found under:
<https://doi.org/10.1002/chem.202003138>.

© 2020 The Authors. Published by Wiley-VCH GmbH. This is an open access article under the terms of the Creative Commons Attribution License, which permits use, distribution and reproduction in any medium, provided the original work is properly cited.

This manuscript is part of an Indo-German special collection.



Scheme 1. Chemical structure of the phycocyanobilin (PCB) chromophore. The arrow indicates the photoisomerization of the $C_{15}=C_{16}$ double bond and the counterclockwise rotation of ring D.^[8]

lecular systems (e.g., azobenzenes^[26,27] and rhodopsins^[28–30]) is typically ultrafast, which raises the question about the origin of the remarkably slow photoisomerization rates in phytochromes. Recently, we could show that the excited state decay kinetics in a single GAF domain (g1) derived from a knotless phytochrome (All2699g1g2 from *Nostoc* sp. PCC7120) is strongly distributed, and we assigned this behavior to conformational changes in the bilin-binding pocket that control the photoisomerization of the chromophore.^[8] Here, we report on the forward ($P_r \rightarrow P_{fr}$) photoisomerization dynamics of the complete knotless phytochrome All2699g1g2 (structurally similar to Cph2).^[31,32] The homology model of All2699g1g2^[32] (Figure 1) shows that the “tongue” region of the g2 domain interacts with the chromophore bound to g1, just like the PHY domains of canonical phytochromes. Therefore, the g1g2 construct provides a unique opportunity to directly evaluate the role of the “tongue” and thereby of the protein matrix in the photoisomerization of phytochromes. Furthermore, our results give insight into the photochemistry of knotless phytochromes, as their ultrafast dynamics has not been studied previously.

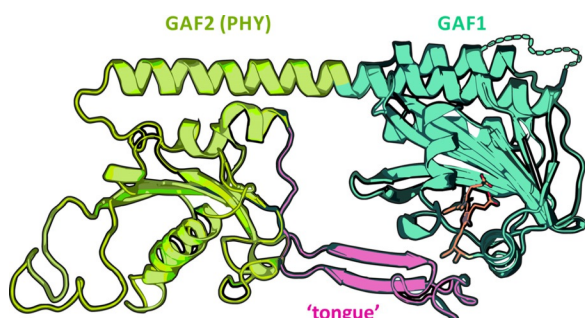


Figure 1. Schematic representation of the structural homology model of the P_r state of the All2699g1g2 construct.^[32] The structure of the GAF1 domain is based on the crystal structure of the sole GAF1 module (PDB ID 6OZA), while the GAF2 domain was modelled based on the crystal structure of the structurally similar Cph2^[32] (PDB ID 4BWI). The PCB chromophore (orange) embedded in the GAF1 domain (green) is in close interaction with a tongue-like protrusion (pink) from the GAF2 domain (yellow), which also shields the PCB from the solvent.

Results and Discussion

Photochromism of All2699g1g2

The P_r form of g1g2 has an absorption maximum at 637 nm, which is similar to that in g1,^[8,33] while the P_{fr} form is significantly red shifted (by 73 nm) to 710 nm (689 nm in g1,^[8,33] Figure 2A). Thus, the observed spectral shift of P_{fr} appears to be induced by interactions of the PCB chromophore with the “tongue” region of the g2 domain in g1g2.^[32,34] Interestingly, we find that the quantum yield (QY) of the $P_r \rightarrow P_{fr}$ transition is increased from ~8% to ~13% (a similar QY is observed in the related Cph2^[35]). Hence, it follows that while the presence of the g2 domain does not directly affect the spectral properties of the P_r form it does affect its photochemistry.

The circular dichroism (CD) spectra of both proteins (g1g2 vs. g1) have similar shape and undergo a sign inversion of the

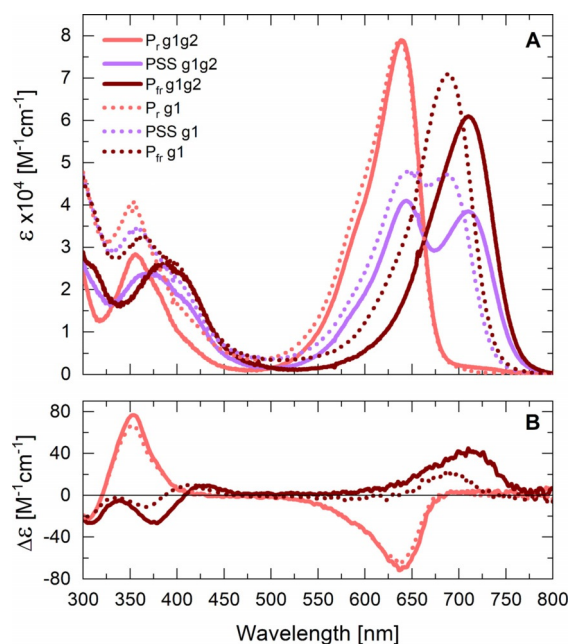


Figure 2. A) Stationary absorption spectra of the P_r and P_{fr} forms of g1g2 (solid lines) and g1^[8] (dotted lines). The pure P_{fr} spectrum was obtained by conservative subtraction of 38% of the pure P_r spectrum from the PSS spectrum, followed by multiplication with a factor of 1.61 to yield the spectrum for the fully converted system. The extinction coefficient of P_r is ~79 000 M⁻¹ cm⁻¹ (similar to g1^[33]), while the extinction coefficient of P_{fr} is ~61 000 M⁻¹ cm⁻¹. B) CD spectra of the P_r and P_{fr} states of g1g2 (solid lines) and g1^[8] (dotted lines). The pure P_{fr} CD spectrum was derived from the PSS CD as described in A).

Q-band CD signal upon $P_r \leftrightarrow P_{fr}$ switching (Figure 2B).^[8,33] The Q-band CD signals exhibit opposite signs for the different states, negative for P_r and positive for P_{fr} . The P_{fr} signal of g1g2 is further red shifted and shows an increased extinction coefficient.

The signs of these signals indicate the orientation of the peripheral rings A and D with respect to the co-plane of rings B and C.^[8,36] This overall orientation appears unaffected by the presence of the “tongue”, which is in line with the slight changes in the dihedral angle of rings A and D observed by NMR.^[32] In comparison, other phytochromes like Cph1^[37] and Cph2^[35] exhibit a similar sign change of the Q-band, while most CBCRs and bacteriophytochromes show no sign change upon switching.^[36,38–40]

Ultrafast dynamics of P_r^* and formation of Lumi-R

The role of the protein environment on the ultrafast photoisomerization dynamics of the PCB chromophore was investigated by femtosecond transient absorption (TA) measurements on g1g2 as compared with the single-domain g1.^[8] The TA data of g1g2 show three main features (Figure 3A): i) a broad positive signal below 575 nm which can be assigned to excited state absorption (ESA), ii) a negative signal above 575 nm due to ground state bleach (GSB) and stimulated emission (SE), and iii) a positive photoproduct absorption (PA) appearing at later times at 670 nm associated with the formation of the primary

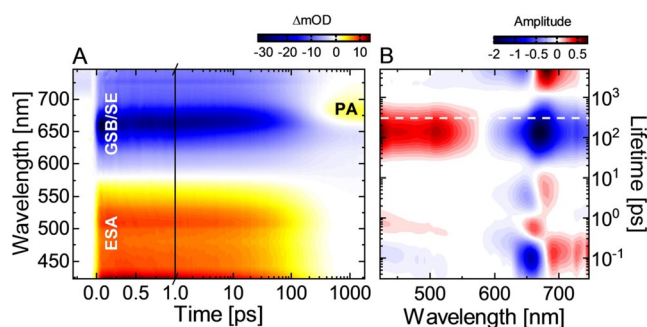


Figure 3. A) TA data from the forward, $P_r \rightarrow P_{fr}$ dynamics of g1g2 after 635 nm excitation. B) Corresponding lifetime density map (LDM) obtained from the lifetime distribution analysis of the TA data. The reading of the LDMs is as for a decay-associated spectrum from global lifetime analysis: i) positive (red) amplitudes account for decay of excited state and product absorption (ESA, PA) or rise of ground state bleach and stimulated emission (GSB and SE); ii) negative (blue) amplitudes account for rise of absorption (ESA, PA) or decay of GSB and SE. The white dashed line indicates the center of the lifetime distribution of the P_r^* decay of g1.^[8]

photoproduct (Lumi-R). The rise of the Lumi-R signal coincides with the decay of the ESA, GSB and SE on the timescale of 100 to 400 ps.

The lifetime distribution analysis of the experimental data (see Supporting Information and Ref. [41] for methodology) gives further insight into the early ES dynamics of P_r (Figure 3B). The positive- (> 690 nm) and the negative-amplitude (< 690 nm) distributions with a lifetime of 100 fs can be assigned to a red shift of the SE and therefore to the departure of the ES wavepacket from the Franck-Condon (FC) region. The lifetime distributions between 1 ps and 10 ps are located at the overlap of the steep edges of the GSB and SE, making this region very sensitive to slight spectral changes.

Because there is no substantial decay of the ES on this timescale, we assign these distributions to dynamics on the ES potential energy surface. Based on the spectral position of the ESA, GSB and SE signals, the broad lifetime distributions (stretching from 30 ps to 1 ns) with positive (420–575 nm) and negative (600–740 nm) amplitudes can be attributed to the simultaneous decay of these signals, and thus to the decay of P_r^* .

Compared with the positive-amplitude distribution representing the decay of the ESA signal, the negative-amplitude distribution, especially at 675 nm, appears stretched in lifetime. This can be explained by an overlaid additional negative-amplitude distribution describing the rise of the primary photoproduct Lumi-R commencing with the ES decay. On the scale longer than 1 ns, the negative and positive-amplitude lifetime distributions correspond to the non-decaying GSB and Lumi-R signals.

Distributed character of the P_r^* photoisomerization kinetics

Previously, we showed that the P_r^* decay kinetics in the single-domain g1 is described by broad and structureless lifetime distributions (see Figure S2B and discussion in^[8]) and can be modelled well using a stretched exponential function,^[42,43] thereby

avoiding introduction of unnecessary kinetic components. The lifetime distributions describing the P_r^* decay of g1g2 (from 30 ps to 1 ns in Figure 3B) are similarly broad and structureless, thus we followed our previous approach and analyzed the TA data using a four-state model in which one of the states is modelled by a stretched exponent (Figure 4). This model yields an excellent fit of the data without additional kinetic components (compare the case of the five-state model (Figure S5)). Stretched exponentials are used to model distributed kinetics occurring in constrained environments^[44–46] and here underline the importance of the protein in the isomerization kinetics of the PCB chromophore.

The evolutionary associated difference spectra (EADS) of the first three states (Figure 4B) clearly show that at early times no significant change in the amplitude of the ESA occurs, reaffirming the conclusion that the sub-20 ps dynamics of P_r^* is not associated with ES decay. Therefore, similarly to the single GAF domains All2699g1^[8] and Slr1393g3,^[47] the EADS of S2 and S3 of g1g2 show only a minor spectral shift in the GSB and SE overlap area, indicating that the ~3 ps component (Figure 4) is due to ES dynamics of the chromophore. The P_r^* relaxation and the associated PCB photoisomerization occur on the 100 ps timescale from state S3 after overcoming a barrier on the ES potential energy surface.^[8] This state is modeled as a stretched exponent, showing that the P_r^* decay of g1g2 follows a distributed type kinetics.

Recently, it was reported that in g1 and in g1g2 there exists a broad distribution of ground state subconformations that rapidly interconvert in solution.^[32,48] These subconformations could partially contribute to the observed distributed character of the P_r^* decay kinetics. However, their rapid interconversion denotes that they are separated by low energetic barriers, and thus cannot explain the large excited state barrier that determines the relatively slow P_r^* decay kinetics (100 ps timescale).^[8] Such a barrier can be overcome only via dynamic reorganization of the system, which in turn provides the dominant contribution to the distributed kinetics of P_r^* decay. Therefore, our

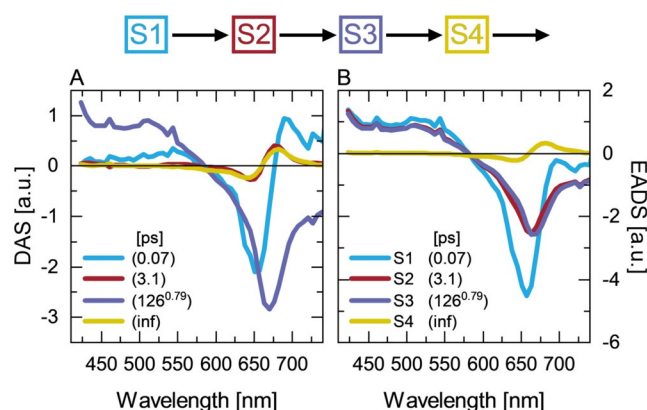


Figure 4. Analysis of the experimental data from the $P_r \rightarrow P_{fr}$ dynamics of g1g2 after 635 nm excitation using a sequential kinetic scheme. The kinetic model fitting results in the so-called evolution-associated difference spectra (EADS) and decay associated spectra (DAS): A) DAS and B) EADS from fitting a sequential scheme with four states, with the third state (S3) being modeled with a stretched exponent with $\beta = 0.79$.

results point to a more dynamic picture of the kinetics in knotless phytochromes. In contrast, distinct ES decay components, including such on the sub-50 ps timescale, have been reported for other phytochromes (e.g., Cph1, PhyA) and CBCRs, and were discussed in the framework of static ground state heterogeneity of the P_r form.^[15, 18, 20, 38, 49, 50]

Comparison of the ultrafast dynamics of g1g2 and g1: the effect of the g2 (PHY) domain

The comparison of the ultrafast dynamics of the g1g2 construct with the dynamics of the sole GAF domain g1^[8] provides a direct assessment of the effect of the g2 (PHY) domain. Strikingly, the early dynamics of both proteins are identical and even the coherent oscillations observed in the SE region up to ~2 ps (Figure 5B) match in frequency and phase.

The similarity in the g1g2 and g1 early kinetics is in agreement with the lack of an immediate effect of the PHY domain on the steady state properties of the P_r form (Figure 2), and thus further supports the conclusion that the primary dynamics are indeed due to conformational changes in the PCB chromophore. Only at later times, the P_r^* kinetics of g1g2 deviates from that of g1. Figure 5 clearly shows that in the g1g2 construct the ES decay and the formation of the primary photoproduct Lumi-R are accelerated relative to g1. This effect is also illustrated by the corresponding LDMs (Figure S2). Considering the time range up to 10 ps, the lifetime distribution structure remains the same for both proteins, while the later lifetime distributions (from 30 ps to 1 ns) describing the ES decay are shifted to shorter lifetimes in the case of g1g2 (for comparison, the center lifetime of the corresponding g1 distribution is indicated by a white dashed line in the LDM of g1g2, Figure 3B). Therefore, the direct comparison of the P_r^* kinetics

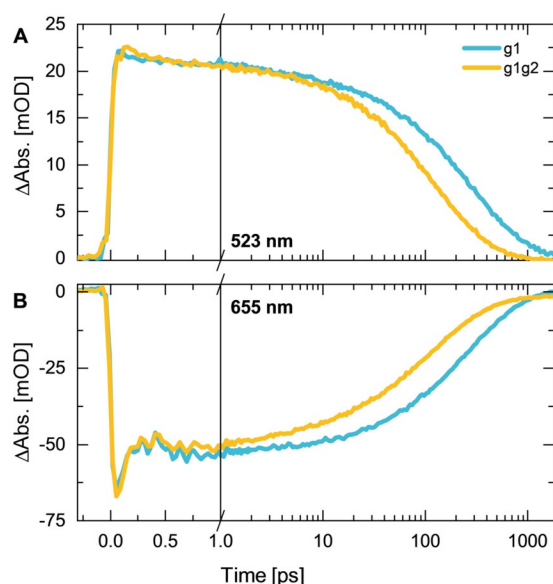


Figure 5. Comparison of the transient absorption decays of g1g2 (orange) and g1^[8] (cyan) at selected wavelengths within A) the ESA (523 nm), and B) the GSB/SE (655 nm) spectral regions. The transient decays were measured after 635 nm excitation of the P_r form.

of g1g2 and g1 reveals the impact of the g2 (PHY) domain and categorically demonstrates the critical role of the protein environment on the photoisomerization step of the PCB chromophore.

Mechanistic model

Based on the analysis presented above, we propose the following molecular picture for the photoisomerization dynamics of g1g2 (Figure 6). After excitation, the PCB chromophore leaves the FC region (~100 fs) and undergoes ES conformational dynamics on the early ps timescale (< 20 ps). This dynamics acts as a trigger for larger scale motions in the protein environment, which alleviates restrictions hindering further evolution on the ES (illustrated by the barrier on the ES potential energy surface). Interestingly, similar conclusions were derived in recent studies on related bacteriophytochromes^[51, 52] and a cyanobacteriochrome.^[53] As the protein reorganizes, the barrier on the ES decreases which allows P_r^* relaxation to proceed. This model explains the distributed character of the P_r^* decay kinetics as it is imposed by the conformational dynamics of the protein. Eventually, P_r^* decays (~130 ps) yielding the primary photoproduct Lumi-R.

Previously, we demonstrated that the ring D rotation of the PCB chromophore in g1 is hindered by a nearby Tyr residue (Tyr142).^[8] In the g1g2 (GAF-PHY) construct, the interaction of

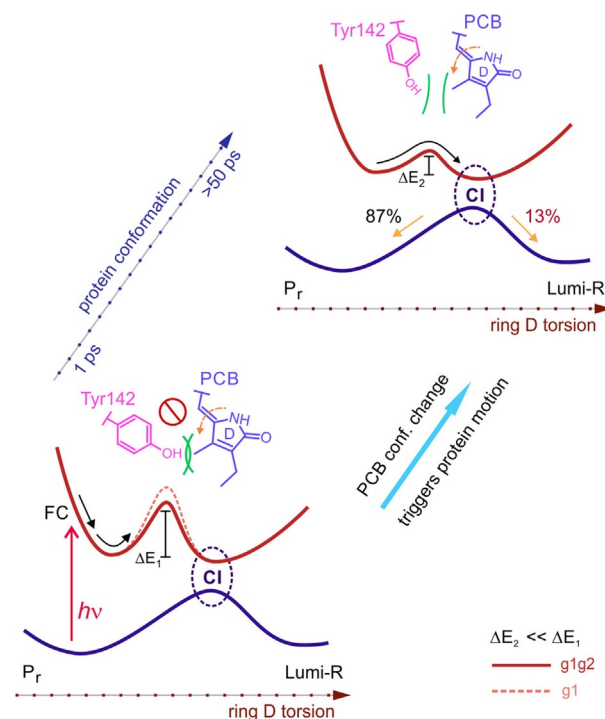


Figure 6. Main reaction coordinates determining the photoconversion kinetics in the P_r form of g1 and g1g2. For the larger construct, the interaction of the “tongue” region with the PCB chromophore results in a lower barrier (red, solid vs. orange, dashed lines). The early (< 10 ps) dynamics of the PCB chromophore triggers reorganizations in the protein binding pocket, which lower the energetic barrier at later timescales (ΔE_1 vs. ΔE_2) and unlock the photoisomerization.

the “tongue” region of the PHY domain with the chromophore-binding pocket in the GAF domain limits the conformational space of rings A and D of the PCB and drives the Tyr142 residue away from the chromophore as compared with g1.^[32] Therefore, it appears as if the “tongue” region keeps the chromophore and the binding pocket in a more reactive conformation. This decreases the extent of protein conformation reorganization required for facilitating the isomerization of the PCB chromophore and results in an accelerated P_r^* decay kinetics (Figure 5) and a more efficient $P_r \rightarrow P_{fr}$ photoconversion (less energy being lost on nonproductive degrees of freedom).

Conclusions

Our work provides direct evidence for the essential role of the protein environment in the control of the photoisomerization kinetics of the PCB chromophore and outlines a detailed mechanistic picture of the P_r^* photoisomerization dynamics in knotless phytochromes. From an evolutionary perspective, the PHY domain “tongue” represents a development in phytochromes that tunes the photoreception efficiency. This is a key design principle for the development of optimized photoreceptors for biotechnological applications.

Acknowledgements

C.S. and J.W. acknowledge Deutsche Forschungsgemeinschaft (WA 1850/4-2 and WA 1850/4-3). W.G. is grateful for the continuous support from the University of Leipzig. K.-H.Z. acknowledges the National Natural Science Foundation of China (NSFC: 31861143029; 31770822). Q.X. is recipient of a research-exchange grant from the Chinese Scholar Council (CSC). The authors thank Dr. Chen Song for providing the homology model of the All2699g1g2 construct. Open access funding enabled and organized by Projekt DEAL.

Conflict of interest

The authors declare no conflict of interest.

Keywords: bilin-binding photoreceptors · photochemistry · photoisomerization · time-resolved spectroscopy

- [1] K. Anders, L. O. Essen, *Curr. Opin. Struct. Biol.* **2015**, *35*, 7–16.
- [2] N. C. Rockwell, J. C. Lagarias, *Curr. Opin. Plant Biol.* **2017**, *37*, 87–93.
- [3] N. C. Rockwell, J. C. Lagarias, *Plant Cell* **2006**, *18*, 4–14.
- [4] A. Möglich, X. Yang, R. A. Ayers, K. Moffat, *Annu. Rev. Plant Biol.* **2010**, *61*, 21–47.
- [5] N. C. Rockwell, Y.-S. Su, J. C. Lagarias, *Annu. Rev. Plant Biol.* **2006**, *57*, 837–858.
- [6] C. M. Park, J. I. Kim, S. S. Yang, J. G. Kang, J. H. Kang, J. Y. Shim, Y. H. Chung, Y. M. Park, P. S. Song, *Biochemistry* **2000**, *39*, 10840–10847.
- [7] B. L. Montgomery, J. C. Lagarias, *Trends Plant Sci.* **2002**, *7*, 357–366.
- [8] C. Slavov, T. Fischer, A. Barnoy, H. Shin, A. G. Rao, C. Wiebeler, X. Zeng, Y. Sun, Q. Xu, A. Gutt, K. Zhao, W. Gärtner, X. Yang, I. Schapiro, J. Wachtveitl, *Proc. Natl. Acad. Sci. USA* **2020**, *117*, 16356–16362.
- [9] M. Ikeuchi, T. Ishizuka, *Photochem. Photobiol. Sci.* **2008**, *7*, 1159.

- [10] A. T. Ulijasz, G. Cornilescu, D. Von Stetten, S. Kaminski, M. A. Mroginski, J. Zhang, D. Bhaya, P. Hildebrandt, R. D. Vierstra, *J. Biol. Chem.* **2008**, *283*, 21251–21256.
- [11] C. Gasser, S. Taiber, C. M. Yeh, C. H. Wittig, P. Hegemann, S. Ryu, F. Wunder, A. Möglich, *Proc. Natl. Acad. Sci. USA* **2014**, *111*, 8803–8808.
- [12] O. S. Oliinyk, A. A. Shemetov, S. Pletnev, D. M. Shcherbakova, V. V. Verkhusha, *Nat. Commun.* **2019**, *10*, 1–13.
- [13] M. Bischoff, G. Hermann, S. Rentsch, D. Strehlow, *Biochemistry* **2001**, *40*, 181–186.
- [14] C. Schumann, R. Groß, N. Michael, T. Lamparter, R. Diller, *ChemPhysChem* **2007**, *8*, 1657–1663.
- [15] M. G. Müller, I. Lindner, I. Martin, W. Gärtner, A. R. Holzwarth, *Biophys. J.* **2008**, *94*, 4370–4382.
- [16] J. Dasgupta, R. R. Frontiera, K. C. Taylor, J. C. Lagarias, R. A. Mathies, *Proc. Natl. Acad. Sci. USA* **2009**, *106*, 1784–1789.
- [17] Y. Yang, M. Linke, T. von Haimberger, J. Hahn, R. Matute, L. González, P. Schmieder, K. Heyne, *J. Am. Chem. Soc.* **2012**, *134*, 1408–1411.
- [18] Y. Yang, M. Linke, T. von Haimberger, R. Matute, L. González, P. Schmieder, K. Heyne, *Struct. Dyn.* **2014**, *1*, 014701.
- [19] K. Heyne, J. Herbst, D. Stehlik, B. Esteban, T. Lamparter, J. Hughes, R. Diller, *Biophys. J.* **2002**, *82*, 1004–1016.
- [20] P. W. Kim, N. C. Rockwell, S. S. Martin, J. C. Lagarias, D. S. Larsen, *Biochemistry* **2014**, *53*, 2818–2826.
- [21] K. C. Toh, E. A. Stojković, I. H. M. M. Van Stokkum, K. Moffat, J. T. M. M. Kennis, *Proc. Natl. Acad. Sci. USA* **2010**, *107*, 9170–9175.
- [22] H. Lehtivuori, I. Rissanen, H. Takala, J. Bamford, N. V. Tkachenko, J. A. Ihalainen, *J. Phys. Chem. B* **2013**, *117*, 11049–11057.
- [23] T. Mathes, J. Ravensbergen, M. Klotz, T. Gleichmann, K. D. Gallagher, N. C. Woitowich, R. St. Peter, S. E. Kovaleva, E. A. Stojković, J. T. M. M. Kennis, *J. Phys. Chem. Lett.* **2015**, *6*, 239–243.
- [24] P. Singer, S. Wörner, T. Lamparter, R. Diller, *ChemPhysChem* **2016**, *17*, 1288–1297.
- [25] C. Wang, M. L. Flanagan, R. D. McGillicuddy, H. Zheng, A. R. Ginzburg, X. Yang, K. Moffat, G. S. Engel, *Biophys. J.* **2016**, *111*, 2125–2134.
- [26] T. Nägele, R. Hoche, W. Zinth, J. Wachtveitl, *Chem. Phys. Lett.* **1997**, *272*, 489–495.
- [27] A. Nenov, R. Borrego-Varillas, A. Oriana, L. Ganzer, F. Segatta, I. Conti, J. Segarra-Martí, J. Omachi, M. Dapor, S. Taioli, C. Manzoni, S. Mukamel, G. Cerullo, M. Garavelli, *J. Phys. Chem. Lett.* **2018**, *9*, 1534–1541.
- [28] R. Schoenlein, L. Peteanu, R. Mathies, C. Shank, *Science* **1991**, *254*, 412–415.
- [29] D. Polli, P. Altoè, O. Weingart, K. M. Spillane, C. Manzoni, D. Brida, G. Tomasello, G. Orlandi, P. Kukura, R. A. Mathies, M. Garavelli, G. Cerullo, *Nature* **2010**, *467*, 440–443.
- [30] C. Bamann, E. Bamberg, J. Wachtveitl, C. Glaubitz, *Biochim. Biophys. Acta Bioenerg.* **2014**, *1837*, 614–625.
- [31] K. Anders, G. Daminelli-Widany, M. A. Mroginski, D. Von Stetten, L. O. Essen, *J. Biol. Chem.* **2013**, *288*, 35714–35725.
- [32] Q.-Z. Xu, P. Bielytskyi, J. Otis, C. Lang, J. Hughes, K.-H. Zhao, A. Losi, W. Gärtner, C. Song, *Int. J. Mol. Sci.* **2019**, *20*, 3656.
- [33] Y. Chen, J. Zhang, J. Luo, J. M. Tu, X. L. Zeng, J. Xie, M. Zhou, J. Q. Zhao, H. Scheer, K. H. Zhao, *FEBS J.* **2012**, *279*, 40–54.
- [34] Q.-Z. Xu, L. Goett-Zink, W. Gärtner, K.-H. Zhao, T. Kottke, *Biochemistry* **2020**, *59*, 2047–2054.
- [35] K. Anders, D. Von Stetten, J. Mailliet, S. Kiontke, V. A. Sineshchekov, P. Hildebrandt, J. Hughes, L. O. Essen, *Photochem. Photobiol.* **2011**, *87*, 160–173.
- [36] N. C. Rockwell, L. Shang, S. S. Martin, J. C. Lagarias, *Proc. Natl. Acad. Sci. USA* **2009**, *106*, 6123–6127.
- [37] B. Borucki, H. Otto, G. Rottwinkel, J. Hughes, M. P. Heyn, T. Lamparter, *Biochemistry* **2003**, *42*, 13684–13697.
- [38] P. W. Kim, L. H. Freer, N. C. Rockwell, S. S. Martin, J. C. Lagarias, D. S. Larsen, *Biochemistry* **2012**, *51*, 608–618.
- [39] N. C. Rockwell, S. L. Njuguna, L. Roberts, E. Castillo, V. L. Parson, S. Dwojak, J. C. Lagarias, S. C. Spiller, *Biochemistry* **2008**, *47*, 7304–7316.
- [40] Y. Hirose, N. C. Rockwell, K. Nishiyama, R. Narikawa, Y. Ukaji, K. Inomata, J. C. Lagarias, M. Ikeuchi, *Proc. Natl. Acad. Sci. USA* **2013**, *110*, 4974–4979.
- [41] C. Slavov, H. Hartmann, J. Wachtveitl, *Anal. Chem.* **2015**, *87*, 2328–2336.
- [42] R. Kohlrausch, *Ann. Phys. Chem.* **1854**, *167*, 179–214.
- [43] G. Williams, D. C. Watts, *Trans. Faraday Soc.* **1970**, *66*, 80–85.

- [44] H. Frauenfelder, S. G. Sligar, P. G. Wolynes, *Science* **1991**, *254*, 1598–1603.
- [45] H. Yang, G. Luo, P. Karnchanaphanurach, T.-M. M. Louie, I. Rech, S. Cova, L. Xun, X. S. Xie, *Science* **2003**, *302*, 262–266.
- [46] O. Flomenbom, K. Velonia, D. Loos, S. Masuo, M. Cotlet, Y. Engelborghs, J. Hofkens, A. E. Rowan, R. J. M. Nolte, M. Der Van Auweraer, F. C. De Schryver, J. Klafter, *Proc. Natl. Acad. Sci. USA* **2005**, *102*, 2368–2372.
- [47] C. Slavov, X. Xu, K. H. Zhao, W. Gärtner, J. Wachtveitl, *Biochim. Biophys. Acta Bioenerg.* **2015**, *1847*, 1335–1344.
- [48] Y. Kim, Q.-Z. Xu, K.-H. Zhao, W. Gärtner, J. Matysik, C. Song, *J. Phys. Chem. B* **2020**, *124*, 7115–7127.
- [49] P. W. Kim, N. C. Rockwell, L. H. Freer, C.-W. W. Chang, S. S. Martin, J. C. Lagarias, D. S. Larsen, *J. Phys. Chem. Lett.* **2013**, *4*, 2605–2609.
- [50] J. S. Kirpich, L. T. Mix, S. S. Martin, N. C. Rockwell, J. C. Lagarias, D. S. Larsen, *J. Phys. Chem. Lett.* **2018**, *9*, 3454–3462.
- [51] E. Claesson, W. Y. Wahlgren, H. Takala, S. Pandey, L. Castillon, V. Kuznetsova, L. Henry, M. Panman, M. Carrillo, J. Kübel, R. Nanekar, L. Isaksson, A. Nimmrich, A. Cellini, D. Morozov, M. Maj, M. Kurttila, R. Bosman, E. Nango, R. Tanaka, T. Tanaka, L. Fangjia, S. Iwata, S. Owada, K. Moffat, G. Groenhof, E. A. Stojković, J. A. Ihalainen, M. Schmidt, S. Westenhoff, *eLife* **2020**, *9*, 1–18.
- [52] D. Wang, Y. Qin, M. Zhang, X. Li, L. Wang, X. Yang, D. Zhong, *J. Phys. Chem. Lett.* **2020**, *11*, 5913–5919.
- [53] D. Wang, X. Li, L. Wang, X. Yang, D. Zhong, *J. Phys. Chem. Lett.* **2020**, *11*, 8819–8824.

Manuscript received: July 1, 2020

Revised manuscript received: August 4, 2020

Accepted manuscript online: August 19, 2020

Version of record online: November 27, 2020

5.4 Reference [III]

Fischer et al., *Int. J. Mol. Sci.* **2021, **22**, 10690-10704**

Ultrafast Photoconversion Dynamics of the Knotless Phytochrome *SynCph2*

T. Fischer, L.J.G.W. van Wilderen, P. Gnau, J. Bredenbeck, L.-O. Essen, J. Wachtveitl, C. Slavov

Int. J. Mol. Sci. **2021**, *22*, 10690-10704.

DOI: 10.3390/ijms221910690



Article

Ultrafast Photoconversion Dynamics of the Knotless Phytochrome *SynCph2*

Tobias Fischer ¹, Luuk J. G. W. van Wilderen ², Petra Gnau ³, Jens Bredenbeck ², Lars-Oliver Essen ^{3,4}, Josef Wachtveitl ^{1,*} and Chavdar Slavov ^{1,*}

¹ Institute of Physical and Theoretical Chemistry, Goethe University Frankfurt am Main, Max-von-Laue Straße 7, 60438 Frankfurt, Germany; fischer@theochem.uni-frankfurt.de

² Institute of Biophysics, Goethe University Frankfurt am Main, Max-von-Laue Straße 1, 60438 Frankfurt, Germany; vanwilderen@biophysik.uni-frankfurt.de (L.J.G.W.v.W.); bredenbeck@biophysik.uni-frankfurt.de (J.B.)

³ Department of Chemistry, Philipps-Universität Marburg, Hans-Meerwein-Straße 4, 35032 Marburg, Germany; gnau@staff.uni-marburg.de (P.G.); essen@chemie.uni-marburg.de (L.-O.E.)

⁴ Center for Synthetic Microbiology, Philipps-Universität Marburg, Hans-Meerwein-Straße 6, 35032 Marburg, Germany

* Correspondence: wveitl@theochem.uni-frankfurt.de (J.W.); chslavov@theochem.uni-frankfurt.de (C.S.)

Abstract: The family of phytochrome photoreceptors contains proteins with different domain architectures and spectral properties. Knotless phytochromes are one of the three main subgroups classified by their distinct lack of the PAS domain in their photosensory core module, which is in contrast to the canonical PAS-GAF-PHY array. Despite intensive research on the ultrafast photodynamics of phytochromes, little is known about the primary kinetics in knotless phytochromes. Here, we present the ultrafast $P_r \rightleftharpoons P_{fr}$ photodynamics of *SynCph2*, the best-known knotless phytochrome. Our results show that the excited state lifetime of P_r^* (~200 ps) is similar to bacteriophytochromes, but much longer than in most canonical phytochromes. We assign the slow P_r^* kinetics to relaxation processes of the chromophore-binding pocket that controls the bilin chromophore's isomerization step. The P_{fr} photoconversion dynamics starts with a faster excited state relaxation than in canonical phytochromes, but, despite the differences in the respective domain architectures, proceeds via similar ground state intermediate steps up to Meta-F. Based on our observations, we propose that the kinetic features and overall dynamics of the ultrafast photoreaction are determined to a great extent by the geometrical context (i.e., available space and flexibility) within the binding pocket, while the general reaction steps following the photoexcitation are most likely conserved among the red/far-red phytochromes.

Keywords: tetrapyrrole-binding photoreceptors; phytochromes; photochemistry; photoisomerization; time-resolved spectroscopy



Citation: Fischer, T.; van Wilderen, L.J.G.W.; Gnau, P.; Bredenbeck, J.; Essen, L.-O.; Wachtveitl, J.; Slavov, C. Ultrafast Photoconversion Dynamics of the Knotless Phytochrome *SynCph2*. *Int. J. Mol. Sci.* **2021**, *22*, 10690. <https://doi.org/10.3390/ijms221910690>

Academic Editors: Dieter Leupold and Hugo Scheer

Received: 24 August 2021

Accepted: 28 September 2021

Published: 2 October 2021

Publisher's Note: MDPI stays neutral with regard to jurisdictional claims in published maps and institutional affiliations.



Copyright: © 2021 by the authors. Licensee MDPI, Basel, Switzerland. This article is an open access article distributed under the terms and conditions of the Creative Commons Attribution (CC BY) license (<https://creativecommons.org/licenses/by/4.0/>).

1. Introduction

Phytochromes represent a superfamily of photosensory receptors that regulate photomorphogenesis, photoprotection, phototaxis and other biologically relevant processes in a variety of organisms [1,2]. Their function is enabled by the $Z \leftrightarrow E$ photoisomerization of a bilin chromophore embedded in the protein scaffold. The isomerization is followed by several intermediate steps involving reorganization of the protein matrix. Ultimately, these transformations result in photoswitching between a dark-adapted and a light-adapted state. Recently, phytochromes have attracted considerable attention due to their application potential in optogenetics and as fluorescent probes in biomedical imaging [3–6].

Phytochromes can be classified into subgroups depending on the domain architecture of their photosensory core modules (PSM). In group I phytochromes, comprised of canonical plant and cyanobacterial phytochromes (e.g., PhyA and *SynCph1*) as well as

bacteriophytochromes (e.g., Agp1 and DrBphP), the PSM consists of a PAS-GAF-PHY array where all three domains are necessary for photoconversion [7–9]. The PAS domain forms a figure-of-eight knot structure with the chromophore-binding GAF domain, whereas the phytochrome specific PHY domain interacts with the chromophore in the GAF domain via a tongue like protrusion which stabilizes the chromophore and shields it from the solvent [1,2,10,11]. Group II phytochromes, also termed knotless or Cph2-like phytochromes, lack the PAS domain (Figure 1) and mostly consist of cyanobacterial phytochromes with Cph2 from *Synechocystis* sp. (*SynCph2*) being the most prominent member [1,2,12,13]. Lastly, Group III consists of cyanobacteriochromes (CBCRs) where single GAF domains form the PSM [14]. While the phytochromes of Group I and II photoconvert almost exclusively between P_r (red-absorbing) and P_{fr} (far-red-absorbing) states, CBCRs exhibit significant spectral diversity covering the near-UV/visible/near-IR spectral range [13,15–22].

The primary photoconversion dynamics of phytochromes is highly complex, often involving ground state heterogeneity and/or multiple excited state decay pathways. The P_r photoisomerization kinetics varies significantly amongst the phytochromes from Groups I and III. In canonical phytochromes (e.g., PhyA, *SynCph1*, Agp1), the kinetics can be described by three processes: (i) ultrafast departure from the Franck-Condon region (sub-ps lifetime); (ii) conformational dynamics of the chromophore with the onset of D-ring rotation (~2 to 5 ps lifetime) and (iii) formation of the primary red-shifted photointermediate Lumi-R (~30 to 50 ps lifetime) [23–29]. Alternatively, processes (ii) and (iii) have also been interpreted as kinetics of two different populations in the context of ground state heterogeneity [23,30,31]. In bacteriophytochromes, overall longer excited state lifetimes (~100 to 300 ps) have been observed which were linked to excited state proton transfer and reorganization of the hydrogen bonding network [32–37]. The excited state kinetics is prolonged to hundreds of picoseconds also in CBCRs. In some studies the kinetics was modelled by a series of non-reactive and reactive populations based on ground state heterogeneity [38–40], while other works hint towards active site relaxation and distributed type kinetics rather than distinct heterogeneity [41–43].

Presently, the primary photoisomerization in the reverse reaction ($P_{fr} \rightarrow P_r$) is exclusively studied in Group I phytochromes. It is relatively conserved amongst the different representatives of the group and occurs faster than the forward ($P_r \rightarrow P_{fr}$) reaction. Following the ultrafast departure from the FC-region (~100 fs), the primary photointermediate Lumi-F is formed on the sub-ps time scale (~500 to 700 fs lifetime) [27,28,44–48]. This intermediate evolves on the ps time scale via several relaxation steps resulting in a spectral blue shift [27,45,47]. In *SynCph1*, multiple excited state decays have been proposed and were linked to reactive and non-reactive chromophore conformations with different lifetimes [45,47]. Similar observations in the bacteriophytochromes PaBphP (bathy) and Agp1 were instead interpreted as branching on the excited state surface [48,49]. Such multiphasic kinetics was not reported in oatPhyA, where a single excited state decay was sufficient to describe the data [27].

In contrast, little is known about the ultrafast forward and reverse dynamics of Group II phytochromes. To date, only the forward photoisomerization direction of the knotless phytochrome All2699g1g2 has been examined [50], but no details on the reverse reaction are available. To shed light on the ultrafast primary photoreaction of knotless phytochromes, here we present both the ultrafast forward ($P_r \rightarrow P_{fr}$) and reverse ($P_{fr} \rightarrow P_r$) dynamics of the most prominent group member, *SynCph2*.

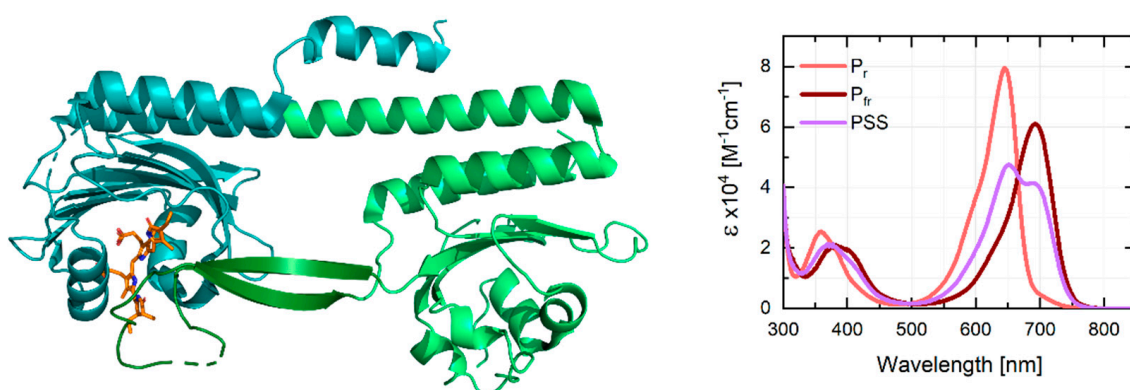


Figure 1. Left: Schematic representation of the structure of *SynCph2* (PDB ID: 4BWI) [51]. The phycocyanobilin (PCB) chromophore (orange) is embedded in the GAF domain (cyan) interacting with a tongue-like protrusion (dark green) of the PHY domain (light green). Right: Absorption spectra of *SynCph2* in the P_r (light red) and P_{fr} (dark red) state. To obtain the pure P_{fr} spectrum 36% of the pure P_r spectrum (factor determined by visual inspection of the resulting spectrum) was subtracted from the photostationary state (PSS) spectrum (purple), followed by multiplication with a factor of 1.56 to simulate full conversion to the P_{fr} state (as done previously [50]). Fluorescence spectra of the P_r state and a fluorescence quantum yield of 3.2% were reported previously while no fluorescence was observed for the P_{fr} state [13].

2. Results and Discussion

2.1. Ultrafast P_r^* Dynamics and Lumi-R Formation

The femtosecond transient absorption (TA) data show three major contributions (Figure 2A): (i) a broad positive signal below ~ 550 nm due to excited state absorption (ESA), (ii) a broad negative signal extending from 575 nm to 740 nm due to P_r ground state bleach (GSB) and stimulated emission (SE) and (iii) a positive signal (product absorption; PA) at 675 nm which is uncovered after the decay of SE and the partial recovery of the GSB and is accordingly assigned to the absorption of the primary photoproduct Lumi-R.

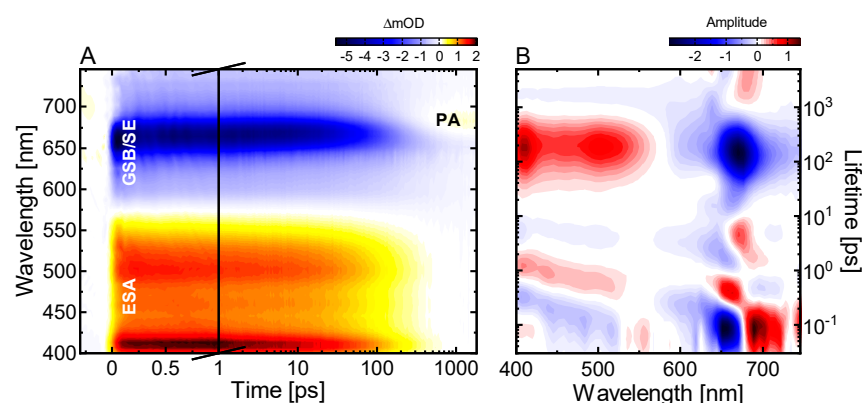


Figure 2. Ultrafast excited state dynamics of the P_r state in *SynCph2* investigated in the vis spectral range. (A) TA data of the $P_r \rightarrow P_{fr}$ dynamics after excitation at 640 nm. (B) Corresponding lifetime density map (LDM) obtained from the lifetime distribution analysis of the TA data displayed in (A). The GSB signal coincides with the ground state absorption spectrum in Figure 1.

We performed lifetime density analysis (LDA) (for details see Material and Methods or [52]) to reveal further features of the excited state dynamics (Figure 2B). The negative- and positive-amplitude lifetime distributions at ~ 100 fs from 600 nm to 675 nm and 675 nm to 740 nm respectively, represent the red shift of the SE signal and can be assigned to the departure from the FC-region. The following pairs of negative- and positive-amplitude distributions at ~ 0.6 ps and 2–8 ps show slight spectral changes at the edge of the GSB and SE signals. These can be ascribed to changes on the excited state surface related to conformational dynamics of the chromophore. The dominant feature of the lifetime density

maps (LDM) is located at ~ 200 ps with a positive-amplitude distribution in the range of the ESA signal (400–575 nm) and a negative-amplitude distribution in the GSB-SE range (600–740 nm) indicating the decay of the excited state, the recovery of the ground state and the formation of the primary photoproduct Lumi-R. The broadness of the lifetime distributions reflects the distributed type of the excited state decay kinetics as shown by the detailed analysis in our previous studies [50,53]. The final pair of lifetime distribution amplitudes at 3 ns represents the remaining GSB and Lumi-R absorption at 680 nm.

Additionally, we performed ultrafast vis pump-IR probe TA experiments covering two regions of interest comprising predominantly the C=O (1750–1670 cm^{-1}) and the C=C (1670–1550 cm^{-1}) vibrations of the bilin chromophore (Figure 3A). In the C=O region, we identify three major contributions: a negative signal at 1705 cm^{-1} , and two positive features at 1745–1715 cm^{-1} and 1682 cm^{-1} . Based on previous reports [23,29,54], we assign the 1705(-)/1682(+) signal pair to the GSB and ESA signals of the $\text{C}_{19}=\text{O}$ stretch vibration at ring-D, and the 1745–1715 cm^{-1} positive features to the $\text{C}_1=\text{O}$ stretch vibration at ring-A. The corresponding $\text{C}_1=\text{O}$ negative GSB signal is plausibly weaker and narrower than the positive ESA band, and thus is responsible for the dip in the 1745–1715 cm^{-1} band. The two prominent negative signals at 1596 and 1630 cm^{-1} and the minimum at 1665 cm^{-1} are related to C=C stretch vibrations of the chromophore. The comparison with previous studies on *SynCph1* and *oatPhyA* suggests that the 1630 cm^{-1} signal originates from the $\text{C}_{15}=\text{C}_{16}$ mode, while the 1596 cm^{-1} signal is either due to the $\text{C}_9=\text{C}_{10}$ mode or to a delocalized mode containing this vibration [23,54,55]. The positive signal at 1560 cm^{-1} , the maximum between the two negative signals at 1596 and 1630 cm^{-1} , and the positive signal at 1654 cm^{-1} represent the respective ESAs of these vibrations which are all short lived and downshifted due to a reduction of the bond order [54,56].

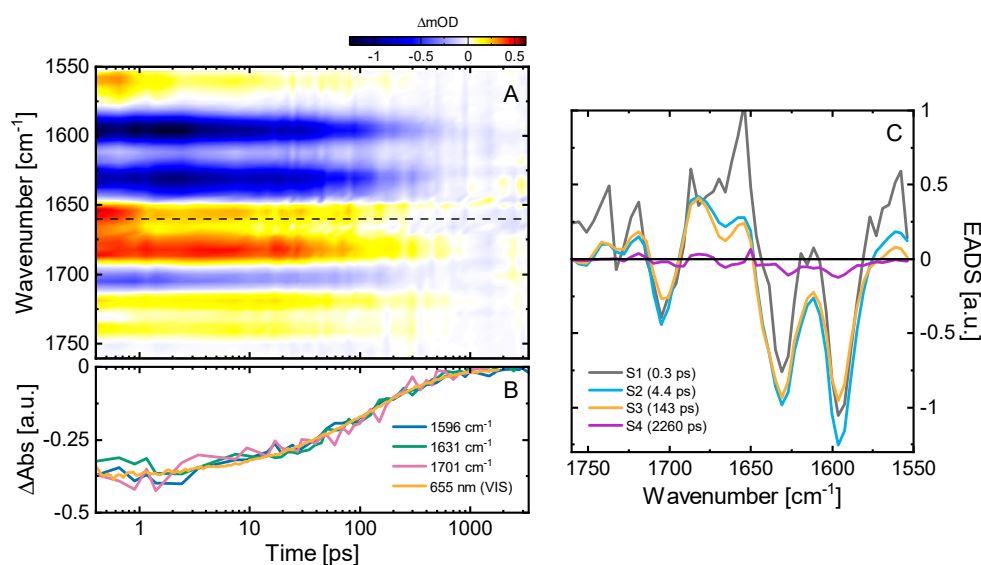


Figure 3. Ultrafast excited state dynamics of the P_r state in *SynCph2* investigated in the IR spectral range. (A) TA data of the $P_r \rightarrow P_{fr}$ dynamics after excitation at 640 nm. The signal sizes in the C=O region were multiplied by a factor of 2 to account for the lower excitation density used as compared to the data of the C=C region. The transition between these regions is indicated by the dashed black line. (B) Scaled transients at selected wavenumbers in comparison to a transient from the GSB of the corresponding vis pump-probe measurements (Figure 2A). (C) Evolution-associated difference spectra (EADS) obtained from a sequential model fit of the transient vis pump-IR probe data of the P_r dynamics.

Our global target analysis (for details see Material and Methods or [52,57,58]) of the IR TA data using a sequential model resulted in four kinetic components (Figure 3C). The first lifetime component (300 fs) is at the limit of our experimental time resolution, and while straightforward assignment is hard, it is plausibly related to early dynamics on the

excited state potential energy surface as indicated by the vis TA data (see above). The 4.4 ps lifetime describes a slight decrease of the GSB of the $C_9=C_{10}$ or delocalized mode, its corresponding ESA and the $C_{19}=O$ GSB, while most other signals remain unaffected. The lack of simultaneous decay of all ESA signatures indicates that this lifetime component is associated with excited state conformational changes within the chromophore. This result agrees well with the vis TA data and with our conclusion that (1) only excited state chromophore dynamics occurs on the sub-50 ps timescale and (2) that the P_r^* kinetics of knotless phytochromes does not involve an early excited state decay. Here, the excited state decay occurs with a 143 ps lifetime as designated by the disappearance of the excited state signatures in the evolution-associated difference spectra (EADS) going from S3 to S4 (Figure 3C). The 143 ps lifetime from the IR TA data (Figure 3A) matches the position of the broad lifetime distribution from the visible TA data (Figure 2B). This remarkable kinetic similarity between the UV/vis and the IR data of P_r^* , despite the use of D_2O buffer for the IR experiments, is also readily observed by direct comparison of the scaled GSB transient decays (Figure 3B). The final EADS corresponds to the IR difference spectrum of the primary photoproduct Lumi-R. The EADS shows remaining GSB signals in the $C=C$ region, while in the $C=O$ region the signals are smaller than what we can resolve at the experimental S/N ratio. The ratio of the GSB amplitudes of the EADSs of S2 and S4 indicates a quantum yield of $\sim 11\%$ for Lumi-R formation, which is in excellent agreement with the $\sim 12\%$ determined previously [13].

2.2. Conserved P_r Kinetics

LDMs can be viewed as a kinetic footprint of a given system. In this regard, we noticed that the LDMs describing the P_r kinetics in the single GAF domain All2699g1 of a knotless phytochrome [53], the complete PSMs of two knotless phytochromes (All2699g1g2 [50], *SynCph2* (Figure 2)) and the red-green CBCR Slr1393g3 [41] show a striking level of similarity despite the structural and evolutionary differences of these phytochromes (Figure 4). The LDMs, as well as the transient data, of all these longer-lived phytochromes exhibit a common pattern of a sub-200 fs departure from the FC-region followed by two pairs of lifetime distributions at ~ 0.6 ps and 2–8 ps and a distributed excited state decay in the hundreds of ps time range. Notably, of this pattern only the distributed decay varies in lifetime and is shifted independently of the first two features. Overall, the similarity hints towards a common mechanistic basis for the P_r kinetics in these phytochromes.

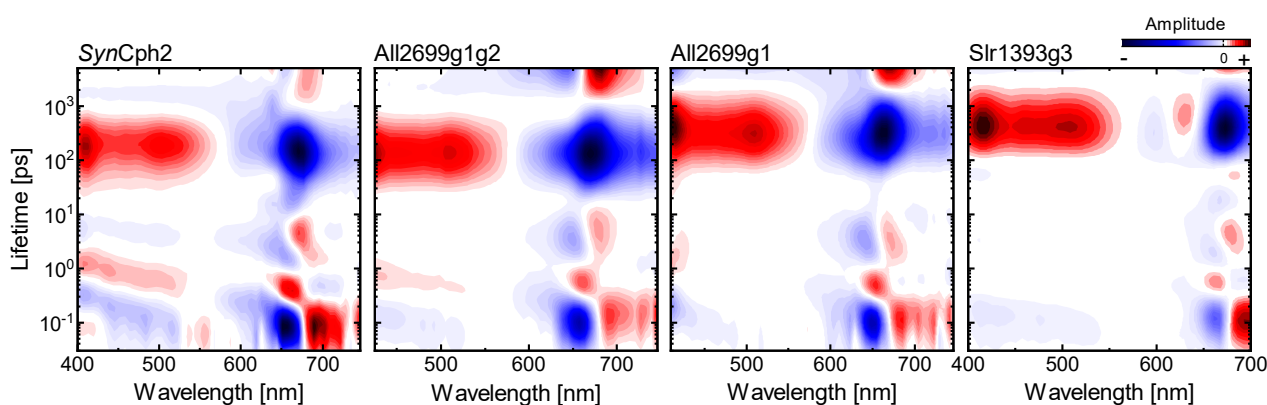


Figure 4. Lifetime density maps of several longer lived phytochromes with similar kinetics including *SynCph2*, All2699g1g2 [50], All2699g1 [53] and Slr1393g3 [41,59].

As we previously concluded based on theoretical calculations and kinetic modelling, the origin of the distributed kinetics can be linked to the protein environment being the controlling factor for excited state relaxation [50,53]. As it constrains the bilin chromophore, and in particular the D-ring, the reaction cannot proceed unless the protein binding pocket undergoes rearrangements that facilitate chromophore isomerization. Potentially, the

pocket rearrangements occurring on timescales >50 ps are triggered by slight conformational changes within the chromophore as deduced by the 0.6 ps and 2–8 ps lifetimes from both the vis and IR TA data. Our conclusions are in agreement with other ultrafast studies on the P_r state of a bacteriophytochrome and two CBCRs, where the authors identified active site relaxation of the protein matrix and solvation as the cause of the extended multiphasic kinetics instead of ground state heterogeneity [36,42,43]. Based on the experimental data similarities, we expect that the P_r forms in the latter studies would yield very similar LDMs as the ones shown in Figure 4.

In contrast, the P_r forms of other phytochromes, such as canonical phytochromes (e.g., Agp1, *SynCph1* and oatPhyA) [23,24,27–29,31] and some CBCRs [38,40] exhibit multiphasic excited state decays with significantly shorter lifetimes in the range of a few ps and 30 to 50 ps. The occurrence of multiphasic P_r behavior has often been linked to distinctly different P_r ground states [23,30,31,39]. The binding-pocket-relaxation model that we have proposed for the dynamics of the slower P_r forms (e.g., the phytochromes shown in Figure 4) does not explicitly exclude this type of heterogeneity as a contributing kinetic factor. However, we do not observe distinctly heterogeneous dynamics in terms of evolution of separable substates, instead some ground state heterogeneity might add to the distributed character of the dynamics. Therefore, we believe that for the longer-lived phytochromes (e.g., knotless phytochromes [50,53], some bacteriophytochromes [35,36,56] and some CBCRs [40–43]) the reorganization of the binding pocket after photoexcitation plays a dominant role in determining the isomerization kinetics.

In this regard, the available space and the flexibility of the chromophore-binding pocket, especially around the D-ring, have been proposed as the main factors to explain the extended P_r kinetics [36,42,50,53]. Mutational studies have identified highly conserved key amino acids (e.g., Y133, Y47, D79 and H160 in *SynCph2* or Y263, Y176, D207 and H290 in *SynCph1* and DrBphP) in the immediate vicinity of the D-ring that directly affect the excited state lifetime and the isomerization quantum yield [10,13,36,42,60–63]. In case of the Tyr residues both their steric interactions with the chromophore as well as their participation in the hydrogen bonding network have been proposed as essential for efficient photochemistry [60,62–65]. Additionally, solvent exposure, the overall hydrogen bonding network and the protonation state of several residues inside the pocket also appear to be important for its properties [34,36,42,43,60,61,66] and the ensuing kinetics.

The concept of pocket flexibility does not contradict the observations made for phytochromes with shorter P_r decay lifetimes (e.g., Agp1, *SynCph1*, oatPhyA, NpR6012g4). Here, the pocket would have to be more flexible and spacious to allow faster relaxation with less steric hindrances. This higher flexibility could also allow for alternative configurations of amino acid side chains and the chromophore itself resulting in the suggested ground state heterogeneity and the distinct kinetics of substates. In essence, the overall rather similar kinetics of phytochromes, despite significant structural differences, can be rationalized well by the binding-pocket-relaxation model when flexibility is considered.

2.3. Ultrafast Dynamics of P_r^*

The femtosecond TA experiments on the primary reverse dynamics of *SynCph2* show four main contributions (Figure 5A). A broad ESA (positive) signal is present below 625 nm, while the GSB and SE (negative) signals extend from 640 nm to 750 nm. At the long wavelength side of our spectral window (730–750 nm), a narrow positive signal appears after ~0.5 ps concomitantly with the decay of the ESA and SE signals. This new absorption signal is assigned to a ground state intermediate (GSI). At longer delay times, positive absorption (550–650 nm) is built up extending to the end of the experimentally accessible time range. These signals can be assigned to later ground state intermediates.

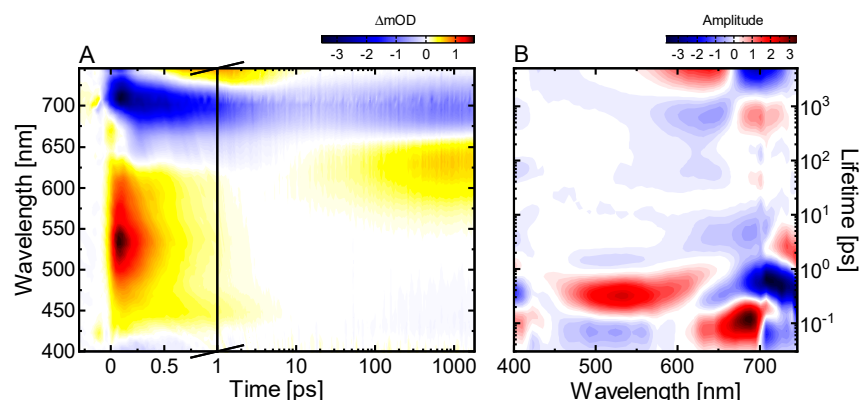


Figure 5. Ultrafast excited state dynamics of the P_{fr} state in *SynCph2* investigated in the UV/vis spectral range. (A) TA data of the $P_{fr} \rightarrow P_r$ dynamics after excitation at 710 nm. (B) Corresponding lifetime density map (LDM) obtained from the lifetime distribution analysis of the TA data displayed in A).

The details of the underlying kinetics are revealed by the corresponding LDM (Figure 5B). The negative- (450–600 nm, 700–750 nm) and positive-amplitude distributions (610–700 nm) at ~ 100 fs represent the spectral shifts of the ESA and the SE associated with the departure of the excited state wavepacket from the FC-region. The following positive-amplitude distribution at ~ 300 fs from 450 nm to 650 nm marks the decay of the ESA, while the simultaneous SE decay and partial ground state recovery are accounted for by the negative-amplitude distribution between 670 nm and 750 nm. The extension of the strong negative amplitude to the red is due to the rise of the positive signal of the first GSI located at ~ 740 nm. In the 1–5 ps lifetime range, the positive- (730 nm to 750 nm) and the negative-amplitude (600 to 700 nm) distributions show the decay of this first GSI to form the next, blue-shifted GSI and to partially recover the GSB. This is clearly visible in the TA data as a decrease in GSB amplitude. The following blue spectral shift evolution over several GSIs is accounted for by the positive- (675–740 nm) and negative- (550–670 nm) amplitude distributions between 50 ps and 1000 ps. On the ns timescale, the last negative- and positive-amplitude lifetime distribution corresponds to the residual signal of the last detectable (on this timescale) GSI and the remaining GSB signal.

The vis pump-probe results are further corroborated by our vis pump-IR probe measurements in the C=O region (Figure 6A). The negative GSB of the $C_{19}=O$ vibration is located at 1705 cm^{-1} while its corresponding broad ESA is located between 1695 cm^{-1} and 1660 cm^{-1} . The positive signal in the $1750\text{--}1715\text{ cm}^{-1}$ range with a dip at 1730 cm^{-1} can be assigned to the broad ESA of the $C_1=O$ and its underlying narrow GSB, respectively. These assignments are based on previous reports on the P_{fr} state of other phytochromes [45,46,48,67]. The target analysis of the data using a sequential model reveals that the ESAs decay with a lifetime of ~ 330 fs (Figure 6B,C). This decay is accompanied by the rise of a new positive contribution at 1690 cm^{-1} which can be linked to the formation of a GSI, as indicated also by the vis TA data (see above). In a next step, this intermediate decays with a 3.9 ps lifetime which leads to a recovery of most of the GSB and concurrent formation of a positive signal at 1720 cm^{-1} . According to the assignment for *SynCph1* [45,46], the 1720 cm^{-1} positive band can be attributed to the Lumi-F intermediate. We observe no further changes in the C=O range in our measurements (up to 40 ps).

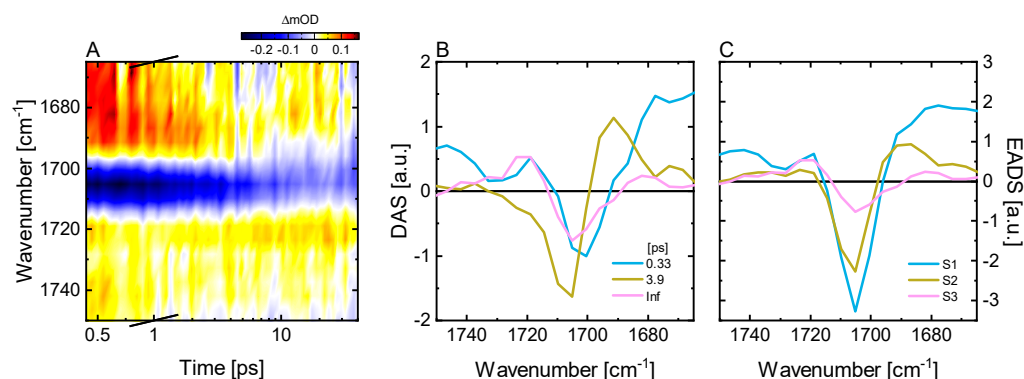


Figure 6. Ultrafast excited state dynamics of the P_{fr} state in *SynCph2* investigated in the IR spectral range. (A) TA data of the $P_{fr} \rightarrow P_r$ dynamics after excitation at 710 nm. (B) Corresponding decay associated spectra and (C) evolution-associated difference spectra (EADS) obtained from a sequential model fit of the data displayed in (A).

2.4. Kinetic Model of the Primary P_{fr} Kinetics

Based on the qualitative insight provided by the LDA of the vis data, we constructed kinetic models and fitted those directly to the experimental data to obtain quantitative information (kinetic rates for the different transition steps and the spectra of the involved species) on the P_{fr} kinetics (see refs [52,57,58] for details on global target analysis and the Methods section for specific technical details). The P_{fr} LDM (Figure 5B) clearly shows only one lifetime distribution (at about 300–400 fs) accounting for the decay of the relaxed excited state. Consequently, we used homogeneous kinetic models in the global target analysis. We added a FC state and several GSI states to account for the kinetic features in the LDM. In a next step, we tested models with different connectivity patterns between the states. To support the selection of the most adequate model, we introduced the overall quantum yield of the productive relaxation channel as an additional constraint. This was set to 0.2 as reported previously [13].

Our analysis resulted in a model with physically reasonable kinetic rates and species-associated difference spectra (SADS) (Figure 7). The model shows that the excited state relaxation occurs with a ~ 300 fs lifetime and leads to the formation of the first ground state intermediate (GSI-1). The SADS of GSI-1 has an absorption peak at about 750 nm (at the edge of our spectral detection window). This state then relaxes with an overall lifetime of 2.6 ps either back to the original P_{fr} ground state (80% yield) or forms GSI-2 (~ 730 nm absorption, 20% yield). The transition of GSI-1 to GSI-2 is also reflected in the 1–4 ps blue spectral shift dynamics captured by the LDM (Figure 5B) where the positive-amplitude (red) lifetime distribution (710–750 nm) accounts for the decay of the initially formed GSI-1. As indicated by the tilted shape of this distribution the dynamics is non-exponential and involves cooling towards either the P_{fr} ground state or the GSI-2. In turn, GSI-2 decays with about 5 ps lifetime. Note, the 3.9 ps lifetime recovered from the IR TA data (Figure 6) appears as a mixture of the GSI-1 and GSI-2 lifetimes, which can be attributed to the low signal-to-noise ratio of the IR data that does not permit resolving both lifetimes. Next, in a series of steps GSI-2 converts towards GSI-5 (Figure 7A,B), which is the final intermediate that we can observe on our detection timescale (i.e., 1.8 ns). The transition is associated with a gradual blue shift of the SADS of the intermediates, first to GSI-3 at ~ 690 nm (strongly overlapping with the GSB), consecutively to GSI-4 at 645 nm, and finally to GSI-5 with a maximum at 640 nm (Figure 7C).

In addition to the model in Figure 7, we also tested several other models that included either direct excited state relaxation to the P_{fr} ground state or a P_{fr} hot ground state (see SI, Figures S4–S6). In the models with P_{fr} hot ground state, the SADS with absorption at 750 nm represent the hot ground state. In addition, the blue side of the corresponding SADS is very similar to the SADS of some of the later intermediates and/or the GSI-1 SADS

shows a relatively broad GSB contribution. These spectral features are unreasonable; thus we clearly favor the model shown in Figure 7.

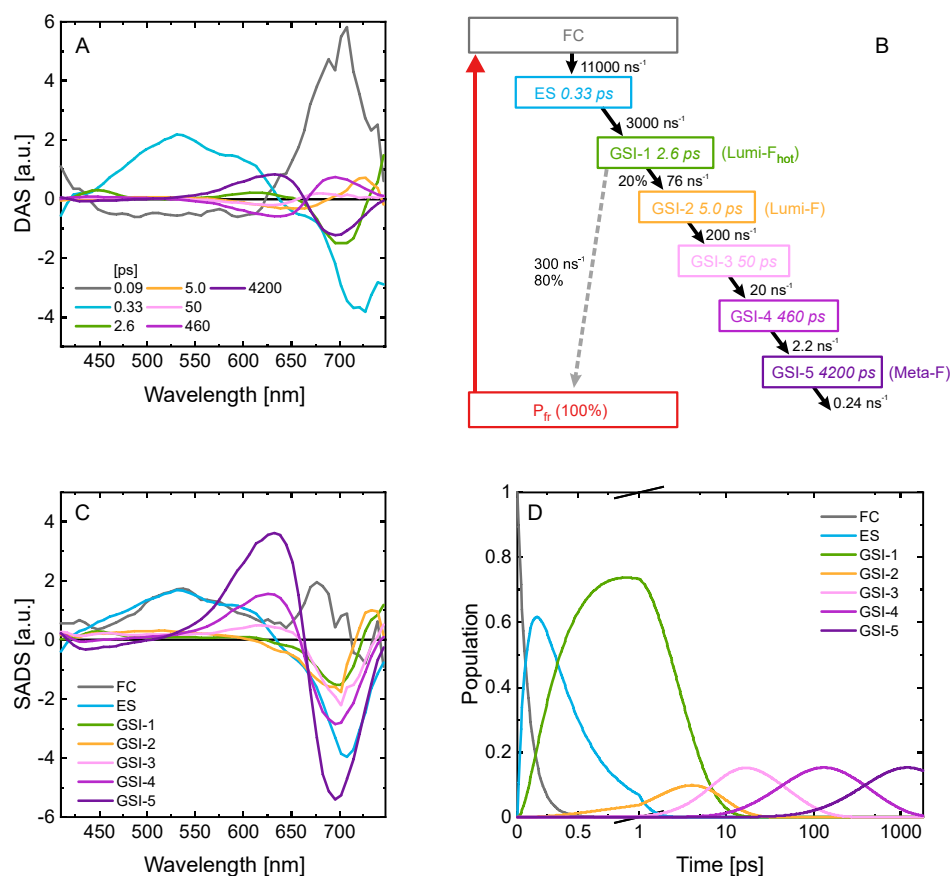


Figure 7. Decay-associated spectra (DAS) (A), species-associated difference spectra (SADS) (C) and populations (D) of individual states obtained from the GTA on the TA data of P_{fr}^* . The assignment to excited state or GS dynamics is based on the presence of ESA in the 410 to 600 nm range. (B) Schematic representation of the best kinetic model showing the rates (in ns^{-1}), the decay lifetimes (in ps), and the efficiencies of the corresponding reactions (in percent). Colors match the respective DAS, SADS and populations. The overall QY of the productive pathway was set to 0.2.

2.5. Comparison to Other Phytochromes

The primary P_{fr} kinetics of *SynCph2* is very similar to what is reported for other phytochromes. After a fast relaxation from the FC-region, the excited state decays on the sub-ps timescale to form the red-shifted GSI-1. Such a red-shifted species has been observed in *SynCph1* and *oatPhyA* [27,28,45,47,68] and was assigned to the primary photoproduct state Lumi-F [47]. Our model expands this picture by attributing GSI-1 to the hot Lumi-F (~750 nm), while GSI-2 to the relaxed Lumi-F (~730 nm). The kinetics of the transition between the two Lumi-Fs and the accompanying recovery of the GSB is not purely exponential as indicated by the lifetime distribution analysis, which is expected given the short timescale and the significant vibrational energy present shortly after the excited state relaxation. The following blue shift dynamics (GSIs-2/3/4) is associated with slow adaptation/relaxation of the isomerized chromophore and its binding pocket, and ultimately leads to the formation of Meta-F (GSI-5) on the sub-ns timescale. The blue shift dynamics resembles the dynamics reported for *oatPhyA* P_{fr} [27,28]. In contrast to *SynCph1* [45,47], in *SynCph2* we do not find an indication for distinctly heterogeneous excited state kinetics.

3. Materials and Methods

3.1. Protein Preparation

Preparation of *SynCph2* was described elsewhere [13]. The final buffer conditions for the experiments were set to 50 mM TRIS, pH 8.0, 300 mM NaCl, and 5 mM EDTA.

3.2. Stationary Characterization

UV/vis stationary absorption spectra of *SynCph2* were recorded using a Specord S600 absorption spectrometer (Analytik Jena). The sample was converted into the P_r and the P_{fr} state by illumination with an appropriate LED (730 nm and 590 nm respectively, 1W, Thorlabs). The stationary FTIR spectra were measured on a Bruker Tensor 27 equipped with a MCT detector under the same illumination conditions as used for the UV/vis absorption measurements. The sample chamber was purged with nitrogen.

3.3. Vis Pump-Probe Transient Absorption Experiments

The time-resolved TA measurements were conducted using a home-built pump-probe setup, as described in detail elsewhere [69]. In short, the fundamental laser pulses (1 mJ, 775 nm, 130 fs, 1 kHz) were provided by a Ti:Sa amplifier system (Clark, MXR-CPA-iSeries). The pump pulses were generated using a home-built two stage NOPA (noncollinear optical parametric amplifier) [70,71] and were compressed in a prism compressor located between the two NOPA stages. White light continuum pulses (300–750 nm) were generated by focusing the laser fundamental beam into a CaF_2 -crystal (5 mm). These probe pulses were split into probe and reference beam. The reference beam was guided directly into a spectrograph, while the probe beam was focused at the sample position and then collected and directed into a second spectrograph. The spectrographs (AMKO Multimode) contained gratings with 600 grooves/mm blazed at 500 nm and a photodiode array with a detection range set to 400–750 nm. The instrument response function (IRF) of ~80 fs in the experiments was estimated from the pump probe cross correlation. To eliminate anisotropic contributions, the measurements were carried out under magic angle conditions (54.7° pump-probe polarization difference). The sample (OD ~0.4 at the excitation wavelength) was held in a fused silica cuvette with an optical path length of 1 mm which was constantly moved in the plane perpendicular to the direction of probe pulse propagation to avoid accumulation of photoproducts. To keep the sample in a defined state the cuvette was constantly illuminated with a high-power LED at 730 nm for the P_r and 590 nm for the P_{fr} state experiments.

3.4. Vis Pump-IR Probe Transient Absorption Experiments

The TA IR measurements were performed with a Ti:Sa regenerative amplifier (4.5 mJ, 800 nm, 90 fs, 1 kHz; Mira Legend Elite HE, Coherent, Santa Clara, CA, USA) that is used to pump two home-built collinear OPAs. The signal and idler beams of one OPA were used to generate broadband IR probe and reference pulses via difference frequency generation (DFG) in AgGaS_2 . The signal beam of the second OPA was frequency-doubled in a BBO to generate the pump pulses at 642 nm and 712 nm to excite the P_r and P_{fr} forms, respectively. Each form was accumulated using the same background illumination as used in the vis TA measurements described above. The relative polarization between the pump and probe/reference beams was set to magic angle. The probe and reference beams were dispersed using a 150 lines/mm grating inside a single spectrometer (Triax, Jobin Yvon), resulting in a spectral resolution of about 5 cm^{-1} . The C=C and C=O spectral regions were probed in two separate spectral windows by shifting the center wavelength from 6220 nm to 5800 nm. The excitation density for the experiment in the C=O region of the P_r state was $1 \mu\text{J}$, while for the rest of the measurements $2 \mu\text{J}$ excitation was used. The detector consisted of a 2×32 pixel mercury cadmium telluride (MCT) detector (Infrared Associates, USA). The IRF was about 200 fs and the pump-probe delay was mechanically scanned from -30 ps up to about 3.5 ns. The sample (OD ~0.2–0.3 at the excitation wavelength)

was sandwiched between two CaF₂ windows, separated by a 50 μm PTFE spacer [72], and continuously moved with a Lissajous scanner to ensure a fresh spot for each shot.

3.5. Data Analysis

Data analysis was performed using OPTIMUS (www.optimusfit.org, accessed on 23 August 2021) [52]. We used the model independent lifetime distribution analysis (LDA) for the ultrafast TA data. This method can account for non-exponential kinetics. In LDA, a set of 100 exponential functions with fixed lifetimes equally distributed on a log₁₀ scale is used to describe the data by determining the pre-exponential amplitudes. Those amplitudes can then be displayed for each detection wavelength in form of a contour plot called lifetime density map (LDM) [73]. LDMs are similar to decay-associated spectra: Positive amplitudes account for decay of excited state and product absorption (ESA, PA) or rise of ground state bleach or stimulated emission (GSB and SE). Negative amplitudes correspond to the rise of absorption (ESA, PA) or the decay of GSB and SE.

In addition, we performed global target analysis [52,57]. In short, kinetic models are fitted directly to the experimental data to verify their adequacy. The analysis results in the so-called species-associated difference spectra (SADS), or when a simple sequential model ($A \rightarrow B \rightarrow C \dots$) is used in evolution-associated difference spectra (EADS). Unlike decay-associated difference spectra (DADS) from global lifetime analysis, SADS and EADS contain pure spectral information—SADS represent the spectra of the species in the kinetic model, while EADS show the overall spectral evolution. Global target analysis also delivers the kinetic rates of the different reaction steps, as well as the lifetimes and the conventional DADS. Our implementation allows us to constrain the quantum yield for formation of the last observable (on the experiment timescale) photoproduct state. This limits the parameter fitting space and facilitates the determination of an adequate model. Since this type of analysis involves a certain level of over-parametrization, the solutions are not unique. Therefore, the adequacy of the models that fit the experimental data is judged based on whether the SADS and the kinetic rates are physically reasonable.

4. Conclusions

Our work provides insight into the unexplored ultrafast dynamics of knotless phytochromes. We show that the excited state P_r dynamics of *SynCph2* occur on the timescale of hundreds of picoseconds, similarly to All2699g1g2 [50], bacteriophytochromes [35,36,56], and a number of red/green CBCRs [40–43]. In contrast to the P_r forms of some canonical phytochromes like *SynCph1*, here we do not find distinctly heterogeneous but rather distributed kinetics, which we attribute to reorganization of the chromophore-binding pocket that controls the isomerization dynamics. The P_{fr} dynamics of *SynCph2* resembles the one observed in oatPhyA with a fast, sub-ps excited state decay followed by consecutive blue shifts of the formed GSIs. In general, the dynamics is also very similar to what is reported in *SynCph1*. However, in *SynCph2* the data again do not point to spectroscopically separable ground states.

Quite remarkably, both the forward and the reverse dynamics of the knotless phytochrome *SynCph2*, which lacks the PAS domain, can be readily compared to other phytochromes containing a PAS-GAF-PHY array as their PSM. Furthermore, the P_r → P_{fr} dynamics of *SynCph2* is also very similar to some CBCRs which are composed only of a single GAF domain. Therefore, it emerges that despite the great variation in the relevant structural components (domains and composition), the primary photoconversion mechanism appears to be fundamentally conserved in most phytochromes. Consequently, the key to the detailed understanding of phytochrome photochemistry is the identification of common structural patterns regulating and defining the photoisomerization step. Importantly, this will also result in a general design principle for optimized phytochromes for biotechnological applications.

Supplementary Materials: The following are available online at <https://www.mdpi.com/article/10.3390/ijms221910690/s1>, Figure S1/S2: Transients and difference spectra at selected delay times for the visible TA data of *SynCph2* for the $P_r \rightarrow P_{fr}$ and $P_{fr} \rightarrow P_r$ dynamics respectively, Figure S3: FTIR difference spectrum of Cph2, Figures S4–S6: Additional kinetic models used to fit the TA data of the P_{fr} dynamics of *SynCph2*, Figure S7: Comparison of data and fit for the ultrafast reverse dynamics of Cph2 using the kinetic model displayed in Figure 7 for selected wavelengths.

Author Contributions: Conceptualization, L.-O.E., J.W. and C.S.; methodology, T.F. and C.S., formal analysis, T.F. and C.S., investigation, T.F., L.J.G.W.v.W. and C.S., sample preparation, P.G., data curation, T.F. and C.S.; writing—original draft preparation, T.F. and C.S., writing—review and editing, T.F., L.J.G.W.v.W., J.B., L.-O.E., J.W. and C.S., supervision, J.B., L.-O.E., J.W. and C.S. All authors have read and agreed to the published version of the manuscript.

Funding: This research was funded by the Deutsche Forschungsgemeinschaft (WA 1850/4-3, ES152/21). J.B. thanks the Alexander von Humboldt Foundation for a Sofia Kovalevskaja Award and the Deutsche Forschungsgemeinschaft for funding (No. INST 161/722-1 FUGG).

Institutional Review Board Statement: Not applicable.

Informed Consent Statement: Not applicable.

Data Availability Statement: Data is available from the authors upon reasonable request.

Acknowledgments: We thank David Buhrke for his helpful comments on the IR bands assignment.

Conflicts of Interest: The authors declare no conflict of interest.

References

1. Anders, K.; Essen, L.O. The family of phytochrome-like photoreceptors: Diverse, complex and multi-colored, but very useful. *Curr. Opin. Struct. Biol.* **2015**, *35*, 7–16. [[CrossRef](#)]
2. Rockwell, N.C.; Lagarias, J.C. Phytochrome diversification in cyanobacteria and eukaryotic algae. *Curr. Opin. Plant Biol.* **2017**, *37*, 87–93. [[CrossRef](#)] [[PubMed](#)]
3. Piatkevich, K.D.; Subach, F.V.; Verkhusha, V.V. Engineering of bacterial phytochromes for near-infrared imaging, sensing, and light-control in mammals. *Chem. Soc. Rev.* **2013**, *42*, 3441–3452. [[CrossRef](#)] [[PubMed](#)]
4. Redchuk, T.A.; Omelina, E.S.; Chernov, K.G.; Verkhusha, V.V. Near-infrared optogenetic pair for protein regulation and spectral multiplexing. *Nat. Chem. Biol.* **2017**, *13*, 633–639. [[CrossRef](#)] [[PubMed](#)]
5. Shcherbakova, D.M.; Stepanenko, O.V.; Turoverov, K.K.; Verkhusha, V.V. Near-Infrared Fluorescent Proteins: Multiplexing and Optogenetics across Scales. *Trends Biotechnol.* **2018**, *36*, 1230–1243. [[CrossRef](#)] [[PubMed](#)]
6. Hörner, M.; Raute, K.; Hummel, B.; Madl, J.; Creusen, G.; Thomas, O.S.; Christen, E.H.; Hotz, N.; Gübeli, R.J.; Engesser, R.; et al. Phytochrome-Based Extracellular Matrix with Reversibly Tunable Mechanical Properties. *Adv. Mater.* **2019**, *31*, e1806727. [[CrossRef](#)] [[PubMed](#)]
7. Rockwell, N.C.; Lagarias, J.C. The structure of phytochrome: A picture is worth a thousand spectra. *Plant Cell* **2006**, *18*, 4–14. [[CrossRef](#)]
8. Rockwell, N.C.; Su, Y.-S.; Lagarias, J.C. Phytochrome Structure and Signaling Mechanisms. *Annu. Rev. Plant Biol.* **2006**, *57*, 837–858. [[CrossRef](#)]
9. Möglich, A.; Yang, X.; Ayers, R.A.; Moffat, K. Structure and Function of Plant Photoreceptors. *Annu. Rev. Plant Biol.* **2010**, *61*, 21–47. [[CrossRef](#)]
10. Yang, X.; Kuk, J.; Moffat, K. Crystal structure of *Pseudomonas aeruginosa* bacteriophytochrome: Photoconversion and signal transduction. *Proc. Natl. Acad. Sci. USA* **2008**, *105*, 14715–14720. [[CrossRef](#)]
11. Essen, L.O.; Mailliet, J.; Hughes, J. The structure of a complete phytochrome sensory module in the P_r ground state. *Proc. Natl. Acad. Sci. USA* **2008**, *105*, 14709–14714. [[CrossRef](#)]
12. Montgomery, B.L.; Lagarias, J.C.C. Phytochrome ancestry: Sensors of bilins and light. *Trends Plant. Sci.* **2002**, *7*, 357–366. [[CrossRef](#)]
13. Anders, K.; Von Stetten, D.; Mailliet, J.; Kiontke, S.; Sineshchikov, V.A.; Hildebrandt, P.; Hughes, J.; Essen, L.O. Spectroscopic and photochemical characterization of the red-light sensitive photosensory module of Cph2 from *Synechocystis* PCC 6803. *Photochem. Photobiol.* **2011**, *87*, 160–173. [[CrossRef](#)] [[PubMed](#)]
14. Ikeuchi, M.; Ishizuka, T. Cyanobacteriochromes: A new superfamily of tetrapyrrole-binding photoreceptors in cyanobacteria. *Photochem. Photobiol. Sci.* **2008**, *7*, 1159. [[CrossRef](#)] [[PubMed](#)]
15. Lamparter, T.; Mittmann, F.; Gartner, W.; Borner, T.; Hartmann, E.; Hughes, J. Characterization of recombinant phytochrome from the cyanobacterium *Synechocystis*. *Proc. Natl. Acad. Sci. USA* **1997**, *94*, 11792–11797. [[CrossRef](#)] [[PubMed](#)]

16. Lamparter, T.; Michael, N.; Mittmann, F.; Esteban, B. Phytochrome from *Agrobacterium tumefaciens* has unusual spectral properties and reveals an N-terminal chromophore attachment site. *Proc. Natl. Acad. Sci. USA* **2002**, *99*, 11628–11633. [[CrossRef](#)] [[PubMed](#)]
17. Chai, Y.G.; Singh, B.R.; Song, P.S.; Lee, J.; Robinson, G.W. Purification and spectroscopic properties of 124-kDa oat phytochrome. *Anal. Biochem.* **1987**, *163*, 322–330. [[CrossRef](#)]
18. Hirose, Y.; Shimada, T.; Narikawa, R.; Katayama, M.; Ikeuchi, M. Cyanobacteriochrome CcaS is the green light receptor that induces the expression of phycobilisome linker protein. *Proc. Natl. Acad. Sci. USA* **2008**, *105*, 9528–9533. [[CrossRef](#)]
19. Rockwell, N.C.; Martin, S.S.; Gulevich, A.G.; Lagarias, J.C. Phycoviolobin formation and spectral tuning in the DXCF cyanobacteriochrome subfamily. *Biochemistry* **2012**, *51*, 1449–1463. [[CrossRef](#)] [[PubMed](#)]
20. Rockwell, N.C.; Martin, S.S.; Feoktistova, K.; Lagarias, J.C. Diverse two-cysteine photocycles in phytochromes and cyanobacteriochromes. *Proc. Natl. Acad. Sci. USA* **2011**, *108*, 11854–11859. [[CrossRef](#)]
21. Rockwell, N.C.; Martin, S.S.; Lagarias, J.C. Identification of Cyanobacteriochromes Detecting Far-Red Light. *Biochemistry* **2016**, *55*, 3907–3919. [[CrossRef](#)]
22. Fushimi, K.; Ikeuchi, M.; Narikawa, R. The Expanded Red/Green Cyanobacteriochrome Lineage: An Evolutionary Hot Spot. *Photochem. Photobiol.* **2017**, *93*, 903–906. [[CrossRef](#)] [[PubMed](#)]
23. Yang, Y.; Linke, M.; von Haimberger, T.; Matute, R.; González, L.; Schmieder, P.; Heyne, K.; von Haimberger, T.; Matute, R.; González, L.; et al. Active and silent chromophore isoforms for phytochrome Pr photoisomerization: An alternative evolutionary strategy to optimize photoreaction quantum yields. *Struct. Dyn.* **2014**, *1*, 014701. [[CrossRef](#)]
24. Linke, M.; Yang, Y.; Zienicke, B.; Hammam, M.A.S.; Von Haimberger, T.; Zacarias, A.; Inomata, K.; Lamparter, T.; Heyne, K. Electronic transitions and heterogeneity of the bacteriophytochrome Pr absorption band: An angle balanced polarization resolved femtosecond VIS pump-IR probe study. *Biophys. J.* **2013**, *105*, 1756–1766. [[CrossRef](#)] [[PubMed](#)]
25. Yang, Y.; Linke, M.; von Haimberger, T.; Hahn, J.; Matute, R.; González, L.; Schmieder, P.; Heyne, K. Real-Time Tracking of Phytochrome's Orientational Changes During Pr Photoisomerization. *J. Am. Chem. Soc.* **2012**, *134*, 1408–1411. [[CrossRef](#)] [[PubMed](#)]
26. Dasgupta, J.; Frontiera, R.R.; Taylor, K.C.; Lagarias, J.C.; Mathies, R.A. Ultrafast excited-state isomerization in phytochrome revealed by femtosecond stimulated Raman spectroscopy. *Proc. Natl. Acad. Sci. USA* **2009**, *106*, 1784–1789. [[CrossRef](#)] [[PubMed](#)]
27. Müller, M.G.; Lindner, I.; Martin, I.; Gärtner, W.; Holzwarth, A.R. Femtosecond kinetics of photoconversion of the higher plant photoreceptor phytochrome carrying native and modified chromophores. *Biophys. J.* **2008**, *94*, 4370–4382. [[CrossRef](#)]
28. Bischoff, M.; Hermann, G.; Rentsch, S.; Strehlow, D. First steps in the phytochrome phototransformation: A comparative femtosecond study on the forward (Pr→Pfr) and back reaction (Pfr→Pr). *Biochemistry* **2001**, *40*, 181–186. [[CrossRef](#)] [[PubMed](#)]
29. Schumann, C.; Groß, R.; Michael, N.; Lamparter, T.; Diller, R. Sub-picosecond mid-infrared spectroscopy of phytochrome Agp1 from *Agrobacterium tumefaciens*. *ChemPhysChem* **2007**, *8*, 1657–1663. [[CrossRef](#)]
30. Song, C.; Psakis, G.; Lang, C.; Mailliet, J.J.; Gärtner, W.; Hughes, J.; Matysik, J.; Gärtner, W.; Hughes, J.; Matysik, J.; et al. Two ground state isoforms and a chromophore D-ring photoflip triggering extensive intramolecular changes in a canonical phytochrome. *Proc. Natl. Acad. Sci. USA* **2011**, *108*, 3842–3847. [[CrossRef](#)]
31. Kim, P.W.; Rockwell, N.C.; Martin, S.S.; Lagarias, J.C.; Larsen, D.S. Dynamic Inhomogeneity in the Photodynamics of Cyanobacterial Phytochrome Cph1. *Biochemistry* **2014**, *53*, 2818–2826. [[CrossRef](#)] [[PubMed](#)]
32. Toh, K.C.; Stojković, E.A.; van Stokkum, I.H.M.M.; Moffat, K.; Kennis, J.T.M.M.; Stojkovic, E.A.; van Stokkum, I.H.M.M.; Moffat, K.; Kennis, J.T.M.M.; Stojković, E.A.; et al. Proton-transfer and hydrogen-bond interactions determine fluorescence quantum yield and photochemical efficiency of bacteriophytochrome. *Proc. Natl. Acad. Sci. USA* **2010**, *107*, 9170–9175. [[CrossRef](#)] [[PubMed](#)]
33. Lehtivuori, H.; Rissanen, I.; Takala, H.; Bamford, J.; Tkachenko, N.V.; Ihalainen, J.A. Fluorescence Properties of the Chromophore-Binding Domain of Bacteriophytochrome from *Deinococcus radiodurans*. *J. Phys. Chem. B* **2013**, *117*, 11049–11057. [[CrossRef](#)] [[PubMed](#)]
34. Mathes, T.; Ravensbergen, J.; Kloz, M.; Gleichmann, T.; Gallagher, K.D.; Woitowich, N.C.; Peter, R.S.; Kovaleva, S.E.; Stojković, E.A.; Kennis, J.T.M.M. Femto- to Microsecond Photodynamics of an Unusual Bacteriophytochrome. *J. Phys. Chem. Lett.* **2015**, *6*, 239–243. [[CrossRef](#)]
35. Singer, P.; Wörner, S.; Lamparter, T.; Diller, R. Spectroscopic Investigation on the Primary Photoreaction of Bathy Phytochrome Agp2-Pr of *Agrobacterium fabrum*: Isomerization in a pH-dependent H-bond Network. *ChemPhysChem* **2016**, *17*, 1288–1297. [[CrossRef](#)]
36. Wang, D.; Qin, Y.; Zhang, M.; Li, X.; Wang, L.; Yang, X.; Zhong, D. The Origin of Ultrafast Multiphasic Dynamics in Photoisomerization of Bacteriophytochrome. *J. Phys. Chem. Lett.* **2020**, *11*, 5913–5919. [[CrossRef](#)]
37. Wang, C.; Flanagan, M.L.; McGillicuddy, R.D.; Zheng, H.; Ginzburg, A.R.; Yang, X.; Moffat, K.; Engel, G.S. Bacteriophytochrome Photoisomerization Proceeds Homogeneously Despite Heterogeneity in Ground State. *Biophys. J.* **2016**, *111*, 2125–2134. [[CrossRef](#)]
38. Kim, P.W.; Freer, L.H.; Rockwell, N.C.; Martin, S.S.; Lagarias, J.C.; Larsen, D.S. Femtosecond photodynamics of the red/green cyanobacteriochrome NpR6012g4 from *Nostoc punctiforme*. 1. Forward dynamics. *Biochemistry* **2012**, *51*, 608–618. [[CrossRef](#)]
39. Chang, C.-W.W.; Gottlieb, S.M.; Kim, P.W.; Rockwell, N.C.; Lagarias, J.C.; Larsen, D.S. Reactive ground-state pathways are not ubiquitous in red/green cyanobacteriochromes. *J. Phys. Chem. B* **2013**, *117*, 11229–11238. [[CrossRef](#)]

40. Gottlieb, S.M.; Kim, P.W.; Chang, C.W.; Hanke, S.J.; Hayer, R.J.; Rockwell, N.C.; Martin, S.S.; Lagarias, J.C.; Larsen, D.S. Conservation and diversity in the primary forward photodynamics of red/green cyanobacteriochromes. *Biochemistry* **2015**, *54*, 1028–1042. [[CrossRef](#)]
41. Slavov, C.; Xu, X.; Zhao, K.H.; Gärtner, W.; Wachtveitl, J. Detailed insight into the ultrafast photoconversion of the cyanobacteriochrome Slr1393 from *Synechocystis* sp. *Biochim. Biophys. Acta-Bioenerg.* **2015**, *1847*, 1335–1344. [[CrossRef](#)]
42. Wang, D.; Li, X.; Wang, L.; Yang, X.; Zhong, D. Elucidating Ultrafast Multiphasic Dynamics in the Photoisomerization of Cyanobacteriochrome. *J. Phys. Chem. Lett.* **2020**, *11*, 8819–8824. [[CrossRef](#)]
43. Tachibana, S.R.; Tang, L.; Chen, C.; Zhu, L.; Takeda, Y.; Fushimi, K.; SeEVERS, T.K.; Narikawa, R.; Sato, M.; Fang, C. Transient electronic and vibrational signatures during reversible photoswitching of a cyanobacteriochrome photoreceptor. *Spectrochim. Acta-Part. A Mol. Biomol. Spectrosc.* **2021**, *250*, 119379. [[CrossRef](#)]
44. Heyne, K.; Herbst, J.; Stehlik, D.; Esteban, B.; Lamparter, T.; Hughes, J.; Diller, R. Ultrafast dynamics of phytochrome from the cyanobacterium *Synechocystis*, reconstituted with phycocyanobilin and phycoerythrobilin. *Biophys. J.* **2002**, *82*, 1004–1016. [[CrossRef](#)]
45. Stensitzki, T.; Yang, Y.; Wölke, A.L.; Knapp, E.W.; Hughes, J.; Mroginski, M.A.; Heyne, K. Influence of Heterogeneity on the Ultrafast Photoisomerization Dynamics of Pfr in Cph1 Phytochrome. *Photochem. Photobiol.* **2017**, *93*, 703–712. [[CrossRef](#)] [[PubMed](#)]
46. Yang, Y.; Heyne, K.; Mathies, R.A.; Dasgupta, J. Non-Bonded Interactions Drive the Sub-Picosecond Bilin Photoisomerization in the Pfr State of Phytochrome Cph1. *ChemPhysChem* **2016**, *17*, 369–374. [[CrossRef](#)] [[PubMed](#)]
47. Kim, P.W.; Rockwell, N.C.; Martin, S.S.; Lagarias, J.C.; Larsen, D.S. Heterogeneous photodynamics of the Pfr state in the cyanobacterial phytochrome Cph1. *Biochemistry* **2014**, *53*, 4601–4611. [[CrossRef](#)]
48. Schumann, C.; Groß, R.; Wolf, M.M.N.; Diller, R.; Michael, N.; Lamparter, T. Subpicosecond Midinfrared Spectroscopy of the Pfr Reaction of Phytochrome Agp1 from *Agrobacterium tumefaciens*. *Biophys. J.* **2008**, *94*, 3189–3197. [[CrossRef](#)] [[PubMed](#)]
49. Wang, D.; Qin, Y.; Zhang, S.; Wang, L.; Yang, X.; Zhong, D. Elucidating the Molecular Mechanism of Ultrafast Pfr-State Photoisomerization in Bathy Bacteriophytochrome PaBphP. *J. Phys. Chem. Lett.* **2019**, *10*, 6197–6201. [[CrossRef](#)]
50. Fischer, T.; Xu, Q.; Zhao, K.H.; Gärtner, W.; Slavov, C.; Wachtveitl, J. Effect of the PHY Domain on the Photoisomerization Step of the Forward Pr→Pfr Conversion of a Knotless Phytochrome. *Chem.-A Eur. J.* **2020**, *26*, 17261–17266. [[CrossRef](#)]
51. Anders, K.; Daminelli-Widany, G.; Mroginski, M.A.; Von Stetten, D.; Essen, L.O. Structure of the cyanobacterial phytochrome 2 photosensor implies a tryptophan switch for phytochrome signaling. *J. Biol. Chem.* **2013**, *288*, 35714–35725. [[CrossRef](#)]
52. Slavov, C.; Hartmann, H.; Wachtveitl, J. Implementation and Evaluation of Data Analysis Strategies for Time-Resolved Optical Spectroscopy. *Anal. Chem.* **2015**, *87*, 2328–2336. [[CrossRef](#)]
53. Slavov, C.; Fischer, T.; Barnoy, A.; Shin, H.; Rao, A.G.; Wiebeler, C.; Zeng, X.; Sun, Y.; Xu, Q.; Gutt, A.; et al. The interplay between chromophore and protein determines the extended excited state dynamics in a single-domain phytochrome. *Proc. Natl. Acad. Sci. USA* **2020**, *117*, 16356–16362. [[CrossRef](#)] [[PubMed](#)]
54. Van Thor, J.J.; Ronayne, K.L.; Towrie, M. Formation of the early photoproduct Lumi-R of cyanobacterial phytochrome Cph1 observed by ultrafast mid-infrared spectroscopy. *J. Am. Chem. Soc.* **2007**, *129*, 126–132. [[CrossRef](#)] [[PubMed](#)]
55. Escobar, F.V.; Kneip, C.; Michael, N.; Hildebrandt, T.; Tavraz, N.; Gärtner, W.; Hughes, J.; Friedrich, T.; Scheerer, P.; Mroginski, M.A.; et al. The Lumi-R Intermediates of Prototypical Phytochromes. *J. Phys. Chem. B* **2020**, *124*, 4044–4055. [[CrossRef](#)] [[PubMed](#)]
56. Toh, K.C.; Stojković, E.A.; Rupenyan, A.B.; van Stokkum, I.H.M.; Salumbides, M.; Groot, M.-L.; Moffat, K.; Kennis, J.T.M. Primary Reactions of Bacteriophytochrome Observed with Ultrafast Mid-Infrared Spectroscopy. *J. Phys. Chem. A* **2011**, *115*, 3778–3786. [[CrossRef](#)]
57. Van Stokkum, I.H.M.M.; Larsen, D.S.; van Grondelle, R. Global and target analysis of time-resolved spectra. *Biochim. Biophys. Acta-Bioenerg.* **2004**, *1657*, 82–104. [[CrossRef](#)]
58. Beckwith, J.S.; Rumble, C.A.; Vauthey, E. Data analysis in transient electronic spectroscopy—an experimentalist’s view. *Int. Rev. Phys. Chem.* **2020**, *39*, 135–216. [[CrossRef](#)]
59. Buhrke, D.; Oppelt, K.T.; Heckmeier, P.J.; Fernández-Terán, R.; Hamm, P. Nanosecond protein dynamics in a red/green cyanobacteriochrome revealed by transient IR spectroscopy. *J. Chem. Phys.* **2020**, *153*, 245101. [[CrossRef](#)]
60. Fischer, A.J.; Rockwell, N.C.; Jang, A.Y.; Ernst, L.A.; Waggoner, A.S.; Duan, Y.; Lei, H.; Lagarias, J.C. Multiple roles of a conserved GAF domain tyrosine residue in cyanobacterial and plant phytochromes. *Biochemistry* **2005**, *44*, 15203–15215. [[CrossRef](#)]
61. Wagner, J.R.; Zhang, J.; Von Stetten, D.; Günther, M.; Murgida, D.H.; Mroginski, M.A.; Walker, J.M.; Forest, K.T.; Hildebrandt, P.; Vierstra, R.D. Mutational analysis of *Deinococcus radiodurans* bacteriophytochrome reveals key amino acids necessary for the photochromicity and proton exchange cycle of phytochromes. *J. Biol. Chem.* **2008**, *283*, 12212–12226. [[CrossRef](#)] [[PubMed](#)]
62. Sineshchekov, V.; Mailliet, J.; Psakis, G.; Feilke, K.; Kopycki, J.; Zeidler, M.; Essen, L.; Hughes, J. Tyrosine 263 in Cyanobacterial Phytochrome Cph1 Optimizes Photochemistry at the prelumi-R→lumi-R Step. *Photochem. Photobiol.* **2014**, *90*, 786–795. [[CrossRef](#)]
63. Mailliet, J.; Psakis, G.; Feilke, K.; Sineshchekov, V.; Essen, L.O.; Hughes, J. Spectroscopy and a high-resolution crystal structure of Tyr263 mutants of cyanobacterial phytochrome Cph1. *J. Mol. Biol.* **2011**, *413*, 115–127. [[CrossRef](#)]
64. Kübel, J.; Chenchilijan, M.; Ooi, S.A.; Gustavsson, E.; Isaksson, L.; Kuznetsova, V.; Ihalainen, J.A.; Westenhoff, S.; Maj, M. Transient IR spectroscopy identifies key interactions and unravels new intermediates in the photocycle of a bacterial phytochrome. *Phys. Chem. Chem. Phys.* **2020**, *22*, 9195–9203. [[CrossRef](#)]

65. Kurttila, M.; Stucki-Buchli, B.; Rumfeldt, J.; Schroeder, L.; Häkkänen, H.; Liukkonen, A.; Takala, H.; Kottke, T.; Ihalainen, J.A. Site-by-site tracking of signal transduction in an azidophenylalanine-labeled bacteriophytochrome with step-scan FTIR spectroscopy. *Phys. Chem. Chem. Phys.* **2021**, *23*, 5615–5628. [[CrossRef](#)]
66. Rumfeldt, J.A.; Takala, H.; Liukkonen, A.; Ihalainen, J.A. UV-Vis Spectroscopy Reveals a Correlation Between Y263 and BV Protonation States in Bacteriophytochromes. *Photochem. Photobiol.* **2019**, *95*, 969–979. [[CrossRef](#)] [[PubMed](#)]
67. Escobar, F.V.; von Stetten, D.; Günther-Lütken, M.; Keidel, A.; Michael, N.; Lamparter, T.; Essen, L.O.; Hughes, J.; Gärtner, W.; Yang, Y.; et al. Conformational heterogeneity of the Pfr chromophore in plant and cyanobacterial phytochromes. *Front. Mol. Biosci.* **2015**, *2*, 1–13. [[CrossRef](#)]
68. Kim, P.W.; Pan, J.; Rockwell, N.C.; Chang, C.W.; Taylor, K.C.; Lagarias, J.C.; Larsen, D.S. Ultrafast e to Z photoisomerization dynamics of the Cph1 phytochrome. *Chem. Phys. Lett.* **2012**, *549*, 86–92. [[CrossRef](#)]
69. Slavov, C.; Bellakbil, N.; Wahl, J.; Mayer, K.; Rück-Braun, K.; Burghardt, I.; Wachtveitl, J.; Braun, M. Ultrafast coherent oscillations reveal a reactive mode in the ring-opening reaction of fulgides. *Phys. Chem. Chem. Phys.* **2015**, *17*, 14045–14053. [[CrossRef](#)] [[PubMed](#)]
70. Wilhelm, T.; Piel, J.; Riedle, E. Sub-20-fs pulses tunable across the visible from a blue-pumped single-pass noncollinear parametric converter. *Opt. Lett.* **1997**, *22*, 1494. [[CrossRef](#)]
71. Riedle, E.; Beutler, M.; Lochbrunner, S.; Piel, J.; Schenkl, S.; Spörlein, S.; Zinth, W. Generation of 10 to 50 fs pulses tunable through all of the visible and the NIR. *Appl. Phys. B* **2000**, *71*, 457–465. [[CrossRef](#)]
72. Bredenbeck, J.; Hamm, P. Versatile small volume closed-cycle flow cell system for transient spectroscopy at high repetition rates. *Rev. Sci. Instrum.* **2003**, *74*, 3188–3189. [[CrossRef](#)]
73. Croce, R.; Müller, M.G.; Bassi, R.; Holzwarth, A.R. Carotenoid-to-chlorophyll energy transfer in recombinant major light-harvesting complex (LHCII) of higher plants. I. Femtosecond transient absorption measurements. *Biophys. J.* **2001**, *80*, 901–915. [[CrossRef](#)]

5.5 Reference [IV] *Fischer et al., Photochem. Photobiol. Sci.* **2022**, *21*, 1627-1636

5.5 Reference [IV]

Fischer et al., *Photochem. Photobiol. Sci.* **2022, *21*,
1627-1636**

**Influence of the PHY domain on the ms-photoconversion dynamics of a knotless
phytochrome**

T. Fischer, L. Köhler, T. Ott, C. Song, J. Wachtveitl, C. Slavov

Photochem. Photobiol. Sci. **2022**, *21*, 1627-1636.

DOI: 10.1007/s43630-022-00245-9



Influence of the PHY domain on the ms-photoconversion dynamics of a knotless phytochrome

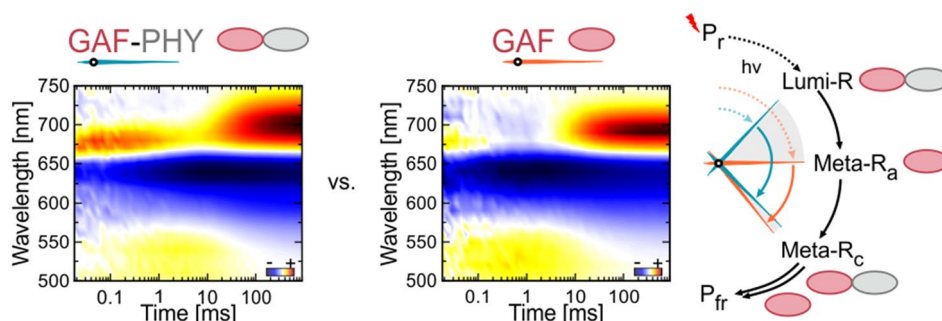
Tobias Fischer¹ · Lisa Köhler² · Tanja Ott¹ · Chen Song² · Josef Wachtveitl¹ · Chavdar Slavov¹

Received: 3 February 2022 / Accepted: 11 May 2022 / Published online: 10 June 2022
© The Author(s) 2022

Abstract

The ability of some knotless phytochromes to photoconvert without the PHY domain allows evaluation of the distinct effect of the PHY domain on their photodynamics. Here, we compare the *ms* dynamics of the single GAF domain (g1) and the GAF-PHY (g1g2) construct of the knotless phytochrome All2699 from cyanobacterium *Nostoc punctiforme*. While the spectral signatures and occurrence of the intermediates are mostly unchanged by the domain composition, the presence of the PHY domain slows down the early forward and reverse dynamics involving chromophore and protein binding pocket relaxation. We assign this effect to a more restricted binding pocket imprinted by the PHY domain. The photoproduct formation is also slowed down by the presence of the PHY domain but to a lesser extent than the early dynamics. This indicates a rate limiting step within the GAF and not the PHY domain. We further identify a pH dependence of the biphasic photoproduct formation hinting towards a pKa dependent tuning mechanism. Our findings add to the understanding of the role of the individual domains in the photocycle dynamics and provide a basis for engineering of phytochromes towards biotechnological applications.

Graphical abstract



Keywords Knotless phytochrome · Photochemistry · Time-resolved spectroscopy · Flash photolysis

1 Introduction

The photoreceptor superfamily of phytochromes is involved in the regulation of a variety of biologically relevant processes like photomorphogenesis, photoprotection and phototaxis in a multitude of different organisms [1, 2]. Their regulatory function is based on the photoconversion between a dark-adapted and a light-adapted state. Specifically, irradiation induces Z ↔ E isomerization of the embedded, covalently bound bilin chromophore that in turn triggers

This publication is dedicated to Prof. Silvia E. Braslavsky, a pioneer in photobiology and photobiophysics, on the occasion of her 80th birthday.

- ✉ Josef Wachtveitl
wveitl@theochem.uni-frankfurt.de
- ✉ Chavdar Slavov
chslavov@theochem.uni-frankfurt.de

Extended author information available on the last page of the article

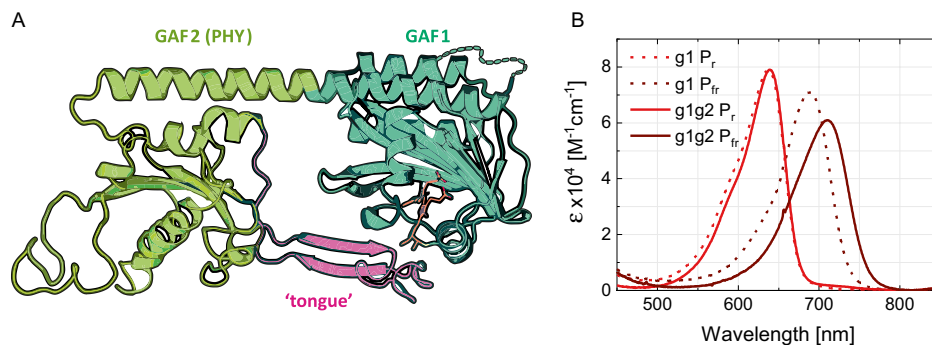


Fig. 1 **A** Schematic drawing of the structural homology model of the P_r state of All2699g1g2. The homology model is based on the crystal structure of the All2699g1 domain (PDB ID 6OZA) [19] and the crystal structure of the structurally similar knotless phytochrome *SynCph2* (PDB ID 4BWI) [22]. The PHY-like GAF2 domain (yellow) interacts with the chromophore (orange) embedded in the GAF1

domain (green) via the tongue-like protrusion displayed in pink. Taken from [23]. **B** Stationary absorption spectra of the P_r and P_{fr} state in All2699g1 (dotted lines) and All2699g1g2 (solid lines). The method to obtain the pure spectrum of the P_{fr} state was described elsewhere in detail [18]

formation of further intermediates characterized by reorganization of the protein scaffold.

Phytochromes can be divided into three groups based on the domain structure and composition of their photosensory core module (PCM). The PCM of Group I phytochromes, comprising canonical plant (e.g. *OatPhyA*), bacterial (e.g. *Agp1*, *DrBphP*), cyanobacterial (e.g. *CphA*, *SynCph1*) and fungal phytochromes (e.g. *FphA*, *NcFph1*), consists of a PAS-GAF-PHY array [3–5]. Group II phytochromes, known as knotless phytochromes, lack the PAS domain with its domain specific figure-of-eight knot formation with the GAF domain [1, 2, 6, 7], while Group III phytochromes, called cyanobacteriochromes (CBCRs), consist only of GAF domains [8]. So far, the latter two groups are found only in cyanobacteria [1]. In contrast to CBCRs, which cover the whole near-IR to UV spectral range, Group I and Group II phytochromes mainly switch between P_r (red-absorbing) and P_{fr} (far-red-absorbing) states [9–17].

Some knotless phytochromes retain their photoconversion abilities even in their isolated GAF domain (after removal of the PHY domain), and thus can be utilized as model systems to investigate the influence of the PHY domain on the photoconversion process [18, 19]. This is of particular interest since the PHY domain interacts directly with the chromophore embedded in the GAF domain via a structural element referred to as “tongue” (Fig. 1A). The latter undergoes secondary structure reorganization during photoconversion [6, 7]. This reorganization not only affects the slower, protein driven dynamics of the later intermediates in the photocycle, but also plays a key role in the signal transduction towards the output domain [20, 21].

The forward (P_r → P_{fr}) reaction in the photocycle of canonical phytochromes typically involves three intermediates termed Lumi-R, Meta-R_a and Meta-R_c. The Lumi-R

intermediate is formed directly after the decay of the excited state on the timescale of tens to hundreds of ps [24]. It contains the isomerized chromophore and a reorganized hydrogen-bonding network. Some studies distinguish Lumi-R_I and Lumi-R_{II} intermediates [24–29]. The structural changes in Lumi-R_I occur on the ps timescale and are limited to the ring D vicinity, while the following hydrogen bonding reorganization and structural changes in the wider vicinity of the chromophore are attributed to Lumi-R_{II} [24, 28, 29]. On the μs timescale, Lumi-R converts into the Meta-R_a intermediate via relaxation of the strained chromophore [21, 26, 27, 30–32]. Within a few ms, in plant and some cyanobacterial and bacterial phytochromes, the chromophore undergoes deprotonation to form the Meta-R_c intermediate [30, 31, 33, 34], which then forms the final state, P_{fr}, upon re-protonation of the chromophore on the tens to hundreds of ms timescale [21, 26, 27, 30–32]. However, the de/re-protonation steps of the chromophore are not observed in all phytochromes, and thus the role of this mechanism in the dynamics of Meta-R_c is still under debate [24]. This formation of P_{fr} involves large-scale protein changes required for the final accommodation of the isomerized chromophore, reorganization of the hydrogen-bonding network and refolding of the tongue [20, 21, 24, 32]. In *SynCph1* and *OatPhyA*, this transition has been observed to be biphasic [27, 30].

Generally, the reverse photoconversion reaction (P_{fr} → P_r) proceeds via two intermediates – Lumi-F and Meta-F. The Lumi-F intermediate contains an isomerized chromophore and is directly formed by the ultrafast photoreaction on the ps timescale [35–39]. Following ground state chromophore relaxation and minor side chain readjustments, a spectrally P_r-like intermediate termed Meta-F is formed on the ps-to-ns timescale [36, 40, 41]. The Meta-F intermediate undergoes rearrangement of the hydrogen-bonding network and the

binding pocket, as well as refolding of the tongue to form the P_r state [41]. These steps occur on the μs - ms timescale and do not involve major spectral changes in the visible spectral range [40, 42, 43].

In this work, we expand our ultrafast studies on knotless phytochromes [18, 19] to the ms timescale. We compare the ms dynamics of the knotless phytochrome All2699g1g2 and its isolated GAF domain All2699g1 to reveal the effect of the PHY-like g2 domain on the forward ($P_r \rightarrow P_{fr}$) and reverse ($P_{fr} \rightarrow P_r$) photoconversion of knotless phytochromes. We further compare our results to the previously investigated knotless phytochrome *SynCph2* and discuss the similarities and differences observed for these structurally related knotless phytochromes.

2 Materials and methods

2.1 Protein preparation

Preparation of All2699g1 and All2699g1g2 was described elsewhere in detail [19, 44]. The final buffer conditions for the experiments were set to 50 mM TRIS, 200 mM NaCl, 5% Glycerol, pH 8.0. For the pH dependence measurements of All2699g1, the following buffer conditions were used: 20 mM MES, 150 mM NaCl, 5% Glycerol, pH 6.1; 20 mM KPBS, 150 mM NaCl, 5% Glycerol, pH 7.2; 20 mM TRIS, 150 mM NaCl, 5% Glycerol, pH 8.4.

Preparation of *SynCph2* was described elsewhere [9]. The final buffer conditions for the experiments were set to 50 mM TRIS, 300 mM NaCl, 5 mM EDTA, pH 8.0.

Samples were measured in a 2×10 mm quartz cuvette with an optical density between 0.4 and 0.8 on 10 mm.

2.2 Stationary characterization

Stationary absorption spectra of the investigated samples were obtained using a Specord S600 absorption spectrometer (Analytik Jena). Conversion between the P_r and the P_{fr} state was achieved by illumination with appropriate LEDs (730 nm and 590 nm respectively, 1 W, Thorlabs).

2.3 Transient flash photolysis experiments

The pump pulses were provided by an optical parametric oscillator (OPO) (preciScan, GWU-Lasertechnik) pumped by a Nd:YAG laser (SpitLight 600, Innolas Laser). The OPO was set to 640 nm for P_r and 702 nm for P_{fr} measurements with an average pulse energy of 2.4–2.6 mJ/cm^2 . The probe light was generated by a spectrally broad continuous wave Xenon lamp (Hamamatsu LC-8) and two matched monochromators before and after the sample. The absorbance changes were then detected with a photomultiplier tube

(PMT) and the resulting signal was converted into an electrical signal and recorded using an oscilloscope (DPO5204B-10RL, Tektronix). Time points were measured every 100 ns, except for the g1g2 P_{fr} measurements where a point was measured every 200 ns. For all samples absorbance changes were recorded between 500 and 750 nm with at least 30 averaged scans per wavelength. Between each individual scan the sample was illuminated for 4 s using an appropriate LED ($P_r \rightarrow P_{fr}$, 730 nm; $P_{fr} \rightarrow P_r$, 590 nm) to avoid accumulation of photoproducts. For analysis, the single transients were reduced by averaging data points in a combined linear and logarithmic timescale to obtain feasible data sizes.

For the pH dependence measurements of the ms dynamics of All2699g1, transients at six key wavelengths (510, 540, 600, 630, 680, and 710 nm) were measured and analyzed like the complete datasets. To validate the reduction to the 6-wavelength datasets, a comparison of the analysis to a complete dataset is shown exemplarily in the SI for pH 7.2 (SI Fig. S1).

2.4 Data analysis

Data analysis was performed using OPTIMUS (<http://www.optimusfit.org/>) [45]. We performed global target analysis (GTA) [45, 46] on all datasets using a sequential model. This model is fitted directly to the experimental data and results in the lifetimes, the decay-associated spectra (DAS) and the so-called evolution-associated difference spectra (EADS) for the respective kinetic components. The DAS contain both spectral and kinetic information, i.e. the positive amplitudes in the DAS account for decay of photoproduct absorption (PA) while negative amplitudes account for rise of absorption or recovery of the ground state bleach. Unlike DAS, EADS contain pure spectral information.

3 Results and discussion

3.1 Forward ($P_r \rightarrow P_{fr}$) ms dynamics

3.1.1 Comparison between All2699g1 and All2699g1g2

The flash photolysis data of the P_r state of All2699g1 and All2699g1g2 (Fig. 2) appear very similar. Both show a dominant negative difference signal visible throughout the entire detected time range, which can be straightforwardly assigned to the ground state bleach (GSB) of the P_r state after excitation. Additionally, several distinct positive signals, at 660–690 nm, 660–700 nm, 500–560 nm and 660–750 nm, are present at different delay times in the data. These absorption changes are associated with the different intermediates observed during the photocycle. We performed global target

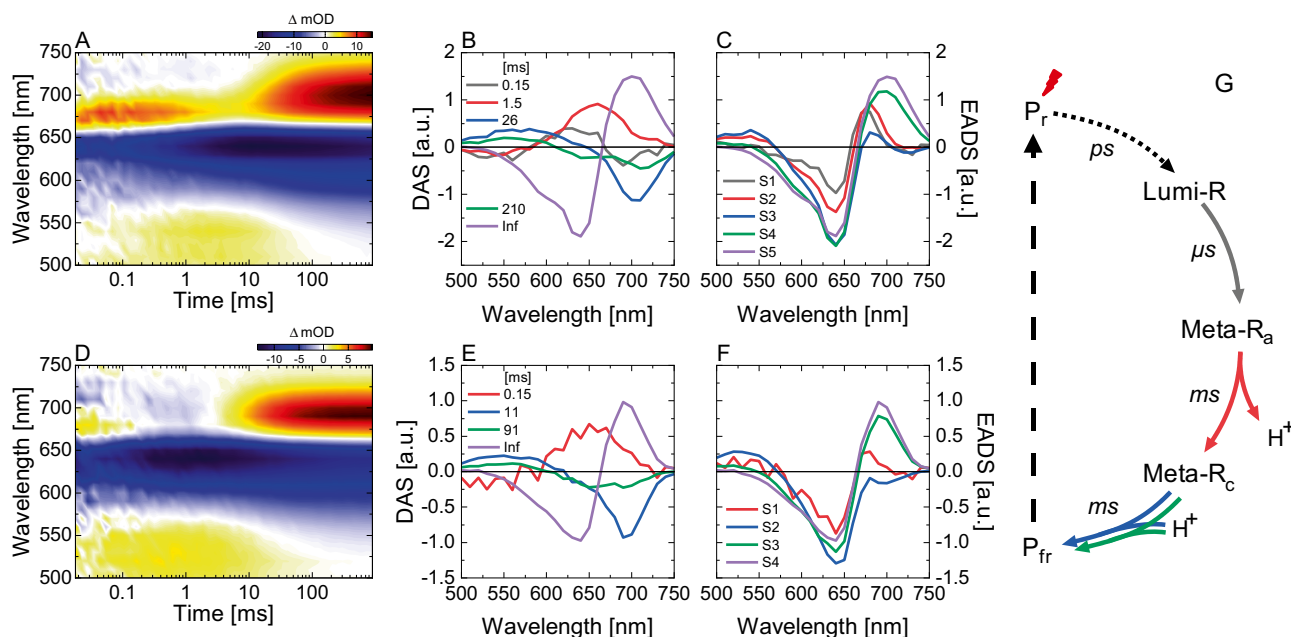


Fig. 2 $P_r \rightarrow P_{fr}$ ms dynamics of All2699g1g2 (A–C) and All2699g1 (D–F) at pH 8. **A, D** Flash photolysis data of the $P_r \rightarrow P_{fr}$ ms dynamics after excitation at 640 nm. **B, E** Corresponding decay-associated spectra (DAS) and **C, F** evolution-associated spectra (EADS) obtained after global target analysis of (A,D). **G** Schematic repre-

sentation of the proposed photocycle for the $P_r \rightarrow P_{fr}$ ms dynamics of All2699g1g2 and All2699g1 at pH 8. The dashed line indicates the thermal reversion from P_{fr} to P_r , while the dotted line represents the initial photoreaction

analysis using a sequential model to reveal the kinetic details of the $P_r \rightarrow P_{fr}$ conversion.

Five components were required to fit the P_r data of All2699g1g2. Based on the resemblance to the primary photoproduct formed on the ultrafast timescale [18], we assign the S1 evolution-associated difference spectrum (EADS, Fig. 2C), peaking at 675 nm, to the Lumi-R intermediate. The positive (575–660 nm) and negative amplitudes (660–730 nm) of the 150 μ s decay-associated spectrum (DAS, Fig. 2B), indicate the Lumi-R-to-Meta- R_a transition, which occurs with a red spectral shift (S1 vs. S2 EADS) induced by the bilin chromophore relaxation. In a next step, the chromophore undergoes a prominent spectral blue shift with a 1.5 ms lifetime to form the Meta- R_c intermediate (positive amplitude DAS at 575–750 nm and negative amplitude DAS at 500–575 nm in Fig. 2B, S2 \rightarrow S3 EADS transition in Fig. 2C). We attribute this blue spectral shift to a chromophore deprotonation step following the assignment made previously for other phytochromes [31, 33, 34]. The following re-protonation of the chromophore is biphasic (S3 and S4 EADS). The corresponding DAS show similar spectral features representing the decay of the Meta- R_c absorption (positive amplitude at about 550 nm in τ_3 (26 ms) and in τ_4 (210 ms)) and the rise of the absorption of the final photoproduct P_{fr} (negative amplitude 650–750 nm). In contrast to τ_3 , the DAS amplitude of τ_4 is negative in the range of 610–650 nm, potentially indicating some recovery of the

spectrally coinciding P_r ground state via a shunt pathway as reported in some bacteriophytochromes [47, 48].

The major difference between the P_r flash photolysis data of All2699g1g2 (Fig. 2A) and All2699g1 (Fig. 2D) is that for g1 the kinetics is accelerated and can be described with only four components (Fig. 2E–F). Following the assignment above, those four components correspond to Meta- R_a (660–700 nm), Meta- R_c (500–560 nm), P_{fr} (660–740 nm) and the P_r GSB. The Lumi-R-to-Meta- R_a transition occurs on a timescale shorter than what is detected in our experiment (i.e. < 20 μ s). Thus, the 150 μ s component represents instead the Meta- R_a -to-Meta- R_c transition as indicated by the negative amplitude between 500 and 550 nm in the corresponding DAS (Fig. 2E). The Meta- R_c decay in All2699g1, albeit accelerated, is also biphasic (11 ms and 91 ms lifetimes, see below for more detailed discussion).

3.1.2 Effect of the PHY domain on the forward dynamics

The Lumi-R-to-Meta- R_a and Meta- R_a -to-Meta- R_c transitions are significantly slower (\sim 10-fold) in All2699g1g2 as compared to All2699g1, which indicates that the presence of the PHY domain imposes a higher energetic barrier for the associated chromophore relaxation and proximal protein structural rearrangements. This conclusion is in line with previous NMR [23, 49] and RR [28] studies, where it was proposed that the interaction with the PHY tongue makes

the chromophore-binding pocket more rigid. In contrast, the final chromophore transition (Meta- R_c -to- P_{fr}), typically associated with major structural changes (tongue refolding [20, 21, 24, 32]) in the protein environment distal to the chromophore, is affected to a smaller extent (twofold) by the lacking PHY domain in All2699g1. Furthermore, the preserved biphasic character of the Meta- R_c -to- P_{fr} transition in All2699g1 suggests that the chromophore transitions associated with this step are predominantly determined by factors within the binding pocket of the GAF domain. Previously, a similar conclusion was derived based on time-resolved X-ray and UV/Vis studies on *DrBphP* [21].

3.1.3 Origin of the biphasic meta- R_c to P_{fr} transition

To further investigate the origin of the biphasic Meta- R_c -to- P_{fr} kinetics in All2699g1 and All2699g1g2, we performed flash photolysis measurements at selected detection wavelengths (510, 540, 600, 630, 680, and 710 nm) and at three different pH values (6.1, 7.2, and 8.4). A direct comparison of the transients at 710 nm reveals that the P_{fr} formation is significantly accelerated at high pH values (Fig. 3A). This clear pH dependence is further corroborated by the DAS of the three datasets (Fig. 3B).

While the lifetime components do not vary significantly, their corresponding amplitudes and especially the amplitude ratio between the shorter and the longer component (correspondingly marked blue and green in Fig. 3B) change with the pH. At pH 6.1, the amplitude of the longer component is higher than that of the shorter one resulting in the slowest overall Meta- R_c -to- P_{fr} transition (Fig. 3A). At pH 8.4 the ratio is reversed, the shorter component clearly dominates, thus making the overall Meta- R_c decay fastest. At pH 7.2 the two components have nearly identical amplitude. Consequently, the process occurring with the shorter lifetime component is favored at high pH, while the process described by the longer lifetime component is favored at low pH. Furthermore, the monoexponential formation of the Meta- R_c and the lack of spectral differences in the two DAS describing

its decay imply that there is a single chromophore population in Meta- R_c and that the following re-protonation reaction is dependent on the pKa value of the proton donor residue and the state of the hydrogen-bonding network linking it to the solvent. Thereby, the faster component represents a chromophore re-protonation reaction occurring from a protonated residue, while for the slower component the residue is deprotonated, and thus the re-protonation requires proton uptake from the environment. Such a proton uptake step has been reported for Cph1 [30]. In effect, the role of the slower component is prominent at low pH, while at higher (H^+ deficient) pH, its contribution is diminished.

While we cannot directly identify the relevant residue, based on the nearly identical amplitudes of the DAS of the two Meta- R_c decay components, we can deduce that its pKa value is close to 7.2. Mutational studies on other phytochromes (*SynCph1*, *DrBphP*, *Agp1*) identified histidine residues that are part of the extended hydrogen-bonding network of the chromophore and affect its protonation state [33, 50–53]. The respective residues in All2699g1, His139 and His169, are therefore potential candidates for the origin of the observed pH dependence. His139 is in direct contact with the pyrrole nitrogens of the bilin chromophore and was reported to be directly involved in the proton uptake leading to the formation of the P_{fr} state as some mutants of this residue do not progress past Meta- R_c in their photocycle [33, 52]. In addition, the His139-homologous residue H260 exhibits a pKa value of 7.4 in the P_r state of *SynCph1*, strikingly similar to the value we derive here for the biphasic transition to P_{fr} [51]. His169 is part of the extended hydrogen-bonding network, and thus it is in an indirect contact with His139. It is also in contact with the chromophore in both P_r and P_{fr} interacting with the D-ring carbonyl or the C-ring propionate, respectively [54]. As such, its protonation state could influence the hydrogen-bonding network potentially contributing to the biphasic kinetics. However, we consider His139 a more likely candidate since mutants of His169 exhibit only minor impact on the chromophore and/or hydrogen-bonding network pKa [50]. The highly

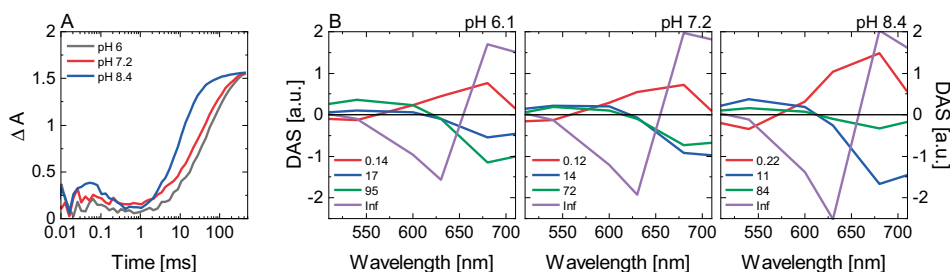


Fig. 3 pH dependence of the $P_r \rightarrow P_{fr}$ ms dynamics of All2699g1 at pH 6.1, 7.2 and 8.4. **A** Transients of the UV/Vis flash photolysis measurements of All2699g1 at 710 nm at different pH values. **B** DAS

obtained by global lifetime analysis of 6 transients at key wavelengths (510, 540, 600, 630, 680 and 710 nm) of All2699g1 after excitation at 640 nm at different pH values

conserved Asp87 may also be considered as a candidate involved in the protonation steps. This residue interacts with the chromophore through the pyrrole water and similar to His139 is involved in tuning the chromophore pKa and its hydrogen-bonding network [33, 52]. However, it is reported that this Asp87 retains its protonation state during the photocycle rendering a direct involvement in the reprotonation unlikely [24]. Indirectly, an increase in the protein mobility, such as that observed in *SynCph1* [34], may also be contributing to the overall acceleration of P_{fr} formation at higher pH.

3.1.4 Comparison of the P_r dynamics to other phytochromes

The lifetimes of the intermediates observed in the knotless phytochrome All2699g1g2 match well with previously reported lifetimes for *SynCph1* [30], *SynCph2* [32], and Agp1 [31] indicating high similarities between the dynamics of knotless and knotted phytochromes on the *ms* timescale. In the only investigated knotless phytochrome *SynCph2*, the lifetimes for the Lumi-R-to-Meta- R_a and Meta- R_a -to-Meta- R_c transition (170 μ s and 1.6 ms, SI Fig. S2) are nearly identical to those found here for All2699g1g2 (150 μ s and 1.5 ms, Fig. 2B). However, the Meta- R_c -to- P_{fr} transition is significantly faster in *SynCph2* and proceeds monoexponentially with a lifetime of 17 ms. In contrast, the

Meta- R_c -to- P_{fr} transition in *SynCph1* is similarly biphasic with lifetimes close to those we find in All2699g1g2. A comparison between *SynCph2* and All2699g1 shows a different involvement of water molecules and propionic side chains in the extended hydrogen-bonding network, which can result in different pKa values and explain the occurrence or lack of biphasic Meta- R_c decay in different phytochromes.

3.2 Reverse ($P_{fr} \rightarrow P_r$) *ms* dynamics

3.2.1 Comparison of All2699g1 and All2699g1g2

To provide a complete picture of the influence of the PHY domain on the dynamics of knotless phytochromes, we investigated the *ms* reverse reaction ($P_{fr} \rightarrow P_r$) in All2699g1 and All2699g1g2. The GSB (negative absorption difference) signal in the P_{fr} flash photolysis data of both samples is located above 650 nm (Fig. 4). However, reflecting the difference in the P_{fr} absorption spectra (Fig. 1), the GSB of All2699g1g2 is red shifted. In addition to the GSB signal, we observe a spectral evolution of the positive absorption difference signal associated with the transitions of the intermediate states towards the final photoproduct P_r (*i.e.* from ~550–650 nm through ~575–660 nm to ~500–630 nm, Fig. 1). This evolution is better discerned for All2699g1g2.

The global target analysis with a sequential scheme yields four lifetime components for both samples. In All2699g1g2,

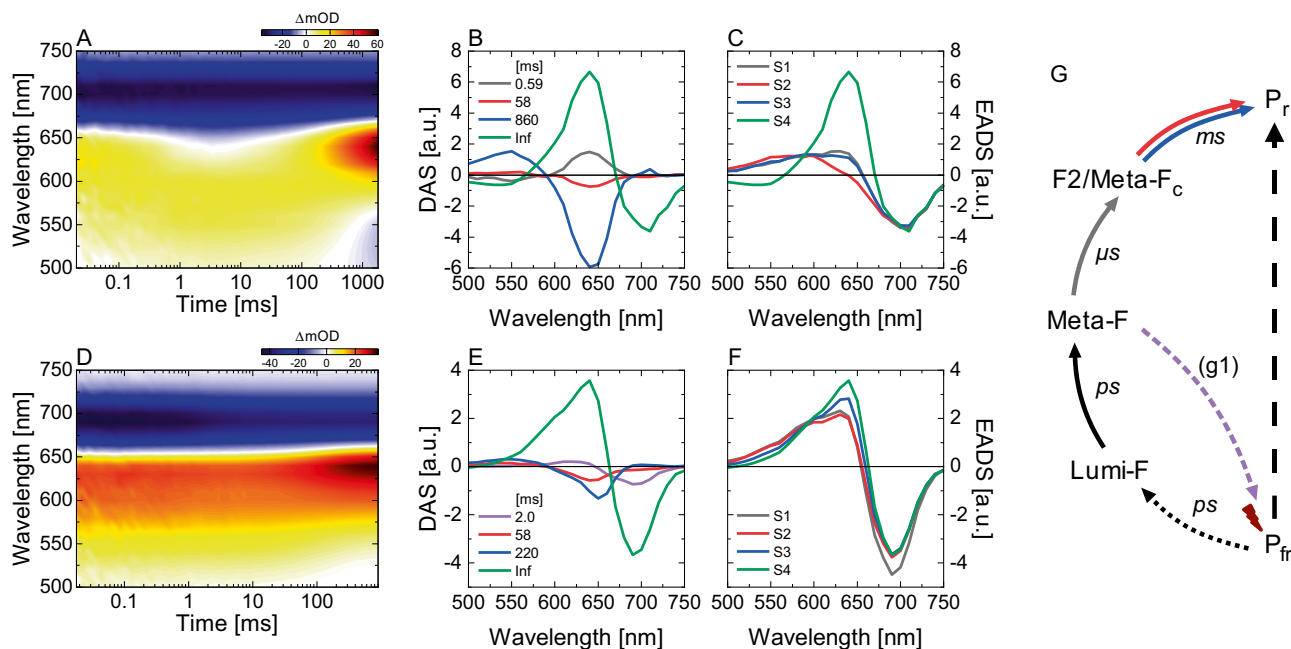


Fig. 4 $P_{fr} \rightarrow P_r$ *ms* dynamics of All2699g1g2 (A–C) and All2699g1 (D–F) at pH 8. **A, D** Flash photolysis data of the $P_{fr} \rightarrow P_r$ *ms* dynamics after excitation at 702 nm. **(B,E)** Corresponding decay-associated spectra (DAS) and **C, F** evolution-associated spectra (EADS) obtained after global target analysis of **A, D**. **G** Schematic represen-

tation of the proposed photocycle for the $P_{fr} \rightarrow P_r$ *ms* dynamics of All2699g1g2 and All2699g1 at pH 8. The vertical black dashed line indicates the thermal reversion from P_{fr} to P_r , while the dotted line represents the initial photoreaction. The short dashed purple line represents the shunt pathway present in All2699g1

the S1 EADS (Fig. 4C) resembles the spectrum of the species present at the end of the ultrafast P_{fr} dynamics in *SynCph2* [37] or *SynCph1* [36], and thus can be assigned to the Meta-F intermediate. Meta-F decays with a lifetime of 590 μ s to form a blue-shifted intermediate (S2 EADS) as described by the positive–negative amplitudes of the corresponding DAS (Fig. 4B). A similar blue-shifted species has also been observed in *SynCph2* and termed F2 [32]. The F2 intermediate then decays to form the final P_r state with two lifetimes where the amplitude of the 860 ms component is significantly higher than that of the 58 ms component (Fig. 4B).

The P_{fr} flash photolysis data of All2699g1 exhibit similar signals (Fig. 4D). However, the S1 EADS is broadened on the blue spectral side, which indicates that the F2 intermediate is already present at the beginning of the measurement in equilibrium with Meta-F (Fig. 4F). Thus, in analogy to Meta- R_a from the forward dynamics of All2699g1, in the reverse direction we cannot clearly detect the rise of F2 in the single domain sample. Instead, the first lifetime component (2 ms) in All2699g1 indicates a shunt pathway to the P_{fr} ground state from a leftover Meta-F population. Such a pathway is not present in the reverse dynamics of All2699g1g2 and is not observed in *SynCph2*, but has been observed in bacteriophytochromes [47, 48]. The following transition from F2 to the P_r state is described again by two lifetimes. However, in contrast to All2699g1g2, the difference in the amplitude of the two components is much smaller. In addition, the second lifetime component is significantly shorter in All2699g1 (i.e. 220 ms). As a result, the overall P_r formation is accelerated in All2699g1. Interestingly, in both samples, there appears to be an equilibrium between the Meta-F and F2 intermediates. This equilibrium is shifted towards Meta-F in All2699g1, while in All2699g1g2 the F2 and Meta-F intermediates have similar amplitudes. The S3 EADS of All2699g1g2 (Fig. 4C) suggests that at longer timescales the equilibrium shifts towards high F2 populations.

3.2.2 Effect of the PHY domain on the reverse dynamics

In both the forward and the reverse dynamics, the photoreaction is accelerated in absence of the PHY domain, i.e. the Meta- R_a in the forward and F2 in the reverse dynamics are formed in All2699g1 earlier than in All2699g1g2. We attribute this to fewer restrictions in the binding pocket in absence of the PHY domain as revealed by previous NMR and cryotrapping experiments [23, 28, 49]. The photoreaction then follows similar steps where an intermediate spectrally close to the final photoproduct (Meta- R_a and Meta-F) converts into a blue-shifted one (Meta- R_c and F2). The final photoproduct (P_{fr} or P_r) is formed with a biphasic kinetics, as indicated by a corresponding red shift on the *ms* timescale. Similar to the spectral shift of Meta- R_c in the forward direction, we

observe a spectral shift of F2 in the reverse direction. This resemblance suggests that the formation and the decay of F2 may also occur via deprotonation and re-protonation steps. For consistency, we propose that F2 is termed Meta- F_c by analogy to Meta- R_c .

3.2.3 Comparison of the P_{fr} dynamics to other phytochromes

It is particularly remarkable that the Meta-F-to-Meta- F_c transition in All2699g1g2 is on a timescale (hundreds of μ s) similar to that found in *SynCph2* and *PhyA* while the P_r formation step is two orders of magnitude slower [32, 40]. Even in comparison to other phytochromes like *CphA* [40] or *PstBphP1* and *PaBphP1* [43] that exhibit slightly different reverse kinetics, the formation of the photoproduct is still exceptionally slow in both All2699g1g2 and All2699g1. The unknown origin of the striking temporal difference for the final photoproduct formation step between the two structurally very similar knotless phytochromes (All2699g1g2 and *SynCph2*) should be addressed in future studies.

4 Conclusion

Our work provides a dynamic picture of the effect of the PHY domain on the *ms* dynamics of knotless phytochromes. We show that the occurrence and spectral signature of the involved intermediates are not significantly affected by the presence of the PHY domain. However, the μ s dynamics involving relaxation of the chromophore are slowed down for both the forward and the reverse direction. We attribute this effect to a more confined chromophore binding pocket in presence of the PHY domain. Quite remarkably, the lifetimes describing the transition to the final photoproduct are much less affected by the presence/absence of the PHY domain. This supports previous findings that the rate limiting step of the photoproduct formation observed by UV/vis spectroscopy is imposed by internal factors of the GAF (PAS-GAF) domain and are not directly related to tongue refolding.

Interestingly, we find that the Meta- R_c -to- P_{fr} transition is biphasic in both All2699g1 and All2699g1g2, but not in *SynCph2*. Based on the pH dependence of the transition in All2699g1, we associate this behavior to the pKa value of the proton donor residue in the Meta- R_c intermediate. The lack of biphasic behavior in some phytochromes suggests that the rate of photoproduct formation can be tweaked through fine tuning of the pKa value of the hydrogen-bonding network.

Supplementary Information The online version contains supplementary material available at <https://doi.org/10.1007/s43630-022-00245-9>.

Acknowledgements Lisa Köhler and Chen Song acknowledge the Deutsche Forschungsgemeinschaft (417685888). Chavdar Slavov and Josef Wachtveitl acknowledge the Deutsche Forschungsgemeinschaft (WA 1850/4-3). The authors thank Wolfgang Gärtner for his insightful comments and his support for the realization of the project. The authors also thank Petra Gnau and Lars-Oliver Essen for providing the *SynCph2* samples for benchmark experiments.

Funding Open Access funding enabled and organized by Projekt DEAL.

Declarations

Conflict of interest The datasets generated during and/or analyzed during the current study are available from the corresponding author upon reasonable request. The authors have no competing interests to declare that are relevant to the content of this article.

Open Access This article is licensed under a Creative Commons Attribution 4.0 International License, which permits use, sharing, adaptation, distribution and reproduction in any medium or format, as long as you give appropriate credit to the original author(s) and the source, provide a link to the Creative Commons licence, and indicate if changes were made. The images or other third party material in this article are included in the article's Creative Commons licence, unless indicated otherwise in a credit line to the material. If material is not included in the article's Creative Commons licence and your intended use is not permitted by statutory regulation or exceeds the permitted use, you will need to obtain permission directly from the copyright holder. To view a copy of this licence, visit <http://creativecommons.org/licenses/by/4.0/>.

References

- Anders, K., & Essen, L. O. (2015). The family of phytochrome-like photoreceptors: Diverse, complex and multi-colored, but very useful. *Current Opinion in Structural Biology*, 35, 7–16. <https://doi.org/10.1016/j.sbi.2015.07.005>
- Rockwell, N. C., & Lagarias, J. C. (2017). Phytochrome diversification in cyanobacteria and eukaryotic algae. *Current Opinion in Plant Biology*, 37, 87–93. <https://doi.org/10.1016/j.pbi.2017.04.003>
- Rockwell, N. C., & Lagarias, J. C. (2006). The structure of phytochrome: A picture is worth a thousand spectra. *The Plant Cell*, 18(1), 4–14. <https://doi.org/10.1105/tpc.105.038513>
- Rockwell, N. C., Su, Y.-S., & Lagarias, J. C. (2006). Phytochrome structure and signaling mechanisms. *Annual Review of Plant Biology*, 57(1), 837–858. <https://doi.org/10.1146/annurev.arplant.56.032604.144208>
- Möglich, A., Yang, X., Ayers, R. A., & Moffat, K. (2010). Structure and function of plant photoreceptors. *Annual Review of Plant Biology*, 61, 21–47. <https://doi.org/10.1146/annurev-arplant-042809-112259>
- Yang, X., Kuk, J., & Moffat, K. (2008). Crystal structure of *Pseudomonas aeruginosa* bacteriophytochrome: Photoconversion and signal transduction. *Proceedings of the National Academy of Sciences of the United States of America*, 105(38), 14715–14720. <https://doi.org/10.1073/pnas.0806718105>
- Essen, L. O., Mailliet, J., & Hughes, J. (2008). The structure of a complete phytochrome sensory module in the Pr ground state. *Proceedings of the National Academy of Sciences of the United States of America*, 105(38), 14709–14714. <https://doi.org/10.1073/pnas.0806477105>
- Ikeuchi, M., & Ishizuka, T. (2008). Cyanobacteriochromes: A new superfamily of tetrapyrrole-binding photoreceptors in cyanobacteria. *Photochemical and Photobiological Sciences*, 7(10), 1159. <https://doi.org/10.1039/b802660m>
- Anders, K., Von Stetten, D., Mailliet, J., Kiontke, S., Sineshchekov, V. A., Hildebrandt, P., Hughes, J., & Essen, L. O. (2011). Spectroscopic and photochemical characterization of the red-light sensitive photosensory module of Cph2 from *Synechocystis* PCC 6803. *Photochemistry and Photobiology*, 87(1), 160–173. <https://doi.org/10.1111/j.1751-1097.2010.00845.x>
- Lamparter, T., Mittmann, F., Gartner, W., Borner, T., Hartmann, E., & Hughes, J. (1997). Characterization of recombinant phytochrome from the cyanobacterium *Synechocystis*. *Proceedings of the National Academy of Sciences*, 94(22), 11792–11797. <https://doi.org/10.1073/pnas.94.22.11792>
- Lamparter, T., Michael, N., Mittmann, F., & Esteban, B. (2002). Phytochrome from *Agrobacterium tumefaciens* has unusual spectral properties and reveals an N-terminal chromophore attachment site. *Proceedings of the National Academy of Sciences*, 99(18), 11628–11633. <https://doi.org/10.1073/pnas.152263999>
- Chai, Y. G., Singh, B. R., Song, P. S., Lee, J., & Robinson, G. W. (1987). Purification and spectroscopic properties of 124-kDa oat phytochrome. *Analytical Biochemistry*, 163(2), 322–330. [https://doi.org/10.1016/0003-2697\(87\)90231-4](https://doi.org/10.1016/0003-2697(87)90231-4)
- Hirose, Y., Shimada, T., Narikawa, R., Katayama, M., & Ikeuchi, M. (2008). Cyanobacteriochrome CcaS is the green light receptor that induces the expression of phycobilisome linker protein. *Proceedings of the National Academy of Sciences*, 105(28), 9528–9533. <https://doi.org/10.1073/pnas.0801826105>
- Rockwell, N. C., Martin, S. S., Gulevich, A. G., & Lagarias, J. C. (2012). Phycoviolobin formation and spectral tuning in the DXCF cyanobacteriochrome subfamily. *Biochemistry*, 51(7), 1449–1463. <https://doi.org/10.1021/bi201783j>
- Rockwell, N. C., Martin, S. S., Feoktistova, K., & Lagarias, J. C. (2011). Diverse two-cysteine photocycles in phytochromes and cyanobacteriochromes. *Proceedings of the National Academy of Sciences of the United States of America*, 108(29), 11854–11859. <https://doi.org/10.1073/pnas.1107844108>
- Rockwell, N. C., Martin, S. S., & Lagarias, J. C. (2016). Identification of Cyanobacteriochromes detecting far-red light. *Biochemistry*, 55(28), 3907–3919. <https://doi.org/10.1021/acs.biochem.6b00299>
- Fushimi, K., Ikeuchi, M., & Narikawa, R. (2017). The expanded red/green Cyanobacteriochrome lineage: An evolutionary hot spot. *Photochemistry and Photobiology*, 93(3), 903–906. <https://doi.org/10.1111/php.12764>
- Fischer, T., Xu, Q.-Z., Zhao, K.-H., Gärtner, W., Slavov, C., & Wachtveitl, J. (2020). Effect of the PHY domain on the photoisomerization step of the forward Pr→Pfr conversion of a knotless phytochrome. *Chemistry A European Journal*. <https://doi.org/10.1002/chem.202003138>
- Slavov, C., Fischer, T., Barnoy, A., Shin, H., Rao, A. G., Wiebeler, C., Zeng, X., Sun, Y., Xu, Q., Gutt, A., Zhao, K., Gärtner, W., Yang, X., Schapiro, I., & Wachtveitl, J. (2020). The interplay between chromophore and protein determines the extended excited state dynamics in a single-domain phytochrome. *Proceedings of the National Academy of Sciences of the United States of America*, 117(28), 16356–16362. <https://doi.org/10.1073/pnas.1921706117>
- Takala, H., Björling, A., Berntsson, O., Lehtivuori, H., Niebling, S., Hoernke, M., Kosheleva, I., Henning, R., Menzel, A., Ihalainen, J. A., & Westenhoff, S. (2014). Signal amplification and transduction in phytochrome photosensors. *Nature*, 509(7499), 245–248. <https://doi.org/10.1038/nature13310>
- Björling, A., Berntsson, O., Lehtivuori, H., Takala, H., Hughes, A. J., Panman, M., Hoernke, M., Niebling, S., Henry, L., Henning,

- R., Kosheleva, I., Chukharev, V., Tkachenko, N. V., Menzel, A., Newby, G., Khakhulin, D., Wulff, M., Ihalainen, J. A., & Westenhoff, S. (2016). Structural photoactivation of a full-length bacterial phytochrome. *Science Advances*, 2(8), e1600920. <https://doi.org/10.1126/sciadv.1600920>
22. Anders, K., Daminelli-Widany, G., Mroginski, M. A., Von Stetten, D., & Essen, L. O. (2013). Structure of the cyanobacterial phytochrome 2 photosensor implies a tryptophan switch for phytochrome signaling. *Journal of Biological Chemistry*, 288(50), 35714–35725. <https://doi.org/10.1074/jbc.M113.510461>
 23. Xu, Q.-Z., Bielytskyi, P., Otis, J., Lang, C., Hughes, J., Zhao, K.-H., Losi, A., Gärtner, W., & Song, C. (2019). MAS NMR on a red/far-red photochromic Cyanobacteriochrome All2699 from Nostoc. *International Journal of Molecular Sciences*, 20(15), 3656. <https://doi.org/10.3390/ijms20153656>
 24. Ihalainen, J. A., Gustavsson, E., Schroeder, L., Donnini, S., Lehtivuori, H., Isaksson, L., Thöing, C., Modi, V., Berntsson, O., Stucki-Buchli, B., Liukkonen, A., Häkkinen, H., Kalenius, E., Westenhoff, S., & Kottke, T. (2018). Chromophore-protein interplay during the phytochrome photocycle revealed by step-scan FTIR spectroscopy. *Journal of the American Chemical Society*, 140(39), 12396–12404. <https://doi.org/10.1021/jacs.8b04659>
 25. Braslavsky, S. E., Gärtner, W., & Schaffner, K. (1997). Phytochrome photoconversion. *Plant, Cell and Environment*, 20(6), 700–706. <https://doi.org/10.1046/j.1365-3040.1997.d01-101.x>
 26. Schmidt, P., Westphal, U. H., Worm, K., Braslavsky, S. E., Gärtner, W., & Schaffner, K. (1996). Chromophore-protein interaction controls the complexity of the phytochrome photocycle. *Journal of Photochemistry and Photobiology B*, 34(1), 73–77. [https://doi.org/10.1016/1011-1344\(95\)07269-1](https://doi.org/10.1016/1011-1344(95)07269-1)
 27. Zhang, C. F., Farrens, D. L., Björling, S. C., Song, P. S., & Kliger, D. S. (1992). Time-resolved absorption studies of native etiolated oat phytochrome. *Journal of the American Chemical Society*, 114(12), 4569–4580. <https://doi.org/10.1021/ja00038a019>
 28. Velazquez Escobar, F., Kneip, C., Michael, N., Hildebrandt, T., Tavraz, N., Gärtner, W., Hughes, J., Friedrich, T., Scheerer, P., Mroginski, M. A., & Hildebrandt, P. (2020). The lumi-R intermediates of prototypical phytochromes. *Journal of Physical Chemistry B*, 124(20), 4044–4055. <https://doi.org/10.1021/acs.jpbc.0c01059>
 29. Kübel, J., Chenchiliyan, M., Ooi, S. A., Gustavsson, E., Isaksson, L., Kuznetsova, V., Ihalainen, J. A., Westenhoff, S., & Maj, M. (2020). Transient IR spectroscopy identifies key interactions and unravels new intermediates in the photocycle of a bacterial phytochrome. *Physical Chemistry Chemical Physics*, 22(17), 9195–9203. <https://doi.org/10.1039/c9cp06995j>
 30. Van Thor, J. J., Borucki, B., Crieleard, W., Otto, H., Lamparter, T., Hughes, J., Hellingwerf, K. J., & Heyn, M. P. (2001). Light-induced proton release and proton uptake reactions in the cyanobacterial phytochrome Cph1. *Biochemistry*, 40(38), 11460–11471. <https://doi.org/10.1021/bi002651d>
 31. Borucki, B., von Stetten, D., Seibeck, S., Lamparter, T., Michael, N., Mroginski, M. A., Otto, H., Murgida, D. H., Heyn, M. P., & Hildebrandt, P. (2005). Light-induced proton release of phytochrome is coupled to the transient deprotonation of the tetrapyrrole chromophore. *Journal of Biological Chemistry*, 280(40), 34358–34364. <https://doi.org/10.1074/jbc.M505493200>
 32. Anders, K., Gutt, A., Gärtner, W., & Essen, L. O. (2014). Photo-transformation of the red light sensor cyanobacterial phytochrome 2 from synechocystis species depends on its tongue motifs. *Journal of Biological Chemistry*, 289(37), 25590–25600. <https://doi.org/10.1074/jbc.M114.562082>
 33. Von Stetten, D., Seibeck, S., Michael, N., Scheerer, P., Mroginski, M. A., Murgida, D. H., Krauss, N., Heyn, M. P., Hildebrandt, P., Borucki, B., & Lamparter, T. (2007). Highly conserved residues Asp-197 and His-250 in Agp1 phytochrome control the proton affinity of the chromophore and Pfr formation. *Journal of Biological Chemistry*, 282(3), 2116–2123. <https://doi.org/10.1074/jbc.M608878200>
 34. Sadeghi, M., Balke, J., Schneider, C., Nagano, S., Stellmacher, J., Lochnit, G., Lang, C., Weise, C., Hughes, J., & Alexiev, U. (2020). Transient deprotonation of the chromophore affects protein dynamics proximal and distal to the linear tetrapyrrole chromophore in phytochrome Cph1. *Biochemistry*, 59(9), 1051–1062. <https://doi.org/10.1021/acs.biochem.9b00967>
 35. Heyne, K., Herbst, J., Stehlik, D., Esteban, B., Lamparter, T., Hughes, J., & Diller, R. (2002). Ultrafast dynamics of phytochrome from the cyanobacterium *Synechocystis*, reconstituted with phycocyanobilin and phycoerythrobilin. *Biophysical Journal*, 82(2), 1004–1016. [https://doi.org/10.1016/S0006-3495\(02\)75460-X](https://doi.org/10.1016/S0006-3495(02)75460-X)
 36. Kim, P. W., Rockwell, N. C., Martin, S. S., Lagarias, J. C., & Larsen, D. S. (2014). Heterogeneous photodynamics of the Pfr state in the cyanobacterial phytochrome Cph1. *Biochemistry*, 53(28), 4601–4611. <https://doi.org/10.1021/bi5005359>
 37. Fischer, T., van Wilderen, L. J. G. W., Gnau, P., Bredenbeck, J., Essen, L.-O., Wachtveitl, J., & Slavov, C. (2021). Ultrafast photoconversion dynamics of the knotless phytochrome SynCph2. *International Journal of Molecular Sciences*, 22(19), 10690. <https://doi.org/10.3390/ijms221910690>
 38. Rohmer, T., Lang, C., Bongards, C., Gupta, K. B. S. S., Neugebauer, J., Hughes, J., Gärtner, W., & Matsysik, J. (2010). Phytochrome as molecular machine: Revealing chromophore action during the Pfr → Pr photoconversion by magic-angle spinning NMR spectroscopy. *Journal of the American Chemical Society*, 132(12), 4431–4437. <https://doi.org/10.1021/ja9108616>
 39. Yang, X., Ren, Z., Kuk, J., & Moffat, K. (2011). Temperature-scan cryocrystallography reveals reaction intermediates in bacteriophytochrome. *Nature*, 479(7373), 428–431. <https://doi.org/10.1038/nature10506>
 40. Chizhov, I., Zorn, B., Manstein, D. J., & Gärtner, W. (2013). Kinetic and thermodynamic analysis of the light-induced processes in plant and cyanobacterial phytochromes. *Biophysical Journal*, 105(9), 2210–2220. <https://doi.org/10.1016/j.bpj.2013.09.033>
 41. Kraskov, A., Nguyen, A. D., Goerling, J., Buhke, D., Velazquez Escobar, F., Fernandez Lopez, M., Michael, N., Sauthof, L., Schmidt, A., Piwowarski, P., Yang, Y., Stensitzki, T., Adam, S., Bartl, F., Schapiro, I., Heyne, K., Siebert, F., Scheerer, P., Mroginski, M. A., & Hildebrandt, P. (2020). Intramolecular proton transfer controls protein structural changes in phytochrome. *Biochemistry*, 59(9), 1023–1037. <https://doi.org/10.1021/acs.biochem.0c00053>
 42. Chen, E., Lapko, V. N., Lewis, J. W., Song, P. S., & Kliger, D. S. (1996). Mechanism of native oat phytochrome photoreversion: A time-resolved absorption investigation. *Biochemistry*, 35(3), 843–850. <https://doi.org/10.1021/bi952115z>
 43. Consiglieri, E., Gutt, A., Gärtner, W., Schubert, L., Viappiani, C., Abbruzzetti, S., & Losi, A. (2019). Dynamics and efficiency of photoswitching in biliverdin-binding phytochromes. *Photochemical and Photobiological Sciences*, 18(10), 2484–2496. <https://doi.org/10.1039/c9pp00264b>
 44. Xu, Q.-Z., Goett-Zink, L., Gärtner, W., Zhao, K.-H., & Kottke, T. (2020). Tongue refolding in the knotless Cyanobacterial phytochrome All2699. *Biochemistry*, 59(22), 2047–2054. <https://doi.org/10.1021/acs.biochem.0c00209>
 45. Slavov, C., Hartmann, H., & Wachtveitl, J. (2015). Implementation and evaluation of data analysis strategies for time-resolved optical spectroscopy. *Analytical Chemistry*, 87(4), 2328–2336. <https://doi.org/10.1021/ac504348h>
 46. Van Stokkum, I. H. M. M., Larsen, D. S., & van Grondelle, R. (2004). Global and target analysis of time-resolved spectra.

- Biochimica et Biophysica Acta*, 1657(2–3), 82–104. <https://doi.org/10.1016/j.bbabi.2004.04.011>
47. Merga, G., Lopez, M. F., Fischer, P., Piwowarski, P., Nogacz, Ż., Kraskov, A., Buhrke, D., Escobar, F. V., Michael, N., Siebert, F., Scheerer, P., Bartl, F., & Hildebrandt, P. (2021). Light- and temperature-dependent dynamics of chromophore and protein structural changes in bathy phytochrome Agp2. *Physical Chemistry Chemical Physics*, 23(33), 18197–18205. <https://doi.org/10.1039/d1cp02494a>
 48. Buhrke, D., Kuhlmann, U., Michael, N., & Hildebrandt, P. (2018). The photoconversion of phytochrome includes an unproductive shunt reaction pathway. *ChemPhysChem*, 19(5), 566–570. <https://doi.org/10.1002/cphc.201701311>
 49. Kim, Y., Xu, Q.-Z., Zhao, K.-H., Gärtner, W., Matysik, J., & Song, C. (2020). Lyophilization reveals a multitude of structural conformations in the chromophore of a Cph2-like phytochrome. *Journal of Physical Chemistry B*, 124(33), 7115–7127. <https://doi.org/10.1021/acs.jpcc.0c03431>
 50. Rumpf, J. A., Takala, H., Liukkonen, A., & Ihalainen, J. A. (2019). UV-Vis spectroscopy reveals a correlation between Y263 and BV protonation states in Bacteriophytochromes. *Photochemistry and Photobiology*, 95(4), 969–979. <https://doi.org/10.1111/php.13095>
 51. Velazquez Escobar, F., Lang, C., Takiden, A., Schneider, C., Balke, J., Hughes, J., Alexiev, U., Hildebrandt, P., & Mroginiski, M. A. (2017). Protonation-dependent structural heterogeneity in the chromophore binding site of Cyanobacterial phytochrome Cph1. *The Journal of Physical Chemistry B*, 121(1), 47–57. <https://doi.org/10.1021/acs.jpcc.6b09600>
 52. Wagner, J. R., Zhang, J., Von Stetten, D., Günther, M., Murgida, D. H., Mroginiski, M. A., Walker, J. M., Forest, K. T., Hildebrandt, P., & Vierstra, R. D. (2008). Mutational analysis of *Deinococcus radiodurans* bacteriophytochrome reveals key amino acids necessary for the photochromicity and proton exchange cycle of phytochromes. *Journal of Biological Chemistry*, 283(18), 12212–12226. <https://doi.org/10.1074/jbc.M709355200>
 53. Hahn, J., Strauss, H. M., Landgraf, F. T., Gimenez, H. F., Lochnit, G., Schmieder, P., & Hughes, J. (2006). Probing protein-chromophore interactions in Cph1 phytochrome by mutagenesis. *FEBS Journal*, 273(7), 1415–1429. <https://doi.org/10.1111/j.1742-4658.2006.05164.x>
 54. Burgie, E. S., Bussell, A. N., Walker, J. M., Dubiel, K., & Vierstra, R. D. (2014). Crystal structure of the photosensing module from a red/far-red light-absorbing plant phytochrome. *Proceedings of the National Academy of Sciences of the United States of America*, 111(28), 10179–10184. <https://doi.org/10.1073/pnas.1403096111>

Authors and Affiliations

Tobias Fischer¹  · Lisa Köhler²  · Tanja Ott¹  · Chen Song²  · Josef Wachtveitl¹  · Chavdar Slavov¹ 

Tobias Fischer
fischer@theochem.uni-frankfurt.de

Lisa Köhler
l.koehler@uni-leipzig.de

Tanja Ott
ott@chemie.uni-frankfurt.de

Chen Song
chen.song@uni-leipzig.de

¹ Institute of Physical and Theoretical Chemistry, Goethe University Frankfurt Am Main, Max-von-Laue-Straße 7, 60438 Frankfurt, Germany

² Institute for Analytical Chemistry, University of Leipzig, Linnéstraße 3, 04103 Leipzig, Germany

5 Publications

5.6 Reference [V]

Fischer et al., *Biochim. Biophys. Acta - Bioenerg.* 2023

Conserved Tyrosine in Phytochromes controls the Photodynamics through Steric Demand and Hydrogen Bonding Capabilities

T. Fischer, L. Köhler, P.D. Engel, C. Song, W. Gärtner, J. Wachtveitl, C. Slavov

Biochim. Biophys. Acta - Bioenerg. 2023.

DOI: 10.1016/j.bbabi.2023.148996



Conserved tyrosine in phytochromes controls the photodynamics through steric demand and hydrogen bonding capabilities

Tobias Fischer^a, Lisa Köhler^b, Philipp D. Engel^a, Chen Song^b, Wolfgang Gärtner^b, Josef Wachtveitl^{a,*}, Chavdar Slavov^{a,c,**}

^a Institute of Physical and Theoretical Chemistry, Goethe University Frankfurt am Main, Max-von-Laue-Straße 7, 60438 Frankfurt, Germany

^b Institute for Analytical Chemistry, University of Leipzig, Linnéstraße 3, 04103 Leipzig, Germany

^c Department of Chemistry, University of South Florida, 4202 E. Fowler Avenue, 33620 Tampa, United States of America

ARTICLE INFO

Keywords:
Phytochromes
Site-specific mutant
Photochemistry
Time-resolved spectroscopy
Ultrafast dynamics

ABSTRACT

Using ultrafast spectroscopy and site-specific mutagenesis, we demonstrate the central role of a conserved tyrosine within the chromophore binding pocket in the forward ($P_r \rightarrow P_{fr}$) photoconversion of phytochromes. Taking GAF1 of the knotless phytochrome All2699g1 from *Nostoc* as representative member of phytochromes, it was found that the mutations have no influence on the early (<30 ps) dynamics associated with conformational changes of the chromophore in the excited state. Conversely, they drastically impact the extended protein-controlled excited state decay (>100 ps). Thus, the steric demand, position and H-bonding capabilities of the identified tyrosine control the chromophore photoisomerization while leaving the excited state chromophore dynamics unaffected. In effect, this residue operates as an isomerization-steric-gate that tunes the excited state lifetime and the photoreaction efficiency by modulating the available space of the chromophore and by stabilizing the primary intermediate Lumi-R. Understanding the role of such a conserved structural element sheds light on a key aspect of phytochrome functionality and provides a basis for rational design of optimized photoreceptors for biotechnological applications.

1. Introduction

Phytochrome photoreceptors operate via a light-induced transition from a thermostable dark state to a light-adapted state (photoproduct). The transition is accomplished by $Z \rightarrow E$ photoisomerization along the C15=C16 double bond of the embedded bilin chromophore (Fig. 1). The isomerization initiates reorganization of the entire protein matrix via several intermediate steps to form the light-adapted state [1,2].

This superfamily of photoreceptors is responsible for the regulation of photomorphogenesis, photoprotection, phototaxis, and other biologically relevant processes in a variety of organisms [3–8]. Moreover, phytochromes have attracted considerable interest due to their application potential in optogenetics and biomedical imaging [9–13]. Evidently, the engineering of phytochromes with properties aiming towards specific applications relies strongly on understanding the intricate mechanism of their photodynamics. However, such detailed understanding is still lacking due to the high complexity and diversity of the

phytochrome dynamics [14–20]. At present, different models have been proposed to explain the observed experimental results. In some phytochromes, the dynamics is described with multiple excited state decays in the context of ground state heterogeneity [21–24]. In contrast, other phytochromes have highly non-exponential dynamics [25–29], plausibly resulting from protein active-site relaxation/solvation and/or distributed type kinetics rather than distinct ground state heterogeneity with reactive and non-reactive populations [25,27–30].

Previously, we pointed out certain shared kinetic features in the multiphasic ultrafast dynamics of the red-absorbing form (P_r) of several cyanobacterial phytochromes exhibiting long excited state lifetimes (All2699g1 [27], All2699g1g2 [28], SynCph2 [30], Slr1393g3 [19]). These phytochromes show nearly identical chromophore-related P_r excited state dynamics until ~50 ps followed by a distributed, non-exponential excited state decay with phytochrome-specific lifetimes [19,27,28,30]. Thus, our results suggested a common mechanism where the distributed kinetics arises from control of the photoisomerization by

* Corresponding author.

** Correspondence to: C. Slavov, Department of Chemistry, University of South Florida, 4202 E. Fowler Avenue, 33620 Tampa, United States of America.

E-mail addresses: fischer@theochem.uni-frankfurt.de (T. Fischer), l.koehler@uni-leipzig.de (L. Köhler), p.engel@stud.uni-frankfurt.de (P.D. Engel), chen.song@uni-leipzig.de (C. Song), wolfgang.gaertner@uni-leipzig.de (W. Gärtner), wveitl@theochem.uni-frankfurt.de (J. Wachtveitl), chslavov@usf.edu (C. Slavov).

<https://doi.org/10.1016/j.bbabio.2023.148996>

Received 17 February 2023; Received in revised form 2 June 2023; Accepted 6 July 2023

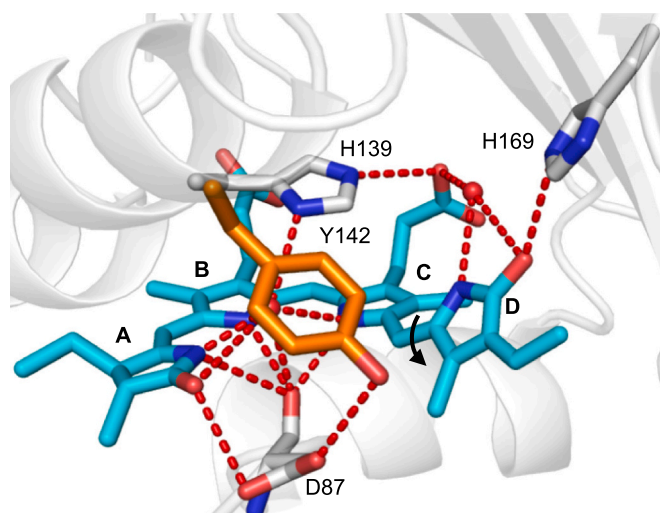


Fig. 1. Structural snapshot of the chromophore binding pocket of All2699g1 (PDB ID: 6OZA) [27]. The phycocyanobilin (PCB) chromophore (cyan) interacts with the highly conserved amino acids D87 and H139 via the pyrrole water (partly obscured by the tyrosine side chain) forming a hydrogen bonding network. This network extends to H169 via another water molecule. Y142 (orange) forms a hydrogen bond to D87 via its hydroxyl group. The black arrow indicates the isomerization direction.

the reorganization of the protein binding pocket. In particular, we identified a conserved tyrosine residue (Y142 in All2699g1, Fig. 1) in the vicinity of the chromophore [27,28,30] with a potentially instrumental role in the photoisomerization process [27,29,31,32]. The positioning of this residue together with the geometry and flexibility of the pocket were assumed to be major factors affecting the photophysical properties of phytochromes [27–29,33].

Therefore, manipulating these properties should result in a shift of the protein reorganization timescale [28] and in turn in a change of the bilin excited state lifetime, thereby affecting the photochemical and fluorescence quantum yields of phytochromes [31,32,34]. To provide direct evidence for the special role of this highly conserved amino acid residue, we designed two different mutants (Y142F and Y142W) of tyrosine 142 in the GAF domain All2699g1 of the knotless phytochrome All2699g1g2 (*Nostoc* sp. PCC 7120) and compared their primary ultrafast P_r photodynamics to the wild type. All2699g1 undergoes a photochemical reaction between 638 nm (dark state) and 689 nm (photoproduct).

2. Materials and methods

2.1. Protein preparation

Preparation of All2699g1 was described elsewhere in detail [27]. The two mutants, Y142F and Y142W of All2699g1, were generated by PCR using the plasmid pET30 encoding All2699g1 from *Nostoc* as a template and the degenerate primers 5'-GTGGAATTYTAAACAGCAATGGGTGTG-3' (fw) and 5'-GCTGTTAARAATTCCACATGACAAGAGTC-3' (rv). The above-mentioned plasmid as well as the plasmid pACYC carrying the PCB-generating enzymes ho1-*pcyA* were co-transformed into *E. coli* BL21 DE3 competent cells to allow heterologous protein expression and in vivo assembly of the phytochromes. Purification was performed as described for the WT [27,35]. The final buffer conditions for the experiments were set to 20 mM KPB, 150 mM NaCl, and 5 % Glycerol at pH 7.2 in the WT and both mutants [27,35].

2.2. Stationary characterization

Stationary absorption spectra of the investigated samples were

obtained using a Specord S600 absorption spectrometer (Analytik Jena). Conversion between the P_r and the P_{fr} state was achieved by illumination with appropriate LEDs (730 nm and 590 nm; respectively, 1 W, Thorlabs). To obtain a pure P_{fr} spectrum from the mixture of P_r and P_{fr} in the photostationary state (PSS) generated after illumination at 590 nm, a scaled P_r spectrum was subtracted to optimally remove P_r contribution. The scaling factor S was determined by visual inspection and the resulting P_{fr} spectrum was then multiplied by $1 + (S/(1 - S))$ to simulate complete conversion to the P_{fr} state.

Fluorescence spectra were measured with an FP 8500 fluorimeter (Jasco) and corrected for background, reabsorption, detector sensitivity, and solvent contributions.

CD spectra were recorded using a J-710 CD-spectrometer (Jasco) under a constant nitrogen flow of 2.0 l/min. To avoid accumulation of the P_{fr} state from the instrument's measuring beam, samples were irradiated with a 730 nm LED (1 W, Thorlabs) after each scan for five single scans in total. These scans were averaged to yield the P_r spectra. The scans were recorded at 20 °C.

Quantum yields (QY) were determined by monitoring the induced absorption increase at 700 nm or decrease at 640 nm using a V-650 spectrometer (Jasco) under constant illumination by the appropriate LED at a set temperature of 20 °C. The LED light was focused, recollimated and coupled into an optical fiber. The fiber was then positioned such that the light emerged from the light guide directly above the sample surface to ensure that the complete output of the fiber is collected within the sample. The light intensity entering the sample cuvette was measured using a calibrated light detector (P-9710, Gigahertz-Optik). The changes in absorption were measured every 2 s for 15 min. The probe light was determined to have negligible actinic effect in absence of the illumination. In the calculations, only the linear part of the absorption changes (typically first 200 s) was used, to avoid contributions of the photoproduct absorption. The calculations were performed as described previously [36], for details see Supporting Information.

2.3. Vis-pump-Vis-probe transient absorption (TA) measurements

The time-resolved TA measurements were recorded using a home-built pump-probe setup, as described in detail previously [36]. To summarize, the fundamental laser pulses (1 mJ, 775 nm, 130 fs, 1 kHz) provided by a Ti:Sapphire amplifier system (Clark, MXR-CPA-iSeries) were used to generate the pump pulses using a home-built two stage NOPA (noncollinear optical parametric amplifier) [37,38] with a prism compressor for pulse compression located between the two NOPA stages. White light continuum probe pulses (300–750 nm) were generated by focusing the laser fundamental beam into a CaF₂-crystal (5 mm). Afterwards, the probe pulses were split into probe and reference beam where the probe beam was focused at the sample position, collected and directed into a spectrograph while the reference beam was guided directly into a second spectrograph. The spectrographs (AMKO Multimode) contained gratings with 1200 grooves/mm blazed at 500 nm and a photodiode array with a detection range set to 490–710 nm. The instrument response function (IRF) of ~70 fs in the experiments was estimated from the pump probe cross correlation and confirmed using an autocorrelator (APE, APE Pulse Check). All measurements were carried out under magic angle conditions (54.7° pump-probe polarization difference) to eliminate anisotropic contributions. The sample (OD ~0.4 at 640 nm) was held in a fused silica cuvette with an optical path length of 1 mm. To avoid accumulation of photoproducts the cuvette was constantly moved in the plane perpendicular to the direction of probe pulse propagation while being constantly illuminated with a high-power LED at 730 nm recovering the P_r state during the measurement.

2.4. Data analysis

Data analysis was performed using OPTIMUS (<http://www.optimus>

sft.org/) [39]. We performed model-independent lifetime distribution analysis (LDA) on all ultrafast transient absorption datasets. LDA utilizes a quasi-continuous set of 100 exponential functions with fixed lifetimes which are equally spaced on a log10 scale where the pre-exponential amplitudes are fitted to the data. By plotting these amplitudes in dependence on the detection wavelength in form of a contour plot the so-called lifetime density maps (LDM) are obtained [40]. LDMs are read similarly to decay-associated spectra (DAS) from global lifetime analysis: positive amplitudes represent the decay of excited state and product absorption (ESA, PA) or rise of ground state bleach or stimulated emission (GSB and SE), while negative amplitudes represent the rise of absorption (ESA, PA) or the decay of GSB and SE. Another main advantage of LDA besides its independence from kinetic models is its ability to account for non-exponential kinetics.

3. Results and discussion

3.1. Photochemical properties of the tyrosine mutants

The normalized absorption spectra of All2699g1 wildtype (WT) and both mutants show that the overall spectral shape and position of the P_r absorption remain mostly unaffected in WT and Y142F ($\lambda_{\max} = 638$ nm), while a red shift (9 nm) is observed for Y142W ($\lambda_{\max} = 647$ nm) (Fig. 2A). In terms of fluorescence, WT and Y142W exhibit similar intensities, while the emission is significantly increased in Y142F (Fig. 2B). In analogy to the absorption, the spectral position of the fluorescence maximum is similar for Y142F and WT and red shifted (~ 7 nm) in Y142W. The CD-spectra of the P_r state show only minor differences in the positive 350 nm band. Similar to the red shift found in the corresponding absorption spectrum, the negative CD band in the Y142W mutant is shifted to ~ 647 nm (Fig. 2C). Overall, these properties suggest that the chromophore geometry is not radically altered upon introduction of the respective mutations in agreement with previous reports on related mutations in other phytochromes [33,34,41,42].

In contrast, we observe significant differences for the P_{fr} state, including reduced P_{fr} formation in both the Y142F and – most dramatically – the Y142W mutants as compared to the WT, and a spectral shift

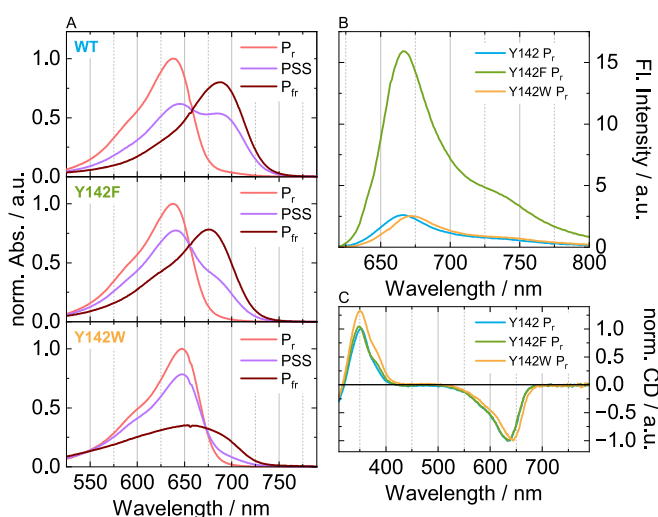


Fig. 2. (A) Normalized stationary absorption spectra of the P_r state, the photostationary state (PSS) and the P_{fr} state (top to bottom) of the All2699g1 WT [27], the Y142F, and the Y142W mutants. The pure P_{fr} spectrum was obtained by subtraction of a scaled P_r spectrum from the PSS spectrum, followed by multiplication with a factor to simulate complete photoconversion to the P_{fr} state. (B) Fluorescence spectra of the P_r state of WT ($\lambda_{fl,\max} = 666$ nm), Y142F ($\lambda_{fl,\max} = 666$ nm) and Y142W ($\lambda_{fl,\max} = 673$ nm) after excitation at 638 nm, 638 nm and 648 nm. (C) Normalized CD spectra of the P_r state of WT, Y142F and Y142W.

and broadening of the P_{fr} absorption band [31,34]. The photoconversion quantum yield (QY) of the $P_r \rightarrow P_{fr}$ reaction is diminished from $\sim 10\%$ in the WT to 2.4 % in Y142F. It is even lower in the Y142W mutant, where we measured a QY of only 0.2 %. These values agree well with the relative amount of P_{fr} state obtained by constant illumination. The reduced product formation QY in Y142F, as compared to the WT, correlates with the increased fluorescence QY (by a factor of ~ 5) and is in agreement with observations for homologous mutants of other phytochromes [29,31–34]. Notably, despite the similar fluorescence intensity with the WT, the Y142W mutant exhibits an even lower photoconversion QY, which implies a dominant role of non-radiative deactivation in the W-mutant.

3.2. Ultrafast P_r^* dynamics in the tyrosine mutants of All2699g1

The critical role of the conserved tyrosine residue is documented by the direct impact of the mutations on the ultrafast excited state dynamics. The TA data (Fig. 3) of all three samples show two signal contributions: a broad positive signal below 550 nm previously assigned [27] to excited state absorption (ESA) and a broad negative signal from 575 nm to >700 nm corresponding to the ground state bleach (GSB) and stimulated emission (SE). Depending on the sample, these features decay

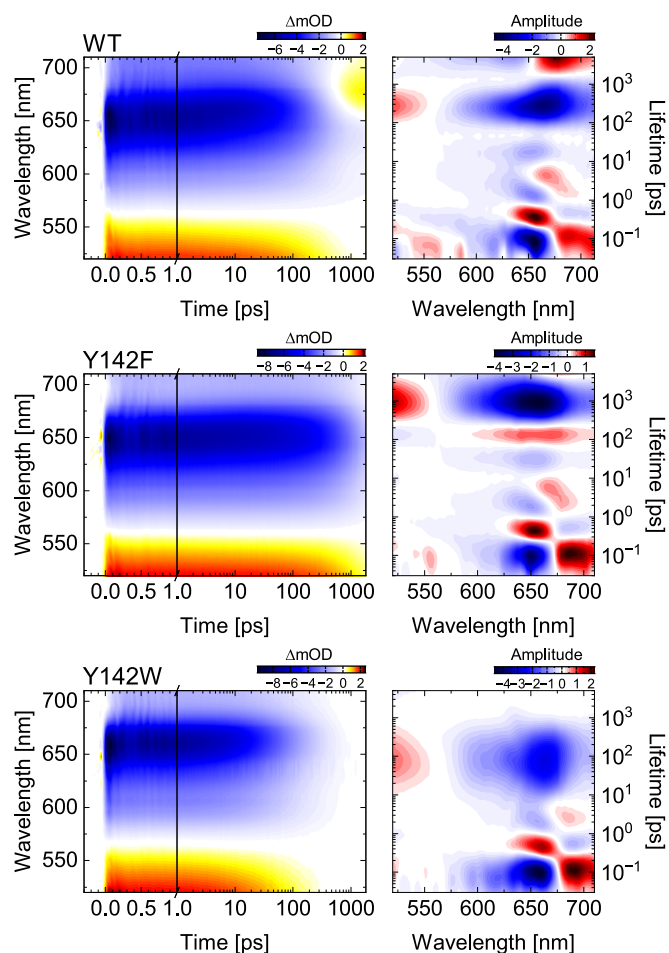


Fig. 3. (Left) Transient absorption data of the forward ($P_r \rightarrow P_{fr}$) dynamics of All2699g1 WT, Y142F, and Y142W phytochromes after excitation at 640 nm. (Right) Lifetime density maps (LDM) obtained from lifetime distribution analysis of the transient absorption data. In analogy to interpreting decay-associated spectra [39,43], the positive (red) amplitudes account for the decay of excited state (ESA) and product absorption (PA) or rise of ground state bleach (GSB) and stimulated emission (SE). Negative amplitudes correspond to rise of absorption (ESA, PA) or decay of GSB and SE.

on the 100 ps to 2 ns timescale. Only in the WT, a positive signal associated with the formation of the primary photoproduct Lumi-R is detected at later delay times between 650 and 710 nm [27]. Due to the low photoisomerization yields, the latter signal is not detectable in the mutants' datasets.

The lifetime distribution analysis (LDA) of the experimental datasets from the investigated samples result in similar kinetic patterns (Fig. 3). The pairs of positive (675–710 nm) and negative amplitude (575–675 nm) distributions at ~100 fs represent departure from the Franck-Condon region. The following lifetime distributions between 1 and 30 ps reflect spectral shift dynamics at the overlap range of the steep edges of the ESA and GSB/SE bands (650–680 nm). The absence of positive-amplitude distributions in the spectral range of the main ESA band (525–560 nm) indicates that essentially no excited state decay occurs with lifetimes below 30 ps. Accordingly, we assign these distributions to dynamics on the excited state potential energy surface, mostly correlated to conformational dynamics of the chromophore and/or active-site relaxation [25,27–30]. In the WT and in Y142F, the negative-amplitude distribution (575–675 nm) with a lifetime of ~20 ps is resolved clearly. In Y142W, the corresponding lifetime distribution is also present, but it merges with the subsequent negative-amplitude distribution.

The following pair of positive (500–550 nm) and negative amplitude (575–710 nm) distributions account for the decay of the excited state based on their spectral positions coinciding with the spectral signature of the ESA and GSB/SE. The distributed nature of this decay is associated with protein controlled dynamics within the binding pocket that determine the excited state relaxation timescale [27,28,30]. The distributions appear significantly broadened in lifetime and their maxima vary between the mutants and the WT – 250 ps in WT, 1000 ps in Y142F, and 90 ps in Y142W. Notably, the relative distribution width (in lifetime) is

significantly increased in Y142W, as indicated by the positive-amplitude distribution of the ESA decay at 500–550 nm. In the WT, the elongation of the negative amplitude distribution at wavelengths >650 nm accounts for the formation of the primary photoproduct Lumi-R. Also in the WT, the formed Lumi-R is represented by the positive (650–710 nm) and negative amplitude (500–650 nm) distributions at >1 ns. In Y142F, the lack of observable Lumi-R formation is due to the long excited state lifetime exceeding the time window of our measurement, while in Y142W the extremely low QY of 0.2 % can be directly correlated to the absence of Lumi-R absorption.

3.3. The key role of the conserved tyrosine in the P_r dynamics

Our results can be summarized in the following scheme (Fig. 4). Strikingly, the mutations of Y142 predominantly affect the lifetime distributions longer than 30 ps, i.e., those components associated with the distributed excited state decay. In contrast, the early sub-30 ps dynamics, arising from conformational changes of the chromophore itself (see above), remain mostly unchanged. Note that slight changes in ring D torsion are not excluded by our model on this timescale. However, due to the limited mobility of ring D, motions in other parts of the chromophore contribute predominantly to the observed spectral shifts. These early chromophore dynamics initiate reorganization of the protein binding pocket which ultimately enables the isomerization by withdrawing the conserved tyrosine from the chromophore (Fig. 4A) [27]. Consequently, the results imply that the mutations do not drastically alter the chromophore conformation and properties in the P_r state which is in line with the similar spectral shape of the absorption, CD and fluorescence spectra of Y142F and Y142W. This interpretation is further supported by structural studies of similar mutants of other

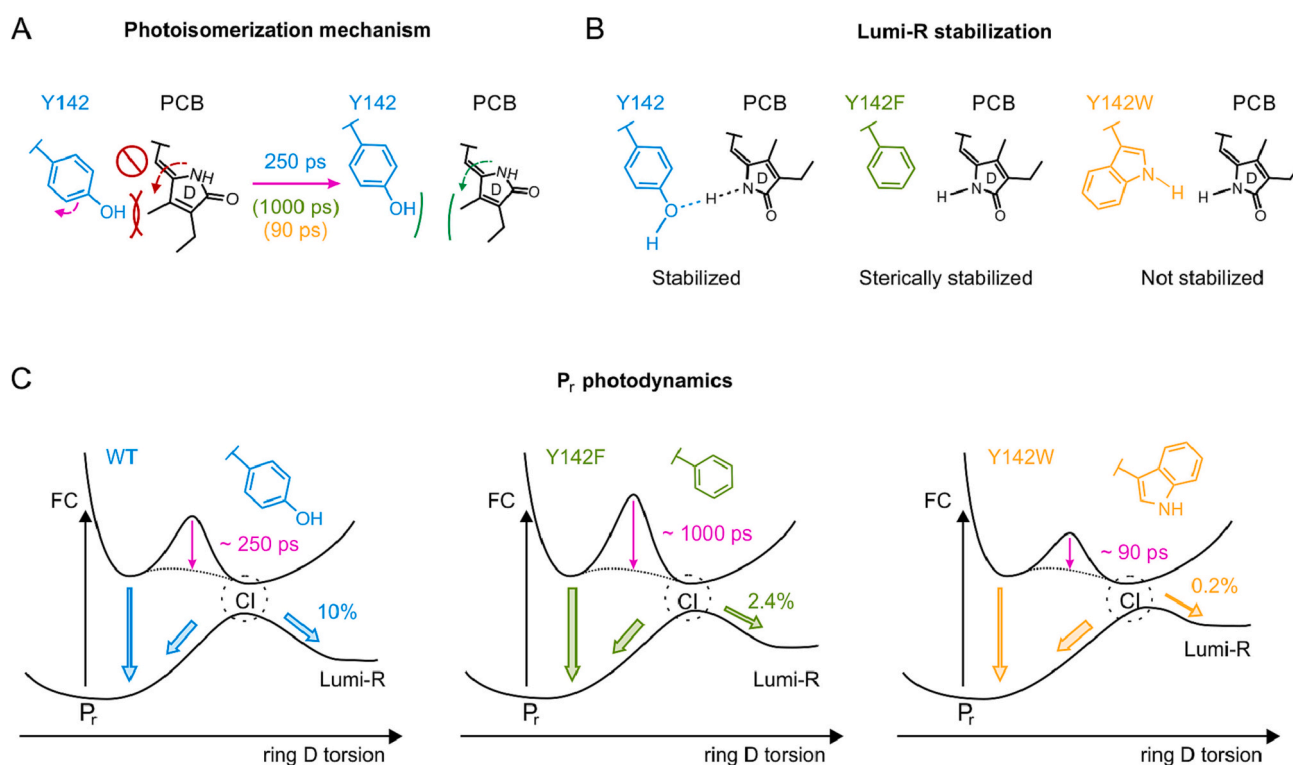


Fig. 4. Schematic representation of the mechanistic understanding derived for the primary P_r photodynamics of the All2699g1 WT (cyan), Y142F (green) and Y142W (yellow) mutants. (A) Photoisomerization mechanism of All2699g1 WT. Initially the isomerization is sterically blocked (red lines/arrow) by Y142. After reorganization of the protein matrix, the residue is withdrawn to allow the isomerization to proceed (green lines/arrow) on the hundreds of ps timescale depending on the mutant. (B) Different types and extents of stabilization of the primary photointermediate Lumi-R for All2699g1 WT, Y142F, and Y142W. While the WT stabilizes the isomerized ring D by both hydrogen bonding to the pyrrole nitrogen and steric interactions, in the Y142F mutant Lumi-R is only stabilized by steric interactions rationalizing the reduced QY. In Y142W, both steric and hydrogen bonding stabilization is mostly absent leading to a lack of stabilization and significantly reduced QY. (C) Schematic representation of the P_r photodynamics in the investigated mutants.

phytochromes [31,33,34].

Beyond 30 ps, the center position of the lifetime distributions describing the excited state decay varies significantly between the mutants and the WT. In Y142F, the excited state lifetime is extended considerably, explaining the observed high fluorescence QY. In contrast, in Y142W, the lifetime distribution describing the excited state decay shifts towards shorter lifetimes (90 ps). The distribution is also comparably broader, hinting towards a larger conformational space of the protein environment and a more flexible binding pocket. We hypothesize that in the binding pocket of the mutant, the tryptophan, due to its steric demand, adopts a more distal position to the chromophore as compared to the smaller aromatic amino acid residues in the WT and Y142F. While this orientation does facilitate the access to the isomerization conical intersection, as indicated by the reduced excited state lifetime, the tryptophan residue lacks the ability to stabilize the primary photoproduct Lumi-R. Effectively, this favors rapid relaxation to the P_r state over formation of the Lumi-R intermediate (Fig. 4B), and explains both the accelerated excited state relaxation and the diminished product QY.

Interestingly, we do not observe a general trend for the QY in relation to the lifetime of the excited state. Our previous studies on All2699g1 and All2699g1g2 WT [27,28] suggested that shorter excited state lifetimes translate to more efficient photoconversion. Similar observations were made in red/green CBCRs [22,24,44,45]. However, in the case of the tyrosine mutants the fastest reaction (Y142W) is in fact the most inefficient one. Evidently, a complex interplay of protein and chromophore dynamics is required to reach and stabilize the primary photo-intermediate, i.e., to ensure efficient photoconversion rather than just fast photochemistry.

Considering the structural differences of tryptophan and phenylalanine as compared to the native tyrosine, the significant reduction in Lumi-R, and consequently in P_{fr} formation, in both Y142F and Y142W, can be rationalized by the lack of the properly positioned hydroxyl group and its hydrogen bonding capabilities. In particular, the conserved tyrosine residue is crucially involved in stabilizing Lumi-R [31,46–48] and P_{fr} [2,42,49,50], either via direct hydrogen bonding to the D ring or through the corresponding hydrogen bonding network; interactions that are missing or strongly modified in the Y142F and Y142W mutants studied here (Fig. 4B). Recently, it has been suggested that the removal of the hydroxyl group alters the water content inside the binding pocket of bacteriophytochrome *DrBphP*, interrupting the hydrogen bonding network [33]. Such a disruption may further hinder or even prevent the proper opening of the steric gate. Note, however, that the presence of such water molecule in the P_r state of knotless phytochromes has not been confirmed [27,51,52].

While Y142F does lack the hydroxyl group of tyrosine, and thereby hydrogen bonds from this substituent, it is still very similar to tyrosine in terms of shape and steric demand, as illustrated by the crystal structures of the Y263F mutant of *SynCph1* (PDB ID: 3ZQ5) [34] and *DrBphP* (PDB ID: 5NWN) [31,33] in their P_r state. However, the phenylalanine adopts a more proximal position to the D ring as compared to the WT tyrosine [33]. This more compact phenylalanine packing correlates with the increased lifetime in the context of our model requiring an extended time to be withdrawn from the chromophore.

Traditionally, the multiphasic kinetics of the P_r state of long lived phytochromes have been described in a rather static manner relying on ground state heterogeneity [21–24]. Recently, Wang and co-workers challenged this picture by evoking active-site solvation [29]. We showed previously that ground state heterogeneity is neither the origin nor a dominant factor defining the kinetic pattern [27,28,30] we observe in multiple phytochromes [30]. Instead, our results offer a distinctly dynamic perspective where the reorganization of the protein matrix assumes control on the timescale of the photoisomerization reaction. Note, photoisomerization reactions especially in photoreceptors are inherently ultrafast (i.e. proceed on the sub-picosecond-to-picosecond timescale) [53–57], and in general hardly occur on the hundreds-of-picoseconds

timescale. Phytochromes defy this general rule by dynamically adjusting the photoisomerization energetic barrier (Fig. 4). In effect, the protein scaffold can serve as an environmental sensor that regulates and fine-tunes the photoreception quantum efficiency [58–61].

4. Conclusion

Overall, the considerable impact of the tyrosine mutations (Y142F and Y142W) on the ultrafast P_r dynamics emphasizes the direct role of this conserved amino acid residue. It is evident that the ultrafast dynamics can be separated into two parts: i) an initial sub-30 ps conformational dynamics linked to the chromophore on the excited state and ii) a slower distributed excited state decay. The former process is unaffected, while the latter is significantly altered by the mutations. The presence of this pattern in multiple long-lived phytochromes (P_r excited state lifetime >100 ps) [19,27,28,30] and in the here reported mutants supports a common mechanism where the excited state-chromophore dynamics trigger changes in the protein environment in proximity of the chromophore necessary to accommodate the isomerization. The associated protein dynamics that effectively opens the steric gate (repositioning of the conserved tyrosine) in turn control the timescale of the photoisomerization reaction, thereby imposing a distributed kinetics character on it [27,28]. In this context, the position of the conserved tyrosine, the available space, the flexibility of the pocket, and the properties of the hydrogen bonding network can be identified as decisive factors for the progression and the resulting photochemical efficiency of phytochromes [25,28,29,33]. Consequently, our study highlights the existence of common structural and mechanistic patterns in the photo-activation of phytochromes, which can serve as a basis for rational design of optimized phytochromes for biotechnological applications.

CRedit authorship contribution statement

Tobias Fischer: Conceptualization, Formal analysis, Investigation, Methodology, Validation, Visualization, Writing – original draft, Writing – review & editing. **Lisa Köhler:** Resources, Writing – review & editing. **Philipp D. Engel:** Investigation, Validation. **Chen Song:** Supervision, Writing – review & editing, Funding acquisition, Project administration. **Wolfgang Gärtner:** Supervision, Writing – review & editing, Funding acquisition, Project administration. **Josef Wachtveitl:** Conceptualization, Supervision, Writing – review & editing, Funding acquisition, Project administration. **Chavdar Slavov:** Conceptualization, Software, Formal analysis, Methodology, Visualization, Writing – original draft, Writing – review & editing, Supervision, Project administration, Funding acquisition.

Declaration of competing interest

The authors declare that they have no known competing financial interests or personal relationships that could have appeared to influence the work reported in this paper.

Data availability

The datasets generated during and/or analyzed during the current study are available from the corresponding author upon reasonable request.

Acknowledgments

Lisa Köhler and Chen Song acknowledge the Deutsche Forschungsgemeinschaft (417685888). Josef Wachtveitl and Chavdar Slavov acknowledge the Deutsche Forschungsgemeinschaft (WA 1850/4-3).

Appendix A. Supplementary data

The following files are available free of charge. Supporting information containing detailed description of the experimental and theoretical methods. (file type, docx) Supplementary data to this article can be found online at doi:<https://doi.org/10.1016/j.bbabo.2023.148996>.

References

- [1] X. Yang, Z. Ren, J. Kuk, K. Moffat, Temperature-scan cryocrystallography reveals reaction intermediates in bacteriophytochrome, *Nature*. 479 (2011) 428–431, <https://doi.org/10.1038/nature10506>.
- [2] C. Song, G. Psakis, C. Lang, J. Mailliet, W. Gärtner, J. Hughes, J. Matysik, Two ground state isoforms and a chromophore D-ring photoflip triggering extensive intramolecular changes in a canonical phytochrome, *Proc. Natl. Acad. Sci. U. S. A.* 108 (2011) 3842–3847, <https://doi.org/10.1073/pnas.1013377108>.
- [3] E.S. Burgie, R.D. Vierstra, Phytochromes: an atomic perspective on Photoactivation and signaling, *Plant Cell* 26 (2014) 4568–4583, <https://doi.org/10.1105/tpc.114.131623>.
- [4] N.C. Rockwell, Y.-S. Su, J.C. Lagarias, Phytochrome structure and signaling mechanisms, *Annu. Rev. Plant Biol.* 57 (2006) 837–858, <https://doi.org/10.1146/annurev.arplant.56.032604.144208>.
- [5] H. Takala, P. Edlund, J.A. Ihalainen, S. Westenhoff, Tips and turns of bacteriophytochrome photoactivation, *Photochem. Photobiol. Sci.* 19 (2020) 1488–1510, <https://doi.org/10.1039/D0PP00117A>.
- [6] N.C. Rockwell, J.C. Lagarias, Phytochrome diversification in cyanobacteria and eukaryotic algae, *Curr. Opin. Plant Biol.* 37 (2017) 87–93, <https://doi.org/10.1016/j.pbi.2017.04.003>.
- [7] Y. Hirose, T. Shimada, R. Narikawa, M. Katayama, M. Ikeuchi, Cyanobacteriochrome CcaS is the green light receptor that induces the expression of phycobilisome linker protein, *Proc. Natl. Acad. Sci. U. S. A.* 105 (2008) 9528–9533, <https://doi.org/10.1073/pnas.0801826105>.
- [8] E. Giraud, J. Fardoux, N. Fourrier, L. Hannibal, B. Genty, P. Bouyer, B. Dreyfus, A. Verméglio, Bacteriophytochrome controls photosystem synthesis in anoxygenic bacteria, *Nature*. 417 (2002) 202–205, <https://doi.org/10.1038/417202a>.
- [9] K.D. Piatkevich, F.V. Subach, V.V. Verkhusha, Engineering of bacterial phytochromes for near-infrared imaging, sensing, and light-control in mammals, *Chem. Soc. Rev.* 42 (2013) 3441–3452, <https://doi.org/10.1039/c3cs35458j>.
- [10] T.A. Redchuk, E.S. Omelina, K.G. Chernov, V.V. Verkhusha, Near-infrared optogenetic pair for protein regulation and spectral multiplexing, *Nat. Chem. Biol.* 13 (2017) 633–639, <https://doi.org/10.1038/nchembio.2343>.
- [11] D.M. Shcherbakova, O.V. Stepanenko, K.K. Tuuroverov, V.V. Verkhusha, Near-infrared fluorescent proteins: multiplexing and Optogenetics across scales, *Trends Biotechnol.* 36 (2018) 1230–1243, <https://doi.org/10.1016/j.tibtech.2018.06.011>.
- [12] M. Hörner, K. Raute, B. Hummel, J. Madl, G. Creusen, O.S. Thomas, E.H. Christen, N. Hotz, R.J. Gübeli, R. Engesser, B. Rebmann, J. Lauer, B. Rolaffs, J. Timmer, W. W.A. Schamel, J. Pruszek, W. Römer, M.D. Zurbriggen, C. Friedrich, A. Walther, S. Minguet, R. Sawarkar, W. Weber, Phytochrome-based extracellular matrix with reversibly tunable mechanical properties, *Adv. Mater.* 31 (2019) 1–11, <https://doi.org/10.1002/adma.201806727>.
- [13] K. Tang, H.M. Beyer, M.D. Zurbriggen, W. Gärtner, The red edge: Bilin-binding photoreceptors as Optogenetic tools and fluorescence reporters, *Chem. Rev.* (2021), <https://doi.org/10.1021/acs.chemrev.1c00194>.
- [14] M.G. Müller, I. Lindner, I. Martin, W. Gärtner, A.R. Holzwarth, Femtosecond kinetics of photoconversion of the higher plant photoreceptor phytochrome carrying native and modified chromophores, *Biophys. J.* 94 (2008) 4370–4382, <https://doi.org/10.1529/biophysj.106.091652>.
- [15] C. Schumann, R. Groß, N. Michael, T. Lamparter, R. Diller, Sub-picosecond mid-infrared spectroscopy of Phytochrome Agp1 from *Agrobacterium tumefaciens*, *ChemPhysChem*. 8 (2007) 1657–1663, <https://doi.org/10.1002/cphc.200700210>.
- [16] K. Heyne, J. Herbst, D. Stehlik, B. Esteban, T. Lamparter, J. Hughes, R. Diller, Ultrafast dynamics of phytochrome from the cyanobacterium *Synechocystis*, reconstituted with phycocyanobilin and phycoerythrobilin, *Biophys. J.* 82 (2002) 1004–1016, [https://doi.org/10.1016/S0006-3495\(02\)75460-X](https://doi.org/10.1016/S0006-3495(02)75460-X).
- [17] K.C. Toh, E.A. Stojković, I.H.M.M. van Stokkum, K. Moffat, J.T.M.M. Kennis, Proton-transfer and hydrogen-bond interactions determine fluorescence quantum yield and photochemical efficiency of bacteriophytochrome, *Proc. Natl. Acad. Sci. U. S. A.* 107 (2010) 9170–9175, <https://doi.org/10.1073/pnas.0911535107>.
- [18] M. Bischoff, G. Hermann, S. Rentsch, D. Strehlow, First steps in the phytochrome phototransformation: a comparative femtosecond study on the forward (Pr → Pfr) and back reaction (Pfr → Pr), *Biochemistry*. 40 (2001) 181–186, <https://doi.org/10.1021/bi0011734>.
- [19] C. Slavov, X. Xu, K.-H. Zhao, W. Gärtner, J. Wachtveitl, Detailed insight into the ultrafast photoconversion of the cyanobacteriochrome Slr1393 from *Synechocystis* sp., *Biochim. Biophys. Acta Bioenerg.* 1847 (2015) 1335–1344, <https://doi.org/10.1016/j.bbabo.2015.07.013>.
- [20] P. Singer, S. Wörner, T. Lamparter, R. Diller, Spectroscopic investigation on the primary photoreaction of bathy Phytochrome Agp2-Pr of *Agrobacterium fabrum*: isomerization in a pH-dependent H-bond network, *ChemPhysChem*. 17 (2016) 1288–1297, <https://doi.org/10.1002/cphc.201600199>.
- [21] P.W. Kim, N.C. Rockwell, S.S. Martin, J.C. Lagarias, D.S. Larsen, Dynamic inhomogeneity in the Photodynamics of cyanobacterial Phytochrome Cph1, *Biochemistry*. 53 (2014) 2818–2826, <https://doi.org/10.1021/bi500108s>.
- [22] P.W. Kim, L.H. Freer, N.C. Rockwell, S.S. Martin, J.C. Lagarias, D.S. Larsen, Femtosecond Photodynamics of the red/green Cyanobacteriochrome NpR6012g4 from *Nostoc punctiforme*. 1. Forward dynamics, *Biochemistry*. 51 (2012) 608–618, <https://doi.org/10.1021/bi201507k>.
- [23] T. Mathes, J. Ravensbergen, M. Kloz, T. Gleichmann, K.D. Gallagher, N. C. Weitowich, R. St. S.E. Peter, E.A. Kovaleva, J.T.M.M. Kennis Stojković, Femto- to microsecond photodynamics of an unusual bacteriophytochrome, *J. Phys. Chem. Lett.* 6 (2015) 239–243, <https://doi.org/10.1021/jz502408n>.
- [24] S.M. Gottlieb, P.W. Kim, C.-W. Chang, S.J. Hanke, R.J. Hayer, N.C. Rockwell, S. S. Martin, J.C. Lagarias, D.S. Larsen, Conservation and diversity in the primary forward Photodynamics of red/green Cyanobacteriochromes, *Biochemistry*. 54 (2015) 1028–1042, <https://doi.org/10.1021/bi5012755>.
- [25] D. Wang, X. Li, L. Wang, X. Yang, D. Zhong, Elucidating ultrafast multiphasic dynamics in the Photoisomerization of Cyanobacteriochrome, *J. Phys. Chem. Lett.* 11 (2020) 8819–8824, <https://doi.org/10.1021/acs.jpcclett.0c02467>.
- [26] S.R. Tachibana, L. Tang, C. Chen, L. Zhu, Y. Takeda, K. Fushimi, T.K. SeEVERS, R. Narikawa, M. Sato, C. Fang, Transient electronic and vibrational signatures during reversible photoswitching of a cyanobacteriochrome photoreceptor, *Spectrochim. Acta - Part Mol. Biomol. Spectrosc.* 250 (2021), 119379, <https://doi.org/10.1016/j.saa.2020.119379>.
- [27] C. Slavov, T. Fischer, A. Barnoy, H. Shin, A.G. Rao, C. Wiebeler, X. Zeng, Y. Sun, Q. Xu, A. Gutt, K. Zhao, W. Gärtner, X. Yang, I. Schapiro, J. Wachtveitl, The interplay between chromophore and protein determines the extended excited state dynamics in a single-domain phytochrome, *Proc. Natl. Acad. Sci. U. S. A.* 117 (2020) 16356–16362, <https://doi.org/10.1073/pnas.1921706117>.
- [28] T. Fischer, Q.-Z. Xu, K.-H. Zhao, W. Gärtner, C. Slavov, J. Wachtveitl, Effect of the PHY domain on the photoisomerization step of the forward Pr → Pfr conversion of a knotless phytochrome, *Chem. Eur. J.* (2020) 17261–17266, <https://doi.org/10.1002/chem.202003138>.
- [29] D. Wang, Y. Qin, M. Zhang, X. Li, L. Wang, X. Yang, D. Zhong, The origin of ultrafast multiphasic dynamics in Photoisomerization of Bacteriophytochrome, *J. Phys. Chem. Lett.* (2020) 5913–5919, <https://doi.org/10.1021/acs.jpcclett.0c01394>.
- [30] T. Fischer, L.J.G.W. van Wilderen, P. Gnaou, J. Bredenbeck, L.-O. Essen, J. Wachtveitl, C. Slavov, Ultrafast Photoconversion dynamics of the knotless Phytochrome SynCph2, *Int. J. Mol. Sci.* 22 (2021) 10690, <https://doi.org/10.3390/ijms221910690>.
- [31] H. Takala, H.K. Lehtivuori, O. Berntsson, A. Hughes, R. Nanekar, S. Niebling, M. Panman, L. Henry, A. Menzel, S. Westenhoff, J.A. Ihalainen, On the (un) coupling of the chromophore, tongue interactions, and overall conformation in a bacterial phytochrome, *J. Biol. Chem.* 293 (2018) 8161–8172, <https://doi.org/10.1074/jbc.RA118.001794>.
- [32] V. Sineshchekov, J. Mailliet, G. Psakis, K. Feilke, J. Kopycki, M. Zeidler, L.-O. Essen, J. Hughes, Tyrosine 263 in cyanobacterial Phytochrome Cph1 optimizes photochemistry at the prelumini-R → lumi-R step, *Photochem. Photobiol.* 90 (2014) 786–795, <https://doi.org/10.1111/php.12263>.
- [33] H. Lehtivuori, J. Rummelt, S. Mustalahti, S. Kurkinen, H. Takala, Conserved histidine and tyrosine determine spectral responses through the water network in *Deinococcus radiodurans* phytochrome, *Photochem. Photobiol. Sci.* (2022), <https://doi.org/10.1007/s43630-022-00272-6>.
- [34] J. Mailliet, G. Psakis, K. Feilke, V. Sineshchekov, L.O. Essen, J. Hughes, Spectroscopy and a high-resolution crystal structure of Tyr263 mutants of cyanobacterial phytochrome Cph1, *J. Mol. Biol.* 413 (2011) 115–127, <https://doi.org/10.1016/j.jmb.2011.08.023>.
- [35] Q.-Z. Xu, L. Goett-Zink, W. Gärtner, K.-H. Zhao, T. Kottke, Tongue refolding in the knotless cyanobacterial Phytochrome All2699, *Biochemistry*. 59 (2020) 2047–2054, <https://doi.org/10.1021/ac.biochem.0c00209>.
- [36] C. Slavov, N. Bellakbil, J. Wahl, K. Mayer, K. Rück-Braun, I. Burghardt, J. Wachtveitl, M. Braun, Ultrafast coherent oscillations reveal a reactive mode in the ring-opening reaction of fulgides, *Phys. Chem. Chem. Phys.* 17 (2015) 14045–14053, <https://doi.org/10.1039/c5cp01878a>.
- [37] T. Wilhelm, J. Piel, E. Riedle, Sub-20-fs pulses tunable across the visible from a blue-pumped single-pass noncollinear parametric converter, *Opt. Lett.* 22 (1997) 1494, <https://doi.org/10.1364/ol.22.001494>.
- [38] E. Riedle, M. Beutter, S. Lochbrunner, J. Piel, S. Schenk, S. Spörlein, W. Zinth, Generation of 10 to 50 fs pulses tunable through all of the visible and the NIR, *Appl. Phys. B Lasers Opt.* 71 (2000) 457–465, <https://doi.org/10.1007/s003400000351>.
- [39] C. Slavov, H. Hartmann, J. Wachtveitl, Implementation and evaluation of data analysis strategies for time-resolved optical spectroscopy, *Anal. Chem.* 87 (2015) 2328–2336, <https://doi.org/10.1021/ac504348h>.
- [40] R. Croce, M.G. Müller, R. Bassi, A.R. Holzwarth, Carotenoid-to-chlorophyll energy transfer in recombinant major light-harvesting complex (LHCI) of higher plants. I. Femtosecond transient absorption measurements, *Biophys. J.* 80 (2001) 901–915, [https://doi.org/10.1016/S0006-3495\(01\)76069-9](https://doi.org/10.1016/S0006-3495(01)76069-9).
- [41] K. Anders, D. Von Stetten, J. Mailliet, S. Kiontke, V.A. Sineshchekov, P. Hildebrandt, J. Hughes, L.O. Essen, Spectroscopic and photochemical characterization of the red-light sensitive photosensory module of Cph2 from *Synechocystis* PCC 6803, *Photochem. Photobiol.* 87 (2011) 160–173, <https://doi.org/10.1111/j.1751-1097.2010.00845.x>.
- [42] J.R. Wagner, J. Zhang, D. Von Stetten, M. Günther, D.H. Murgida, M.A. Mroginski, J.M. Walker, K.T. Forest, P. Hildebrandt, R.D. Vierstra, Mutational analysis of *Deinococcus radiodurans* bacteriophytochrome reveals key amino acids necessary for the photochromicity and proton exchange cycle of phytochromes, *J. Biol. Chem.* 283 (2008) 12212–12226, <https://doi.org/10.1074/jbc.M709355200>.

- [43] I.H.M.M. Van Stokkum, D.S. Larsen, R. van Grondelle, Global and target analysis of time-resolved spectra, *Biochim. Biophys. Acta Bioenerg.* 1657 (2004) 82–104, <https://doi.org/10.1016/j.bbabi.2004.04.011>.
- [44] S.M. Gottlieb, P.W. Kim, N.C. Rockwell, Y. Hirose, M. Ikeuchi, J.C. Lagarias, D. S. Larsen, Primary Photodynamics of the green/red-absorbing Photoswitching regulator of the chromatic adaptation E domain from *Fremyella diplosiphon*, *Biochemistry*. 52 (2013) 8198–8208, <https://doi.org/10.1021/bi400946q>.
- [45] C.-W.W. Chang, S.M. Gottlieb, P.W. Kim, N.C. Rockwell, J.C. Lagarias, D.S. Larsen, Reactive ground-state pathways are not ubiquitous in red/green cyanobacteriochromes, *J. Phys. Chem. B* 117 (2013) 11229–11238, <https://doi.org/10.1021/jp402112u>.
- [46] J. Kübel, M. Chenchiliyan, S.A. Ooi, E. Gustavsson, L. Isaksson, V. Kuznetsova, J. A. Ihalainen, S. Westenhoff, M. Maj, Transient IR spectroscopy identifies key interactions and unravels new intermediates in the photocycle of a bacterial phytochrome, *Phys. Chem. Chem. Phys.* 22 (2020) 9195–9203, <https://doi.org/10.1039/c9cp06995j>.
- [47] J.A. Ihalainen, E. Gustavsson, L. Schroeder, S. Donnini, H. Lehtivuori, L. Isaksson, C. Thöing, V. Modi, O. Berntsson, B. Stucki-Buchli, A. Liukkonen, H. Häkkinen, E. Kalenius, S. Westenhoff, T. Kottke, Chromophore-protein interplay during the Phytochrome Photocycle revealed by step-scan FTIR spectroscopy, *J. Am. Chem. Soc.* 140 (2018) 12396–12404, <https://doi.org/10.1021/jacs.8b04659>.
- [48] G. Salvadori, V. Macaluso, G. Pellicci, L. Cupellini, G. Granucci, B. Mennucci, Protein control of photochemistry and transient intermediates in phytochromes, *Nat. Commun.* 13 (2022) 6838, <https://doi.org/10.1038/s41467-022-34640-8>.
- [49] L.O. Essen, J. Mailliet, J. Hughes, The structure of a complete phytochrome sensory module in the Pr ground state, *Proc. Natl. Acad. Sci. U. S. A.* 105 (2008) 14709–14714, <https://doi.org/10.1073/pnas.0806477105>.
- [50] X. Yang, J. Kuk, K. Moffat, Crystal structure of *Pseudomonas aeruginosa* bacteriophytochrome: Photoconversion and signal transduction, *Proc. Natl. Acad. Sci. U. S. A.* 105 (2008) 14715–14720, <https://doi.org/10.1073/pnas.0806718105>.
- [51] Q.-Z. Xu, P. Bielytskyi, J. Otis, C. Lang, J. Hughes, K.-H. Zhao, A. Losi, W. Gärtner, C. Song, MAS NMR on a red/far-red photochromic Cyanobacteriochrome All2699 from *Nostoc*, *Int. J. Mol. Sci.* 20 (2019) 3656, <https://doi.org/10.3390/ijms20153656>.
- [52] K. Anders, G. Daminelli-Widany, M.A. Mroginiski, D. Von Stetten, L.O. Essen, Structure of the cyanobacterial phytochrome 2 photosensor implies a tryptophan switch for phytochrome signaling, *J. Biol. Chem.* 288 (2013) 35714–35725, <https://doi.org/10.1074/jbc.M113.510461>.
- [53] P.J.M. Johnson, A. Halpin, T. Morizumi, V.I. Prokhorenko, O.P. Ernst, R.J. D. Miller, Local vibrational coherences drive the primary photochemistry of vision, *Nat. Chem.* 7 (2015) 980–986, <https://doi.org/10.1038/nchem.2398>.
- [54] H. Kuramochi, S. Takeuchi, K. Yonezawa, H. Kamikubo, M. Kataoka, T. Tahara, Probing the early stages of photoreception in photoactive yellow protein with ultrafast time-domain Raman spectroscopy, *Nat. Chem.* 9 (2017) 660–666, <https://doi.org/10.1038/nchem.2717>.
- [55] K. Heyne, O.F. Mohammed, A. Usman, J. Dreyer, E.T.J. Nibbering, M. A. Cusanovich, Structural evolution of the chromophore in the primary stages of trans/Cis isomerization in photoactive yellow protein, *J. Am. Chem. Soc.* 127 (2005) 18100–18106, <https://doi.org/10.1021/ja051210k>.
- [56] T. Nakamura, S. Takeuchi, M. Shibata, M. Demura, H. Kandori, T. Tahara, Ultrafast pump–probe study of the primary photoreaction process in pharaonis Halorhodopsin: halide ion dependence and isomerization dynamics, *J. Phys. Chem. B* 112 (2008) 12795–12800, <https://doi.org/10.1021/jp803282s>.
- [57] S. Tahara, S. Takeuchi, R. Abe-Yoshizumi, K. Inoue, H. Ohtani, H. Kandori, T. Tahara, Ultrafast photoreaction dynamics of a light-driven sodium-ion-pumping retinal protein from *Krokinobacter eikastus* revealed by femtosecond time-resolved absorption spectroscopy, *J. Phys. Chem. Lett.* 6 (2015) 4481–4486, <https://doi.org/10.1021/acs.jpcclett.5b01994>.
- [58] M.S. Heschel, J. Selby, C. Butler, G.C. Whitelam, R.A. Sharrock, K. Donohue, A new role for phytochromes in temperature-dependent germination, *New Phytol.* 174 (2007) 735–741, <https://doi.org/10.1111/j.1469-8137.2007.02044.x>.
- [59] J.-H. Jung, M. Domijan, C. Klose, S. Biswas, D. Ezer, M. Gao, A.K. Khattak, M. S. Box, V. Charoensawan, S. Cortijo, M. Kumar, A. Grant, J.C.W. Locke, E. Schäfer, K.E. Jaeger, P.A. Wigge, Phytochromes function as thermosensors in *Arabidopsis*, *Science*. 354 (2016) 886–889, <https://doi.org/10.1126/science.aaf6005>.
- [60] I. Njimonu, R. Yang, T. Lamparter, Temperature effects on bacterial Phytochrome, *PLoS One* 9 (2014), e109794, <https://doi.org/10.1371/journal.pone.0109794>.
- [61] B. Zienicke, I. Molina, R. Glenz, P. Singer, D. Ehmer, F.V. Escobar, P. Hildebrandt, R. Diller, T. Lamparter, Unusual spectral properties of Bacteriophytochrome Agp2 result from a deprotonation of the chromophore in the red-absorbing form Pr^{*}, *J. Biol. Chem.* 288 (2013) 31738–31751, <https://doi.org/10.1074/jbc.M113.479535>.

5.7 Reference [VI]

Fischer *et al.*, *J. Am. Chem. Soc.* 2023, 145, 14811-14822

Mechanistic Elucidation of the Hula-Twist Photoreaction in Hemithioindigo

T. Fischer*, J. Leitner*, A. Gerwien*, P. Mayer, A. Dreuw, H. Dube, J. Wachtveitl

J. Am. Chem. Soc. 2023, 145, 14811-14822.

DOI: 10.1021/jacs.3c03536

Reprinted with permission from T. Fischer*, J. Leitner*, A. Gerwien*, P. Mayer, A. Dreuw, H. Dube, J. Wachtveitl, *J. Am. Chem. Soc.* 2023, 145, 14811-14822. Copyright 2023 American Chemical Society. <https://doi.org/10.1021/jacs.3c03536>

Mechanistic Elucidation of the Hula-Twist Photoreaction in Hemithioindigo

Tobias Fischer,[⊥] Jonas Leitner,[⊥] Aaron Gerwien,[⊥] Peter Mayer, Andreas Dreuw,^{*} Henry Dube,^{*} and Josef Wachtveitl^{*}



Cite This: *J. Am. Chem. Soc.* 2023, 145, 14811–14822



Read Online

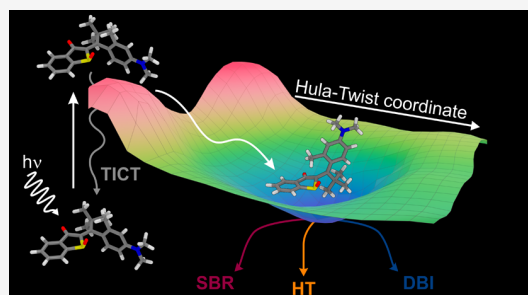
ACCESS |

Metrics & More

Article Recommendations

Supporting Information

ABSTRACT: The Hula-Twist (HT) photoreaction represents a fundamental photochemical pathway for bond isomerizations and is defined by the coupled motion of a double bond and an adjacent single bond. This photoreaction has been suggested as the defining motion for a plethora of light-responsive chromophores such as retinal within opsins, coumaric acid within photoactive yellow protein, or vitamin D precursors, and stilbenes in solution. However, due to the fleeting character of HT photoproducts a direct experimental observation of this coupled molecular motion was severely hampered until recently. To solve this dilemma, the Dube group has designed a molecular framework able to deliver unambiguous experimental evidence of the HT photoreaction. Using sterically crowded atropisomeric hemithioindigo (HTI) the HT photoproducts are rendered thermally stable and can be observed directly after their formation. However, following the ultrafast excited state process of the HT photoreaction itself has not been achieved so far and thus crucial information for an elementary understanding is still missing. In this work, we present the first ultrafast spectroscopy study of the HT photoreaction in HTI and probe the competition between different excited state processes. Together with extensive excited state calculations a detailed mechanistic picture is developed explaining the significant solvent effects on the HT photoreaction and revealing the intricate interplay between productive isomerizations and unproductive twisted intramolecular charge transfer (TICT) processes. With this study essential insights are thus gained into the mechanism of complex multibond rotations in the excited state, which will be of primary importance for further developments in this field.



INTRODUCTION

In recent years, the class of hemithioindigo (HTI) photo-switches has gathered attention based on a multitude of favorable properties such as high thermal bistability, fatigue-resistant switching, and light responsiveness in the visible spectral region.^{1–6} These properties allow for various applications in the fields of biological chemistry,^{7–10} supramolecular chemistry,^{11–14} and molecular machines.¹⁵

Apart from these applications, HTIs have also been used as model systems to study light-induced reaction mechanisms.^{4,16–19} Upon illumination, HTIs typically undergo double bond isomerization (DBI) within a few fs to ps. However, depending on the substitution pattern and solvent polarity, the formation of twisted intramolecular charge transfer (TICT) states associated with single bond twisting (SBT) can be observed as an alternative deactivation channel (Scheme 1).^{18,19}

TICT formation can be induced by introducing a pretwist into the single bond adjacent to the central double bond as well as electron-donating substituents at the stilbene moiety. The ratio of SBT via TICT vs DBI can then be controlled by the polarity of the solvent, where high polarity favors the SBT/

TICT pathway nearly abolishing DBI and low polarity entirely eliminates SBT/TICT favoring very efficient DBI.¹⁸

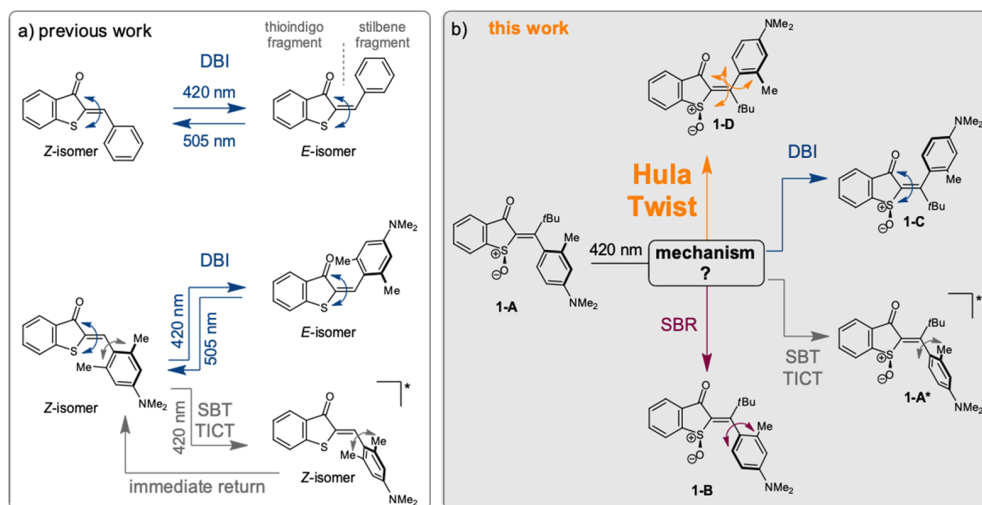
To evidence other possible photochemical bond rotations, the Dube group developed the synthesis of double bond substituted HTIs²⁰ and sulfur oxidized HTIs (Scheme 1b).²¹ By combining these two substitution patterns, it was possible to create derivatives containing a significantly pretwisted single bond, which cannot rotate easily in the ground state because of very strong steric hindrance. If this twisted stilbene fragment is additionally rendered nonsymmetric by different *ortho*-substituents such as in derivative **1** (Scheme 1 and Figure 1), atropisomers can be distinguished as diastereomers in these structures. In total, four diastereomers can be isolated at ambient temperatures for structures like **1** and three different isomerization reactions are possible for each of them. The first one is the long known DBI, the second is a full single bond

Received: April 5, 2023

Published: June 26, 2023



Scheme 1. Different Photoreactions Executed by the Hemithioindigo (HTI) Photoswitch: (a) Two Previously Evidenced Photoreactions of HTIs, DBI (top) and SBT/TICT Formation; (b) Hula-Twist (HT) and SBR as Additional Photoreactions That Can Be Evidenced for Sterically Hindered Sulfoxide HTI Derivatives⁴²



⁴²The molecular structure of HTI **1** was used for elucidation of the excited state mechanism in the present study.

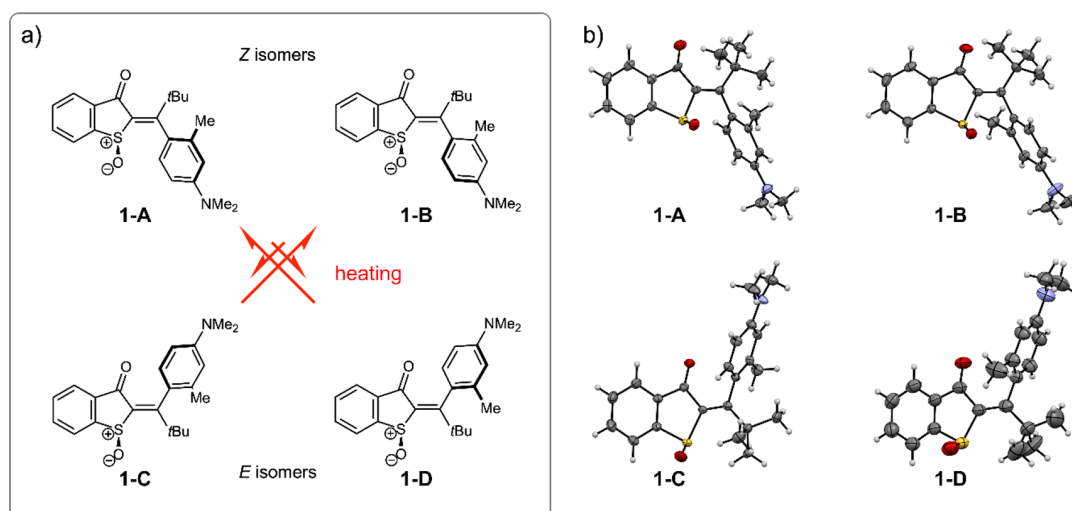


Figure 1. Structures of **1-A** to **1-D** and their thermal conversions. (a) Schematic representations of the four diastereomers of HTI **1** (only enantiomers with (*S*)-configured sulfoxide stereo center are shown). Thermal conversions occur selectively as HT processes between **1-A** and **1-D** as well as **1-B** and **1-C**. (b) Structures of **1-A** to **1-D** in the crystalline state.

rotation (SBR – note that this motion is different from the SBT, as in the latter case no full rotation but rather a twist is executed), and the third is a combined DBI and SBR process also known as Hula-Twist (HT).^{22–24} With a molecular setup similar to **1** it was possible to provide a first direct experimental evidence for the HT isomerization and in addition demonstrate significant influences of solvent polarity, viscosity, and temperature on this photoreaction.¹⁷ Since then, the HT photoreaction was applied in the construction of new archetypes of molecular machines, such as photon-only driven motors,²⁵ or multistate photoswitch architectures that allow high-state densities and extremely selective sequential switching processes.²⁶ These examples already highlight the immense potential of novel photoreactions for the construction of smart and responsive molecular systems.

Despite the progress, conscious design and rational tailoring of HT photoreactions are currently out of reach as no detailed

mechanistic understanding is available. Earlier attempts at mechanism elucidation in e.g. stilbene^{23,27} and vitamin-D precursors^{28,29} were hampered by the ambiguity of different possible and overlapping photoreactions and no direct evidence of the HT photoreaction itself.^{30–32} Similarly, HT photoreactions are also disputed for biologically relevant chromophores such as *p*-coumaric acid.^{33–35} The particular HTI molecular setup allows direct study of the mechanism, dynamics, and environmental influences of the HT photoreaction as well as the competition of HT with DBI and SBR pathways. It thus represents an ideal molecular framework to gain deep knowledge about an intricate and fundamental photoreaction and its mechanism.

In this work, we present a combined ultrafast UV/vis spectroscopic and quantum chemical investigation to elucidate the contribution of HT and other photoreaction mechanisms within a novel donor-substituted HTI photoswitch. We reveal

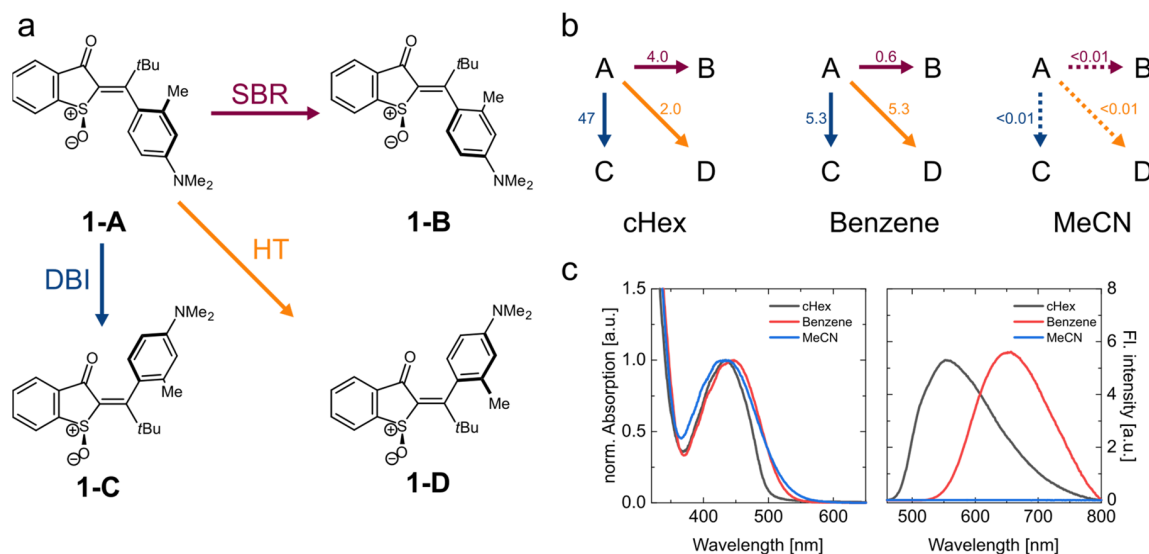


Figure 2. Schematic representation of possible productive photochemical reaction pathways in HTI 1-A. (a) Schematic representation of the four possible diastereomers (1-A to 1-D), where 1-A and 1-B are *Z*-isomers and 1-C and 1-D *E*-isomers. Isomer 1-A can be converted to 1-B via SBR, to 1-C via DBI, or to 1-D via HT. (b) Quantum yields for the individual photoreactions of 1-A in solvents of different polarity (cyclohexane (cHex), benzene and acetonitrile (MeCN)). Dashed arrows indicate quantum yields <0.01%. (c) Normalized absorption (left) and fluorescence spectra (right) of isomer 1-A in different solvents. Fluorescence spectra were recorded after excitation at 460 nm.

the overall photodynamics, identify competing excited state pathways, and test for environmental influences on the photoreactions. We further discuss whether HT and DBI occur on separate pathways or branch from a common pathway on the excited state surface.

EXPERIMENTAL SECTION

Sample Preparation. The investigated compound 1-A was dissolved in the respective solvent and diluted appropriately. For steady state and transient absorption measurements (1 mm cuvette) optical densities (OD) of roughly 0.5 at 460 nm were used in acetonitrile (MeCN) and benzene solution while in cyclohexane (cHex) solution an OD of 0.3 was used due to limited solubility. For the fluorescence measurements (1 cm cuvette) an OD of 0.1 at 460 nm was used.

Spectral Characterization. Absorption spectra were recorded on a Specord S600 absorption spectrometer (Analytik Jena). Fluorescence spectra were obtained on an FP 8500 fluorimeter (Jasco) with excitation at 460 nm. The recorded fluorescence spectra were corrected for reabsorption, background, nonlinearity of detector sensitivity for different wavelengths, excitation intensity, and solvent fluorescence.

Quantum Yield Determination. See Supporting Information (SI) for details.

Transient Absorption (TA). Time-resolved transient absorption (TA) measurements were performed using a home-built pump-probe setup described previously in detail.³⁶ In summary, ultrashort laser pulses (1 mJ, 775 nm, 130 fs, 1 kHz) used for pump and probe generation were provided by a Ti:Sa amplifier system (Clark, MXR-CPA-iSeries). Pump pulses were generated using a home-built two stage NOPA (noncollinear optical parametric amplifier). To obtain short pulses a prism compressor was used and placed between the two NOPA stages. To generate the probe pulses the laser fundamental was focused into a continuously moving CaF₂ crystal (5 mm). The probe pulses were then split into probe and reference beam. The reference beam was guided directly into a spectrograph (AMKO Multimode), while the probe beam was focused at the sample position, collected, and directed into a second spectrograph. The spectrographs contained gratings with 600 grooves/mm blazed at 500 nm and a photodiode array with a detection range of 360 to 720 nm. Anisotropic contributions were eliminated by measuring under magic angle

conditions (54.7° pump-probe polarization difference). The experiments were carried out in a fused silica cuvette with a 1 mm optical path length, which was constantly moved in the plane perpendicular to the pump pulses to avoid accumulation of photoproducts. In the experiments conducted in this work, pump energies of 90 nJ/pulse were used since higher energies induced multiphoton effects in benzene, which led to mixed dynamics. For similar reasons the excitation wavelength was not shifted further into the UV toward the maximum of the observed absorption bands.

Data Analysis. Data analysis was performed using OPTIMUS (www.optimusfit.org).³⁷ We applied global target analysis (GTA) using a sequential model ($A \rightarrow B \rightarrow C \rightarrow \dots$) to adequately fit the data. Aside from the decay-associated spectra (DAS) routinely obtained in global lifetime analysis, GTA yields the so-called evolution-associated difference spectra (EADS), which contain spectral information on the states present in the kinetic model.

Computational Details. All quantum chemical calculations were performed using Gaussian 16³⁸ unless mentioned otherwise. The ground state structures were optimized with density functional theory (DFT)³⁹ using the CAM-B3LYP⁴⁰ exchange-correlation (xc) functional and def2-SVP basis set. Solvent effects were included through the integral equation formalism (IEF) of the polarizable continuum model (PCM).⁴¹ The dielectric and optical dielectric constants of all studied solvents are listed in Table S3 in the SI. Linear-response time-dependent DFT (TD-DFT)⁴² was employed for the calculation of absorption spectra and excited states properties using the same xc-functional/basis set combination. Excited state geometry optimizations of the first excited singlet state *S*₁ were performed to investigate the influence of solvent effects on the emission energy. The *Z/E* isomerization is further studied by means of one-dimensional relaxed scans along the isomerization coordinate represented by the marked dihedral angle in Figure 5. In general, solvent effects were included in excited state calculations by means of the linear-response (LR-) PCM formalism, while single-point energies at specific equilibrium geometries of the *S*₀ and the *S*₁ states, for example, were further calculated using the state-specific (SS-) PCM formulation.

Further investigations of relaxation pathways involving *S*₀/*S*₁ conical intersections (CI) were performed using Q-Chem 5.2.⁴³ Spin-flip DFT (SF-DFT)⁴⁴ has been employed for optimizations of the minimum energy crossing points (MECP) using the CAM-B3LYP/def2-SVP xc-functional/basis set combination and the conductor like polarizable continuum model (C-PCM). Thereby

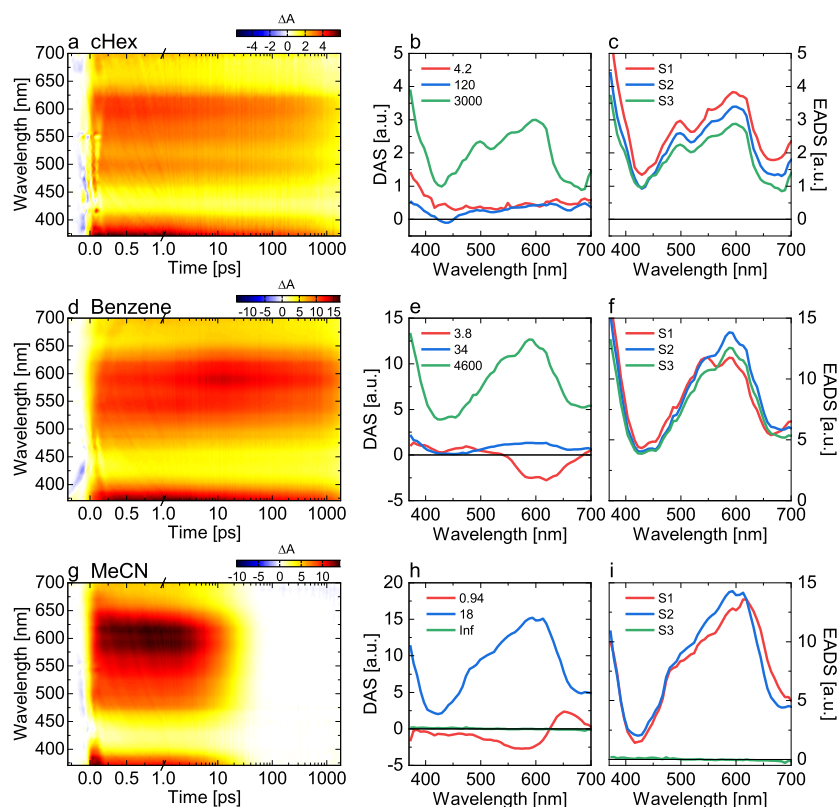


Figure 3. Ultrafast excited state dynamics of **1-A** after excitation at 460 nm in cHex (a,b,c), benzene (d,e,f), and MeCN (g,h,i). (a,d,g) Transient absorption spectra of **1-A**. Red indicates positive signals of ESA and product absorption (PA), while negative signals can be assigned to leftover contributions of a coherent artifact. (b,e,h) Decay-associated spectra (DAS) and (c,f,i) evolution-associated difference spectra (EADS) obtained from the respective global target analysis of (a,d,g). Note that the first sub-100 fs lifetime was omitted in all data sets due to limited time resolution caused by a complex and strong coherent artifact.

two CIs have been optimized along the previously determined isomerization coordinate. Note that the Tamm–Dancoff approximation (TDA)⁴⁵ was applied.

RESULTS AND DISCUSSION

Synthesis of 1. The synthesis of **1** follows an established protocol reported earlier.²⁰ It starts from commercially available thiosalicylic acid (**2**) and α -bromo-ketone **3**. After a nucleophilic substitution reaction, the corresponding thioether **4** is obtained in 98% yield. Base addition leads to formation of the hydroxyl-HTI **5** in 97% yield. Chlorination using thionyl chloride gives the chlorinated HTI **6** quantitatively, which was then cross-coupled with boronic acid **7** to give double-bond substituted HTI **8**. A final oxidation of the sulfur to the corresponding sulfoxide yields HTI **1** again in very good yield.

Properties of HTI 1. HTI **1** can assume four diastereomeric states **1-A** to **1-D** (Figure 1a), which are thermally stable at ambient conditions. Each of these can assume two enantiomeric forms depending on the configuration at the sulfoxide stereo center. For clarity we only show the enantiomers with (*S*) configured sulfoxide, although racemic mixtures were studied here.

All four diastereomers **1-A** to **1-D** were separated, and crystals suitable for X-ray structural analysis were obtained for enantiopure **1-A-(S)** and **1-B-(S)** as well as for racemic **1-C** and **1-D** (Figure 1b), which allowed direct assignment of spectra to a particular diastereomer.

Investigation of the thermal behavior revealed very selective interconversions between isomers of HTI **1**. At elevated temperatures of 80 °C combined double and single bond rotations (i.e., HT) occur as thermal isomerization reactions interconverting only **1-A** and **1-D** or **1-B** and **1-C**. For each interconverting pair the *Z* configured isomers are thermally the most stable (i.e., **1-A** and **1-B**), but an appreciable amount of the *E* configured isomers is present in thermal equilibrium in both cases (for more details and quantitative numbers see the Supporting Information).

Steady State Properties of 1-A. To understand the photophysical properties of sterically restricted HTI **1**, steady state absorption and fluorescence spectra were measured as well as the photoisomerization quantum yields of isomer **1-A** in different solvents (see Figure 2 and Supporting Information). Isomer **1-A** was chosen for this study, as it undergoes pronounced HT photoreactions upon irradiation, the relative propensity of which can be modulated strongly by solvent polarity. Thus, the process of HT can be studied most conveniently for this isomer without the need to resort to low temperature experiments.

In cHex, isomer **1-A** exhibits its main absorption peak at 433 nm, which is slightly red-shifted and broadened in more polar solvents. The bathochromic shift in benzene amounts to 13 nm while in more polar solvents like CH₂Cl₂, DMSO, or MeCN no further red-shifting but instead broadening is observed, indicating only a small influence of the polarity on the S₀ → S₁ gap. In contrast, the fluorescence is significantly more solvent dependent (see Figure 2c and the Supporting Information for

further details). In cHex, the fluorescence maximum is located at 550 nm showing a large Stokes shift of ~ 120 nm. With increasing solvent polarity, the fluorescence undergoes a large bathochromic shift of >100 nm in benzene and >200 nm in CH_2Cl_2 before disappearing completely in the very polar MeCN. In DMSO, a possible dual fluorescence could be present. This behavior is similar to other amine-donor substituted and twisted HTIs where the fluorescence is believed to be quenched by a strongly stabilized conical intersection of a TICT state with the ground state in polar environments.¹⁹

Upon illumination with blue light, photoconversion of isomer **1-A** to the two *E*-isomers **1-C** and **1-D** and the *Z*-isomer **1-B** are observed by NMR spectroscopy in apolar solvents. Using UV/vis spectroscopy, no distinction between the two atropisomers of either *E* or *Z* configuration is possible because of their very similar spectra and only the sum amount of formed *E*-isomer can be estimated. Productive photoisomerization of **1-A** decreases with increasing polarity of the solvent and is completely abolished in MeCN. Precise determination of the photoreaction quantum yields with NMR spectroscopy revealed more details on the influence of solvent polarity on the individual reaction pathways, as all isomers **1-A** to **1-D** can be distinguished with this method. In cHex, DBI is the most pronounced pathway with a 47% quantum yield while SBR and HT are less pronounced with 4% and 2%, respectively. However, already in the slightly more polar benzene the DBI quantum yield is reduced to only 5%, while the SBR vanishes almost completely. Interestingly, the proposed HT pathway is significantly less affected by the solvent change, which leads to a situation in which DBI and HT possess similar quantum yields. A further increase of polarity to $\text{CD}_2\text{Cl}_2/\text{CH}_2\text{Cl}_2$ or MeCN abolishes any form of photoproduct formation while also fluorescence is quenched entirely. Similar solvent polarity dependencies of the product formation quantum yield have been observed in other HTIs, especially in pretwisted systems.^{18,19}

Ultrafast Dynamics of 1-A. To obtain a dynamic picture of the excited state behavior of **1-A**, we performed ultrafast transient absorption measurements in cHex, benzene, and MeCN solutions (Figure 3). In all measurements, only positive signals are observed, which can be assigned to excited state absorption (ESA). The small negative signals at times <100 fs in all solvents can be assigned to a coherent artifact, which could not be removed completely. Surprisingly, no ground state bleach (GSB) or stimulated emission (SE) signals were observed, which are most likely overcompensated by the strong ESA signals. The ESA signals in cHex and benzene persist until the end of the time range of our experiments showing a very long-lived excited state (Figure 3a,d), while in MeCN the excited state is shorter lived decaying completely within 30 ps (Figure 3g). The short lifetime in MeCN is in good agreement with the drastically reduced fluorescence observed in the stationary experiments.

We performed global target analysis applying a sequential model to uncover further details of the excited state dynamics (Figure 3 b,c,e,f,h,i). In cHex, the first lifetime component at 4.2 ps shows an overall decrease of the ESA (Figure 3b). This could be assigned to an initial decay of the excited state or alternatively to solvent reorganization. A similar low ps lifetime can be observed in both benzene and MeCN with 3.8 and 0.9 ps, respectively, but with different spectral signatures, which is most likely due to the different electrostatic properties of the

three solvents. Considering the presence of such a component in all three solvents this lifetime is most likely due to solvent reorganization. The necessity of solvent reorganization occurring on the excited state surface is based on the considerable difference in polarity of **1-A** between ground and excited state. This becomes evident by the different shifting behavior of absorption and fluorescence upon changing the solvent polarity.

At later times, a second lifetime component of 120 and 34 ps, respectively, can be observed in both cHex and benzene showing a positive amplitude in the DAS <420 nm and >450 nm indicating a decay or change in extinction coefficient of the ESA and potentially a ground state recovery. Due to significant overlap of the strong ESA signal, the ground state absorption of isomer **1-A**, and the photoproducts, it is challenging to assign photoproduct formation to this step. If this process was related to ESA decay, a prior excited state branching would be required yielding a second excited state population with the same absorption profile, which is quite unlikely. Note, additionally, that the small amplitude compared to the following main excited state decay indicates that this cannot be the main productive channel for the *Z/E* isomerization. In such case, a significantly larger amplitude would be expected in cHex compared to the amplitude of the main excited state decay because of the high DBI quantum yield in this solvent. Hence, it is more plausible that this process is related to relaxation in the excited state or further solvent reorganization modulating the extinction of the excited state and in turn the amplitude of the ESA.

The excited state then decays on a much longer time scale where the decay occurs later in benzene than in cHex as readily observable by the higher amplitude of the ESA at long delay times. Consequently, the kinetic analysis yields lifetimes of 3.0 ns in cHex and ~ 4.6 ns in benzene. In contrast, in the polar MeCN an overall excited state lifetime of only 18 ps was observed. Thus, there is an interesting behavior established for the overall excited state lifetime maximum, when changing the polarity of the solvent. First, the excited state lifetime increases upon increasing the polarity from cHex to benzene, but when moving to the very polar MeCN the lifetime is shortened significantly (Figure 3g,h,i). This contrasts the behavior in many photoswitches and most HTIs, where only a continuous trend is seen when increasing solvent polarity.

Such discontinuity typically signifies a change of mechanism and a change of photoreactive pathways (for a related discontinuity of the excited state mechanism in response to systematic substituent changes, see ref 5). In twisted HTIs bearing strong donor groups, a similar maximum behavior in terms of excited state lifetimes as well as a significant decrease in photoisomerization quantum yield in response to increasing solvent polarity is observed. This behavior could be associated with a second deexcitation pathway via a TICT state, which competes with the DBI pathway starting from an initial excited state $S_{1,\text{min}}$.^{18,19} In another study, planar HTIs were reported to show a continued increase in excited state lifetime and fluorescence intensity with increasing solvent polarity. In that case, the barrier in the excited state increased due to stabilization of the prior polar S_1 minimum ($S_{1,\text{min}}$) but TICT formation was not observed due to a lack of pretwisting in the ground state.⁴⁶ For HTI **1-A**, we observe a behavior more similar to twisted HTIs with the excited state lifetime first increasing, then decreasing with rising solvent polarity.

Apart from the different excited state lifetimes, the overall dynamics are similar in all three solvents with different degrees of solvent reorganization followed by excited state decay. Additionally, throughout all measurements the spectral shape of the ESA itself remains rather similar despite the significant change in excited state lifetime and product ratios. This behavior rules out the occurrence of completely separate reaction pathways for the individual reaction processes like SBR or DBI. In such a case, a significant difference in the shape of the ESA would have been expected for HTI **1-A** in benzene and cHex based on the significant reduction in population of the DBI pathway. Therefore, it seems that all photoproducts are generated on a shared pathway, or the distinctions can only be observed on the ns-time scale outside our measurement window. This contrasts with other HTIs where a clear spectral separation into a TICT/SBT pathway and a DBI pathway is observed.^{18,19}

Based on these findings a preliminary model can be constructed. With the long-lived excited state in benzene and cHex, a significant barrier is expected on the excited state surface for productive photoreactions, which increases at first with rising polarity. This is in good agreement with the observed red shift in the fluorescence, indicating that the $S_{1,\min}$ state, formed after excitation and before passing the barrier, is likely stabilized in polar conditions similar to a previously proposed model.⁴⁶ To accommodate for the decrease in lifetime and quantum yield, an additional pathway draining the $S_{1,\min}$ population has to be present at higher polarity of the solvent. We can further characterize this pathway based on the observation that the spectral shape of the ESA is only weakly solvent dependent and does not change significantly during the photoreaction. Therefore, the additional pathway must originate from the same $S_{1,\min}$. Otherwise, a different state with identical ESA features generated by excited state branching would have to be present, which is unlikely. To further support and refine our model, we performed ground and excited state quantum chemical calculations to identify the specific reactive pathways.

Quantum Chemical Calculations. In a first step, we calculated the $S_0 \rightarrow S_1$ vertical excitation energies of **1-A** at its ground state equilibrium geometries (Table 1). All energetically higher excited states do not play a role in the investigated isomerization mechanism. Within the expected accuracy of our calculations, the results agree well with the experimental absorption bands and show only a small dependence on the solvent polarity. The natural transition orbitals (NTO)

Table 1. Excitation Energy ω and Dipole Moment μ for the Excited S_1 State Computed at the Ground State ($S_{0,\min}$; the FC Geometry) and S_1 ($S_{1,\min}$) Equilibrium Geometries at TD-DFT/CAM-B3LYP/def2-SVP/SS-PCM Level of Theory^a

	$S_{0,\min}$ /FC geometry		$S_{1,\min}$ geometry		Excess energy $E_{1,S_{0,\min}} - E_{1,S_{1,\min}}$ [eV]
	ω_1 [eV]	μ_1 [D]	ω_1 [eV]	μ_1 [D]	
gas phase	3.36	12.9	2.60	15.9	0.33
cHex	2.55	20.5	1.96	18.9	0.20
benzene	2.44	20.9	1.86	19.3	0.20
MeCN	2.57	20.5	0.52	23.4	1.32

^aAdditionally, the difference in the absolute energies of the S_1 state at $S_{0,\min}$ and $S_{1,\min}$ configuration, the excess energy, is given.

calculated without a solvation model are shown in Figure 4, and the static dipole moments of S_1 are listed in Table 1, which allow for a judgment of the charge transfer (CT) character of the S_1 state. Indeed, S_1 possesses CT character: electron density is transferred from the stilbene fragment to the thioindigo fragment. Furthermore, S_1 can be identified as a TICT state, which is already present at the Franck–Condon (FC) geometry, due to the strong pretwisting of **1-A**. In contrast, previous calculations on unsubstituted HTI identified S_1 to be of $\pi\pi^*$ character,^{4,46,47} while the corresponding TICT state is reached via a competing relaxation channel that renders the DBI less productive.¹⁸

This difference in excited state character is a consequence of the electron-donating substituents on the stilbene fragment and the oxidation of the sulfur on the thioindigo part, which increases the electron-donating and -accepting capabilities of the stilbene and thioindigo fragments, respectively. Altogether, this stabilizes the CT state as S_1 , and thus isomer **1-A** is initially excited into S_1 , which has strongly pronounced CT character.

In a next step, the equilibrium geometry of the S_1 state has been optimized starting at the FC geometry, i.e., the equilibrium geometry of the ground state. However, the structure of **1-A** changes only slightly during this geometry optimization. Therefore, the experimentally observed strong Stokes shift in polar solvents is most likely dominated by the CT and the subsequent relaxation of the surrounding solvent molecules rather than by exhaustive structural relaxation of **1-A** itself. The corresponding calculated emission energies from the S_1 minimum are listed in Table 1. In contrast to the absorption energies, the fluorescence energies show a strong dependence on the solvent polarity: the S_1 emission energies decrease strongly with increasing solvent polarity. This is a consequence of the strong stabilization of the polar S_1 CT state in polar environments, which reproduces the experimentally observed red shift of the fluorescence qualitatively. Only state-specific (SS) PCM is capable of correctly reproducing this trend, while LR-PCM only yields a minor red shift below 0.1 eV comparing cHex and MeCN, since SS-PCM is able to capture the strong response of the solvent to the CT excitation. Therefore, the stabilization of the polar S_1 state is much stronger with SS-PCM than with LR-PCM.⁴⁸ However, these results emphasize the importance of performing additional SS-PCM single point calculations to improve the description of the CT S_1 state.

A first preliminary explanation for the reduced excited state lifetime in polar environments can already be given: due to the increasing difference between the S_1 energies at the FC geometry and the S_1 equilibrium geometry, $E_{1,S_{0,\min}} - E_{1,S_{1,\min}}$, more excess energy is available in polar solvents once the S_1 equilibrium structure is reached. In other words, the S_1 state is more strongly vibrationally excited, i.e., simply hotter. Simultaneously, the S_0 and S_1 states approach each other in the $S_{1,\min}$ region strongly hinting at a spatially close-by conical intersection, which should become more accessible in polar solvents due to the significantly higher excess energy. This generally leads to an acceleration of the radiation-less relaxation with increasing solvent polarity.

To further investigate the *Z/E*-isomerization of **1-A**, the energetically most favorable isomerization pathway starting from the S_1 *Z*-minimum has been calculated using LR-PCM for one apolar solvent, i.e., benzene, and one polar solvent, i.e., MeCN. Therefore, relaxed scans along the central dihedral angle of **1-A** have been computed by fixing the angle to a

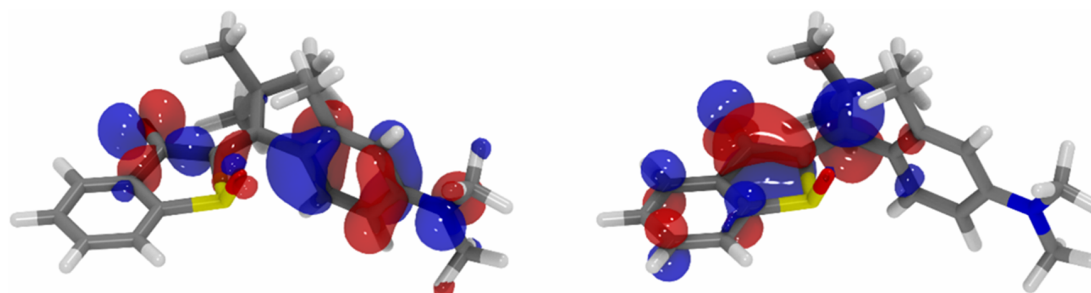


Figure 4. Highest occupied (left) and lowest unoccupied (right) NTO for S_1 of **1-A** in the gas phase with an isovalue of 0.035.

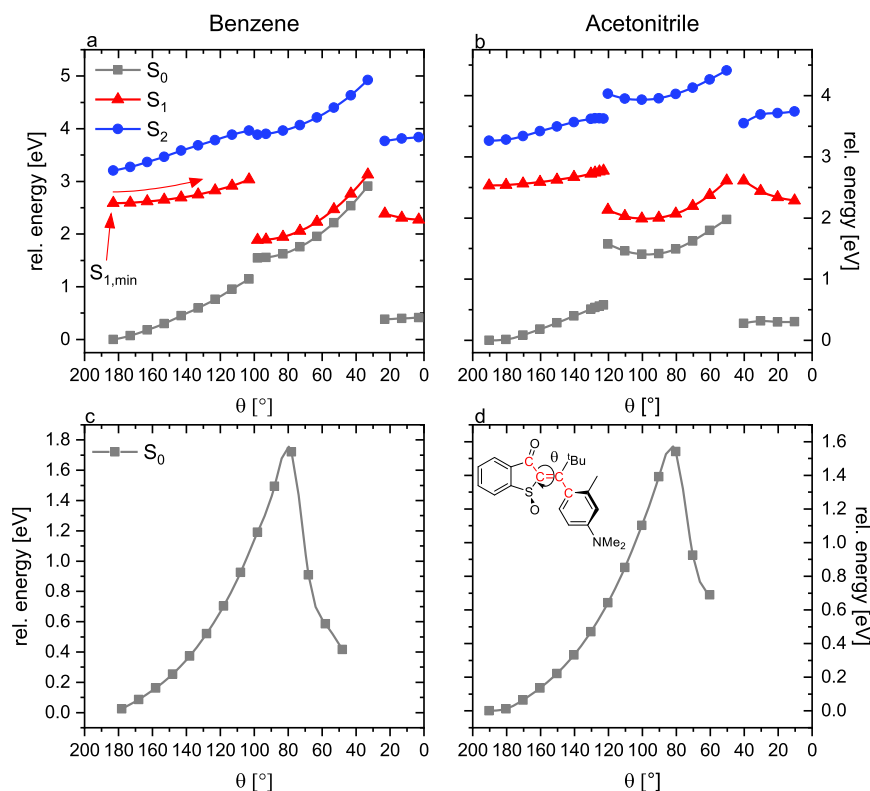


Figure 5. Relaxed one-dimensional scans of the PES of **1-A** leading to **1-D** along the dihedral angle θ (marked red in the inset). In the upper row (a,b), the S_1 relaxed scans are shown, while in the lower row (c,d) the relaxation has been calculated in the electronic ground state. Note that these correspond to two different reaction coordinates although the same dihedral angle θ has been scanned, therefore the ground state energies differ in the upper and lower panels. For the scans in the left column (a,c) a PCM for benzene has been employed, while for the right column (b,d) one for MeCN has been used.

constant value between 190° and 0° and allowing all other nuclear coordinates to relax freely. The one-dimensional PES cuts are shown in Figure 5. In Figure 5a and b, the S_1 state is relaxed; i.e., a S_1 minimum energy path is depicted along with the corresponding ground state energies. In Figure 5c and d, the S_0 state is structurally relaxed, these curves thus display a thermal isomerization path in the ground state. Hence, the pathways in Figure 5a,b and Figure 5c,d describe generally different isomerization pathways with different ground state energies. Analysis of the nuclear motions along these relaxed scans reveals an HT isomerization mechanism; i.e., HT is energetically more favorable than the exclusive DBI for the Z/E -isomerization, in both the ground and excited state. The sterically demanding substituents hinder Z/E -isomerization via DBI, since the methyl group on the stilbene fragment is clamped between the two oxygens of the thioindigo fragment,

which immediately leads to a corotation of the phenyl ring when rotating around the central double bond.

The relaxed scans in the S_1 state (Figure 5a and b) feature similar shapes in MeCN and benzene: starting from the S_1 minimum of the Z -isomer **1-A** on the left, an isomerization barrier must be passed, which depends on the solvent polarity. The barrier height in benzene is 0.45 eV, while in MeCN a smaller barrier of 0.25 eV is found when the LR-PCM formalism is applied. However, the barrier heights drastically increase to 0.94 and 1.54 eV in benzene and MeCN, respectively, if the more reliable SS-PCM is applied, i.e., the barrier now grows with increasing solvent polarity, which agrees well with the experimentally observed decreasing quantum yield in more polar solvents. The increasing barrier height can be explained by means of the stabilization of the polar S_1 state: the S_1 minimum is more strongly stabilized than

the maximum of the barrier, as indicated by the lower dipole moments of 11.6 and 13.5 D in benzene and MeCN, respectively. Recalling the previously discussed excess energies of 0.20 eV in benzene and 1.32 eV in MeCN, the energy in both solvents is insufficient to cross the isomerization barrier easily. However, in MeCN only 0.22 eV is missing making it more likely to pass the barrier, while in benzene most of the population is trapped in the S_1 minimum.

At dihedral angles $\theta = 120^\circ$ and 100° in MeCN and benzene, respectively, an S_0/S_1 conical intersection is passed, which leads to the observed discontinuities in the one-dimensional cut through the PES. By inspection of the state dipole moments, it becomes evident that S_0 and S_1 have interchanged, i.e., in the central parts of the scans at dihedral angles θ between 50° and 120° in MeCN and 30° and 100° in benzene, the initially excited CT state has become the ground state. In other words, in this region of the PES, the ground state can be assigned as the TICT state. Thus, the seeming discontinuities arise from the change of the optimized state and the resulting structural modifications. In particular, the carbonyl oxygen can now pass a methyl group of the *tert*-butyl group due to the constrained dihedral angle. Together, the sudden concomitant changes of electronic and geometric structure of S_1 explain the discontinuity of the energy in the one-dimensional representation of Figure 5a and b. Note that the second discontinuity at lower dihedral angles can be explained similarly. In the central part of the relaxed scans between the two discontinuities in Figure 5b, it is suggestive that a stable ground state TICT equilibrium structure should exist in MeCN. However, this is not the case, since unconstrained ground-state geometry optimizations starting at these structures have always led back to the minima of the apolar ground state. On the contrary, the S_1 state, which is the non-CT state in this PES region, possesses an excited-state equilibrium structure at a dihedral angle of 97° in MeCN and 98° in benzene.

Overall, S_0 and S_1 possess a similar shape in the central part of the relaxed S_1 scan and are energetically separated by only a small energy gap. This suggests that an S_0/S_1 CI may be spatially close. Therefore, we validated the TD-DFT results by recalculating the relaxed scans with SF-DFT (Figure S56 in the SI), which can generally better cope with such multiconfigurational situations. Indeed, SF-DFT reproduces the TD-DFT results qualitatively. In addition, a minimum-energy crossing point (MECP) optimization has been performed starting at the optimized non-CT S_1 minimum between the discontinuities in the central part of the PES cuts at the SF-DFT level to locate and investigate the CI. In both solvents, a CI could be identified with a dihedral angle of 103° lying structurally close to the isomerization coordinate. Due to almost degeneracy of S_0 and S_1 between the two discontinuities visible in Figure 5a and b, relaxation back to the electronic ground state can in principle occur at any point in this region. The molecular motion between the two discontinuities can be understood as a motion within the 3N-8 dimensional branching space of one CI. Since the *E*-isomer is formed when the excited molecules reach this CI and relax back to the ground state, this CI will be termed “productive” CI (CI_p) in the following. The productivity of this CI, however, also depends on whether the *Z* to *E* isomerization is completed in the ground state once the excited molecules reach it through the CI. This information is provided by the relaxed scans performed in the ground state. As can be seen from Figure 5c and d, the excited molecules

must return to S_0 after the ground state barrier for the *Z* to *E* isomerization to be completed, i.e., at dihedral angles θ smaller than 80° , since they otherwise revert to the *Z*-isomer. Because in MeCN the CI is reached at an angle of 120° , while in benzene the CI is shifted toward a smaller angle of 100° , the excited molecules can relax back to the ground state earlier in more polar solvents. As a result, less molecules will isomerize to the *E* form in MeCN than in benzene once the productive CI_p is reached.

Due to the very fast unproductive relaxation in MeCN, a second unproductive CI is very likely to be present, possibly in the vicinity of the S_1 *Z*-minimum geometry. Another MECP optimization starting at the $S_{1,\min}$ geometry did indeed reveal the presence of an additional CI, which lies energetically 0.35 and 0.5 eV above the S_1 *Z*-minimum in benzene and MeCN, respectively when the LR-PCM formalism is used. This represents an unproductive, immediate relaxation channel back to the S_0 *Z*-minimum, a so-called quenching CI (CI_Q). Since the energy difference between the CI and the S_1 minimum depends strongly on the stabilization of the latter by the solvent and LR-PCM is known to underestimate the latter, the energy difference computed by LR-PCM is certainly too small. A more reliable SS-PCM calculation is unfortunately not possible at the CI due to the degeneracy of the relevant states. Considering the excess energies of 0.20 and 1.32 eV and barrier heights larger than 0.35 and 0.5 eV in benzene and MeCN, respectively, this unproductive channel is energetically accessible only in polar environments.

Finally, we are now able to discuss the availability of the two competing relaxation channels involving either the productive or the quenching CI. The key quantity to consider is the excess energy, that is the energy available in the S_1 state for the molecules to perform reactions. In MeCN, the HTI molecules gain 1.32 eV of excess energy when relaxing from the Franck–Condon geometry to the S_1 *Z*-minimum, while in benzene they gain only as little as 0.2 eV. In MeCN, this energy is only sufficient to reach the quenching CI_Q at about 0.5 eV, which brings most of the excited state population back to the ground state, while the productive CI_p is unavailable due to a high isomerization barrier of 1.54 eV. Therefore, most of the excited state population should immediately relax through the quenching CI_Q . This is in line with the experimentally observed fast unproductive relaxation in MeCN. Furthermore, the productive CI_p is shifted toward more unfavorable dihedral angles in polar solvents, decreasing the probability of product formation in MeCN. Overall, the calculations show that in MeCN most of the excited state population is drained through a quenching channel, while product formation is barely possible.

Moving on to benzene, the excess energy is significantly reduced, preventing efficient relaxation through either of the CIs, independent of the chosen solvation model. Most of the population is thus trapped in the S_1 *Z*-minimum resulting in a significantly extended excited state lifetime. Since the barrier of 0.35 eV toward the quenching CI_Q only represents a lower boundary of the true barrier, it is not possible to identify a main decay channel in benzene solely from the quantum chemical calculations. However, according to the low combined quantum yield of $\sim 10\%$, the quenching CI_Q should be at least as accessible as the productive CI_p . Overall, most of the excited state population relaxes back to the ground state without isomerization, while those few molecules that

eventually arrive at the productive CI_P most likely isomerize to the E -isomer.

Model of HTI Photodynamics. Overall, the findings of our quantum chemical calculations reproduce and explain the experimental data very well and allow us to construct a concise model for the ultrafast dynamics of the investigated sterically restricted HTI 1-A (Figure 6). Following the excitation to the

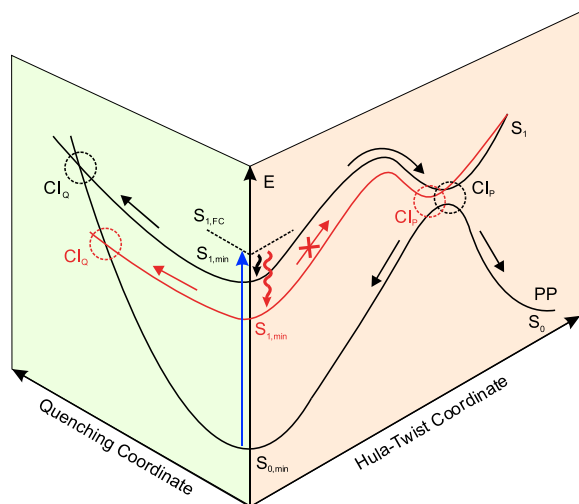


Figure 6. Schematic PES for the HTI 1-A photoisomerization in benzene (black) and MeCN (red). Upon excitation to the FC-region (located at similar energies in both solvents) the excess energy in benzene is not sufficient to pass the barriers to the quenching CI (CI_Q) or productive CI (CI_P) immediately, trapping the molecule in the $S_{1,min}$. In MeCN, the excess energy is strongly increased due to the greater stabilization of $S_{1,min}$ with respect to $S_{1,FC}$, allowing fast relaxation through the accessible CI_Q . As the barrier to the CI_P possesses a lower dipole moment, it is less stabilized by MeCN and cannot be passed from the strongly stabilized $S_{1,min}$. In benzene, both CIs are accessible but only after passing significant barriers of similar height, which leads to the observed long excited state lifetime. Eventually, both CIs may be accessed, and photoproduct can be formed through the CI_P , in contrast to MeCN and in agreement with the experimental quantum yields.

FC-region, the system relaxes quickly into the $S_{1,min}$. In contrast to the ground state S_0 , the S_1 exhibits significant CT character. This is reflected by the solvent dependent stabilization of $S_{1,min}$ as evident by the strong red shift of the fluorescence with increasing polarity and supported by the calculated energies (Table 1). Due to the drastic change of the dipole moment between the S_0 and S_1 , the solvent molecules reorganize on the few ps time scale causing shifts or small changes in the ESA intensity.

From the $S_{1,min}$ a barrier has to be overcome in all solvents to reach the CIs with the S_0 ground state based on the lifetimes in the range of tens to thousands of ps. The height of this barrier depends on the stabilization of the $S_{1,min}$ and the respective CI. Two CIs, a productive CI_P following a HT pathway and a quenching CI_Q exhibiting only small geometric changes with respect to the $S_{1,min}$ structure, determine the relaxation of the excited state population to the ground state. The accessibility of these CIs depends predominantly on the excess energy generated by relaxation from the FC-region and the barrier height to the CI.

In the case of the polar solvent MeCN, it can be concluded that the excess energy exceeds the barrier toward the

quenching CI_Q in the excited state to explain the observed short excited state lifetime despite the uncertainty of the calculated barrier height. On the other hand, the high isomerization barrier prevents relaxation through the productive CI_P . In combination with the lower probability of product formation at the productive CI_P , this explains the vanishingly small quantum yields in MeCN.

In the apolar benzene, the excess energy is insufficient to immediately cross the barriers leading to vibrational cooling and the population being trapped in the S_1 minimum. This is in good agreement with the increased fluorescence intensities and excited state lifetimes observed in the TA. The excited state population is then drained through both the productive CI_P and quenching CI_Q where the ratio approximately correlates to the ratio of the barrier heights. Therefore, it is expected that the majority of the excited molecules undergo unproductive relaxation. However, those molecules accessing the productive CI_P most likely undergo efficient isomerization due to the more favorable location of the CI_P in apolar solvents reasonably explaining the observed low quantum yields. The finding that we do not observe distinct excited state populations that evolve separately indicates that the formation of photoproducts probably occurs on a shared pathway through the productive CI_P instead of distinct pathways with individual CIs as observed for other HTIs previously.^{18,19} If one would assign the observed small excited state decay within

tens to hundreds of ps to a distinct productive pathway, it would be expected that its ratio with the main decay correlates with the quantum yield if the solvent polarity is changed. A shared pathway seems plausible, due to the fact that the $S_{1,min}$ geometry already has significant resemblance and similar properties to a TICT state, which is typically the alternative relaxation pathway besides DBI.

It is likely that from the geometry of the productive CI_P relaxation via DBI or SBR is also possible instead of only forming the HT product. The distribution between these processes strongly depends on the exact landscape of the CI_P , which as we show in our calculations is strongly modified by the solvent polarity. The calculation of the direct SBR and DBI was not possible here, as the forced change of the appropriate coordinates would result in immediate steric clashes within the molecule due to significant steric constraints. Nevertheless, we were able to explain the different excited state lifetimes and investigated the quenching CI_Q , which should represent a competing relaxation channel for all three isomerization pathways.

CONCLUSION

In summary, our work provides first insights into the excited state dynamics and HT mechanism of a sterically restricted HTI by using a combination of ultrafast spectroscopy and quantum chemical calculations. We show that the HT photoreaction is a concerted process in which the central double bond and the adjacent single bond rotate concomitantly in the excited state to form the HT photoproduct. Due to large steric constraints and the presence of a strong electron-donating anilin fragment, the excited state lifetimes are extended and very sensitive to changes in solvent polarity. We assign this sensitivity to the strong CT character of the first excited state, which leads to significant modifications of the barrier height, excess energy in the excited state, and the resulting availability of alternative relaxation pathways. In contrast to other HTIs, we do not observe an obvious splitting

into different photoreaction pathways like DBI and TICT formation, as there is only one major excited state decay. This behavior is consistent throughout all three investigated solvents of different polarity even though the product yields and ratios change significantly. Therefore, we propose that in strongly constrained HTIs the product formation occurs on a shared pathway and splits into the individual product pathways from the same CI. The variation in solvent polarity might be enough to shift the PES landscape around the productive CI and modify the product ratios accordingly as evident by the solvent dependent shift of the productive CI in the theoretical description. The gained detailed insights thus lay the foundation for an atomistic understanding of the HT photoreaction and will aid future design and control of complex light-powered bond rotations in a fully conscious manner.

■ ASSOCIATED CONTENT

SI Supporting Information

The Supporting Information is available free of charge at <https://pubs.acs.org/doi/10.1021/jacs.3c03536>.

Details of synthesis, conformational analyses, photochemical, photophysical, and thermal behavior, quantum yield measurements, crystal structural data and calculated geometries of important structures as xyz-coordinates. (PDF)

Accession Codes

CCDC 2250057–2250060 contain the supplementary crystallographic data for this paper. These data can be obtained free of charge via www.ccdc.cam.ac.uk/data_request/cif, or by emailing data_request@ccdc.cam.ac.uk, or by contacting The Cambridge Crystallographic Data Centre, 12 Union Road, Cambridge CB2 1EZ, UK; fax: +44 1223 336033.

■ AUTHOR INFORMATION

Corresponding Authors

Andreas Dreuw – Interdisciplinary Center for Scientific Computing, Ruprecht-Karls University Heidelberg, 69120 Heidelberg, Germany; Email: dreuw@uni-heidelberg.de

Henry Dube – Department of Chemistry and Pharmacy, Friedrich-Alexander University Erlangen-Nürnberg, 91058 Erlangen, Germany; orcid.org/0000-0002-5055-9924; Email: henry.dube@fau.de

Josef Wachtveitl – Institute of Physical and Theoretical Chemistry, Goethe University Frankfurt am Main, 60438 Frankfurt, Germany; orcid.org/0000-0002-8496-8240; Email: wveitl@theochem.uni-frankfurt.de

Authors

Tobias Fischer – Institute of Physical and Theoretical Chemistry, Goethe University Frankfurt am Main, 60438 Frankfurt, Germany; orcid.org/0000-0002-4196-5509

Jonas Leitner – Interdisciplinary Center for Scientific Computing, Ruprecht-Karls University Heidelberg, 69120 Heidelberg, Germany

Aaron Gerwien – Department of Chemistry and Center for Integrated Protein Science CIPSM, Ludwig-Maximilians Universität München, 81377 Munich, Germany

Peter Mayer – Department of Chemistry and Center for Integrated Protein Science CIPSM, Ludwig-Maximilians Universität München, 81377 Munich, Germany

Complete contact information is available at:

<https://pubs.acs.org/10.1021/jacs.3c03536>

Author Contributions

[†]These authors contributed equally.

Notes

The authors declare no competing financial interest.

■ ACKNOWLEDGMENTS

H.D. thanks the Deutsche Forschungsgemeinschaft (DFG) for an Emmy Noether fellowship (DU 1414/1-2). J.W. acknowledges the DFG (WA 1850/4-3) for funding. J.L. acknowledges funding of the DFG through the research training group CLiC (GRK 1986, Complex Light-Control). This project has also received funding from the European Research Council (ERC) under the European Union's Horizon 2020 research and innovation programme (PHOTOMECH, grant agreement No. 101001794).

■ ABBREVIATIONS

cHex, cyclohexane; CI, conical intersection; CT, charge transfer; DAS, decay-associated spectra; DBI, double bond isomerization; ESA, excited state absorption; GSB, ground state bleach; GTA, global target analysis; HT, Hula-Twist; HTI, hemithioindigo; LR-PCM, linear response polarizable continuum model; MeCN, acetonitrile; MECF, minimum energy crossing point; NOPA, noncollinear optical parametric amplifier; NTO, natural transition orbital; OD, optical density; PES, Potential energy surface; SBR, single bond rotation; SBT, single bond twisting; SE, stimulated emission; SF-DFT, Spin-flip density functional theory; SS-PCM, state specific polarizable continuum model; TA, transient absorption; TDA, Tamm-Dancoff approximation; TD-DFT, Time-dependent density functional theory; TICT, Twisted intramolecular charge transfer

■ REFERENCES

- (1) Cordes, T.; Weinrich, D.; Kempa, S.; Riesselmann, K.; Herre, S.; Hoppmann, C.; Rück-Braun, K.; Zinth, W. Hemithioindigo-Based Photoswitches as Ultrafast Light Trigger in Chromopeptides. *Chem. Phys. Lett.* **2006**, *428* (1–3), 167–173.
- (2) Cordes, T.; Schadendorf, T.; Rück-Braun, K.; Zinth, W. Chemical Control of Hemithioindigo-Photoisomerization - Substituent-Effects on Different Molecular Parts. *Chem. Phys. Lett.* **2008**, *455* (4–6), 197–201.
- (3) Cordes, T.; Schadendorf, T.; Priewisch, B.; Rück-Braun, K.; Zinth, W. The Hammett Relationship and Reactions in the Excited Electronic State: Hemithioindigo Z/E-Photoisomerization. *J. Phys. Chem. A* **2008**, *112* (4), 581–588.
- (4) Nenov, A.; Cordes, T.; Herzog, T. T.; Zinth, W.; De Vivie-Riedle, R. Molecular Driving Forces for Z/E Isomerization Mediated by Heteroatoms: The Example Hemithioindigo. *J. Phys. Chem. A* **2010**, *114* (50), 13016–13030.
- (5) Maerz, B.; Wiedbrauk, S.; Oesterling, S.; Samoylova, E.; Nenov, A.; Mayer, P.; De Vivie-Riedle, R.; Zinth, W.; Dube, H. Making Fast Photoswitches Faster - Using Hammett Analysis to Understand the Limit of Donor-Acceptor Approaches for Faster Hemithioindigo Photoswitches. *Chem. - Eur. J.* **2014**, *20* (43), 13984–13992.
- (6) Wiedbrauk, S.; Dube, H. Hemithioindigo-An Emerging Photoswitch. *Tetrahedron Lett.* **2015**, *56* (29), 4266–4274.
- (7) Regner, N.; Herzog, T. T.; Haiser, K.; Hoppmann, C.; Beyermann, M.; Saueremann, J.; Engelhard, M.; Cordes, T.; Rück-Braun, K.; Zinth, W. Light-Switchable Hemithioindigo-Hemistilbene-Containing Peptides: Ultrafast Spectroscopy of the Z → e Isomerization of the Chromophore and the Structural Dynamics of the Peptide Moiety. *J. Phys. Chem. B* **2012**, *116* (14), 4181–4191.

- (8) Füllbeck, M.; Michalsky, E.; Jaeger, I. S.; Henklein, P.; Kuhn, H.; Rück-Braun, K.; Preissner, R. Design and Biological Evaluation of Photo-Switchable Inhibitors. *Genome Inform. Int. Conf. Genome Inform.* **2006**, *17* (1), 141–151.
- (9) Eggers, K.; Fyles, T. M.; Montoya-Pelaez, P. J. Synthesis and Characterization of Photoswitchable Lipids Containing Hemithioindigo Chromophores. *J. Org. Chem.* **2001**, *66* (9), 2966–2977.
- (10) Kitzig, S.; Thilemann, M.; Cordes, T.; Rück-Braun, K. Light-Switchable Peptides with a Hemithioindigo Unit: Peptide Design, Photochromism, and Optical Spectroscopy. *ChemPhysChem* **2016**, *17* (9), 1252–1263.
- (11) Tanaka, K.; Taguchi, K.; Iwata, S.; Irie, T. Application of Benzoyl-Substituted Hemithioindigo as a Molecular Switch in Porphyrin-Quinone Recognition. *Supramol. Chem.* **2005**, *17* (8), 637–642.
- (12) Tanaka, K.; Kohayakawa, K.; Iwata, S.; Irie, T. Application of 2-Pyridyl-Substituted Hemithioindigo as a Molecular Switch in Hydrogen-Bonded Porphyrins. *J. Org. Chem.* **2008**, *73* (10), 3768–3774.
- (13) Dube, H.; Rebek, J. Selective Guest Exchange in Encapsulation Complexes Using Light of Different Wavelengths. *Angew. Chem. - Int. Ed.* **2012**, *51* (13), 3207–3210.
- (14) Guentner, M.; Uhl, E.; Mayer, P.; Dube, H. Photocontrol of Polar Aromatic Interactions by a Bis-Hemithioindigo Based Helical Receptor. *Chem. - Eur. J.* **2016**, *22* (46), 16433–16436.
- (15) Guentner, M.; Schildhauer, M.; Thumser, S.; Mayer, P.; Stephenson, D.; Mayer, P. J.; Dube, H. Sunlight-Powered kHz Rotation of a Hemithioindigo-Based Molecular Motor. *Nat. Commun.* **2015**, *6* (1), 8406.
- (16) Stallhofer, K.; Nuber, M.; Schüppel, F.; Thumser, S.; Iglev, H.; De Vivie-Riedle, R.; Zinth, W.; Dube, H. Electronic and Geometric Characterization of TICT Formation in Hemithioindigo Photoswitches by Picosecond Infrared Spectroscopy. *J. Phys. Chem. A* **2021**, *125* (20), 4390–4400.
- (17) Gerwien, A.; Schildhauer, M.; Thumser, S.; Mayer, P.; Dube, H. Direct Evidence for Hula Twist and Single-Bond Rotation Photo-products. *Nat. Commun.* **2018**, *9* (1), 2510.
- (18) Wiedbrauk, S.; Maerz, B.; Samoylova, E.; Mayer, P.; Zinth, W.; Dube, H. Ingredients to TICT Formation in Donor Substituted Hemithioindigo. *J. Phys. Chem. Lett.* **2017**, *8* (7), 1585–1592.
- (19) Wiedbrauk, S.; Maerz, B.; Samoylova, E.; Reiner, A.; Trommer, F.; Mayer, P.; Zinth, W.; Dube, H. Twisted Hemithioindigo Photoswitches: Solvent Polarity Determines the Type of Light-Induced Rotations. *J. Am. Chem. Soc.* **2016**, *138* (37), 12219–12227.
- (20) Gerwien, A.; Reinhardt, T.; Mayer, P.; Dube, H. Synthesis of Double-Bond-Substituted Hemithioindigo Photoswitches. *Org. Lett.* **2018**, *20* (1), 232–235.
- (21) Köttner, L.; Schildhauer, M.; Wiedbrauk, S.; Mayer, P.; Dube, H. Oxidized Hemithioindigo Photoswitches—Influence of Oxidation State on (Photo)Physical and Photochemical Properties. *Chem. - Eur. J.* **2020**, *26* (47), 10712–10718.
- (22) Liu, R. S.; Asato, A. E. The Primary Process of Vision and the Structure of Bathorhodopsin: A Mechanism for Photoisomerization of Polyenes. *Proc. Natl. Acad. Sci. U. S. A.* **1985**, *82* (2), 259–263.
- (23) Fuß, W.; Kosmidis, C.; Schmid, W. E.; Trushin, S. A. The Photochemical Cis-Trans Isomerization of Free Stilbene Molecules Follows a Hula-Twist Pathway. *Angew. Chem. - Int. Ed.* **2004**, *43* (32), 4178–4182.
- (24) Warshel, A. Bicycle-Pedal Model for the First Step in the Vision Process. *Nature* **1976**, *260* (5553), 679–683.
- (25) Gerwien, A.; Mayer, P.; Dube, H. Photon-Only Molecular Motor with Reverse Temperature-Dependent Efficiency. *J. Am. Chem. Soc.* **2018**, *140* (48), 16442–16446.
- (26) Gerwien, A.; Jehle, B.; Irmeler, M.; Mayer, P.; Dube, H. An Eight-State Molecular Sequential Switch Featuring a Dual Single-Bond Rotation Photoreaction. *J. Am. Chem. Soc.* **2022**, *144* (7), 3029–3038.
- (27) Imamoto, Y.; Kuroda, T.; Kataoka, M.; Shevyakov, S.; Krishnamoorthy, G.; Liu, R. S. H. Photoisomerization by Hula Twist: 2,2'-Dimethylstilbene and a Ring-Fused Analogue. *Angew. Chem., Int. Ed.* **2003**, *42* (31), 3630–3633.
- (28) Müller, A. M.; Lochbrunner, S.; Schmid, W. E.; Fuß, W. Low-Temperature Photochemistry of Previtamin D: A Hula-Twist Isomerization of a Triene. *Angew. Chem., Int. Ed.* **1998**, *37* (4), 505–507.
- (29) Maessen, P. A.; Jacobs, H. J. C.; Cornelisse, J.; Havinga, E. Photochemistry of Previtamin D3 at 92 K: Formation of an Unstable Tachysterol3 Rotamer. *Angew. Chem., Int. Ed.* **1983**, *22* (9), 718–719.
- (30) Saltiel, J.; Megarity, E. D.; Kneipp, K. G. The Mechanism of Direct Cis-Trans Photoisomerization of the Stilbenes. *J. Am. Chem. Soc.* **1966**, *88* (10), 2336–2338.
- (31) Bayda, M.; Redwood, C. E.; Gupta, S.; Dmitrenko, O.; Saltiel, J. Lumisterol to Tachysterol Photoisomerization in EPA Glass at 77 K. A Comparative Study. *J. Phys. Chem. A* **2017**, *121* (12), 2331–2342.
- (32) Redwood, C.; Bayda, M.; Saltiel, J. Photoisomerization of Pre-and Provitamin D3 in EPA at 77 K: One-Bond-Twist, Not Hula-Twist. *J. Phys. Chem. Lett.* **2013**, *4* (5), 716–721.
- (33) Jung, Y. O.; Lee, J. H.; Kim, J.; Schmidt, M.; Moffat, K.; Šrajer, V.; Ihee, H. Volume-Conserving Trans–Cis Isomerization Pathways in Photoactive Yellow Protein Visualized by Picosecond X-Ray Crystallography. *Nat. Chem.* **2013**, *5* (3), 212–220.
- (34) Kaila, V. R. I.; Schotte, F.; Cho, H. S.; Hummer, G.; Anfinrud, P. A. Contradictions in X-Ray Structures of Intermediates in the Photocycle of Photoactive Yellow Protein. *Nat. Chem.* **2014**, *6* (4), 258–259.
- (35) Jung, Y. O.; Lee, J. H.; Kim, J.; Schmidt, M.; Moffat, K.; Šrajer, V.; Ihee, H. Reply to “Contradictions in X-Ray Structures of Intermediates in the Photocycle of Photoactive Yellow Protein. *Nat. Chem.* **2014**, *6* (4), 259–260.
- (36) Slavov, C.; Bellakbil, N.; Wahl, J.; Mayer, K.; Rück-Braun, K.; Burghardt, I.; Wachtveitl, J.; Braun, M. Ultrafast Coherent Oscillations Reveal a Reactive Mode in the Ring-Opening Reaction of Fulgides. *Phys. Chem. Chem. Phys.* **2015**, *17*, 14045–14053.
- (37) Slavov, C.; Hartmann, H.; Wachtveitl, J. Implementation and Evaluation of Data Analysis Strategies for Time-Resolved Optical Spectroscopy. *Anal. Chem.* **2015**, *87* (4), 2328–2336.
- (38) Frisch, M. J.; Trucks, G. W.; Schlegel, H. B.; Scuseria, G. E.; Robb, M. A.; Cheeseman, J. R.; Scalmani, G.; Barone, V.; Petersson, G. A.; Nakatsuji, H.; Li, X.; Caricato, M.; Marenich, A. V.; Bloino, J.; Janesko, B. G.; Gomperts, R.; Mennucci, B.; Hratchian, H. P.; Ortiz, J. V.; Izmaylov, A. F.; Sonnenberg, J. L.; Williams-Young, D.; Ding, F.; Lipparini, F.; Egidi, F.; Goings, J.; Peng, B.; Petrone, A.; Henderson, T.; Ranasinghe, D.; Zakrzewski, V. G.; Gao, J.; Rega, N.; Zheng, G.; Liang, W.; Hada, M.; Ehara, M.; Toyota, K.; Fukuda, R.; Hasegawa, J.; Ishida, M.; Nakajima, T.; Honda, Y.; Kitao, O.; Nakai, H.; Vreven, T.; Throssell, K.; Montgomery, J. A., Jr.; Peralta, J. E.; Ogliaro, F.; Bearpark, M. J.; Heyd, J. J.; Brothers, E. N.; Kudin, K. N.; Staroverov, V. N.; Keith, T. A.; Kobayashi, R.; Normand, J.; Raghavachari, K.; Rendell, A. P.; Burant, J. C.; Iyengar, S. S.; Tomasi, J.; Cossi, M.; Millam, J. M.; Klene, M.; Adamo, C.; Cammi, R.; Ochterski, J. W.; Martin, R. L.; Morokuma, K.; Farkas, O.; Foresman, J. B.; Fox, D. J. *Gaussian 16*, Revision B.01; Gaussian, Inc.: Wallingford, CT, 2016.
- (39) Parr, R. G. In *Density Functional Theory of Atoms and Molecules BT - Horizons of Quantum Chemistry*; Fukui, K., Pullman, B., Eds.; Springer Netherlands: Dordrecht, 1980; pp 5–15.
- (40) Yanai, T.; Tew, D. P.; Handy, N. C. A New Hybrid Exchange-Correlation Functional Using the Coulomb-Attenuating Method (CAM-B3LYP). *Chem. Phys. Lett.* **2004**, *393* (1–3), 51–57.
- (41) Scalmani, G.; Frisch, M. J. Continuous Surface Charge Polarizable Continuum Models of Solvation. I. General Formalism. *J. Chem. Phys.* **2010**, *132* (11), 114110.
- (42) Dreuw, A.; Head-Gordon, M. Single-Reference Ab Initio Methods for the Calculation of Excited States of Large Molecules. *Chem. Rev.* **2005**, *105* (11), 4009–4037.
- (43) Epifanovsky, E.; Gilbert, A. T. B.; Feng, X.; Lee, J.; Mao, Y.; Mardirossian, N.; Pokhilko, P.; White, A. F.; Coons, M. P.; Dempwolff, A. L.; Gan, Z.; Hait, D.; Horn, P. R.; Jacobson, L. D.; Kaliman, I.; Kussmann, J.; Lange, A. W.; Lao, K. U.; Levine, D. S.; Liu,

J.; McKenzie, S. C.; Morrison, A. F.; Nanda, K. D.; Plasser, F.; Rehn, D. R.; Vidal, M. L.; You, Z. Q.; Zhu, Y.; Alam, B.; Albrecht, B. J.; Aldossary, A.; Alguire, E.; Andersen, J. H.; Athavale, V.; Barton, D.; Begam, K.; Behn, A.; Bellonzi, N.; Bernard, Y. A.; Berquist, E. J.; Burton, H. G. A.; Carreras, A.; Carter-Fenk, K.; Chakraborty, R.; Chien, A. D.; Closser, K. D.; Cofer-Shabica, V.; Dasgupta, S.; De Wergifosse, M.; Deng, J.; Diedenhofen, M.; Do, H.; Ehlert, S.; Fang, P. T.; Fatehi, S.; Feng, Q.; Friedhoff, T.; Gayvert, J.; Ge, Q.; Gidofalvi, G.; Goldey, M.; Gomes, J.; González-Espinoza, C. E.; Gulania, S.; Gunina, A. O.; Hanson-Heine, M. W. D.; Harbach, P. H. P.; Hauser, A.; Herbst, M. F.; Hernández Vera, M.; Hodecker, M.; Holden, Z. C.; Houck, S.; Huang, X.; Hui, K.; Huynh, B. C.; Ivanov, M.; Jász, Á.; Ji, H.; Jiang, H.; Kaduk, B.; Kähler, S.; Khistyayev, K.; Kim, J.; Kis, G.; Klunzinger, P.; Koczor-Benda, Z.; Koh, J. H.; Kosenkov, D.; Koulias, L.; Kowalczyk, T.; Krauter, C. M.; Kue, K.; Kunitsa, A.; Kus, T.; Ladjanski, I.; Landau, A.; Lawler, K. V.; Lefrancois, D.; Lehtola, S.; Li, R. R.; Li, Y. P.; Liang, J.; Liebenthal, M.; Lin, H. H.; Lin, Y. S.; Liu, F.; Liu, K. Y.; Loipersberger, M.; Luenser, A.; Manjanath, A.; Manohar, P.; Mansoor, E.; Manzer, S. F.; Mao, S. P.; Marenich, A. V.; Markovich, T.; Mason, S.; Maurer, S. A.; McLaughlin, P. F.; Menger, M. F. S. J.; Mewes, J. M.; Mewes, S. A.; Morgante, P.; Mullinax, J. W.; Oosterbaan, K. J.; Paran, G.; Paul, A. C.; Paul, S. K.; Pavošević, F.; Pei, Z.; Prager, S.; Proynov, E. I.; Rák, A.; Ramos-Cordoba, E.; Rana, B.; Rask, A. E.; Rettig, A.; Richard, R. M.; Rob, F.; Rossomme, E.; Scheele, T.; Scheurer, M.; Schneider, M.; Sergueev, N.; Sharada, S. M.; Skomorowski, W.; Small, D. W.; Stein, C. J.; Su, Y. C.; Sundstrom, E. J.; Tao, Z.; Thirman, J.; Tornai, G. J.; Tsuchimochi, T.; Tubman, N. M.; Veccham, S. P.; Vydrov, O.; Wenzel, J.; Witte, J.; Yamada, A.; Yao, K.; Yeganeh, S.; Yost, S. R.; Zech, A.; Zhang, I. Y.; Zhang, X.; Zhang, Y.; Zuev, D.; Aspuru-Guzik, A.; Bell, A. T.; Besley, N. A.; Bravaya, K. B.; Brooks, B. R.; Casanova, D.; Chai, J.; Da; Coriani, S.; Cramer, C. J.; Cserey, G.; DePrince, A. E.; Distasio, R. A.; Dreuw, A.; Dunietz, B. D.; Furlani, T. R.; Goddard, W. A.; Hammes-Schiffer, S.; Head-Gordon, T.; Hehre, W. J.; Hsu, C. P.; Jagau, T. C.; Jung, Y.; Klamt, A.; Kong, J.; Lambrecht, D. S.; Liang, W.; Mayhall, N. J.; McCurdy, C. W.; Neaton, J. B.; Ochsenfeld, C.; Parkhill, J. A.; Peverati, R.; Rassolov, V. A.; Shao, Y.; Slipchenko, L. V.; Stauch, T.; Steele, R. P.; Subotnik, J. E.; Thom, A. J. W.; Tkatchenko, A.; Truhlar, D. G.; Van Voorhis, T.; Wesolowski, T. A.; Whaley, K. B.; Woodcock, H. L.; Zimmerman, P. M.; Faraji, S.; Gill, P. M. W.; Head-Gordon, M.; Herbert, J. M.; Krylov, A. I. Software for the Frontiers of Quantum Chemistry: An Overview of Developments in the Q-Chem 5 Package. *J. Chem. Phys.* **2021**, *155* (8), 084801.

(44) Shao, Y.; Head-Gordon, M.; Krylov, A. I. The Spin-Flip Approach within Time-Dependent Density Functional Theory: Theory and Applications to Diradicals. *J. Chem. Phys.* **2003**, *118* (11), 4807–4818.

(45) Hirata, S.; Head-Gordon, M. Time-Dependent Density Functional Theory within the Tamm-Dancoff Approximation. *Chem. Phys. Lett.* **1999**, *314* (3–4), 291–299.

(46) Graupner, F. F.; Herzog, T. T.; Rott, F.; Oesterling, S.; de Vivie-Riedle, R.; Cordes, T.; Zinth, W. Photoisomerization of Hemithioindigo Compounds: Combining Solvent- and Substituent-Effects into an Advanced Reaction Model. *Chem. Phys.* **2018**, *515*, 614–621.

(47) Plötner, J.; Dreuw, A. Molecular Mechanism of the Z/E-Photoisomerization of Hemithioindigo Hemistilbene. *J. Phys. Chem. A* **2009**, *113* (43), 11882–11887.

(48) Corni, S.; Cammi, R.; Mennucci, B.; Tomasi, J. Electronic Excitation Energies of Molecules in Solution within Continuum Solvation Models: Investigating the Discrepancy between State-Specific and Linear-Response Methods. *J. Chem. Phys.* **2005**, *123* (13), 134512.

Recommended by ACS

Ultrafast Ring Closure Reaction of Gaseous *cis*-Stilbene from $S_1(\pi\pi^*)$

Shutaro Karashima, Toshinori Suzuki, *et al.*

FEBRUARY 06, 2023

JOURNAL OF THE AMERICAN CHEMICAL SOCIETY

READ 

Ultrafast Excited State Aromatization in Dihydroazulene

Svetlana Shostak, Cheol Ho Choi, *et al.*

JANUARY 12, 2023

JOURNAL OF THE AMERICAN CHEMICAL SOCIETY

READ 

Solvent-Dependent Structural Dynamics in the Ultrafast Photodissociation Reaction of Triiodide Observed with Time-Resolved X-ray Solution Scattering

Amke Nimmrich, Sebastian Westenhoff, *et al.*

MAY 10, 2023

JOURNAL OF THE AMERICAN CHEMICAL SOCIETY

READ 

Photochemical Ring-Opening Reaction of 1,3-Cyclohexadiene: Identifying the True Reactive State

Oksana Travnikova, Maria Novella Piancastelli, *et al.*

NOVEMBER 29, 2022

JOURNAL OF THE AMERICAN CHEMICAL SOCIETY

READ 

Get More Suggestions >

List of Abbreviations

Aha	azidohomoalanine
Ala	alanine
BBO	β -barium borate
Boc	<i>tert</i> -Butyloxycarbonyl
BV	biliverdin IX α
CBCR	cyanobacteriochrome
CPA	chirped pulse amplification
CD	circular dichroism
cw	continuous wave
DAS	decay-associated spectra
DBI	double bond isomerization
DFG	difference frequency generation
DMA	dimethylamino
DMSO	dimethylsulfoxid
DNA	deoxyribonucleic acid
EADS	evolution-associated difference spectra
eq	equation
ES	excited state
ESA	excited state absorption
GAF	cGMP-specific phosphodiesterases, adenylyl cyclases, and FhlA
GLA	global lifetime analysis
GTA	global target analysis
GS	ground state
GSB	ground state bleach
GSH	ground state heterogeneity
HI	Hemiindigo
HK	histidine kinase

HT	Hula-Twist
HTI	Hemithioindigo
HOS	2-helix output sensors
IR	infrared
IRF	instrument response function
ISC	intersystem crossing
ITI	Iminothioindoxyl
J	julolidin
LBO	lithium triborate
LDA	lifetime distribution analysis
LDM	lifetime density map
MAS-NMR	magic angle spinning nuclear magnetic resonance
MeCN	acetonitrile
MeOH	methanol
NIR	near infrared
NMR	nuclear magnetic resonance
NOPA	non-collinear optical parametric amplifier
OPA	optical parametric amplifier
OPM	output module
OPO	optical parametric oscillator
PAS	Per-Arnt-Sim
PBS	phosphate-buffered saline
PCB	phycocyanobilin
PCM	photosensory core module
PDB ID	protein database identifier
PHY	phytochrome specific
P_r	red-absorbing ground state in phytochromes
P_{fr}	far red-absorbing ground state in phytochromes
PSS	photostationary state

PVB	phycoviolobilin
PΦB	phytochromobilin
QY	quantum yield
RNA	ribonucleid acid
RR	resonance raman
SADS	species-associated difference spectra
SBR	single bond rotation
SBT	single bond twisting
SE	stimulated emission
SFG	sum frequency generation
SHG	second harmonic generation
ssNMR	solid state nuclear magnetic resonance
TICT	twisted intermediate charge transfer
Ti:Sa	Ti ³⁺ doped sapphire
UV	ultraviolet
VET	vibrational energy transfer
Vis	visible
WT	wildtype

List of Figures

Figure 2.1	Radiative and non-radiative relaxation pathways in excited molecules summarized in the Jablonski diagram.	6
Figure 2.2	Amplification of a seed pulse with a pump pulse in an OPA and a NOPA.	10
Figure 2.3	Schematic depiction of the fs-transient absorption setup.	12
Figure 2.4	Chopping scheme applied in the transient absorption experiments.	13
Figure 2.5	Types of observable signals in time-resolved transient absorption measurements and their origin.	14
Figure 2.6	Schematic representation of the monochromatic flash photolysis setup used in this thesis.	15
Figure 2.7	Schematic illustration of the typical domain architectures of the characteristic PCMs for different groups of phytochromes.	20
Figure 2.8	Covalent adducts of bilin chromophores in phytochromes.	21
Figure 2.9	Structural snapshot of a selection of highly conserved amino acid residues in the chromophore binding pocket of <i>SynCph1</i> in the P_r state (PDB ID: 2VEA). ^[83]	23
Figure 2.10	Structural snapshot of the aliphatic pocket surrounding the chromophore (cyan) in the P_r state of <i>SynCph1</i> (PDB ID: 2VEA). ^[83]	25
Figure 2.11	Structural snapshot of the extended hydrogen bonding network in the chromophore binding pocket of <i>SynCph1</i> (PDB ID: 2VEA) in its P_r state. ^[83]	27
Figure 2.12	Illustration of the conserved PRXSF, WGG, and WXE motifs in the PHY tongue in the P_r state of <i>SynCph1</i> (PDB ID: 2VEA). ^[83]	30
Figure 2.13	Schematic photocycle of group I and II phytochromes.	34
Figure 2.14	Left: Crystal structure of the P_r state of <i>SynCph2</i> module (PDB ID: 4BWI). ^[90] Right: Absorption spectra of <i>SynCph2</i> in the P_r (light red) state, the PSS (purple) and the P_{fr} (dark red) state.	41
Figure 2.15	Basic structure of Hemiindigo, Hemithioindigo, and Iminothioindoxyl photoswitches.	42
Figure 2.16	Diastereomers 1-A to 1-D of the investigated HTI compound with indicated reaction mechanisms for photoconversion between the diastereomers.	45
Figure 2.17	ITI compounds investigated in this thesis.	46

Figure 3.1	Illustration of the conserved kinetic pattern and its associated processes in the LDM and single transients of the ultrafast forward dynamics of the P _r state of All2699g1.	49
Figure 3.2	LDMs corresponding to the P _r dynamics from all groups of phytochromes displaying the conserved kinetic footprint identified in this work.	54
Figure 3.3	Transient absorption data and corresponding LDMs of the ultrafast P _{fr} dynamics of All2699g1, All2699g1g2, and <i>SynCph2</i>	56
Figure 3.4	Schematic illustration of the kinetic model derived from the transient absorption data of All2699g1g2/ <i>SynCph2</i> (left) and All2699g1 (right).	58
Figure 3.5	LDMs corresponding to the P _{fr} dynamics of All2699g1, <i>SynCph2</i> , and selected mutants displaying the effects of the respective mutation on the lifetime and distribution of populations based on GSH.	59
Figure 3.6	Structural representation of the hydrogen bonding interactions of the chromophore ring D in the P _{fr} state of <i>DrBphP</i> F469W (PDB ID:5C5K). ^[127]	60
Figure 3.7	Flash photolysis data and GLA of the P _r state in All2699g1 and All2699g1g2 at pH 8.	63
Figure 3.8	DAS obtained from GLA of the pH dependent flash photolysis data of the P _r state in All2699g1 at pH 6.1, 7.2 and 8.4.	64
Figure 3.9	Complete photocycle of All2699g1 and All2699g1g2.	65
Figure 3.10	Overview of the spectroscopic data on diastereomer 1-A	69
Figure 3.11	Schematic representation of the developed mechanistic model of the kinetics of the investigated sterically crowded HTI.	70
Figure 3.12	UV/Vis absorption spectra of the two investigated ITI dipeptides DMA-ITI-Ala(Boc)-Aha and J-ITI-Ala(Boc)-Aha in different solvents.	72
Figure 3.13	Transient absorption data and the corresponding LDM obtained by LDA of the DMA-ITI-Ala(Boc)-Aha and J-ITI-Ala(Boc)-Aha dipeptides in MeOH after excitation at 520 nm and 560 nm respectively.	73
Figure 3.14	Solvent dependence of the transient absorption data and the corresponding LDM of the DMA-ITI-Ala(Boc)-Aha and J-ITI-Ala(Boc)-Aha dipeptides in DMSO (top), MeOH (center), and PBS/MeOH (1:1 mixture) (bottom).	75
Figure 3.15	Excitation wavelength dependence of the transient absorption data and the corresponding LDM obtained by LDA of the DMA-ITI-Ala(Boc)-Aha and J-ITI-Ala(Boc)-Aha dipeptides in MeOH.	76

Figure 3.16 Selected transients at 454 nm (left) and 625 nm (right) extracted from the transient absorption data of DMA-ITI-Ala(Boc), DMA-ITI-Ala(Boc)-Aha, and DMA-ITI-Ala-Aha after excitation at 520 nm scaled to similar intensities. The transients correspond to ESA and the hot GS respectively. 77

List of Tables

Table 2.1	Numbering of conserved amino acids in different phytochromes.	24
-----------	---	----

Bibliography

- [1] N. Nelson, A. Ben-Shem, *Nature Reviews Molecular Cell Biology* **2004**, *5*, 971–982.
- [2] M. Baslam, T. Mitsui, M. Hodges, E. Priesack, M. T. Herritt, I. Aranjuelo, Á. Sanz-Sáez, *Frontiers in Plant Science* **2020**, *11*, 882.
- [3] I. McConnell, G. Li, G. W. Brudvig, *Chemistry & Biology* **2010**, *17*, 434–447.
- [4] S. C. Cowley, *Nature Physics* **2016**, *12*, 384–386.
- [5] M. Barbarino, *Nature Reviews Physics* **2022**, *4*, 2–4.
- [6] V. Y. Arshavsky, M. E. Burns, *Journal of Biological Chemistry* **2012**, *287*, 1620–1626.
- [7] C.-H. Sung, J.-Z. Chuang, *The Journal of Cell Biology* **2010**, *190*, 953–963.
- [8] A. Möglich, X. Yang, R. A. Ayers, K. Moffat, *Annual Review of Plant Biology* **2010**, *61*, 21–47.
- [9] D. M. Kehoe, A. Gutu, *Annual Review of Plant Biology* **2006**, *57*, 127–150.
- [10] C. Brieke, F. Rohrbach, A. Gottschalk, G. Mayer, A. Heckel, *Angewandte Chemie - International Edition* **2012**, *51*, 8446–8476.
- [11] C. Petermayer, H. Dube, *Accounts of Chemical Research* **2018**, *51*, 1153–1163.
- [12] V. Emiliani, E. Entcheva, R. Hedrich, P. Hegemann, K. R. Konrad, C. Lüscher, M. Mahn, Z.-H. Pan, R. R. Sims, J. Vierock, O. Yizhar, *Nature Reviews Methods Primers* **2022**, *2*, 1–25.
- [13] K. Tang, H. M. Beyer, M. D. Zurbriggen, W. Gärtner, *Chemical Reviews* **2021**, *121*, 14906–14956.
- [14] A. C. Kneuttinger, *Biological Chemistry* **2022**, *403*, 573–613.
- [15] H. Cheng, J. Yoon, H. Tian, *Coordination Chemistry Reviews* **2018**, *372*, 66–84.
- [16] V. García-López, D. Liu, J. M. Tour, *Chemical Reviews* **2020**, *120*, 79–124.
- [17] J. Franck, E. G. Dymond, *Transactions of the Faraday Society* **1926**, *21*, 536–542.
- [18] E. U. Condon, *American Journal of Physics* **1947**, *15*, 365–374.
- [19] M. Born, R. Oppenheimer, *Annalen der Physik* **1927**, *389*, 457–484.

- [20] Beer, *Annalen der Physik* **1852**, 162, 78–88.
- [21] D. F. Swinehart, *Journal of Chemical Education* **1962**, 39, 333.
- [22] C. Slavov, N. Bellakbil, J. Wahl, K. Mayer, K. Rück-Braun, I. Burghardt, J. Wachtveitl, M. Braun, *Physical Chemistry Chemical Physics* **2015**, 17, 14045–14053.
- [23] A. Jablonski, *Nature* **1933**, 131, 839–840.
- [24] N. C. Rockwell, D. Duanmu, S. S. Martin, C. Bachy, D. C. Price, D. Bhattacharya, A. Z. Worden, J. C. Lagarias, *Proceedings of the National Academy of Sciences of the United States of America* **2014**, 111, 3871–3876.
- [25] A. J. Miles, R. W. Janes, B. A. Wallace, *Chemical Society Reviews* **2021**, 50, 8400–8413.
- [26] B. Ranjbar, P. Gill, *Chemical Biology and Drug Design* **2009**, 74, 101–120.
- [27] G. R. Bishop, J. B. Chaires, *Current Protocols in Nucleic Acid Chemistry* **2002**, 11, 7.11.1–7.11.8.
- [28] R. Berera, R. van Grondelle, J. T. M. Kennis, *Photosynthesis Research* **2009**, 101, 105–118.
- [29] A. H. Zewail, *The Journal of Physical Chemistry A* **2000**, 104, 5660–5694.
- [30] S. Mukamel, *Annual Review of Physical Chemistry* **1990**, 41, 647–681.
- [31] A. M. Zheltikov, *Physics-Uspexhi* **2006**, 49, 605.
- [32] T. Wilhelm, J. Piel, E. Riedle, *Optics Letters* **1997**, 22, 1494.
- [33] E. Riedle, M. Beutter, S. Lochbrunner, J. Piel, S. Schenkl, S. Spörlein, W. Zinth, *Applied Physics B* **2000**, 71, 457–465.
- [34] S. Backus, C. G. Durfee, M. M. Murnane, H. C. Kapteyn, *Review of Scientific Instruments* **1998**, 69, 1207–1223.
- [35] D. N. Bailey, D. M. Hercules, *Journal of Chemical Education* **1965**, 42, A83.
- [36] C. Slavov, H. Hartmann, J. Wachtveitl, *Analytical Chemistry* **2015**, 87, 2328–2336.
- [37] S. A. Kovalenko, A. L. Dobryakov, J. Ruthmann, N. P. Ernsting, *Physical Review A* **1999**, 59, 2369–2384.

- [38] M. N. Islam, L. F. Mollenauer, R. H. Stolen, J. R. Simpson, H. T. Shang, *Optics Letters* **1987**, *12*, 625–627.
- [39] I. A. Walmsley, C. Dorrer, *Advances in Optics and Photonics* **2009**, *1*, 308–437.
- [40] I. H. M. Van Stokkum, D. S. Larsen, R. van Grondelle, *Biochimica et Biophysica Acta - Bioenergetics* **2004**, *1657*, 82–104.
- [41] R. Croce, M. G. Müller, R. Bassi, A. R. Holzwarth, *Biophysical Journal* **2001**, *80*, 901–915.
- [42] M. Chen, J. Chory, C. Fankhauser, *Annual Review of Genetics* **2004**, *38*, 87–117.
- [43] K. A. Franklin, P. H. Quail, *Journal of Experimental Botany* **2010**, *61*, 11–24.
- [44] B. M. Parks, *Plant Physiology* **2003**, *133*, 1437–1444.
- [45] D. Duanmu, C. Bachy, S. Sudek, C. H. Wong, V. Jiménez, N. C. Rockwell, S. S. Martin, C. Y. Ngan, E. N. Reistetter, M. J. Van Baren, D. C. Price, C. L. Wei, A. Reyes-Prieto, J. C. Lagarias, A. Z. Worden, *Proceedings of the National Academy of Sciences of the United States of America* **2014**, *111*, 15827–15832.
- [46] K. C. Yeh, S. H. Wu, J. T. Murphy, J. C. Lagarias, *Science* **1997**, *277*, 1505–1508.
- [47] J. Hughes, T. Lamparter, F. Mittmann, E. Hartmann, W. Gärtner, A. Wilde, T. Börner, *Nature* **1997**, *386*, 663–663.
- [48] D. M. Kehoe, A. R. Grossman, *Science* **1996**, *273*, 1409–1412.
- [49] Z. Jiang, L. R. Swem, B. G. Rushing, S. Devanathan, G. Tollin, C. E. Bauer, *Science* **1999**, *285*, 406–409.
- [50] S. J. Davis, A. V. Vener, R. D. Vierstra, *Science* **1999**, *286*, 2517–2520.
- [51] A. Blumenstein, K. Vienken, R. Tasler, J. Purschwitz, D. Veith, N. Frankenberg-Dinkel, R. Fischer, *Current Biology* **2005**, *15*, 1833–1838.
- [52] B. Karniol, J. R. Wagner, J. M. Walker, R. D. Vierstra, *Biochemical Journal* **2005**, *392*, 103–116.
- [53] E. S. Burgie, R. D. Vierstra, *The Plant Cell* **2014**, *26*, 4568–4583.
- [54] N. C. Rockwell, Y.-S. Su, J. C. Lagarias, *Annual Review of Plant Biology* **2006**, *57*, 837–858.

- [55] H. Takala, P. Edlund, J. A. Ihalainen, S. Westenhoff, *Photochemical & Photobiological Sciences* **2020**, *19*, 1488–1510.
- [56] N. C. Rockwell, J. C. Lagarias, *Current Opinion in Plant Biology* **2017**, *37*, 87–93.
- [57] Y. Hirose, T. Shimada, R. Narikawa, M. Katayama, M. Ikeuchi, *Proceedings of the National Academy of Sciences of the United States of America* **2008**, *105*, 9528–9533.
- [58] E. Giraud, J. Fardoux, N. Fourrier, L. Hannibal, B. Genty, P. Bouyer, B. Dreyfus, A. Verméglio, *Nature* **2002**, *417*, 202–205.
- [59] X. Yang, Z. Ren, J. Kuk, K. Moffat, *Nature* **2011**, *479*, 428–431.
- [60] C. Song, G. Psakis, C. Lang, J. Mailliet, W. Gärtner, J. Hughes, J. Matysik, *Proceedings of the National Academy of Sciences of the United States of America* **2011**, *108*, 3842–3847.
- [61] N. C. Rockwell, J. C. Lagarias, *ChemPhysChem* **2010**, *11*, 1172–1180.
- [62] K. Anders, L. O. Essen, *Current Opinion in Structural Biology* **2015**, *35*, 7–16.
- [63] M. Ikeuchi, T. Ishizuka, *Photochemical & Photobiological Sciences* **2008**, *7*, 1159.
- [64] R. Narikawa, Y. Fukushima, T. Ishizuka, S. Itoh, M. Ikeuchi, *Journal of Molecular Biology* **2008**, *380*, 844–855.
- [65] T. Ishizuka, R. Narikawa, T. Kohchi, M. Katayama, M. Ikeuchi, *Plant and Cell Physiology* **2007**, *48*, 1385–1390.
- [66] N. C. Rockwell, S. L. Njuguna, L. Roberts, E. Castillo, V. L. Parson, S. Dwojak, J. C. Lagarias, S. C. Spiller, *Biochemistry* **2008**, *47*, 7304–7316.
- [67] K. Fushimi, M. Ikeuchi, R. Narikawa, *Photochemistry and Photobiology* **2017**, *93*, 903–906.
- [68] N. C. Rockwell, S. S. Martin, K. Feoktistova, J. C. Lagarias, *Proceedings of the National Academy of Sciences of the United States of America* **2011**, *108*, 11854–11859.
- [69] S. Lim, N. C. Rockwell, S. S. Martin, J. L. Dallas, J. C. Lagarias, J. B. Ames, *Photochemical & Photobiological Sciences* **2014**, *13*, 951–962.
- [70] G. Enomoto, Y. Hirose, R. Narikawa, M. Ikeuchi, *Biochemistry* **2012**, *51*, 3050–3058.

- [71] K. D. Piatkevich, F. V. Subach, V. V. Verkhusha, *Chemical Society Reviews* **2013**, *42*, 3441–3452.
- [72] T. A. Redchuk, E. S. Omelina, K. G. Chernov, V. V. Verkhusha, *Nature Chemical Biology* **2017**, *13*, 633–639.
- [73] D. M. Shcherbakova, O. V. Stepanenko, K. K. Turoverov, V. V. Verkhusha, *Trends in Biotechnology* **2018**, *36*, 1230–1243.
- [74] M. Hörner, K. Raute, B. Hummel, J. Madl, G. Creusen, O. S. Thomas, E. H. Christen, N. Hotz, R. J. Gübeli, R. Engesser, B. Rebmann, J. Lauer, B. Rolauffs, J. Timmer, W. W. Schamel, J. Pruszek, W. Römer, M. D. Zurbriggen, C. Friedrich, A. Walther, S. Minguet, R. Sawarkar, W. Weber, *Advanced Materials* **2019**, *31*, 1–11.
- [75] Y. G. Chai, B. R. Singh, P. S. Song, J. Lee, G. W. Robinson, *Analytical Biochemistry* **1987**, *163*, 322–330.
- [76] R. A. Sharrock, P. H. Quail, *Genes & development* **1989**, *3*, 1745–1757.
- [77] T. Lamparter, F. Mittmann, W. Gartner, T. Borner, E. Hartmann, J. Hughes, *Proceedings of the National Academy of Sciences of the United States of America* **1997**, *94*, 11792–11797.
- [78] H. J. Jorissen, B. Quest, A. Remberg, T. Coursin, S. E. Braslavsky, K. Schaffner, N. T. De Marsac, W. Gärtner, *European Journal of Biochemistry* **2002**, *269*, 2662–2671.
- [79] T. Lamparter, N. Michael, F. Mittmann, B. Esteban, *Proceedings of the National Academy of Sciences of the United States of America* **2002**, *99*, 11628–11633.
- [80] B. Karniol, R. D. Vierstra, *Proceedings of the National Academy of Sciences of the United States of America* **2003**, *100*, 2807–2812.
- [81] A. C. Froehlich, B. Noh, R. D. Vierstra, J. Loros, J. C. Dunlap, *Eukaryotic Cell* **2005**, *4*, 2140–2152.
- [82] J. R. Wagner, J. S. Brunzelle, K. T. Forest, R. D. Vierstra, *Nature* **2005**, *438*, 325–331.
- [83] L. O. Essen, J. Mailliet, J. Hughes, *Proceedings of the National Academy of Sciences of the United States of America* **2008**, *105*, 14709–14714.
- [84] X. Yang, J. Kuk, K. Moffat, *Proceedings of the National Academy of Sciences of the United States of America* **2008**, *105*, 14715–14720.

- [85] E. S. Burgie, A. N. Bussell, J. M. Walker, K. Dubiel, R. D. Vierstra, *Proceedings of the National Academy of Sciences of the United States of America* **2014**, *111*, 10179–10184.
- [86] T. Lamparter, N. Michael, O. Caspani, T. Miyata, K. Shirai, K. Inomata, *Journal of Biological Chemistry* **2003**, *278*, 33786–33792.
- [87] T. Lamparter, M. Carrascal, N. Michael, E. Martinez, G. Rottwinkel, J. Abian, *Biochemistry* **2004**, *43*, 3659–3669.
- [88] Q.-Z. Xu, P. Bielytskyi, J. Otis, C. Lang, J. Hughes, K.-H. Zhao, A. Losi, W. Gärtner, C. Song, *International Journal of Molecular Sciences* **2019**, *20*, 3656.
- [89] H. Takala, A. Björling, O. Berntsson, H. Lehtivuori, S. Niebling, M. Hoernke, I. Kosheleva, R. Henning, A. Menzel, J. A. Ihalainen, S. Westenhoff, *Nature* **2014**, *509*, 245–248.
- [90] K. Anders, G. Daminelli-Widany, M. A. Mroginski, D. Von Stetten, L. O. Essen, *Journal of Biological Chemistry* **2013**, *288*, 35714–35725.
- [91] A. Björling, O. Berntsson, H. Lehtivuori, H. Takala, A. J. Hughes, M. Panman, M. Hoernke, S. Niebling, L. Henry, R. Henning, I. Kosheleva, V. Chukharev, N. V. Tkachenko, A. Menzel, G. Newby, D. Khakhulin, M. Wulff, J. A. Ihalainen, S. Westenhoff, *Science Advances* **2016**, *2*, e1600920.
- [92] H. Takala, S. Niebling, O. Berntsson, A. Björling, H. Lehtivuori, H. Häkkänen, M. Panman, E. Gustavsson, M. Hoernke, G. Newby, F. Zontone, M. Wulff, A. Menzel, J. A. Ihalainen, S. Westenhoff, *Structural Dynamics* **2016**, *3*, 054701.
- [93] B. L. Montgomery, J. C. Lagarias, *Trends in Plant Science* **2002**, *7*, 357–366.
- [94] K. Anders, D. Von Stetten, J. Mailliet, S. Kiontke, V. A. Sineshchekov, P. Hildebrandt, J. Hughes, L. O. Essen, *Photochemistry and Photobiology* **2011**, *87*, 160–173.
- [95] Y. Chen, J. Zhang, J. Luo, J. M. Tu, X. L. Zeng, J. Xie, M. Zhou, J. Q. Zhao, H. Scheer, K.-H. Zhao, *FEBS Journal* **2011**, *279*, 40–54.
- [96] K. Anders, A. Gutt, W. Gärtner, L. O. Essen, *Journal of Biological Chemistry* **2014**, *289*, 25590–25600.
- [97] C. Slavov, X. Xu, K.-H. Zhao, W. Gärtner, J. Wachtveitl, *Biochimica et Biophysica Acta - Bioenergetics* **2015**, *1847*, 1335–1344.

- [98] P. W. Kim, L. H. Freer, N. C. Rockwell, S. S. Martin, J. C. Lagarias, D. S. Larsen, *Biochemistry* **2012**, *51*, 608–618.
- [99] T. Ishizuka, A. Kamiya, H. Suzuki, R. Narikawa, T. Noguchi, T. Kohchi, K. Inomata, M. Ikeuchi, *Biochemistry* **2011**, *50*, 953–961.
- [100] A. T. Ulijasz, G. Cornilescu, D. Von Stetten, S. Kaminski, M. A. Mroginski, J. Zhang, D. Bhaya, P. Hildebrandt, R. D. Vierstra, *Journal of Biological Chemistry* **2008**, *283*, 21251–21256.
- [101] Y. Hirose, N. C. Rockwell, K. Nishiyama, R. Narikawa, Y. Ukaji, K. Inomata, J. C. Lagarias, M. Ikeuchi, *Proceedings of the National Academy of Sciences of the United States of America* **2013**, *110*, 4974–4979.
- [102] H. M. Strauss, J. Hughes, P. Schmieder, *Biochemistry* **2005**, *44*, 8244–8250.
- [103] D. Von Stetten, S. Seibeck, N. Michael, P. Scheerer, M. A. Mroginski, D. H. Murgida, N. Krauss, M. P. Heyn, P. Hildebrandt, B. Borucki, T. Lamparter, *Journal of Biological Chemistry* **2007**, *282*, 2116–2123.
- [104] E. S. Burgie, T. Wang, A. N. Bussell, J. M. Walker, H. Li, R. D. Vierstra, *Journal of Biological Chemistry* **2014**, *289*, 24573–24587.
- [105] T. Rohmer, C. Lang, J. Hughes, L.-O. Essen, W. Gärtner, J. Matysik, *Proceedings of the National Academy of Sciences of the United States of America* **2008**, *105*, 15229–15234.
- [106] D. Stöppler, C. Song, B. J. van Rossum, M. A. Geiger, C. Lang, M. A. Mroginski, A. P. Jagtap, S. T. Sigurdsson, J. Matysik, J. Hughes, H. Oschkinat, *Angewandte Chemie - International Edition* **2016**, *55*, 16017–16020.
- [107] Y. Yang, M. Linke, T. von Haimberger, J. Hahn, R. Matute, L. González, P. Schmieder, K. Heyne, *Journal of the American Chemical Society* **2012**, *134*, 1408–1411.
- [108] C. Wiebeler, A. G. Rao, W. Gärtner, I. Schapiro, *Angewandte Chemie - International Edition* **2019**, *58*, 1934–1938.
- [109] S. Lim, Q. Yu, S. M. Gottlieb, C.-W. Chang, N. C. Rockwell, S. S. Martin, D. Madsen, J. C. Lagarias, D. S. Larsen, J. B. Ames, *Proceedings of the National Academy of Sciences of the United States of America* **2018**, *115*, 4387–4392.

- [110] N. C. Rockwell, S. S. Martin, A. G. Gulevich, J. C. Lagarias, *Biochemistry* **2014**, *53*, 3118–3130.
- [111] N. C. Rockwell, S. S. Martin, S. Lim, J. C. Lagarias, J. B. Ames, *Biochemistry* **2015**, *54*, 3772–3783.
- [112] N. C. Rockwell, S. S. Martin, A. G. Gulevich, J. C. Lagarias, *Biochemistry* **2012**, *51*, 1449–1463.
- [113] J. R. Wagner, J. Zhang, D. Von Stetten, M. Günther, D. H. Murgida, M. A. Mroginski, J. M. Walker, K. T. Forest, P. Hildebrandt, R. D. Vierstra, *Journal of Biological Chemistry* **2008**, *283*, 12212–12226.
- [114] J. Mailliet, G. Psakis, K. Feilke, V. Sineshchekov, L. O. Essen, J. Hughes, *Journal of Molecular Biology* **2011**, *413*, 115–127.
- [115] J. A. Rumfeldt, H. Takala, A. Liukkonen, J. A. Ihalainen, *Photochemistry and Photobiology* **2019**, *95*, 969–979.
- [116] J. S. Kirpich, L. T. Mix, S. S. Martin, N. C. Rockwell, J. C. Lagarias, D. S. Larsen, *The Journal of Physical Chemistry Letters* **2018**, *9*, 3454–3462.
- [117] M. E. Auldridge, K. A. Satyshur, D. M. Anstrom, K. T. Forest, *Journal of Biological Chemistry* **2012**, *287*, 7000–7009.
- [118] J. Zhang, R. J. Stankey, R. D. Vierstra, *Plant Physiology* **2013**, *161*, 1445–1457.
- [119] C. Slavov, T. Fischer, A. Barnoy, H. Shin, A. G. Rao, C. Wiebeler, X. Zeng, Y. Sun, Q. Xu, A. Gutt, K.-H. Zhao, W. Gärtner, X. Yang, I. Schapiro, J. Wachtveitl, *Proceedings of the National Academy of Sciences of the United States of America* **2020**, *117*, 16356–16362.
- [120] S. Nagano, P. Scheerer, K. Zubow, N. Michael, K. Inomata, T. Lamparter, N. Krauß, *Journal of Biological Chemistry* **2016**, *291*, 20674–20691.
- [121] C. Song, M. A. Mroginski, C. Lang, J. Kopycki, W. Gärtner, J. Matysik, J. Hughes, *Frontiers in Plant Science* **2018**, *9*, 1–15.
- [122] N. C. Rockwell, J. C. Lagarias, *Plant Cell* **2006**, *18*, 4–14.
- [123] J. A. Ihalainen, E. Gustavsson, L. Schroeder, S. Donnini, H. Lehtivuori, L. Isaksson, C. Thöing, V. Modi, O. Berntsson, B. Stucki-Buchli, A. Liukkonen, H. Häkkänen,

- E. Kalenius, S. Westenhoff, T. Kottke, *Journal of the American Chemical Society* **2018**, *140*, 12396–12404.
- [124] A. J. Fischer, N. C. Rockwell, A. Y. Jang, L. A. Ernst, A. S. Waggoner, Y. Duan, H. Lei, J. C. Lagarias, *Biochemistry* **2005**, *44*, 15203–15215.
- [125] A. J. Fischer, J. C. Lagarias, *Proceedings of the National Academy of Sciences of the United States of America* **2004**, *101*, 17334–17339.
- [126] M. Kurttila, B. Stucki-Buchli, J. Rumfeldt, L. Schroeder, H. Häkkänen, A. Liukkonen, H. Takala, T. Kottke, J. A. Ihalainen, *Physical Chemistry Chemical Physics* **2021**, *23*, 5615–5628.
- [127] E. S. Burgie, J. Zhang, R. D. Vierstra, *Structure* **2016**, *24*, 448–457.
- [128] H. Takala, H. K. Lehtivuori, O. Berntsson, A. Hughes, R. Nanekar, S. Niebling, M. Panman, L. Henry, A. Menzel, S. Westenhoff, J. A. Ihalainen, *Journal of Biological Chemistry* **2018**, *293*, 8161–8172.
- [129] V. Sineshchekov, J. Mailliet, G. Psakis, K. Feilke, J. Kopycki, M. Zeidler, L.-O. Essen, J. Hughes, *Photochemistry and Photobiology* **2014**, *90*, 786–795.
- [130] D. Wang, Y. Qin, M. Zhang, X. Li, L. Wang, X. Yang, D. Zhong, *The Journal of Physical Chemistry Letters* **2020**, 5913–5919.
- [131] H. Lehtivuori, J. Rumfeldt, S. Mustalahti, S. Kurkinen, H. Takala, *Photochemical & Photobiological Sciences* **2022**, *21*, 1975–1989.
- [132] E. Claesson, W. Y. Wahlgren, H. Takala, S. Pandey, L. Castillon, V. Kuznetsova, L. Henry, M. Panman, M. Carrillo, J. Kübel, R. Nanekar, L. Isaksson, A. Nimmrich, A. Cellini, D. Morozov, M. Maj, M. Kurttila, R. Bosman, E. Nango, R. Tanaka, T. Tanaka, L. Fangjia, S. Iwata, S. Owada, K. Moffat, G. Groenhof, E. A. Stojković, J. A. Ihalainen, M. Schmidt, S. Westenhoff, *eLife* **2020**, *9*, 1–18.
- [133] R. González, M. A. Mroginski, *Journal of Physical Chemistry B* **2019**, *123*, 9819–9830.
- [134] J. Kübel, M. Chenchiliyan, S. A. Ooi, E. Gustavsson, L. Isaksson, V. Kuznetsova, J. A. Ihalainen, S. Westenhoff, M. Maj, *Physical Chemistry Chemical Physics* **2020**, *22*, 9195–9203.
- [135] O. Anders Borg, B. Durbeej, *Physical Chemistry Chemical Physics* **2008**, *10*, 2528–2537.

- [136] J. J. Van Thor, B. Borucki, W. Crielaard, H. Otto, T. Lamparter, J. Hughes, K. J. Hellingwerf, M. P. Heyn, *Biochemistry* **2001**, *40*, 11460–11471.
- [137] C. Song, F. Velazquez Escobar, X. L. Xu, R. Narikawa, M. Ikeuchi, F. Siebert, W. Gärtner, J. Matysik, P. Hildebrandt, *Biochemistry* **2015**, *54*, 5839–5848.
- [138] N. Lenngren, P. Edlund, H. Takala, B. Stucki-Buchli, J. Rumfeldt, I. Peshev, H. Häkkinen, S. Westenhoff, J. A. Ihalainen, *Physical Chemistry Chemical Physics* **2018**, *20*, 18216–18225.
- [139] T. Mathes, J. Ravensbergen, M. Kloz, T. Gleichmann, K. D. Gallagher, N. C. Woitowich, R. St. Peter, S. E. Kovaleva, E. A. Stojković, J. T. M. Kennis, *The Journal of Physical Chemistry Letters* **2015**, *6*, 239–243.
- [140] K. C. Toh, E. A. Stojković, I. H. M. van Stokkum, K. Moffat, J. T. M. Kennis, *Proceedings of the National Academy of Sciences of the United States of America* **2010**, *107*, 9170–9175.
- [141] K. C. Toh, E. A. Stojković, A. B. Rupenyan, I. H. M. van Stokkum, M. Salumbides, M.-L. Groot, K. Moffat, J. T. M. Kennis, *The Journal of Physical Chemistry A* **2011**, *115*, 3778–3786.
- [142] G. Salvadori, V. Macaluso, G. Pellicci, L. Cupellini, G. Granucci, B. Mennucci, *Nature Communications* **2022**, *13*, 6838.
- [143] A. Kraskov, A. D. Nguyen, J. Goerling, D. Buhrke, F. Velazquez Escobar, M. Fernandez Lopez, N. Michael, L. Sauthof, A. Schmidt, P. Piwowarski, Y. Yang, T. Stenzitzki, S. Adam, F. Bartl, I. Schapiro, K. Heyne, F. Siebert, P. Scheerer, M. A. Mroginski, P. Hildebrandt, *Biochemistry* **2020**, *59*, 1023–1037.
- [144] F. Velazquez Escobar, P. Piwowarski, J. Salewski, N. Michael, M. Fernandez Lopez, A. Rupp, B. Muhammad Qureshi, P. Scheerer, F. Bartl, N. Frankenberg-Dinkel, F. Siebert, M. Andrea Mroginski, P. Hildebrandt, *Nature Chemistry* **2015**, *7*, 423–430.
- [145] J. Hahn, H. M. Strauss, F. T. Landgraf, H. F. Gimenez, G. Lochnit, P. Schmieder, J. Hughes, *FEBS Journal* **2006**, *273*, 1415–1429.
- [146] F. Velazquez Escobar, C. Lang, A. Takiden, C. Schneider, J. Balke, J. Hughes, U. Alexiev, P. Hildebrandt, M. A. Mroginski, *The Journal of Physical Chemistry B* **2017**, *121*, 47–57.

- [147] X. Yang, J. Kuk, K. Moffat, *Proceedings of the National Academy of Sciences of the United States of America* **2009**, *106*, 15639–15644.
- [148] D. Von Stetten, M. Günther, P. Scheerer, D. H. Murgida, M. A. Mroginski, N. Krauß, T. Lamparter, J. Zhang, D. M. Anstrom, R. D. Vierstra, K. T. Forest, P. Hildebrandt, *Angewandte Chemie - International Edition* **2008**, *47*, 4753–4755.
- [149] F. Velazquez Escobar, D. von Stetten, M. Günther-Lütken, A. Keidel, N. Michael, T. Lamparter, L.-O. Essen, J. Hughes, W. Gärtner, Y. Yang, K. Heyne, M. A. Mroginski, P. Hildebrandt, *Frontiers in Molecular Biosciences* **2015**, *2*, 1–13.
- [150] Y. Yang, M. Linke, T. von Haimberger, R. Matute, L. González, P. Schmieder, K. Heyne, *Structural Dynamics* **2014**, *1*, 014701.
- [151] P. W. Kim, N. C. Rockwell, S. S. Martin, J. C. Lagarias, D. S. Larsen, *Biochemistry* **2014**, *53*, 4601–4611.
- [152] P. W. Kim, N. C. Rockwell, S. S. Martin, J. C. Lagarias, D. S. Larsen, *Biochemistry* **2014**, *53*, 2818–2826.
- [153] D. Buhrke, G. Battocchio, S. Wilkening, M. Blain-Hartung, T. Baumann, F. J. Schmitt, T. Friedrich, M. A. Mroginski, P. Hildebrandt, *Biochemistry* **2020**, *59*, 509–519.
- [154] T. Stensitzki, Y. Yang, A. L. Wölke, E.-W. Knapp, J. Hughes, M. A. Mroginski, K. Heyne, *Photochemistry and Photobiology* **2017**, *93*, 703–712.
- [155] Y. Yang, K. Heyne, R. A. Mathies, J. Dasgupta, *ChemPhysChem* **2016**, *17*, 369–374.
- [156] J. Salewski, F. V. Escobar, S. Kaminski, D. Von Stetten, A. Keidel, Y. Rippers, N. Michael, P. Scheerer, P. Piwowarski, F. Bartl, N. Frankenberg-Dinkel, S. Ringsdorf, W. Gärtner, T. Lamparter, M. A. Mroginski, P. Hildebrandt, *Journal of Biological Chemistry* **2013**, *288*, 16800–16814.
- [157] C. Wang, M. L. Flanagan, R. D. McGillicuddy, H. Zheng, A. R. Ginzburg, X. Yang, K. Moffat, G. S. Engel, *Biophysical Journal* **2016**, *111*, 2125–2134.
- [158] P. W. Kim, L. H. Freer, N. C. Rockwell, S. S. Martin, J. C. Lagarias, D. S. Larsen, *Biochemistry* **2012**, *51*, 619–630.
- [159] A. G. Rao, C. Wiebeler, S. Sen, D. S. Cerutti, I. Schapiro, *Physical Chemistry Chemical Physics* **2021**, *23*, 7359–7367.

- [160] L. K. Scarbath-Evers, S. Jähnigen, H. Elgabarty, C. Song, R. Narikawa, J. Matysik, D. Sebastiani, *Physical Chemistry Chemical Physics* **2017**, *19*, 13882–13894.
- [161] S. M. Gottlieb, P. W. Kim, C.-W. Chang, S. J. Hanke, R. J. Hayer, N. C. Rockwell, S. S. Martin, J. C. Lagarias, D. S. Larsen, *Biochemistry* **2015**, *54*, 1028–1042.
- [162] A. J. Jenkins, S. M. Gottlieb, C.-W. Chang, P. W. Kim, R. J. Hayer, S. J. Hanke, S. S. Martin, J. C. Lagarias, D. S. Larsen, *Biochemistry* **2020**, *59*, 4015–4028.
- [163] F. Velazquez Escobar, C. Kneip, N. Michael, T. Hildebrandt, N. Tavraz, W. Gärtner, J. Hughes, T. Friedrich, P. Scheerer, M. A. Mroginski, P. Hildebrandt, *Journal of Physical Chemistry B* **2020**, *124*, 4044–4055.
- [164] C. Song, G. Psakis, C. Lang, J. Mailliet, J. Zaanen, W. Gärtner, J. Hughes, J. Matysik, *Biochemistry* **2011**, *50*, 10987–10989.
- [165] M. Sadeghi, J. Balke, C. Schneider, S. Nagano, J. Stellmacher, G. Lochnit, C. Lang, C. Weise, J. Hughes, U. Alexiev, *Biochemistry* **2020**, *59*, 1051–1062.
- [166] C. Song, L.-O. Essen, W. Gärtner, J. Hughes, J. Matysik, *Molecular Plant* **2012**, *5*, 698–715.
- [167] P. Singer, S. Wörner, T. Lamparter, R. Diller, *ChemPhysChem* **2016**, *17*, 1288–1297.
- [168] J. S. Kirpich, C. W. Chang, J. Franse, Q. Yu, F. V. Escobar, A. J. Jenkins, S. S. Martin, R. Narikawa, J. B. Ames, J. C. Lagarias, D. S. Larsen, *Biochemistry* **2021**, *60*, 274–288.
- [169] D. Wang, Y. Qin, S. Zhang, L. Wang, X. Yang, D. Zhong, *The Journal of Physical Chemistry Letters* **2019**, *10*, 6197–6201.
- [170] D. Wang, X. Li, L. Wang, X. Yang, D. Zhong, *The Journal of Physical Chemistry Letters* **2020**, *11*, 8819–8824.
- [171] S. R. Tachibana, L. Tang, C. Chen, L. Zhu, Y. Takeda, K. Fushimi, T. K. Seevers, R. Narikawa, M. Sato, C. Fang, *Spectrochimica Acta - Part A: Molecular and Biomolecular Spectroscopy* **2021**, *250*, 119379.
- [172] M. G. Müller, I. Lindner, I. Martin, W. Gärtner, A. R. Holzwarth, *Biophysical Journal* **2008**, *94*, 4370–4382.
- [173] M. Bischoff, G. Hermann, S. Rentsch, D. Strehlow, *Biochemistry* **2001**, *40*, 181–186.

- [174] C. Schumann, R. Groß, N. Michael, T. Lamparter, R. Diller, *ChemPhysChem* **2007**, *8*, 1657–1663.
- [175] K. Heyne, J. Herbst, D. Stehlik, B. Esteban, T. Lamparter, J. Hughes, R. Diller, *Biophysical Journal* **2002**, *82*, 1004–1016.
- [176] P. W. Kim, N. C. Rockwell, L. H. Freer, C.-W. W. Chang, S. S. Martin, J. C. Lagarias, D. S. Larsen, *The Journal of Physical Chemistry Letters* **2013**, *4*, 2605–2609.
- [177] S. M. Gottlieb, P. W. Kim, N. C. Rockwell, Y. Hirose, M. Ikeuchi, J. C. Lagarias, D. S. Larsen, *Biochemistry* **2013**, *52*, 8198–8208.
- [178] C.-W. W. Chang, S. M. Gottlieb, P. W. Kim, N. C. Rockwell, J. C. Lagarias, D. S. Larsen, *Journal of Physical Chemistry B* **2013**, *117*, 11229–11238.
- [179] H. Lehtivuori, I. Rissanen, H. Takala, J. Bamford, N. V. Tkachenko, J. A. Ihalainen, *The Journal of Physical Chemistry B* **2013**, *117*, 11049–11057.
- [180] P. Schwinté, H. Foerstendorf, Z. Hussain, W. Gärtner, M. A. Mroginski, P. Hildebrandt, F. Siebert, *Biophysical Journal* **2008**, *95*, 1256–1267.
- [181] M. Carrillo, S. Pandey, J. Sanchez, M. Noda, I. Poudyal, L. Aldama, T. N. Malla, E. Claesson, W. Y. Wahlgren, D. Feliz, V. Šrajer, M. Maj, L. Castillon, S. Iwata, E. Nango, R. Tanaka, T. Tanaka, L. Fangjia, K. Tono, S. Owada, S. Westenhoff, E. A. Stojković, M. Schmidt, *Structure* **2021**, *29*, 743–754.e4.
- [182] B. Borucki, D. von Stetten, S. Seibeck, T. Lamparter, N. Michael, M. A. Mroginski, H. Otto, D. H. Murgida, M. P. Heyn, P. Hildebrandt, *Journal of Biological Chemistry* **2005**, *280*, 34358–34364.
- [183] E. Consiglieri, A. Gutt, W. Gärtner, L. Schubert, C. Viappiani, S. Abbruzzetti, A. Losi, *Photochemical and Photobiological Sciences* **2019**, *18*, 2484–2496.
- [184] H. Foerstendorf, E. Mummert, E. Schäfer, H. Scheer, F. Siebert, *Biochemistry* **1996**, *35*, 10793–10799.
- [185] M. A. Mroginski, D. H. Murgida, P. Hildebrandt, *Accounts of Chemical Research* **2007**, *40*, 258–266.
- [186] C. Kneip, P. Hildebrandt, W. Schlamann, S. E. Braslavsky, F. Mark, K. Schaffner, *Biochemistry* **1999**, *38*, 15185–15192.

- [187] Y. Mizutani, S. Tokutomi, T. Kitagawa, *Biochemistry* **1994**, *33*, 153–158.
- [188] C. F. Zhang, D. L. Farrens, S. C. Björling, P. S. Song, D. S. Kliger, *Journal of the American Chemical Society* **1992**, *114*, 4569–4580.
- [189] A. Schmidt, L. Sauthof, M. Szczepek, M. F. Lopez, F. V. Escobar, B. M. Qureshi, N. Michael, D. Buhrke, T. Stevens, D. Kwiatkowski, D. von Stetten, M. A. Mrogin-ski, N. Krauß, T. Lamparter, P. Hildebrandt, P. Scheerer, *Nature Communications* **2018**, *9*, 1–13.
- [190] T. Rohmer, C. Lang, C. Bongards, K. B. S. S. Gupta, J. Neugebauer, J. Hughes, W. Gärtner, J. Matysik, *Journal of the American Chemical Society* **2010**, *132*, 4431–4437.
- [191] C. Schumann, R. Groß, M. M. Wolf, R. Diller, N. Michael, T. Lamparter, *Biophysical Journal* **2008**, *94*, 3189–3197.
- [192] P. W. Kim, J. Pan, N. C. Rockwell, C. W. Chang, K. C. Taylor, J. Clark Lagarias, D. S. Larsen, *Chemical Physics Letters* **2012**, *549*, 86–92.
- [193] Y. Yang, T. Stensitzki, L. Sauthof, A. Schmidt, P. Piwowarski, F. Velazquez Escobar, N. Michael, A. D. Nguyen, M. Szczepek, F. N. Brünig, R. R. Netz, M. A. Mrogin-ski, S. Adam, F. Bartl, I. Schapiro, P. Hildebrandt, P. Scheerer, K. Heyne, *Nature Chemistry* **2022**, *14*, 823–830.
- [194] H. Foerstendorf, T. Lamparter, J. Hughes, W. Gärtner, F. Siebert, *Photochemistry and Photobiology* **2000**, *71*, 655–661.
- [195] P. Eilfeld, W. Rüdiger, *Zeitschrift für Naturforschung - Section C Journal of Biosciences* **1985**, *40*, 109–114.
- [196] I. Chizhov, B. Zorn, D. J. Manstein, W. Gärtner, *Biophysical Journal* **2013**, *105*, 2210–2220.
- [197] E. Chen, V. N. Lapko, J. W. Lewis, P. S. Song, D. S. Kliger, *Biochemistry* **1996**, *35*, 843–850.
- [198] P. Savakis, S. De Causmaecker, V. Angerer, U. Ruppert, K. Anders, L. O. Essen, A. Wilde, *Molecular Microbiology* **2012**, *85*, 239–251.
- [199] C. M. Park, J. I. Kim, S. S. Yang, J. G. Kang, J. H. Kang, J. Y. Shim, Y. H. Chung, Y. M. Park, P. S. Song, *Biochemistry* **2000**, *39*, 10840–10847.

- [200] M. A. Mostoslavskii, M. D. Kravchenko, *Chemistry of Heterocyclic Compounds* **1970**, *4*, 45–47.
- [201] S. Wiedbrauk, H. Dube, *Tetrahedron Letters* **2015**, *56*, 4266–4274.
- [202] B. Maerz, S. Wiedbrauk, S. Oesterling, E. Samoylova, A. Nenov, P. Mayer, R. De Vivie-Riedle, W. Zinth, H. Dube, *Chemistry - A European Journal* **2014**, *20*, 13984–13992.
- [203] Z. Zhang, W. Wang, M. O'Hagan, J. Dai, J. Zhang, H. Tian, *Angewandte Chemie - International Edition* **2022**, *134*, e202205758.
- [204] S. Wang, B. Li, F. Zhang, *ACS Central Science* **2020**, *6*, 1302–1316.
- [205] A. Gerwien, M. Schildhauer, S. Thumser, P. Mayer, H. Dube, *Nature Communications* **2018**, *9*, 1–9.
- [206] A. Nenov, T. Cordes, T. T. Herzog, W. Zinth, R. De Vivie-Riedle, *Journal of Physical Chemistry A* **2010**, *114*, 13016–13030.
- [207] J. Plötner, A. Dreuw, *Journal of Physical Chemistry A* **2009**, *113*, 11882–11887.
- [208] K. Stallhofer, M. Nuber, F. Schüppel, S. Thumser, H. Iglev, R. De Vivie-Riedle, W. Zinth, H. Dube, *Journal of Physical Chemistry A* **2021**, *125*, 4390–4400.
- [209] S. Wiedbrauk, B. Maerz, E. Samoylova, A. Reiner, F. Trommer, P. Mayer, W. Zinth, H. Dube, *Journal of the American Chemical Society* **2016**, *138*, 12219–12227.
- [210] S. Wiedbrauk, B. Maerz, E. Samoylova, P. Mayer, W. Zinth, H. Dube, *Journal of Physical Chemistry Letters* **2017**, *8*, 1585–1592.
- [211] N. Regner, T. T. Herzog, K. Haiser, C. Hoppmann, M. Beyermann, J. Sauermann, M. Engelhard, T. Cordes, K. Rück-Braun, W. Zinth, *Journal of Physical Chemistry B* **2012**, *116*, 4181–4191.
- [212] K. Eggers, T. M. Fyles, P. J. Montoya-Pelaez, *Journal of Organic Chemistry* **2001**, *66*, 2966–2977.
- [213] S. Kitzig, M. Thilemann, T. Cordes, K. Rück-Braun, *ChemPhysChem* **2016**, *17*, 1252–1263.
- [214] K. Tanaka, K. Taguchi, S. Iwata, T. Irie, *Supramolecular Chemistry* **2005**, *17*, 637–642.

- [215] K. Tanaka, K. Kohayakawa, S. Iwata, T. Irie, *Journal of Organic Chemistry* **2008**, *73*, 3768–3774.
- [216] H. Dube, J. Rebek, *Angewandte Chemie - International Edition* **2012**, *51*, 3207–3210.
- [217] M. Guentner, E. Uhl, P. Mayer, H. Dube, *Chemistry - A European Journal* **2016**, *22*, 16433–16436.
- [218] K. Grill, H. Dube, *Journal of the American Chemical Society* **2020**, *142*, 19300–19307.
- [219] M. Guentner, M. Schildhauer, S. Thumser, P. Mayer, D. Stephenson, P. J. Mayer, H. Dube, *Nature Communications* **2015**, *6*, 8406.
- [220] A. Gerwien, P. Mayer, H. Dube, *Nature Communications* **2019**, *10*, 4449.
- [221] L. A. Huber, S. Thumser, K. Grill, D. Voříek, N. N. Bach, P. Mayer, H. Dube, *Chemistry – A European Journal* **2021**, *27*, 10758–10765.
- [222] N. N. Bach, V. Josef, H. Maid, H. Dube, *Angewandte Chemie - International Edition* **2022**, *61*, e202201882.
- [223] K. Ichimura, T. Seki, T. Tamaki, T. Yamaguchi, *Chemistry Letters* **1990**, *19*, 1645–1646.
- [224] T. Seki, T. Tamaki, T. Yamaguchi, K. Ichimura, *Bulletin of the Chemical Society of Japan* **1992**, *65*, 657–663.
- [225] T. Yamaguchi, T. Seki, T. Tamaki, K. Ichimura, *Bulletin of the Chemical Society of Japan* **1992**, *65*, 649–656.
- [226] T. Cordes, D. Weinrich, S. Kempa, K. Riesselmann, S. Herre, C. Hoppmann, K. Rück-Braun, W. Zinth, *Chemical Physics Letters* **2006**, *428*, 167–173.
- [227] T. Cordes, T. Schadendorf, K. Rück-Braun, W. Zinth, *Chemical Physics Letters* **2008**, *455*, 197–201.
- [228] T. Cordes, T. Schadendorf, B. Priewisch, K. Rück-Braun, W. Zinth, *Journal of Physical Chemistry A* **2008**, *112*, 581–588.
- [229] F. F. Graupner, T. T. Herzog, F. Rott, S. Oesterling, R. de Vivie-Riedle, T. Cordes, W. Zinth, *Chemical Physics* **2018**, *515*, 614–621.
- [230] A. Gerwien, T. Reinhardt, P. Mayer, H. Dube, *Organic Letters* **2018**, *20*, 232–235.

- [231] L. Köttner, M. Schildhauer, S. Wiedbrauk, P. Mayer, H. Dube, *Chemistry - A European Journal* **2020**, *26*, 10712–10718.
- [232] A. Warshel, *Nature* **1976**, *260*, 679–683.
- [233] W. Fuß, C. Kosmidis, W. E. Schmid, S. A. Trushin, *Angewandte Chemie - International Edition* **2004**, *43*, 4178–4182.
- [234] J. Saltiel, M. A. Bremer, S. Laohhasurayotin, T. S. Krishna, *Angewandte Chemie - International Edition* **2008**, *47*, 1237–1240.
- [235] M. W. Hoorens, M. Medved', A. D. Laurent, M. Di Donato, S. Fanetti, L. Slappendel, M. Hilbers, B. L. Feringa, W. Jan Buma, W. Szymanski, *Nature Communications* **2019**, *10*, 1–11.
- [236] M. Medved', M. W. Hoorens, M. Di Donato, A. D. Laurent, J. Fan, M. Taddei, M. Hilbers, B. L. Feringa, W. J. Buma, W. Szymanski, *Chemical Science* **2021**, *12*, 4588–4598.
- [237] S. Crespi, N. A. Simeth, M. Di Donato, S. Doria, C. N. Stindt, M. F. Hilbers, F. L. Kiss, R. Toyoda, S. Wesseling, W. J. Buma, B. L. Feringa, W. Szymański, *Angewandte Chemie - International Edition* **2021**, *133*, 25494–25499.
- [238] M. A. Kienzler, A. Reiner, E. Trautman, S. Yoo, D. Trauner, E. Y. Isacoff, *Journal of the American Chemical Society* **2013**, *135*, 17683–17686.
- [239] M. Izquierdo-Serra, M. Gascón-Moya, J. J. Hirtz, S. Pittolo, K. E. Poskanzer, È. Ferrer, R. Alibés, F. Busqué, R. Yuste, J. Hernando, P. Gorostiza, *Journal of the American Chemical Society* **2014**, *136*, 8693–8701.
- [240] K. Moritsugu, O. Miyashita, A. Kidera, *Physical Review Letters* **2000**, *85*, 3970–3973.
- [241] T. Ishikura, T. Yamato, *Chemical Physics Letters* **2006**, *432*, 533–537.
- [242] L. Martínez, A. C. M. Figueira, P. Webb, I. Polikarpov, M. S. Skaf, *The Journal of Physical Chemistry Letters* **2011**, *2*, 2073–2078.
- [243] N. Ota, D. A. Agard, *Journal of Molecular Biology* **2005**, *351*, 345–354.
- [244] S. Burendahl, L. Nilsson, *Proteins: Structure Function and Bioinformatics* **2012**, *80*, 294–306.
- [245] B. Erman, *Physical Biology* **2011**, *8*, 056003.

- [246] F. Piazza, Y.-H. Sanejouand, *EPL (Europhysics Letters)* **2009**, *88*, 68001.
- [247] H. M. Müller-Werkmeister, J. Bredenbeck, *Physical Chemistry Chemical Physics* **2014**, *16*, 3261–3266.
- [248] J. G. Löffler, E. Deniz, C. Feid, V. G. Franz, J. Bredenbeck, *Angewandte Chemie - International Edition* **2022**, *61*, e202200648.
- [249] V. Botan, E. H. G. Backus, R. Pfister, A. Moretto, M. Crisma, C. Toniolo, P. H. Nguyen, G. Stock, P. Hamm, *Proceedings of the National Academy of Sciences of the United States of America* **2007**, *104*, 12749–12754.
- [250] M. Linke, Y. Yang, B. Zienicke, M. A. Hammam, T. Von Haimberger, A. Zacarias, K. Inomata, T. Lamparter, K. Heyne, *Biophysical Journal* **2013**, *105*, 1756–1766.
- [251] J. Dasgupta, R. R. Frontiera, K. C. Taylor, J. C. Lagarias, R. A. Mathies, *Proceedings of the National Academy of Sciences of the United States of America* **2009**, *106*, 1784–1789.
- [252] X. Xu, A. Höppner, C. Wiebeler, K.-H. Zhao, I. Schapiro, W. Gärtner, *Proceedings of the National Academy of Sciences of the United States of America* **2020**, *117*, 2432–2440.
- [253] S. J. O. Hardman, D. J. Heyes, I. V. Sazanovich, N. S. Scrutton, *Biochemistry* **2020**, *59*, 2909–2915.
- [254] Y. Kim, Q.-Z. Xu, K.-H. Zhao, W. Gärtner, J. Matysik, C. Song, *Journal of Physical Chemistry B* **2020**, *124*, 7115–7127.
- [255] D. Buhrke, U. Kuhlmann, N. Michael, P. Hildebrandt, *ChemPhysChem* **2018**, *19*, 566–570.
- [256] A. R. D'Souza, M. R. Necelis, A. Kulesha, G. A. Caputo, O. V. Makhlynets, *Biomolecules* **2021**, *11*, 421.